REASSESSING THE BIOGENICITY OF PUTATIVE MICROFOSSILS IN THE 3.5 BILLION YEAR OLD APEX CHERT

By

Julienne Ruth Emry

Submitted to the graduate degree program in Geology and the Graduate Faculty of the University of Kansas in partial fulfillment of the requirements for the degree of Doctor of Philosophy.

_____

Alison Olcott Marshall, Co-Chair

_____

Craig Marshall, Co-Chair

_____

Greg Ludvigson

_____

Steven Egbert

_____

Robert Goldstein

Date approved: 7/20/2015

The Thesis Committee for Julienne Ruth Emry

certifies that this is the approved version of the following thesis:

REASSESSING THE BIOGENICITY OF PUTATIVE MICROFOSSILS IN THE 3.5 BILLION YEAR OLD APEX CHERT

_____

Alison Olcott Marshall, Co-Chair

_____

Craig Marshall, Co-Chair

Date approved: 7/24/2015

ABSTRACT

Scientists generally agree that life first arose on Earth over 3.5 Ga years ago, but the search for evidence of ancient life is a complex and difficult task due to the scarcity of relatively unaltered Archean rocks. The Pilbara craton contains some of the oldest, best exposed, relatively low-metamorphic grade Archean rocks and has therefore been a target of a variety of studies of ancient life. The Apex chert is a unit that has been extensively studied with a variety of analytical techniques primarily because it contains microstructures that were originally described as the oldest microbial fossils nearly 30 years ago. However, researchers have argued over the origin and composition of these microstructures and the debate continues today. The goal of this dissertation is to utilize a suite of samples collected from the Apex chert in 2006 in order to better understand the possible origin and composition of the microstructures, potential evidence for Archean life preserved in the rock record, and to highlight methodological issues that can affect the ability to accurately identify evidence for ancient life.

The introduction in Chapter 1 discusses issues with identifying signs of Archean life, introduces Raman spectroscopy, includes a brief introduction of the Apex chert to provide historical and geologic context and outlines the content of this dissertation. Chapter 2 is a literature review of the complex formational and alteration history of the Apex chert to provide geologic context. Chapter 3 documents the identification of hematite pseudofossils in the new samples and shows that carbonaceous material is present in the chert matrix instead of being associated with the microstructures as previously believed. Data quality issues can lead to the

misinterpretation of Raman spectroscopic data and the use of multiple types of data collection techniques and analyses that can aid in the identification of materials in geological datasets are presented. Chapter 4 includes an investigation of the structure and context of the previously identified matrix carbonaceous material. Petrographic and Raman spectroscopic data showed the presence of multiple generations of carbon in the Apex chert which raises questions about the degree of thermal alteration of the Apex chert and illustrates the importance of paragenetic context when studying evidence for ancient life such as carbonaceous material or putative microfossils. Chapter 5 illustrates how advanced Raman imaging data collection techniques can be affected by data quality issues such as autofluorescence and can lead to misidentification of materials. In order to address this problem, a software-based analytical method was developed to identify the spatial distribution of autofluorescence and a statistical method was developed to evaluate the quality of a post-acquisition data processing technique that is commonly used to address autofluorescence issues in Raman imaging datasets.

ACKNOWLEDGEMENTS

I would first like to thank my advisors Craig Marshall and Alison Olcott Marshall for providing me with the opportunity to study such fascinating samples and for introducing and promoting independent discovery of the pros and cons of a powerful and interesting analytical method that I had never heard of before starting my PhD. I'm also grateful to my committee members, Bob Goldstein, Greg Ludvigson, and Steve Egbert for their advice, moral support, and for being generous with their time. I must also thank John Kelly for being an invaluable sounding board for statistical questions and prompting me to think about things in different ways and develop my own methods. I would also like to thank NSF (grant EAR-1053241) and the Australian Research Council for funding my dissertation work. My Lawrence family, especially Jessica Clatterbuck, Bida Ingenloff, Karla Leslie, Ian Bowen, Tandis Bidgoli, Chad LaFever, Gabe Dalton, Amy Miller and Andreas Moller provided balanced degrees of support and distraction. In particular, I must thank my "creepy twin" Kate Ingenloff, for her continuous love, support, and fastidious editing skills, I wouldn't have made it this far without her. During the two summers I spent at OXY, Eric Arney, Koda Arney, Courtney Libben, Stefano Mizzoni, Heidi Hoffower, Claire Bailey, Gregg Pyke, Manuel Paz, and Robin Reith made Cali feel like another home. Special thanks go to Dave Defalice, my advocate and mentor in much more than just my internship, who pushed me by providing perspective on life, the universe, and everything when I needed it. I must also thank my parents, Larry and Pat, for choosing to make me a Ruth, and my brothers and sister, Laird, Dan, Ricardo Montano, and Laura Liggett for everyone's support of my crazy decision to leave a lucrative oil job to become a poor graduate student again. I'm also grateful to have been blessed with an amazing and constantly supportive second family, Gay and

David Emry, and Darci, Michael, Emry and Molly Davis. And last, but most definitely not least, my husband Jason. He willingly uprooted from Houston, supported us by crawling around in crawl spaces and attics chasing brown recluse spiders and other pests, brought me dinner and breakfast during all-night data collecting stints, and “de-Faulknerized” my writing. Jason, your love and support has allowed me to be the person I am, this degree is as much yours as it is mine. You were absolutely right when you joked you deserved your own acknowledgments page.

TABLE OF CONTENTS

The most exciting phrase to hear in science, the one that heralds new discoveries, is not 'Eureka!' but 'That's funny. . .'

--Issac Asimov

Chapter 1: General Introduction

INTRODUCTION

Scientists generally agree that life on Earth likely arose during the Archean, but the exact timing, environmental conditions, and the preservation of evidence in the geologic record continues to undergo substantial debate. The search for evidence of early life on Earth is particularly difficult because well-exposed Archean rocks are rare, typically tectonically and metamorphically complex, and have often undergone substantial surficial weathering. Potential evidence for life in the Precambrian was virtually unknown until the description of acritarch fossils from the 1.0 Ga Torridonian Sandstone in Scotland in 1899 (Peach *et al.*, 1907). Since then, researchers have utilized a variety of analytical techniques to propose multiple forms of evidence for identifying traces of life in the geologic record including isotopes, biomarkers, biominerals, and physical features such stromatolites, trace fossils, microbially-induced sedimentary structures (MISS), and microbial fossils (Wacey, 2009).

Evidence for life prior to ~1.0 Ga was nonexistent until the 1960's when researchers began to focus their searches on Archean aged rocks. Researchers have reported Archean microfossil-like features from the less than 3.7 Ga Greenland Isua Supracrustal Belt (Pflug and Jaeschke-Boyer, 1979), the 3.5-3.0 Ga African Barberton craton (Engel *et al.*, 1968; Glikson *et*

al., 2008; Javaux *et al.*, 2010; Knoll and Barghoorn, 1977; Schopf and Barghoorn, 1967; Walsh, 1992; Walsh and Lowe, 1985; Westall, de Ronde, *et al.*, 2006; Westall *et al.*, 2001) and the Pilbara Craton in Western Australia (Awramik *et al.*, 1983; Duck *et al.*, 2007; Kiyokawa *et al.*, 2006; Marshall *et al.*, 1964; Rasmussen, 2000; Schopf and Packer, 1987; Schopf, 1983; Ueno *et al.*, 2006; Wacey *et al.*, 2011; Westall, de Vries, *et al.*, 2006). Historically, putative Archean microfossils were identified and classified based on observed morphological similarities to modern microbes (e.g. Awramik *et al.* 1983, Marshall *et al.* 1964, Schopf and Packer 1987, Schopf, 1983). Further study of these microstructures and lab based studies have shown that abiotic processes can create mineral biomorphic features and petrographic structures such as fluid inclusions or veins can mimic the morphology of microfossils; therefore identification based on morphology alone is insufficient (e.g. Brasier and Wacey, 2012; Bridgwater *et al.*, 1981; Carnerup *et al.*, 2004; Garcia Ruiz, 2002; Garcia Ruiz *et al.*, 2003; Kellermeier *et al.*, 2012; Schopf *et al.*, 2010; Wacey, 2009). As a result, researchers have proposed criteria based on a combination of context, morphology, and chemistry that must be met in order to identify *bona fide* microfossils (Brasier and Wacey, 2012; Schopf *et al*., 2010; Wacey, 2009).

Experimental fossilization studies and work based on younger rocks is providing information on the likelihood, methods, and conditions that may lead to the preservation of microbial fossils, but the results have been mixed depending on complex interactions of several factors including: microbial species and metabolism, experimental and natural chemical conditions, and the timing and degree of thermal treatment or alteration (e.g. Benning *et al.*, 2004; Hinman and Walter, 2005; Li *et al.*, 2014; Orange *et al.*, 2013; Toporski *et al.*, 2002; Westall *et al.*, 1995) These factors coupled with the complex alteration histories Archean rocks have undergone make evaluating the likelihood for the preservation of microbial body fossils in

Archean rocks a complex issue. Even if body fossils are not preserved, remnants of organic carbon may be preserved in Archean rocks and carbonaceous materials from a variety of Archean units have been studied to search for evidence of early life (e.g. Allwood *et al.*, 2006; Bernard and Papineau, 2014; Gourier *et al.*, 2013; Lindsay *et al.*, 2005; Marshall *et al.*, 2014; Marshall *et al.*, 2007; Ohtomo *et al.*, 2014; Sforna *et al.*, 2014; Wanger *et al.*, 2012). But, the simple presence of carbonaceous material in Archean rocks is not necessarily evidence for Archean life and similar criteria based on chemistry, structure, and context is necessary to understand the origin of carbonaceous materials in Archean rocks (Lindsay *et al*., 2005; Marshall *et al.*, 2010b; Pasteris, 1989; Pasteris and Wopenka, 2003). Raman spectroscopy has been shown to be a powerful technique to characterize the composition and structure of graphitic and other carbonaceous materials and has been utilized by several researchers to study carbonaceous material found in Archean rocks (e.g. Allwood *et al.;* Bower *et al.*, 2013; Brasier *et al.*, 2002; Crosby *et al.*, 2014; Fries and Steele, 2011; Foucher and Westall, 2012; Javaux *et al.*, 2010; Marshall *et al.*, 2007; Marshall *et al*., 2010; Schopf *et al.*, 2002a; Sforna *et al.*, 2014)

Raman Spectroscopy in the Geosciences

Although Raman scattering in minerals was first studied in the 1930's, it was not until the 1960's when Raman spectroscopy became more commonly used to analyze geological samples (Neuville *et al.*, 2014). Raman spectroscopy has become a popular technique for geoscience and geomaterials applications because it is generally non-destructive, requires little to no sample preparation, and can provide chemical and structural information relatively quickly and researchers have noted an exponential increase in Raman studies in mineralogy, crystallography

and geochemistry research over the past 25-30 years (Bernard *et al.*, 2008; Marshall *et al.*, 2010a; Marshall and Marshall, 2011; Marshall and Olcott Marshall, 2013; Nasdala *et al.*, 2012; Nasdala *et al.*, 2004). Researchers have also observed a substantial increase over the past 30 years in the application of Raman based techniques to astro- and geobiological studies including the composition of microfossils, the study of ancient carbonaceous material, and other potential evidence of life in the geological record (Bernard *et al*., 2008; Marshall *et al*., 2010b; Marshall and Marshall, 2011; Marshall and Olcott Marshall, 2013; Nasdala *et al*., 2012; Nasdala *et al*., 2004). Geoscientists are typically self-taught in Raman spectroscopic techniques which has led to the identification and discussion of a variety of published misunderstandings regarding limitations of the data collection techniques, the use of inappropriate data processing methods, and the misidentification of materials (Marshall and Olcott Marshall 2011, Marshall and Olcott Marshall, 2013; Nasdala *et al*., 2012; Nasdala *et al*., 2004; Lee, 2012) The use of Raman spectroscopic techniques will likely continue to rise due to the increasing availability and ease of use of commercial Raman systems. Recent technological advances have also allowed for advanced data collection techniques including confocal depth profiling and Raman imaging which require more complex, computer based analytical techniques (Bernard *et al*., 2008; Delhaye and Dhamelincourt, 1975; Lee, 2012; Rosasco *et al.*, 1975). Additionally, the 2018 ExoMars rover includes a Raman spectrometer (ESA, 2015) and the 2020 NASA will contain two Raman instruments (SuperCam and SHERLOC) that will be utilized to identify materials and search for and analyze organic compounds (NASA, n.d.). Understanding the strengths and weaknesses of Raman analytical techniques, data analysis, and the types of geological data that may provide evidence for life is an important endeavor not only to better understand the history of Earth, but also the search for life on other planets.

Raman Spectroscopic Theory

Raman spectroscopy is a form of vibrational spectroscopy based on inelastic scattering of light which can be used to identify and provide compositional and structural information for chemical compounds. When a monochromatic laser source is impinged on a sample, light can be either Rayleigh scattered or Raman scattered. In Rayleigh scattering the energy (or wavelength) of the incident and scattered light are equal. Raman scattering involves a shift in the energy (wavelength) of the light by a quantum of energy that corresponds to a specific molecular transition (rotational, translational, vibrational, or electronic) within the material (Marshall *et al.*, 2010b). If a change in the polarizability of a molecule occurs during molecular vibration, the vibrational mode will Raman scatter light and is referred to as Raman active. Raman active vibrational modes produce the characteristic bands seen in Raman spectra. In solids, the molecular vibrations occur as waves of similar frequency throughout the crystal lattice and these quantized units of vibrational energy are called phonons. Solids can have two types of phonons, acoustical (A) in which the neighboring atoms move in phase, and optical (O) in which the neighboring atoms move out of phase (Smith and Dent, 2005). The phonons can be longitudinal (L) or transverse (T) which occur parallel or perpendicular, respectively, to the way the atoms are being displaced during vibration (Smith and Dent, 2005). The composition, crystal structure, and symmetry of minerals and mineraloids affects which phonon modes will be Raman active, therefore the presence or absence of diagnostic Raman bands can be used to identify materials and study their molecular structure (Smith and Dent, 2006).

Raman Hyperspectral Imaging Techniques

Traditionally, Raman spectroscopic analyses involved collecting a spectrum from a single point of interest at the surface of a sample. Technological advancements over the past 40 years have expanded the analytical capabilities of Raman systems providing more advanced and complex data collection techniques including hyperspectral imaging (Bernard *et al*., 2008; Lee, 2012). Rather than providing a single spectrum from one location in a sample, Raman imaging creates a 2-D or 3-D grid composed of multiple spectra based on a user defined region of interest and *x*,*y* spatial resolution (Figure 1).

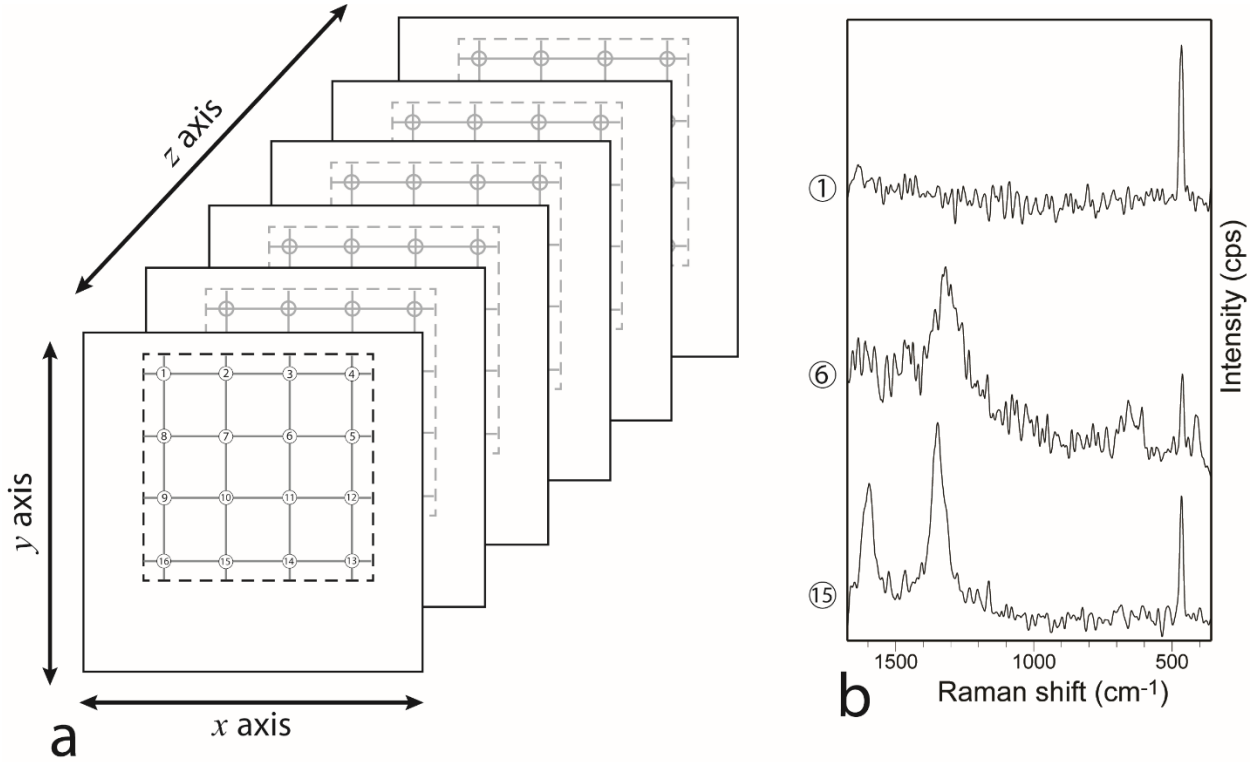

Figure 1. Schematic diagram of a Raman hyperspectral dataset. The dashed boxes represent the two-dimensional (*x*, *y* axes) region where the hyperspectral dataset was acquired at multiple focal planes at depth (*z* axis) within a sample (a). Raman hyperspectral datasets are composed of multiple spectra that are acquired based on an operator defined spatial resolution schematically represented in this figure by the numbered circles (a) which correspond to individual spectra from the dataset. Adapted from Lee, 2012. (Emry *et al*, 2015)

These datasets are then analyzed using computer-based statistical techniques to create Raman images. Before the development of software-based line scanning and global imaging techniques, acquiring comparable datasets on a point by point basis was an extremely time consuming endeavor (Lee, 2012). Therefore, hyperspectral Raman imaging techniques have the advantage of rapid collection of hundreds to tens of thousands of spectra that can be analyzed to create Raman images which are visual representations of the spatial distribution of materials. This technique has been used for a variety of geological applications (e.g. Bernard *et al*., 2008; Marshall and Olcott Marshall, 2013; Nasdala *et al*., 2012; Nasdala *et al*., 2004). Specifically for paleobiological applications it has been used to study the composition of microfossil-like features (Bower *et al.*, 2013; Crosby *et al.*, 2014; Fries and Steele, 2011; Marshall *et al.*, 2011a; Schopf and Kudryavtsev, 2009; Schopf and Kudryavtsev, 2014; Schopf *et al.*, 2002a) and search for biomarkers (Foucher and Westall, 2012).

Unfortunately, there is an important trade-off to consider when utilizing hyperspectral imaging compared to point spectral analysis. During point spectral analysis operators can change various collection parameters including the spectral range, laser excitation wavelength, power, excitation time, and the number of spectral acquisitions collected and integrated into the final spectrum to maximize data quality. In order to collect large numbers of spectra quickly, software-based line scanning and global imaging techniques typically require fixed collection parameters for a single dataset which can significantly affect data quality (Lee, 2012). Geological samples are heterogeneous, therefore the limitation of fixed spectral collection parameters may substantially affect data quality on a spectrum by spectrum scale. Spatial variations in data quality can subsequently affect the results of the statistical analyses used to

create Raman images and ultimately, negatively impact the ability to characterize or interpret the spatial distribution of materials.

The Apex chert

Microstructures in the 3.5 Ga Apex chert from Western Australia are arguably the most well known, best publicised, and highly debated putative Archean microfossils. These microstructures were originally described and classified as the fossilized remains of chroococcalean bacteria preserved in rocks formed in a fluviomarine environment (Schopf and Packer, 1983). The biogenecity of these structures was initially based on morphological description and whole rock or kerogen isolate carbon isotope analyses (Schopf, 1999; Schopf and Packer, 1987; Schopf, 1983). In 2002, a paper published in the journal *Nature* presented point Raman spectra and Raman images that were used to interpret that the microstructures were composed of biogenic carbon (Schopf *et al*., 2002a). In the same issue of *Nature*, Brasier *et al.* (2002) presented point Raman spectra that verified the presence of carbon in the microstructures, but reinterpreted the Apex chert a fault-controlled hydrothermal dike system based on field mapping and SEM-EDX chemical analysis. The researchers then reinterpreted the microstructures as abiotic hydrothermally produced carbonaceous artifacts based on their petrographic context (Brasier *et al*., 2002). Discussion of the origin of these microstructures, the environment of formation of the Apex chert and whether evidence of life would have likely been preserved in continued consistently for the next 9 years (Brasier, 2004; Brasier *et al.*, 2005; Brasier *et al.*, 2011; Pinti *et al.*, 2009; Schopf, 1993; Schopf, 1999; Schopf and Kudryavtsev, 2005; Schopf and Kudryavtsev, 2009, 2011; Schopf *et al.*, 2002b; Schopf *et al.*, 2007). More

recent debate regarding the origin and composition of the microstructures and carbonaceous material in the Apex chert has been sparked by publication of a portion of the work presented in Chapter 3 indentifying hematite pseudofossils in the new samples (Marshall *et al.*, 2011b), the Raman study of the Apex chert carbon in Chapter 4, and several studies by other researchers on the Apex chert carbonaceous material and mineral assemblages (Olcott Marshall *et al*, 2012, Olcott Marshall and Marshall, 2014; Pinti *et al*., 2009; Pinti *et al.*, 2013; Schopf and Kudryavtsev, 2011, 2012, 2013; Schopf and Kudryavtsev, 2014; Sforna *et al*., 2014).

Dissertation Content

The work presented here is a characterization of a new suite of Apex chert samples collected in 2006. Petrographic and Raman spectroscopic techniques applied to these samples reinforced the importance of studying the context and chemistry of putative microfossils and other potential evidence for life preserved in geological samples. Additionally, these samples provided insights on potential issues with the use of Raman imaging to appropriately characterize the distribution of materials in geological samples. To set the stage for more in depth analysis of this unit, Chapter 2 provides a review of the geologic history of the Pilbara craton and the Apex chert to provide context on why it has been an important target of studies of early life and why evidence may be difficult to find in such tectonically and metamorphically complex rocks.

Chapter 3 is an expansion on our published study that identified hematite pseudofossils in the new samples and documented the presence of carbonaceous material in the chert matrix including subsequently collected and analyzed Raman point, confocal depth profile, and Raman

image data. Data quality issues that may lead to misinterpretations and the use of multiple types of Raman image data collection techniques and analyses that can aid in the identification of materials in geological datasets is also discussed.

In Chapter 4, further investigation of the structure and possible origin of the previously identified matrix carbonaceous material is presented. Petrographic and Raman spectroscopic data showed the presence of multiple generations of carbon in the Apex chert. This work raises questions regarding the degree and nature of thermal and metamorphic alteration of the Apex chert, the autochthonous or allochthonous nature of the carbonaceous material, and illustrates the importance of paragenetic context when studying ancient carbon and putative microfossils.

Chapter 5 illustrates how autofluorescence issues can cause misidentification of materials in hyperspectral datasets. A software-based analytical method to identify spectra affected by autofluorescence in Raman image datasets and a statistical method to compare baseline correction methods in order to better understand the strengths and weaknesses of hyperspectral data collection and subsequent image generation from geological samples are presented.

Two Appendices are included to present additional data and analyses that were performed as a part of this dissertation. Appendix A includes a commentary on Raman image computer-based image manipulation techniques that can affect the accuracy of the spatial resolution of materials in Raman images. Appendix B includes preliminary fluid inclusion data from one of the vein phases in the Apex chert.

References

Allwood, A. C., Walter, M. R., & Marshall, C. P. (2006). Raman spectroscopy reveals thermal palaeoenvironments of c.3.5 billion-year-old organic matter. *Vibrational Spectroscopy, 41*(2), 190-197.

Awramik, S. M., Schopf, J. W., & Walter, M. R. (1983). Filamentous Fossil Bacteria from the Archean of Western Austraila.. *Precambrian Research, 20*(2-4), 357-374.

Benning, L. G., Phoenix, V. R., Yee, N., & Konhauser, K. O. (2004). The dynamics of cyanobacterial silicification: an infrared micro-spectroscopic investigation1. *Geochimica et Cosmochimica Acta, 68*(4), 743-757.

Bernard, S., Beyssac, O., & Benzerara, K. (2008). Raman Mapping Using Advanced Line-Scanning Systems: Geological Applications. *Applied Spectroscopy, 62* (11), 1180-1188.

Bernard, S., & Papineau, D. (2014). Graphitic Carbons and Biosignatures. *Elements, 10*(6), 435-440.

Bower, D. M., Steele, A., Fries, M. D., & Kater, L. (2013). Micro Raman Spectroscopy of Carbonaceous Material in Microfossils and Meteorites: Improving a Method for Life Detection. *Astrobiology, 13*(1), 103-113.

Brasier, M. (2004). Earth's Oldest (3.5 Ga) Fossils and the 'Early Eden Hypothesis: Questioning the Evidence. *Origins of Life and Evolution of the Biosphere, 34*, 257-269.

Brasier, M. D., Green, O. R., Lindsay, J. F., McLoughlin, N., Steele, A., & Stoakes, C. (2005). Critical testing of Earth's oldest putative fossil assemblage from the ~3.5 Ga Apex chert, Chinaman Creek, Western Australia. *Precambrian Research, 140*, 55-102.

Brasier, M. D., Green, O. R., Lindsay, J. F., McLoughlin, N., Stoakes, C., Brasier, A. T., & Wacey, D. (2011). *Geology and Putative Microfossil Assemblage of the c. 3460 Ma "Apex chert", Chinaman Creek, Western Austraila-A Field and Petrographic Guide* (Vol. 2011/7). Perth, Austraila: Geological Society of Western Australia.

Brasier, M. D., & Wacey, D. (2012). Fossils and astrobiology: new protocols for cell evolution in deep time. *International Journal of Astrobiology, 11*(4), 217-228.

Bridgwater, D., Allaart, J. H., Schopf, J. W., Klein, C., Walter, M. R., Barghoorn, E. S., Strother, P., Knoll, A. & Gorman, B. E. (1981). Microfossil-like objects from the Archaean of Greenland: a cautionary note. *Nature, 289* (5793), 51-53.

Carnerup, A., Hyde, S., Larsson, A.-K., Christy, A., & GarcÍa-Ruiz, J. (2004). Silica-Carbonate Biomorphs and the Implications for Identification Of Microfossils. In J. Seckbach, J. Chela-Flores, T. Owen & F. Raulin (Eds.), *Life in the Universe* (Vol. 7, pp. 221-222): Springer Netherlands.

Crosby, C. H., Bailey, J. V., & Sharma, M. (2014). Fossil evidence of iron-oxidizing chemolithotrophy linked to phosphogenesis in the wake of the Great Oxidation Event. *Geology, 42*(11), 1015-1018.

Delhaye, M., & Dhamelincourt, P. (1975). Raman microprobe and microscope with laser excitation. *Journal of Raman Spectroscopy, 3*(1), 33-43.

Duck, L. J., Glikson, M., Golding, S. D., & Webb, R. E. (2007). Microbial remains and other carbonaceous forms from the 3.24 Ga Sulphur Springs black smoker deposit, Western Australia. *Precambrian Research, 154*(3–4), 205-220.

Emry J.R., Marshall A.O. and Marshall C.P. (2015) Evaluating the Effects of Autofluorescence during Raman Hyperspectral Imaging. *Geostandards and Geoanalytical Research***,** DOI: 0.1111/j.1751-908X.2015.00354.x

Engel, A. E. J., Nagy, B., Nagy, L. A., Engel, C. G., Kremp, G. O. W., & Drew, C. M. (1968). Algal-like forms in Onverwacht Series, South Africa: oldest recognized lifelike forms on Earth. *Science, 161*, 1005-1008.

ESA, (2015), *Robotic Exploration of Mars*, European Space Agency, Web. 23 Feb 2015. http://exploration.esa.int/jump.cfm?oid=45103

Foucher, F., & Westall, F. (2012). Raman Imaging of Metastable Opal in Carbonaceous Microfossils of the 700–800 Ma Old Draken Formation. *Astrobiology, 13*(1), 57-67.

Fries, M., & Steele, A. (2011). Raman Spectroscopy and Confocal Raman Imaging in Mineralogy and Petrography. In T. Dieing, O. Hollricher & J. Toporski (Eds.), *Confocal Raman Microscopy* (Vol. 158, pp. 111-135): Springer Berlin Heidelberg.

Garcia Ruiz, J. M. (2002). Morphology: An Ambiguous Indicator of Biogenicity. *Astrobiology, 2*, 353-369.

Garcia Ruiz, J. M., Hyde, S. T., Carnerup, A. M., Christy, A. G., Van Kranendonk, M. J., & Welham, N. J. (2003). Self-Assembled Silica-Carbonate Structure sand Detection of Ancient Microfossils. *Science, 302*, 1194-1197.

Glikson, M., Duck, L. J., Golding, S. D., Hofmann, A., Bolhar, R., Webb, R., . . . Sly, L. I. (2008). Microbial remains in some earliest Earth rocks: Comparison with a potential modern analogue. *Precambrian Research, 164*(3–4), 187-200.

Gourier, D., Delpoux, O., Binet, L., & Vezin, H. (2013). Nuclear Magnetic Biosignatures in the Carbonaceous Matter of Ancient Cherts: Comparison with Carbonaceous Meteorites. *Astrobiology, 13*(10), 932-947.

Hinman, N. W., & Walter, M. R. (2005). Textural Preservation in Siliceous Hot Spring Deposits During Early Diagenesis: Examples from Yellowstone National Park and Nevada, U.S.A. *Journal of Sedimentary Research, 75*(2), 200-215.

Javaux, E. J., Marshall, C. P., & Bekker, A. (2010). Organic-walled microfossils in 3.2-billion-year-old shallow-marine siliciclastic deposits. *Nature, 463*(7283), 934-938.

Kellermeier, M., Cölfen, H., & García-Ruiz, J. M. (2012). Silica Biomorphs: Complex Biomimetic Hybrid Materials from "Sand and Chalk". *European Journal of Inorganic Chemistry, 2012*(32), 5123-5144.

Kiyokawa, S., Ito, T., Ikehara, M., & Kitajima, F. (2006). Middle Archean volcano-hydrothermal sequence: Bacterial microfossil-bearing 3.2 Ga Dixon Island Formation, coastal Pilbara terrane, Australia. *Geological Society of America Bulletin, 118*(1-2), 3-22.

Knoll, A. H., & Barghoorn, E. S. (1977). Archean Microfossils Showing Cell Division from the Swaziland System of South Africa. *Science, 198*(4315), 396-398.

Lee, E. (2012). Imaging Modes. In A. Zoubir (Ed.), *Raman Imaging* (Vol. 168, pp. 1-37): Springer Berlin Heidelberg.

Li, J., Bernard, S., Benzerara, K., Beyssac, O., Allard, T., Cosmidis, J., & Moussou, J. (2014). Impact of biomineralization on the preservation of microorganisms during fossilization: An experimental perspective. *Earth and Planetary Science Letters, 400*(0), 113-122.

Lindsay, J. F., Brasier, M. D., McLoughlin, N., Green, O. R., Fogel, M., Steele, A., & Mertzman, S. A. (2005). The problem of deep carbon--An Archean paradox. *Precambrian Research, 143*(1-4), 1-22.

Marshall, C. G. A., May, J. W., & Perret, C. J. (1964). Fossil Microorganisms: Possible Presence in Precambrian Shield of Western Australia. *Science, 144*(3616), 290-292.

Marshall, C. P., Edwards, H. G., & Jehlicka, J. (2010). Understanding the application of Raman spectroscopy to the detection of traces of life. *Astrobiology, 10*(2), 229-243.

Marshall, C. P., Emry, J. R., & Olcott Marshall, A. (2011b). Haematite pseudomicrofossils present in the 3.5-billion-year-old Apex Chert. *Nature Geoscience, 4*(4), 240-243.

Marshall, C. P., Love, G. D., Snape, C. E., Hill, A. C., Allwood, A. C., Walter, M. R.,Van Kranandonk, M., Bowden, S. Sylva, S., Summons, R. E. (2007). Structural characterization of kerogen in 3.4 Ga Archaean cherts from the Pilbara Craton, Western Australia. *Precambrian Research, 155*(1-2), 1-23.

Marshall, C. P., & Olcott Marshall, A. (2011). Hematite and carbonaceous materials in geological samples: A cautionary tale. *Spectrochimica Acta Part A: Molecular and Biomolecular Spectroscopy, 80*(1), 133-137.

Marshall, C. P., & Olcott Marshall, A. (2013). Raman hyperspectral imaging of microfossils: potential pitfalls. *Astrobiology, 13*(10), 920-931.

NASA, (n.d.), Mars Future Rover Plans, NASA Jet Propulsion Laboratory, California Institute of Technology, Web. Feb 2015. http://mars.nasa.gov/mars2020/mission.

Nasdala, L., Beyssac, O., William Schopf, J., & Bleisteiner, B. (2012). Application of Raman-based images in the Earth sciences. In A. Zoubir (Ed.), *Raman Imaging* (Vol. 168, pp. 145-187): Springer Berlin Heidelberg.

Nasdala, L., Smith, D. C., Kaindl, R., & Ziemann, M. A. (2004). Raman spectroscopy: analytical perspectives in mineralogical research. *EMU notes in mineralogy*, 281-343.

Neuville, D. R., de Ligny, D., & Henderson, G. S. (2014). Advances in Raman Spectroscopy Applied to Earth and Material Sciences. *Reviews in Mineralogy and Geochemistry, 78*(1), 509-541.

Ohtomo, Y., Kakegawa, T., Ishida, A., Nagase, T., & Rosing, M. T. (2014). Evidence for biogenic graphite in early Archaean Isua metasedimentary rocks. *Nature Geosci, 7*(1), 25-28.

Olcott Marshall, A., Jehlicka, J., Rouzaud, J. N., & Marshall, C. P. (2014). Multiple generations of carbonaceous material deposited in Apex chert by basin-scale pervasive hydrothermal fluid flow. *Gondwana Research, 25*(1), 284-289.

Olcott Marshall, A. & Marshall, C. P. (2013). Comment on "Biogenicity of Earth's earliest fossils: A resolution of the controversy" by J. W. Schopf and A. B. Kudryavtsev, Gondwana Research, Volume 22, Issue 3-4, Pages 761-771. *Gondwana Research, 23*(4), 1654-1655.

Orange, F., Dupont, S., Goff, O. L., Bienvenu, N., Disnar, J.-R., Westall, F., & Le Romancer, M. (2013). Experimental fossilization of the Thermophilic Gram-positive Bacterium Geobacillus SP7A: A Long Duration Preservation Study. *Geomicrobiology Journal, 31*(7), 578-589.

Pasteris, J. D. (1989). In situ analysis in geological thin-sections by laser Raman microprobe microspectroscopy: a cautionary tale. *Applied Spectroscopy, 43*, 567-570.

Pasteris, J. D., & Wopenka, B. (2003). Necessary, but Not Sufficient: Raman Identification of Disordered Carbon as a Signature of Ancient Life. *Astrobiology, 3*(4), 727-738.

Peach, B. N., Horne, J., Gunn, W., Clough, C. T., & Hinxman, L. W. (1907). *The Geological Structure of the Northwest Highlands of Scotland* (Vol. accessed March 3 2015). Internet Archive https://archive.org/details/geologicalstruc00peacgoog.

Pflug, H. D., & Jaeschke-Boyer, H. (1979). Combined structural and chemical analysis of 3,800-Myr-old microfossils. *Nature, 280*(5722), 483-486.

Pinti, D. L., Mineau, R., & Clement, V. (2009). Hydrothermal alteration and microfossil artefacts of the 3,465-million-year-old Apex chert. *Nature Geosci, 2*(9), 640-643.

Pinti, D. L., Mineau, R., & Clement, V. (2013). Comment on "Biogenicity of Earth's earliest fossils: a resolution of the controversy" by J. William Schopf and Anatoliy B. Kudryavtsev, Gondwana Research 22 (2012), 761-771. *Gondwana Research, 23*(4), 1652-1653.

Rasmussen, B. (2000). Filamentous microfossils in a 3,235-million-year-old volcanogenic massive sulphide deposit. *Nature, 405*(6787), 676-679.

Rosasco, G. J., Etz, E. S., & Cassatt, W. A. (1975). Analysis of Discrete Fine Particles by Raman Spectroscopy *Applied Spectroscopy, 29*(5), 396-404.

Schopf, J. W. (1993). Microfossils of the Early Archean Apex Chert: New Evidence of the Antiquity of Life. *Science, 260*(5108), 640-646.

Schopf, J. W. (1999). *Cradle of Life: Discovery of Earth's Earliest Fossils*. New York: Princeton University Press.

Schopf, J. W., & Barghoorn, E. S. (1967). Alga-Like Fossils from the Early Precambrian of South Africa. *Science, 156*(3774), 508-512.

Schopf, J. W., & Kudryavtsev, A. B. (2005). Three-dimensional Raman imagery of precambrian microscopic organisms. *Geobiology, 3*(1), 1-12.

Schopf, J. W., & Kudryavtsev, A. B. (2009). Confocal laser scanning microscopy and Raman imagery of ancient microscopic fossils. *Precambrian Research, 173*(1-4), 39-49.

Schopf, J. W., & Kudryavtsev, A. B. (2011). Biogenicity of Apex Chert microstructures. *Nature Geosci, 4*(6), 346-347.

Schopf, J. W., & Kudryavtsev, A. B. (2012). Biogenicity of Earth's earliest fossils: A resolution of the controversy. *Gondwana Research, 22*(3–4), 761-771.

Schopf, J. W., & Kudryavtsev, A. B. (2013). Reply to the comments of D.L. Pinti, R. Mineau and V. Clement, and of A.O. Marshall and C.P. Marshall on “Biogenicity of Earth's earliest fossils: A resolution of the controversy” by J. William Schopf and Anatoliy B. Kudryavtsev, Gondwana Research 22 (2012), 761-771. *Gondwana Research, 23*(4), 1656-1658.

Schopf, J. W., & Kudryavtsev, A. B. (2014). *Biogenecity of Earth's Earliest Fossils* (Vol. 7). New York: Springer.

Schopf, J. W., Kudryavtsev, A. B., Agresti, D. G., Wdowiak, T. J., & Czaja, A. D. (2002a). Laser-Raman imagery of Earth's earliest fossils. *Nature, 416*, 73-76.

Schopf, J. W., Kudryavtsev, A. B., Agresti, D. G., Wdowiak, T. J., & Czaja, A. D. (2002b). Laser-Raman spectroscopy (Communication arising): Images of the Earth's earliest fossils? *Nature, 420*(6915), 477-477.

Schopf, J. W., Kudryavtsev, A. B., Czaja, A. D., & Tripathi, A. B. (2007). Evidence of Archean life: Stromatolites and microfossils. *Precambrian Research, 158*(3-4), 141-155.

Schopf, J. W., Kudryavtsev, A. B., Sugitani, K., & Walter, M. R. (2010). Precambrian microbe-like pseudofossils: A promising solution to the problem. *Precambrian Research, 179*(1–4), 191-205.

Schopf, J. W., & Packer, B. M. (1987). Early Archean (3.3-Billion to 3.5-Billion-Year-Old) Microfossils from Warrawoona Group, Australia. *Science, 237*(4810), 70-73.

Schopf, J. W. a. W., MR. (1983). *Archean microfossils: new evidence of ancient microbes*: Princeton University Press.

Sforna, M. C., van Zuilen, M. A., & Philippot, P. (2014). Structural characterization by Raman hyperspectral mapping of organic carbon in the 3.46 billion-year-old Apex chert, Western Australia. *Geochimica et Cosmochimica Acta, 124*, 18-33.

Smith, E., & Dent, G. (2005). *Modern Raman Spectroscopy: A Practical Approach*. West Sussex, Engand: John Wiley and Sons.

Toporski, J. K. W., Steele, A., Westall, F., Thomas-Keprta, K. L., & McKay, D. S. (2002). The Simulated Silicification of Bacteria— New Clues to the Modes and Timing of Bacterial Preservation and Implications for the Search for Extraterrestrial Microfossils. *Astrobiology, 2*(1), 1-26.

Ueno, Y., Isozaki, Y., & McNamara, K. J. (2006). Coccoid-like microstructures in a 3.0 Ga chert from western Australia. *International Geology Review, 48*(1), 78-88.

Wacey, D. (2009). *Early Life on Earth: A Practical Guide*: Springer.

Wacey, D., Kilburn, M. R., Saunders, M., Cliff, J., & Brasier, M. D. (2011). Microfossils of sulphur-metabolizing cells in 3.4-billion-year-old rocks of Western Australia. *Nature Geoscience, 4*(10), 698-702.

Walsh, M. M. (1992). Microfossils and Possible Microfossils from the Early Archean Onverwacht Group, Barberton Mountain Land, South Africa. *Precambrian Research, 54*(2-4), 271-293.

Walsh, M. M., & Lowe, D. R. (1985). Filamentous microfossils from the 3,500-Myr-old Onverwacht Group, Barberton Mountain Land, South Africa. *Nature, 314*(6011), 530-532.

Wanger, G., Moser, D., Hay, M., Myneni, S., Onstott, T. C., & Southam, G. (2012). Mobile hydrocarbon microspheres from > 2-billion-year-old carbon-bearing seams in the South African deep subsurface. *Geobiology, 10*(6), 496-505.

Westall, F., Boni, L., & Guerzoni, E. (1995). The Experimental Silicification of Microorganisms. *Paleontology, 38*(3), 495-528.

Westall, F., de Ronde, C. E. J., Southam, G., Grassineau, N., Colas, M., Cockell, C., & Lammer, H. (2006). *Implications of a 3.472–3.333 Gyr-old subaerial microbial mat from the Barberton greenstone belt, South Africa for the UV environmental conditions on the early Earth* (Vol. 361).

Westall, F., de Vries, S. T., Nijman, W., Rouchon, V., Orberger, B., Pearson, V., Watson, J., Verchovsky, A., Wright, I., Rouzaud, J., Marchesini, D., & Severine, A. (2006). The 3.466 Ga "Kitty's Gap Chert," an early Archean microbial ecosystem. *Geological Society of America Special Papers, 405*, 105-131.

Westall, F., de Wit, M. J., Dann, J., van der Gaast, S., de Ronde, C. E. J., & Gerneke, D. (2001). Early Archean fossil bacteria and biofilms in hydrothermally-influenced sediments from the Barberton greenstone belt, South Africa. *Precambrian Research, 106*(1–2), 93-116.

Chapter 2: Geologic History and Context of the Apex chert

GENERAL GEOLOGY OF AUSTRALIA AND THE WESTERN AUSTRALIAN ELEMENT

The Archean-aged rocks of Australia are relatively well exposed and are often considered to be among the best preserved on Earth. Because of this, Australian Archean rocks are some the most well-studied of the 35 identified and dated Archean cratonic fragments (Bleeker, 2003). The continent has been typically divided into at least 4 regions based on the age of the basement and the geologic history. In general, the western two-thirds of the Australian continental crust is made of Archean proto-continental nuclei sutured together by Proterozoic-Mesoproterozoic orogenic events, and the eastern third is composed of a series of Phanerozoic accretionary complexes (Cawood and Korsch, 2008). Researchers have divided the western two-thirds of the continent into three geologically unique domains commonly referred to as cratons, but the term craton has also been used to refer to individual suites of Archean rocks within the larger domains.

Huston *et al*. (2012) applied the term "Element" to define "a part of a continent that has some shared broad-scale geological history; often interpreted proto-continent or collection of such continental fragments (including cratons) that now forms part of an extant continent". Following this nomenclature, the western Precambrian basement dominated portion of Australia can be divided into the West, North, and South Australian Elements and the eastern Phanerozoic basement dominated region referred to as the Tazman Element (Huston *et al*, 2012).

The region between the North, South, and West Australian Elements is composed of the Central Australian terranes which are a series of accreted crustal units that formed between 1.9-1.3 Ga (Myers *et al.*, 1996). The location of the Elements, the inferred presence of Precambrian

basement based on mapping and geophysical data (Myers et al., 1996) and the locations where Archean cratonic rocks and Proterozoic basins and orogenic belts crop out is shown in Figure 1.

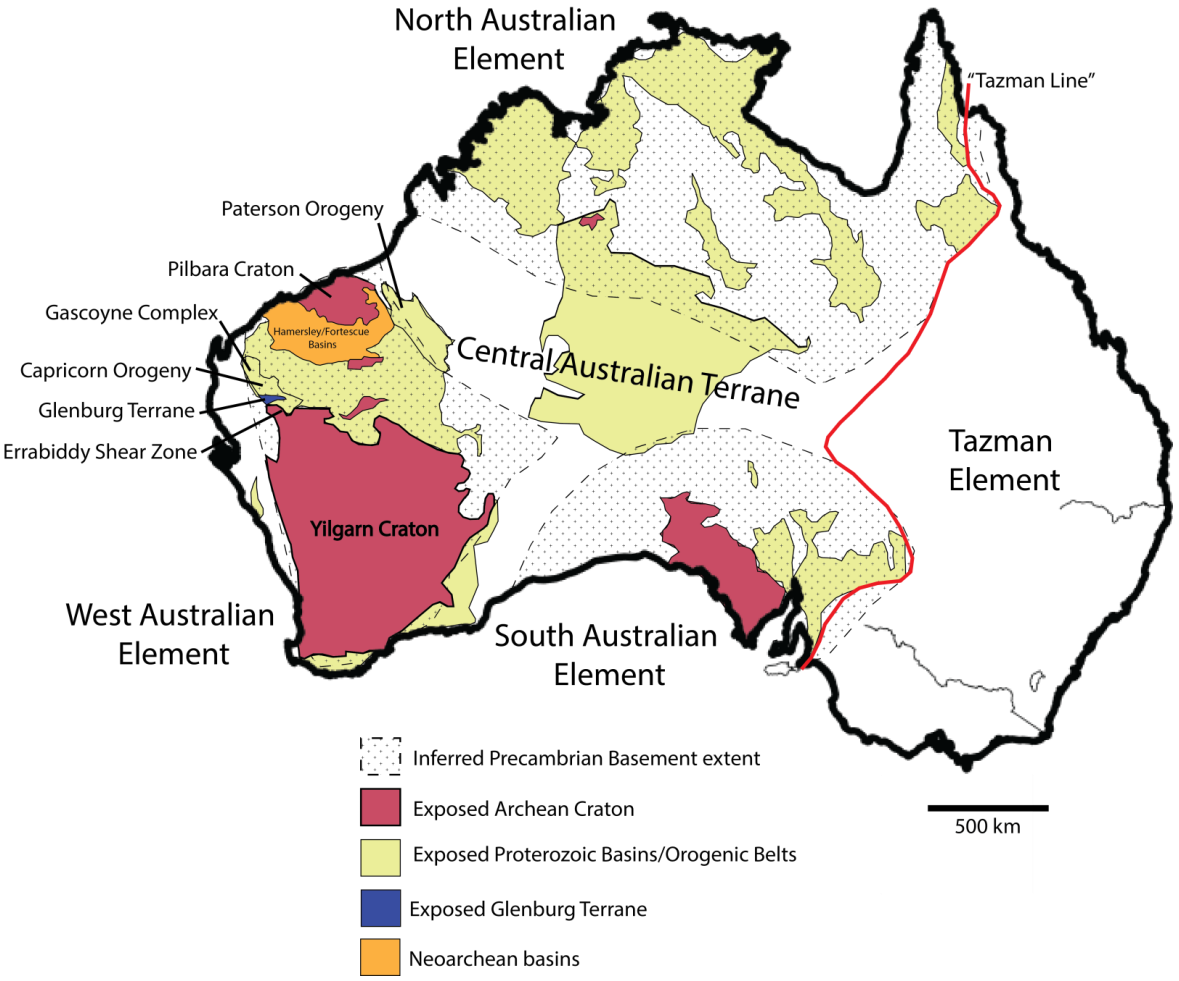

Figure 1. Simplified geologic map of Australia illustrating the distribution of exposed Archean, Proterozoic and Phanerozoic aged rocks, inferred distribution of Archean crust and subdivision of the continent into the West, South and North Australian Elements, Central Australian Terranes and the Tazman Element (modified from Cawood and Korsch, 2008 and Hickman et al., 2012).

Traditionally, the Tazman line was considered to be the boundary between the older Archean-Proterozoic basement to the west and the younger Phanerozoic basement to the east (Veevers, 1984). However, several studies based on field mapping, geochemistry and

interpretation of gravity and magnetic data have shown that the contacts between the predominantly western Archean-Proterozoic crust and eastern Phanerozoic crust record a more complicated and diverse geological history than previously thought (Direen and Crawford, 2003; Myers et al., 1996; Saygin and Kennett, 2010). The western Precambrian basement portion of Australia records a complex history of Archean-Proterozoic crustal formation and continental assembly from ~3.8 to 1.3 Ga (Cawood and Korsch, 2008; Huston *et al.*, 2012b).

The West Australian Element consists of two Archean-aged cratons, the Yilgarn and Pilbara cratons, and a series of Late-Archean to early Proterozic sedimentary basins and orogenic belts (Huston et al., 2012b). The assembly of the West Australian Element was originally attributed to one event, the Capricorn orogeny, but many studies have shown that the assembly and related deformation of this region is extremely complex. The West Australia Element was formed through at least three major collisional or accretionary events: the 2.215-2.145 Ga Opthalamian orogeny, the 1.956-1.95 Ga Glenburg orogeny and the ~1.83-1.78 Ga Capricorn orogeny (Cawood and Tyler, 2004; Johnson *et al.*, 2011).

The Opthalamian orogeny records the collision of the Glenburg Terrane, a piece of exotic crust, with a crustal fragment composed of the Archean Pilbara Craton and late Archean to early Paleoproterozoic Fortescue, Hammersley, and Turee Creek Basins (Johnson et al., 2011; Sheppard *et al.*, 2004). A magmatic arc system is interpreted to have formed along the southern margin of this crustal fragment at 2.47 Ga in response to northward subduction of oceanic crust (Martin and Morris, 2010). The subduction of the more buoyant Glenburg terrain is believed to have caused compression and uplift that deformed the southern margin of the Pilbara Craton and rocks in the Hammersley Basin subsequently leading to the formation of the Opthalamian fold and thrust belt (Cawood and Tyler, 2004; de Vries *et al.*, 2008).

Evidence for the Glenburg orogeny is preserved on the northern edge of the Yilgarn craton in metamorphic rocks of the Glenburg Terrane and in the Errabiddy Shear Zone (Occhipinti *et al.*, 2004). The Errabiddy shear zone, is composed of a variety of metamorphic rocks and slices of Archean-aged granites derived from the Yilgarn Craton and marks the contact between the Glenburg Terrain and the Yilgarn Craton (Martin *et al.*, 2007). The Glenburg orogeny is believed to record accretion of the combined Pilbara Craton-Glenburg Terrain with the Yilgarn craton (Johnson et al., 2011). Structures and deformation originally associated with the ~1.83-1.78 Capricorn Orogeny have undergone re-evaluation due to the interpretation that both the Glenburg and Opthalamian orogenies record the collisional events that formed the West Australia Terrane. These structures are also contemporaneous with a series of orogenic events in the northeast part of the Pilbara craton including the Paterson Orogeny which records the collision of the West Australia Element with the North Australia Element (Betts *et al.*, 2002; Huston *et al.*, 2012a; Myers et al., 1996). Therefore, it has been suggested that structures attributed to the Capricorn Orogeny in the southeastern part of the West Australian Terrane may be the result of intracratonic forces associated with the assembly of the North and West Australia Elements (Cawood and Tyler, 2004; Occhipinti et al., 2004)

GENERAL GEOLOGIC HISTORY OF THE PILBARA CRATON REGION

The Pilbara region in the northern portion of the West Australian Craton has been extensively studied due to its relatively well exposed Archean and early Proterozoic geologic units. This region has been divided into three major domains: the ~3.6-2.83 Pilbara Craton, the 2.7-2.42 Ga Fortescue, Hammersley, and Turee Creek Basins, and the 2.21-1.79 Ga Ashburton

Basin (Hickman and Van Kranendonk, 2012). These subdivisions were the result of a large-scale mapping project and revision of the stratigraphic nomenclature applied to the rocks that crop out in this region (Van Kranendonk *et al.*, 2006). The term "Pilbara Craton" refers to the oldest suites of rocks in this area and includes fragments of <3.6 Ga crust, 3.53-3.07 Ga granite-greenstone terranes, 3.05-2.93 Ga volcanosedimentary basins, and 2.89-2.83 Ga granites (Hickman and Van Kranendonk, 2012).

Evidence for the existence of crust older than 3.6 Ga is present in enclaves of biotite tonalite gneiss dated to 3.655-3.576 Ga that occur in younger granodiorites and monzogranites (Hickman *et al.*, 2010). Xenoliths of gabbroic anorthosite dated to 3.578 Ga preserved in ~3.430 Ga granites have also been identified in the Pilbara Craton (McNaughton *et al.*, 1988). A study utilizing SHRIMP U-Pb geochronology by the Geological Survey of Western Australia across the northern Pilbara Craton identified detrital zircons ~3.6 Ga in Paleo-Mesoarchean sedimentary sequences also supports the existence of older crust in the region (Hickman et al., 2010).

Rocks in the Pilbara Craton have been subdivided into a series of tectonic units, he Regal, Karratha, Sholl, East Pilbara, and Kurrana Terranes, which are unconformably overlain by rocks of the De Grey Superbasin (Figure. 2) (Hickman, 2012). These five terranes record the formation, break-up, and reassembly of an Archean protocontinent between ~3.5 and 2.9 Ga (Van Kranendonk, 2006a). Post-orogenic sedimentary rocks and granites of the The De Grey Superbasin assemblage were later deposited over large parts of the Pilbara Craton (Van Kranendonk, Hugh Smithies, *et al.*, 2007). 28

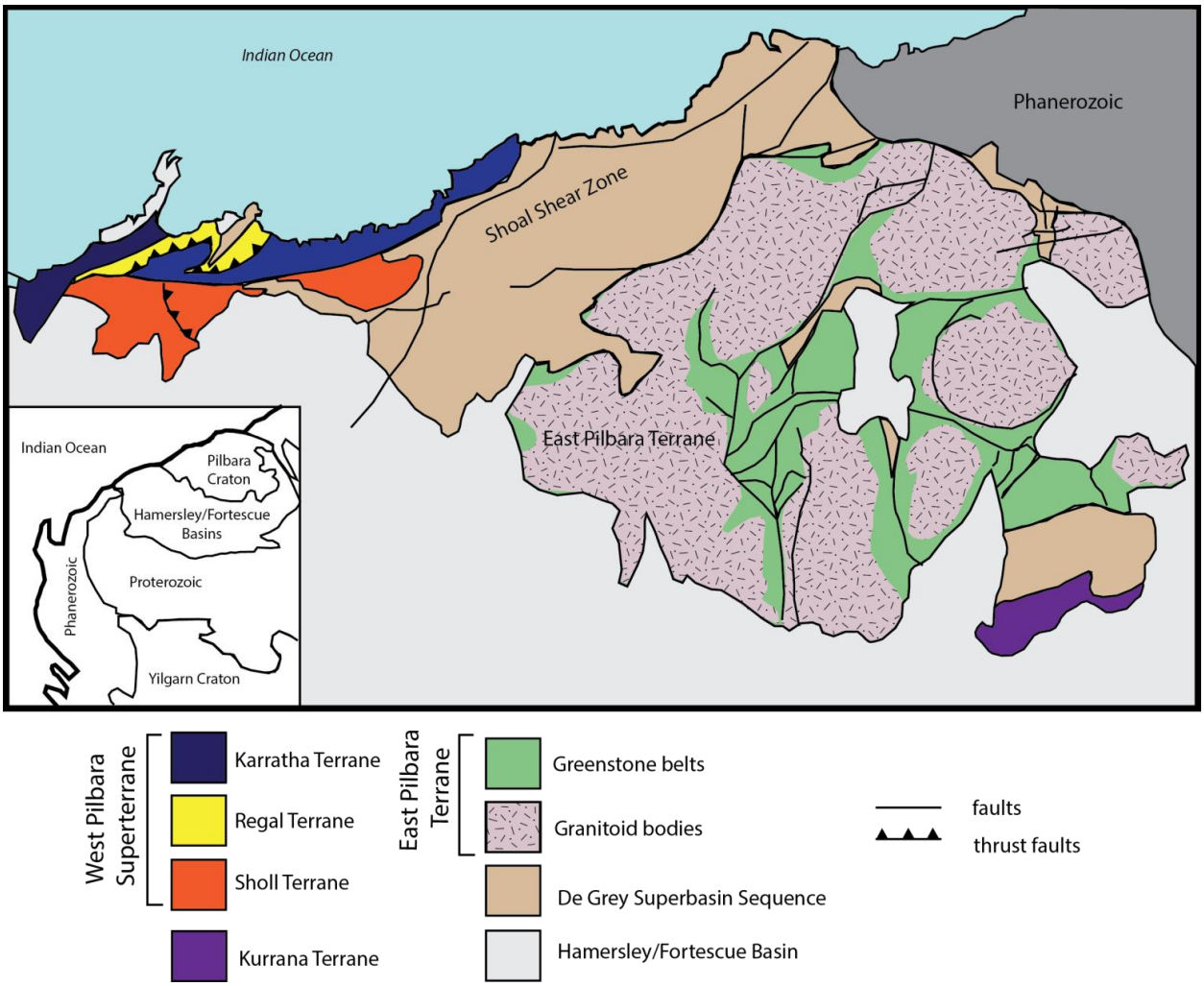

Figure 2. Generalized geologic map of the Pilbara Craton showing the location of the component terranes, major fault systems, and distribution of granitoid and greenstone units in the East Pilbara terrane (modified from Hickman, 2012).

The oldest part of the Pilbara Craton, the East Pilbara Terrane, is composed of 20 greenstone belts and eight granitic complexes (Figure. 2) (Hickman, 2012). The granitic complexes are primarily tonalite-trondhiemite-granodiorite (TTG) in composition, but some of the youngest intrusions are granitic or syenitic in composition (Van Kranendonk, Hugh Smithies, et al., 2007). The greenstone belts are composed of metamorphosed volcanic and sedimentary rocks preserved in synclines that are either in fault contact or are juxtaposed to the granitoid bodies by shear zones (Van Kranendonk *et al.*, 2002b). The East Pilbara Terrane displays the

classic “dome and keel” topography seen in many granite-greenstone terranes and has been the focus of many studies directed at understanding the formation of this characteristic topography. The most commonly accepted model involves an initial vertical tectonic phase of eruption of volcanic rocks and intrusion of granitoid bodies into older sialic crust forming a volcanic plateau (Hickman and Van Kranendonk, 2012; Van Kranendonk *et al.*, 2004; Van Kranendonk, Hugh Smithies, et al., 2007). The formation of the main amplitude of the “dome and keel” topography is attributed to a phase of partial convective overturn of the upper crust and mantle before 3.2 Ga (Van Kranendonk, Hugh Smithies, et al., 2007). Evidence for rifting of the volcanic plateau into the East Pilbara, Kurrana, and Karatha Terranes at 3.23-3.16 Ga is interpreted to record a secular change from vertical diapir-based tectonics to a more modern horizontal plate-tectonic regime (Van Kranendonk et al., 2004; Van Kranendonk, Hugh Smithies, et al., 2007).

Shortly after rifting of the granite-greenstone protocontinent, a subduction zone formed which initiated reconvergence of the continental fragments resulting in obduction of oceanic crust forming the Regal Terrain and accretion of an island-arc system, the Sholl Terrain, to the Karratha Terrane to form the West Pilbara Superterrane (Hickman et al., 2010). Continued convergence resulted in the collision of the West Pilbara Superterrane with the East Pilbara Craton during the Princep orogeny at 3.07 (Van Kranendonk, Hugh Smithies, et al., 2007). Concurrently, subduction to the southwest resulted in accretion of the Kurrana Terrane to the southeast margin of the East Pilbara Terrane (Hickman and Van Kranendonk, 2012). Unconformably overlying portions of the West Pilbara Superterrane and East Pilbara Terrane are rocks of the DeGray Superbasin, which consists of a series of sedimentary basins that likely formed due to crustal relaxation, subsidence, and extension following the Princep Orogeny (Hickman, 2012).

GENERAL STRATIGRAPHY OF THE PILBARA SUPERGROUP, EAST PILBARA TERRANE

Eighteen of the twenty greenstone belts in the East Pilbara Terrane are composed of rocks from the 3.53-3.23 Pilbara Supergroup (Hickman, 2012). These rocks record at least eight cycles of volcanism and have been divided into three tectonostratigraphic Groups: The 3.515-3.427 Ga Warrawoona Group, 3.350-3.315 Ga Kelly Group and 3.255-3.235 Ga Sulphur Springs Group (Van Kranendonk, Smithies, *et al.*, 2007). The unconformities between the Groups are marked by deformation, metamorphism, subaerial erosion, and clastic deposition (Hickman and Van Kranendonk, 2012). The Pilbara Supergroup has a lateral extent of over 30 km encompassing most of the East Pilbara Terrane and a vertical thickness estimated to be no more than 15 km (Van Kranendonk, Hugh Smithies, et al., 2007). The actual depositional thickness of the unit remains unclear as it is in contact with younger intrusive granitoids at the base and has an erosional unconformity at the top (Van Kranendonk, Hugh Smithies, et al., 2007). Geologic mapping and extensive SHRIMP geochronology has shown that there appears to be no stratigraphic repetition of the units within the greenstone belts (Van Kranendonk *et al.*, 2002a).

A generalized stratigraphic column of the Pilbara Supergroup, stratigraphic nomenclature and volcanic cycles are shown in Figure 3. The Warawoona Group has been divided into the Coonterunah, Talga Talga, Coongan, and Salgash Subgroups which are interpreted to record at least 5 cycles of predominantly mafic-ultramafic volcanism between 3.53-3.43 Ga (Hickman, 2012; Van Kranendonk et al., 2006). It is composed primarily of pillow basalt and komatittic basalt with smaller amounts of tholeiite (Van Kranendonk, Hugh Smithies, et al., 2007). Felsic

units are typically less common and thinner than the mafic-ultramafic units and consist of primarily of tuffaceous horizons a few 10's of meters thick, but dacite horizons in the Coucal, Duffer and Panorama Formations can be several km thick in some regions(Van Kranendonk, Hugh Smithies, et al., 2007).

The Warawoona Group is believed to be primarily deposited under relatively deep submarine conditions, but evidence for shallow water deposition including ripples and dessication cracks have been identified in the Dresser Formation (Van Kranendonk, 2006a). After the last volcanic cycle that formed the Panorama Formation a 76 Ma hiatus marked by deformation and submarine and subaerial erosion occurred before deposition of the Strelly Pool Chert, the lowermost unit of the Kelly Group.

The Strelly Pool Chert is composed of three different facies: basal fluvatile to shallow marine quartzites and conglomerates, silicified stromatolitic marine carbonates, and an upper coarse-grained clastic unit (Van Kranendonk, 2003). These sedimentary rocks were overlain by tholeiitic and komatiitic basalts of the 3.35-3.32 Euro Basalt Formation (Van Kranendonk, Hugh Smithies, et al., 2007).

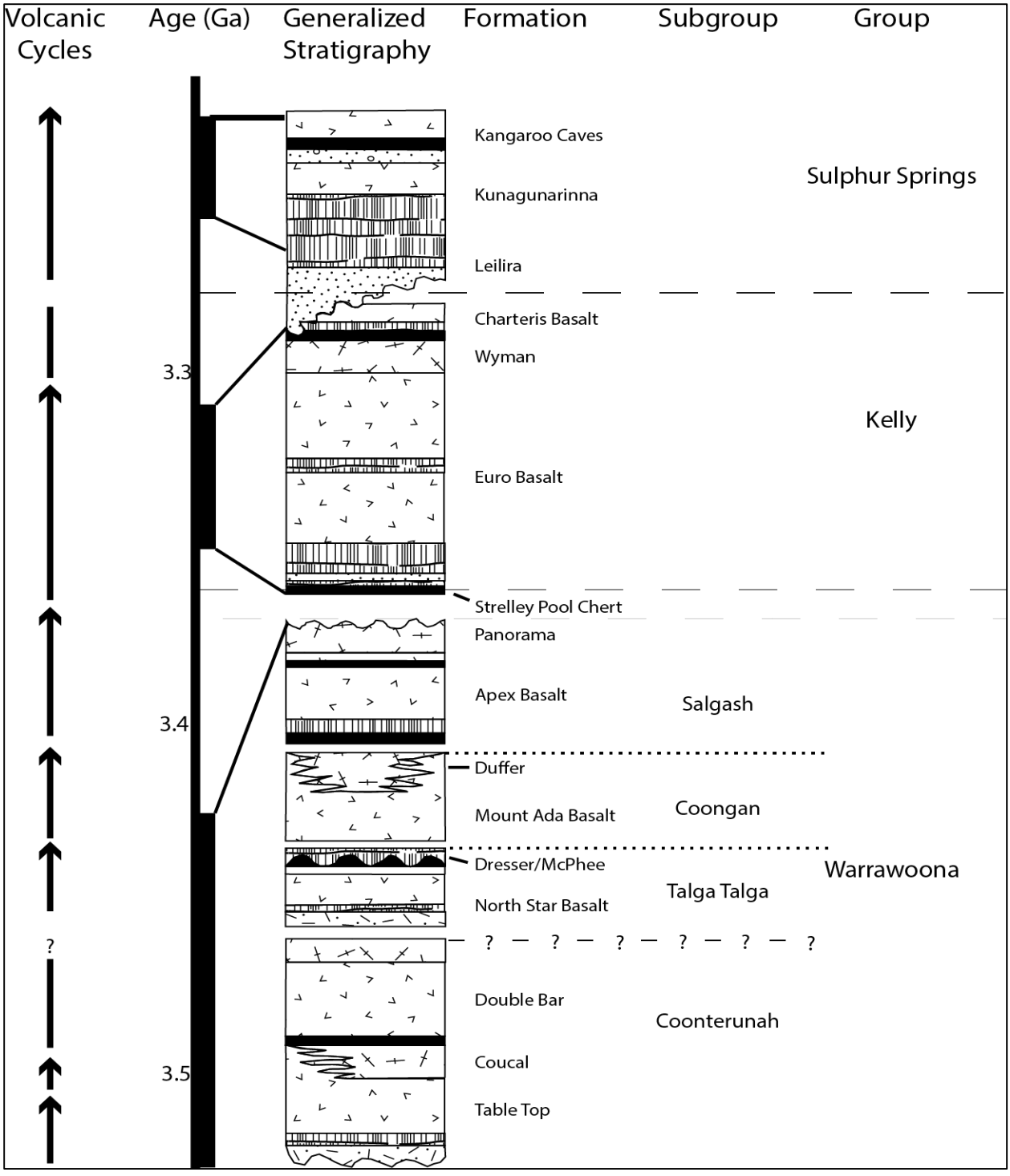

Figure 3. Generalized stratigraphic column of the Pilbara Supergroup showing the volcanic cycles that formed the units, generalized lithology of the units and stratigraphic nomenclature (modified from Van Kranendonk et al., 2006).

Eruption of the subsequent Euro Basalt Formation was followed by eruption of the ~3.32 Ga rhyolitic Wyman Formation, and intrusion of large monzogranite plutons (Van Kranendonk, Hugh Smithies, et al., 2007). The volcanic rocks then shifted in composition to primarily mafic units recorded by the overlying Charteris Basalt (Hickman, 1983).

The Sulphur Springs Group was deposited on an ~ 9 Ma erosional unconformity on older greenstones in the western part of the Pilbara craton (Hickman, 2012). The basal unit consists of felsic volcanoclastic rocks of the Leilira Formation which are overlain by up to 1.5 km of andesite basalt and rhyolite of the Kangaroo Caves Formation (Van Kranendonk, Hugh Smithies, et al., 2007). The upper part of the Kangaroo Caves Formation is composed of silicified epiclastic and siliclastic sediments (Buick *et al.*, 2002).

ENVIRONMENT OF FORMATION AND ALTERATION OF THE APEX CHERT, MARBLE BAR GREENSTONE BELT

The Salgash Subgroup of the Warawoona Group is composed of the Apex Basalt and Panorama Formation which crops out in several of the greenstone belts, but is thickest (~1000 m) in the Marble Bar greenstone belt (Van Kranendonk et al., 2006). The Apex Basalt at the Chinaman Creek locality on the western edge of the Marble Bar greenstone belt contains the exposure where the Apex chert occurs (Brasier *et al.*, 2011). In this area the Apex Basalt occurs over three growth fault bounded blocks: the South, Central, and North Blocks (Brasier *et al.*, 2005). Each block preserves a different sequence of facies composed of pillow basalts, komatiites, various tuffs, ignimbrites, pyroclastic breccias, the stratiform chert informally referred to as "Apex chert", and a series of black, upward thickening, cross-cutting chert dikes

(Brasier et al., 2011). The relationships of the stratiform and dike chert units with the overlying and underlying predominantly volcanic units are shown in Figure 4. The stratiform cherts are characterized by planar bedding and moderate to good grain sorting and orientation (Brasier et al., 2005). These chert beds are interpreted to record several 1-5 m thick volcanic cycles which follow a general stratigraphic pattern: deposition of 1-4 cm thick grey-green planar bedded siliceous tuffs and jaspilitic cherts, formation of 1-10 cm grey, black or white planar laminated cherts, and finally black and white banded cherts that may contain breccias and soft-sediment deformation features (Brasier et al., 2005). Within the chert dikes, Brasier *et al*. (2005) identified fabrics interpreted to record a complex history of repeated fracturing, spalling, precipitation of hydrocarbon-rich botyroidal and spherulitic chalcedony and chert, and megaquartz vein fills.

In the field, the stratiform and dike chert units are contained within grey-green volcaniclastics, tuffs, komatiites, and basalts which preserve evidence of underwater eruption such as pillow textures, chilled margins, and hyaloclastic breccias (Brasier et al., 2005). The dikes are interpreted as feeder conduits formed by synsedimentary faulting which channeled fluids upward through the volcanic units to form the stratiform cherts in a phreatomagmatic hydrothermal system (Van Kranendonk, 2006a). As the hydrothermal system waned, the conduits then progressively backfilled with barite and black carbon-rich cherts forming the vertical cross-cutting dikes (Brasier et al., 2005). The stratiform and vein cherts are overlain by a regionally correlative breccia bed, tuffs, basalts and komatiites, and in the South block are unconformably overlain by rocks of the Fortescue Group (Brasier et al., 2005).

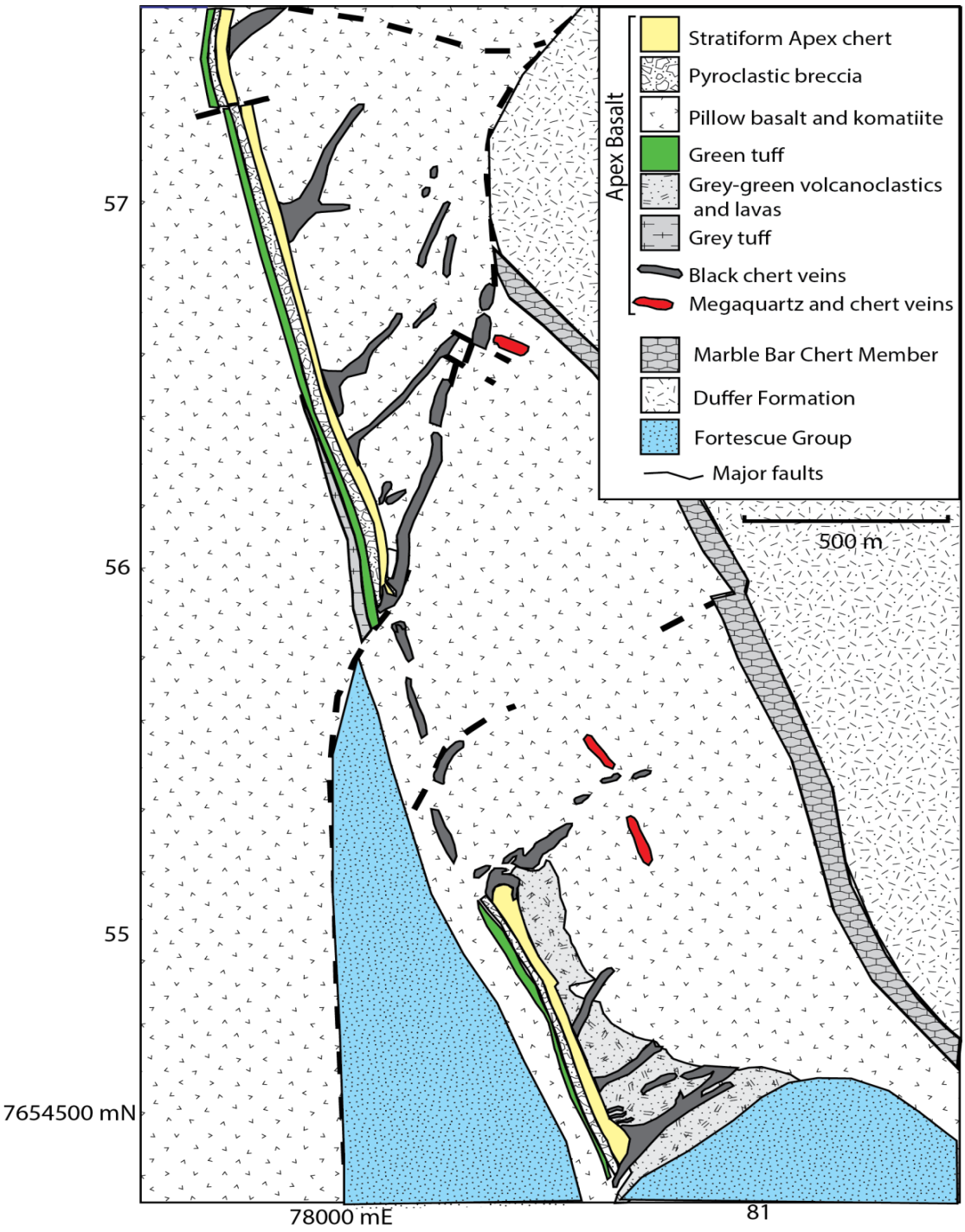

Figure 4. Geologic map showing the distribution of the Apex Basalt and Apex chert in the Chinaman Creek area in the Marble Bar greenstone belt (modified from Brasier et al., 2011).

The large, cross-cutting chert dike that defines the southern edge of the North Block contains the original microfossil locality of Schopf (1987) (Brasier et al., 2005). The location of the microfossil locality within the dike and the field relationships of the units in the North Block is shown in Figure 5. The dike extends to a paleodepth of 1.2 km and the original samples described by Schopf and Packer (1987) were collected approximately 100 m from the top of the dike outcrop (Brasier et al., 2005). In this area, the host rocks for the stratiform and dike cherts consist of locally silicified pillow basalts (Brasier et al., 2005). Overlying the basalt units is a wedge of grey-green, glassy volcanic tuff that appears to thicken toward the dike (Brasier et al., 2005). The stratiform Apex chert is approximately 40 m thick and consists of chert interbedded with silicified tuffs (Brasier et al., 2011). Based on mineral assemblages and isotopic composition, the Apex chert has been interpreted to have formed as the result of multiple fluid pulses in a relatively high temperature hydrothermal system (Brasier *et al.*, 2002; Brasier et al., 2005; Brasier et al., 2011). The Apex chert is overlain by a breccia bed, green tuff, pillow basalts and komatiites interpreted to record the beginning of the next volcanic cycle (Brasier et al., 2005).

Due to the age and complex tectonic history of the Pilbara Craton, it is unsurprising that the deformational and alteration history is complicated. The East Pilbara Terrane has experienced multiple local and regional metamorphic events during the Archean (Blewett, 2002; Van Kranendonk et al., 2002a; Van Kranendonk, Hugh Smithies, et al., 2007). Several early events prior to the Princep Orogeny at 3.07 Ga have been identified based on field mapping identification of features including: mineral elongations, stretching lineations, folds, and faults that occur in the Marble Bar and other nearby greenstone belts (Van Kranendonk, Hugh Smithies, et al., 2007).

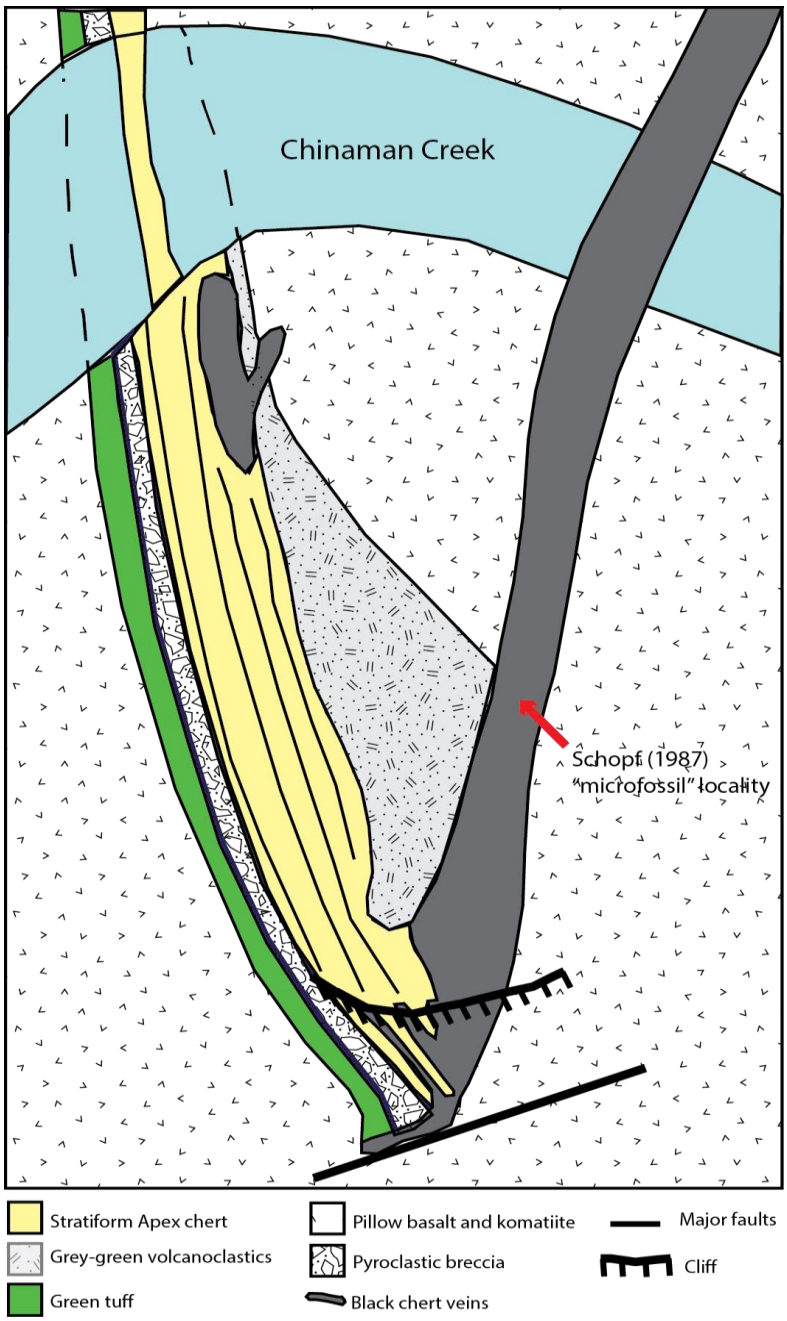

Figure 5. Geologic map of the Schopf (1987) microfossil locality showing the distribution of the Apex Basalt and Apex chert and the sample locality within the black cross-cutting chert dike (modified from Brasier et al., 2011).

The most commonly accepted explanation for these early deformation events involves granitoid intrusion via the proposed vertical tectonic evolution model for the initial formation of the Pilbara Craton granite-greenstone terranes (Hickman and Van Kranendonk, 2012; Van Kranendonk et al., 2004; Van Kranendonk, Hugh Smithies, et al., 2007). In contrast, other researchers have suggested that these early deformation events may be related to compressional and extensional events caused by more modern horizontal plate tectonic processes (Kloppenburg *et al.*, 2001; van Haaften and White, 1998; Zegers *et al.*, 2001).

In this region, many of the synclinal greenstones also show evidence of amphibolite facies metamorphism proximal to the granitoid intrusions which decreases to greenschist, and prehnite-pumpellyite facies distal to the intrusive bodies (Van Kranendonk et al., 2002b). Researchers have shown that rocks in the Marble Bar Belt record multiple events of early local at least greenschist facies metamorphism (Brasier et al., 2011; Van Kranendonk, 2006b; Van Kranendonk and Pirajno, 2004).

Other deformation events have been interpreted as phases of regional hydrothermal alteration recorded by the presence of massive sulfide deposits and evidence of gold mineralization (Van Kranendonk, Hugh Smithies, et al., 2007). For example, less than 30 km southeast of the Chinaman Creek locality, Warawoona Group rocks in the Warawoona syncline on the southeast edge of the Mount Edgar Batholith contain one of the largest mafic-ultramafic hosted gold deposits in the East Pilbara terrane (Thébaud *et al.*, 2008). These deposits which are located in large shear zone that permeate highly deformed rocks were dated using Pb model ages from galenas to between .38-3.05 Ga (Huston, 2001). Fluid inclusion analyses identified at least three stages of pervasive fluid flow associated with this mineralization event (Thebaud *et al.*, 2006).

Recent studies of Apex chert samples have shed light on the complex alteration and metamorphic history of the unit. SEM EDX and petrographic analyses of the mineral assemblages revealed several potential low temperature (~60-80 ºC) hydrothermal fluid alteration events that post-dated the formation of the silica matrix in the Apex chert veins (Pinti *et al.*, 2009). A study utilizing Raman point spectroscopy and Raman imaging documented a mixed population of carbonaceous material with varying structural order present in the Apex chert interpreted as a result of different hydrothermal or metamorphic overprints and potential late stage meteoric fluid alteration (Sforna *et al.*, 2014). Additionally, a high-resolution TEM study of isolated carbonaceous material from the Apex chert documented 4 different microtextural phases of carbonaceous material some of which was likely emplaced into the chert matrix more than a billion years after it formed (Marshall *et al.*, 2014). This study interpreted a primary phase of carbon formed abiotically in the vein forming hydrothermal system, a phase emplaced between 3.660-2.830 Ga that experienced greenschist metamorphic conditions, a phase that experienced prehnite-pumpellyite metamorphic conditions emplaced before 2.145 Ga, but after greenschist metamorphism, and a phase similar to carbonaceous material found in meteorites that may be associated with 4 meteorite impacts in the region between 3.470-2.480 (Marshall et al., 2014). Although it was previously thought that this unit was relatively well preserved, these studies show that the Apex chert has undergone a variety of complex alteration and metamorphic events throughout its long history.

Several generations of Proterozoic-age structures record deformation events that have also affected the Pilbara region. There is evidence for a regional metamorphic event in the Panorama belt that metamorphosed rocks to prehnite-pumpellyite facies under low-strain conditions between 2.95-2.76 Ga (Hickman, 1983). The 2.215-2.145 Ga Opthalamian Orogeny

caused considerable structural deformation within the Pilbara Craton associated with pervasive fluid alteration identified by reset isotope systems in older rocks and the presence of phosphates dated to ~2.2 Ga found throughout the Pilbara granite-greenstone terranes (Rasmussen, Fletcher, *et al.*, 2005). The 2.2-1.8 Ga Capricorn orogeny may have also resulted in subsequent prehnite-pumpellyite or lower greenschist facies metamorphism in the Panorama Belt region (Hickman, 1983). Blewett (2002) identified at least six phases of post-Archean deformation that affected the eastern margin of the East Pilbara Terrane that may also be related to the 1.83 and 1.765 Ga Paterson Orogeny.

A study based Re-O isotope systematics suggested that the hematite in the Marble Bar chert was primary and formed in an oxygenated sea (Hoashi *et al.*, 2009). In contrast, more recent work utilizing U-Th-Pb isotopes from Apex Basalt samples interpreted the formation of ferric oxides as the result of Phanerozoic groundwater alteration (Li *et al.*, 2012).

Along with episodes of contact and regional metamorphism, rocks of the Pilbara Craton as a whole show evidence of deformation related to meteorite impacts in the Archean or early Proterozoic. The Antarctic chert, an informal unit in the Mount Ada Basalt (Hickman, 2013) located approximately 10-15 km northeast of the Chinaman Creek locality, contains impact spherules formed by an impact dated to approximately 3.47 Ga (Byerly *et al.*, 2002; Glikson *et al.*, 2004). This spherule unit has also been correlated by Ur-Pb isotope geochronology to 1 of 4 impact-related units dated between 3.8-3.2 Ga from the Barberton Greenstone Belt in the Archean Kaapvaal craton, South Africa (Byerly et al., 2002). Mounting evidence from paleomagnetic, geochemical, geochronological, structural, and stratigraphic studies suggest that the Pilbara Craton and Kaapvaal Craton were part of a single Archean continent called Vaalbara (de Kock *et al.*, 2009; Zegers *et al.*, 1998). The exact timing of the separation of the Pilbara and

Kaapvaal Cratons is not well constrained, but studies suggest that the two cratons were separate landmasses by approximately 2.0 Ga (de Kock et al., 2009). Researchers have noted that the unconformities within the Pilbara Supergroup between the Coongan and Salgash Subgroups, the Warawoona Group and the Kelly Group, and the major unconformity at the top of the Sulphur Springs Group are contemporaneous with impact events identified in the Kaapvaal Craton (Glikson and Vickers, 2006). Around the time of the break-up of Vaalbaara, three Neoarchean impact spherule units dated at 2.63, 2.56-2.5, 2.5-2.48 Ga have also been identified in the Hammersly Group in the Pilbara Craton (Rasmussen, Blake, *et al.*, 2005).

The post Mesoproterozoic history of the Pilbara region is more difficult to constrain as there are very few rocks younger than 1 Ga preserved. Australia was involved in the assembly and break-up of Rodinia from 1.3 Ga to 700 Ma, and there is evidence for reactivation of Capricorn-age structures at the southern margin of the Pilbara granite-greenstone terrains at this time. (Cawood and Tyler, 2004; Huston et al., 2012a).

References

Betts, P. G., Giles, D., Lister, G. S., & Frick, L. R. (2002). Evolution of the Australian lithosphere. *Australian Journal of Earth Sciences, 49*(4), 661-695.

Bleeker, W. (2003). The late Archean record: a puzzle in ca. 35 pieces. *Lithos, 71*(2–4), 99-134.

Blewett, R. S. (2002). Archaean tectonic processes: a case for horizontal shortening in the North Pilbara Granite-Greenstone Terrane, Western Australia. *Precambrian Research, 113*(1–2), 87-120. Brasier, M. D., Green, O. R., Jephcoat, A. P., Kleppe, A. K., Van Kranendonk, M. J., Lindsay, J. F., Grassineau, N. V. (2002). Questioning the evidence for Earth's oldest fossils. *Nature, 416*, 76-81.

Brasier, M. D., Green, O. R., Lindsay, J. F., McLoughlin, N., Steele, A., & Stoakes, C. (2005). Critical testing of Earth's oldest putative fossil assemblage from the ~3.5 Ga Apex chert, Chinaman Creek, Western Australia. *Precambrian Research, 140*, 55-102.

Brasier, M. D., Green, O. R., Lindsay, J. F., McLoughlin, N., Stoakes, C., Brasier, A. T., & Wacey, D. (2011). *Geology and Putative Microfossil Assemblage of the c. 3460 Ma "Apex chert", Chinaman Creek, Western Austraila-A Field and Petrographic Guide* (Vol. 2011/7). Perth, Austraila: Geological Society of Western Australia.

Buick, R., Brauhart, C. W., Morant, P., Thornett, J. R., Maniw, J. G., Archibald, N. J., . . . Groves, D. I. (2002). Geochronology and stratigraphic relationships of the Sulphur Springs Group and Strelley Granite: a temporally distinct igneous province in the Archaean Pilbara Craton, Australia. *Precambrian Research, 114*(1–2), 87-120. Byerly, G. R., Lowe, D. R., Wooden, J. L., & Xie, X. (2002). An Archean Impact Layer from the Pilbara and Kaapvaal Cratons. *Science, 297*(5585), 1325-1327.

Cawood, P. A., & Korsch, R. J. (2008). Assembling Australia: Proterozoic building of a continent. *Precambrian Research, 166*(1–4), 1-35.

Cawood, P. A., & Tyler, I. M. (2004). Assembling and reactivating the Proterozoic Capricorn Orogen: lithotectonic elements, orogenies, and significance. *Precambrian Research, 128*(3–4), 201-218.

de Kock, M. O., Evans, D. A. D., & Beukes, N. J. (2009). Validating the existence of Vaalbara in the Neoarchean. *Precambrian Research, 174*(1–2), 145-154.

de Vries, S. T., Pryer, L. L., & Fry, N. (2008). Evolution of Neoarchaean and Proterozoic basins of Australia. *Precambrian Research, 166*(1-4), 39-53.

Direen, N. G., & Crawford, A. J. (2003). The Tasman Line: Where is it, what is it, and is it Australia's Rodinian breakup boundary? *Australian Journal of Earth Sciences, 50*(4), 491-502.

Glikson, A., & Vickers, J. (2006). The 3.26-3.24 Ga Barberton asteroid impact cluster: Tests of tectonic and magmatic consequences, Pilbara Craton, Western Australia. *Earth and Planetary Science Letters, 241*(1-2), 11-20.

Glikson, A. Y., Allen, C., & Vickers, J. (2004). Multiple 3.47-Ga-old asteroid impact fallout units, Pilbara Craton, Western Australia. *Earth and Planetary Science Letters, 221*(1-4), 383-396.

Hickman, A. H. (1983). *Geology of the Pilbara Block and its environs / by Arthur H. Hickman*. Perth [W.A.] :: Geological Survey of Western Australia.

Hickman, A. H. (2012). Review of the Pilbara Craton and Fortescue Basin, Western Australia: Crustal evolution providing environments for early life. *Island Arc, 21*(1), 1-31.

Hickman, A. H. (Cartographer). (2013). North Shaw W.A. 1:100000 geological sheet 2755.

Hickman, A. H., Smithies, R. H., & Tyler, I. M. (2010). *Evolution of Active Plate Margins: West Pilbara Superterrane, De Grey Superbasin, and the Fortescue and Hammersley Basins--A Field Guide* (Vol. 2010/3). Perth, Australia: Geological Survey of Western Australia.

Hickman, A. H., & Van Kranendonk, M. J. (2012). Early Earth evolution: evidence from the 3.5-1.8 Ga geological history of the Pilbara region of Western Australia. *Episodes, 35*(1), 283-297.

Hoashi, M., Bevacqua, D. C., Otake, T., Watanabe, Y., Hickman, A. H., Utsunomiya, S., & Ohmoto, H. (2009). Primary haematite formation in an oxygenated sea 3.46 billion years ago. *Nature Geosci, 2*(4), 301-306.

Huston, D. (2001). *Gold deposits of the Pilbara Craton: results of AGSO research, 1998-200* (Vol. 2001/10). Canberra, Australia: Geoscience Australia.

Huston, D., Blewett, R. S., & Champion, D. C. (2012a). Australia through time: a summary of its tectonic and metallogenic evoution. *Episodes, 35*(1), 23-42.

Huston, D. L., Blewett, R. S., & Champion, D. C. (2012b). Australia through time: a summary of its tectonic and metallogenic evolution. *Episodes, 35*(1), 23-43.

Johnson, S. P., Sheppard, S., Rasmussen, B., Wingate, M. T. D., Kirkland, C. L., Muhling, J. R., Belousova, E. A. (2011). Two collisions, two sutures: Punctuated pre-1950 Ma assembly of the West Australian Craton during the Ophthalmian and Glenburgh Orogenies. *Precambrian Research, 189*(3–4), 239-262.

Kloppenburg, A., White, S. H., & Zegers, T. E. (2001). Structural evolution of the Warrawoona Greenstone Belt and adjoining granitoid complexes, Pilbara Craton, Australia: implications for Archaean tectonic processes. *Precambrian Research, 112*(1–2), 107-147.

Li, W., Johnson, C. M., & Beard, B. L. (2012). U–Th–Pb isotope data indicate phanerozoic age for oxidation of the 3.4 Ga Apex Basalt. *Earth and Planetary Science Letters, 319–320*(0), 197-206.

Marshall, A. O., Jehlicka, J., Rouzaud, J. N., & Marshall, C. P. (2014). Multiple generations of carbonaceous material deposited in Apex chert by basin-scale pervasive hydrothermal fluid flow. *Gondwana Research, 25*(1), 284-289.

Martin, D. M., & Morris, P. A. (2010). Tectonic setting and regional implications of ca 2.2 Ga mafic magmatism in the southern Hamersley Province, Western Australia. *Australian Journal of Earth Sciences, 57*(7), 911-931.

Martin, D. M., Sheppard, A. M., Thorne, A. M., Farrell, T. R., & Groenewald, P. B. (2007). *Proterozoic Geology of the Western Capricorn Orogen--A Field Guide* (Vol. Record 2006/18). Perth, Australia: Geological Survey of Western Australia.

McNaughton, N. J., Green, M. D., Compston, W., & Williams, I. S. (1988). Are anorthositic rocks basement to the Pilbara Craton? *Geological Society of Australia Abstracts, 21*, 272-273.

Myers, J. S., Shaw, R. D., & Tyler, I. M. (1996). Tectonic evolution of Proterozoic Australia. *Tectonics, 15*(6), 1431-1446.

Occhipinti, S. A., Sheppard, S., Passchier, C., Tyler, I. M., & Nelson, D. R. (2004). Palaeoproterozoic crustal accretion and collision in the southern Capricorn Orogen: the Glenburgh Orogeny. *Precambrian Research, 128*(3–4), 237-255. doi: http://dx.doi.org/10.1016/j.precamres.2003.09.002

Pinti, D. L., Mineau, R., & Clement, V. (2009). Hydrothermal alteration and microfossil artefacts of the 3,465-million-year-old Apex chert. *Nature Geoscience, 2*(9), 640-643.

Rasmussen, B., Blake, T. S., & Fletcher, I. R. (2005). U-Pb zircon age constraints on the Hamersley spherule beds: Evidence for a single 2.63 Ga Jeerinah-Carawine impact ejecta layer. *Geology, 33*(9), 725-728. doi: 10.1130/g21616.1

Rasmussen, B., Fletcher, I. R., & Sheppard, S. (2005). Isotopic dating of the migration of a low-grade metamorphic front during orogenesis. *Geology, 33*(10), 773-776. doi: 10.1130/g21666.1

Saygin, E., & Kennett, B. L. N. (2010). Ambient seismic noise tomography of Australian continent. *Tectonophysics, 481*(1–4), 116-125.

Schopf, J. W., & Packer, B. M. (1987). Early Archean (3.3-Billion to 3.5-Billion-Year-Old) Microfossils from Warrawoona Group, Australia. *Science, 237*(4810), 70-73.

Sforna, M. C., van Zuilen, M. A., & Philippot, P. (2014). Structural characterization by Raman hyperspectral mapping of organic carbon in the 3.46 billion-year-old Apex chert, Western Australia. *Geochimica et Cosmochimica Acta, 124*, 18-33. doi: 10.1016/j.gca.2013.09.031

Sheppard, S., Occhipinti, S. A., & Tyler, I. M. (2004). A 2005–1970 Ma Andean-type batholith in the southern Gascoyne Complex, Western Australia. *Precambrian Research, 128*(3–4), 257-277.

Thébaud, N., Philippot, P., Rey, P., Brugger, J., Van Kranendonk, M., & Grassineau, N. (2008). Protracted fluid–rock interaction in the Mesoarchaean and implication for gold mineralization: Example from the Warrawoona syncline (Pilbara, Western Australia). *Earth and Planetary Science Letters, 272*(3–4), 639-655.

Thebaud, N., Philippot, P., Rey, P., & Cauzid, J. (2006). Composition and origin of fluids associated with lode gold deposits in a Mesoarchean greenstone belt (Warrawoona

Syncline, Pilbara Craton, Western Australia) using synchrotron radiation X-ray fluorescence. *Contributions to Mineralogy and Petrology, 152*(4), 485-503.

van Haaften, W. M., & White, S. H. (1998). Evidence for multiphase deformation in the Archean basal Warrawoona Group in the Marble Bar area, East Pilbara, Western Australia. *Precambrian Research, 88*(1–4), 53-66.

Van Kranendonk, M. J. (2003). Geological and trace element evidence for a marine sedimentary environment of deposition and biogenicity of 3.45 Ga stromatolitic carbonates in the Pilbara Craton, and support for a reducing Archaean ocean. *Geobiology, 1*, 91-108.

Van Kranendonk, M. J. (2006a). Volcanic degassing, hydrothermal circulation and the flourishing of early life on Earth: A review of the evidence from c. 3490-3240 Ma rocks of the Pilbara Supergroup, Pilbara Craton, Western Australia. *Earth-Science Reviews, 74*(3-4), 197-240.

Van Kranendonk, M. J. (2006b). Volcanic degassing, hydrothermal circulation and the flourishing of early life on Earth: A review of the evidence from c. 3490-3240 Ma rocks of the Pilbara Supergroup, Pilbara Craton, Western Australia. *Earth-Science Reviews, 74*, 197-240.

Van Kranendonk, M. J., Collins, W. J., Hickman, A., & Pawley, M. J. (2004). Critical tests of vertical vs. horizontal tectonic models for the Archaean East Pilbara Granite–Greenstone Terrane, Pilbara Craton, Western Australia. *Precambrian Research, 131*(3–4), 173-211. Van Kranendonk, M. J., Hickman, A. H., Smithies, R. H., Nelson, D. R., & Pike, G. (2002a). Geology and Tectonic Evolution of the Archean North Pilbara Terrain,Pilbara Craton, Western Australia. *Economic Geology, 97*(4), 695-732.

Van Kranendonk, M. J., Hickman, A. H., Smithies, R. H., Williams, I. R., Bagas, L., & Farrell, T. R. (2006). *Revised lithostratigraphy of Archean supracrustal and intrusive rocks in the northern Pilbara Craton Western Australia* (Vol. 2006/15). Perth, Australia: Geological Survey of Western Australia.

Van Kranendonk, M. J., Hugh Smithies, R., Hickman, A. H., & Champion, D. C. (2007). Review: secular tectonic evolution of Archean continental crust: interplay between horizontal and vertical processes in the formation of the Pilbara Craton, Australia. *Terra Nova, 19*(1), 1-38. Van Kranendonk, M. J., & Pirajno, F. (2004). Geochemistry of metabasalts and hydrothermal alteration zones associated with c. 3.45 Ga chert and barite deposits: implications for the geological setting of the Warrawoona Group, Pilbara Craton, Australia. *Geochemistry: Exploration, Environment, Analysis, 4*(3), 253-278.

Van Kranendonk, M. J., Smithies, R. H., & Bennet, V. C. (2007). *Earth's Oldest Rocks* (Vol. 15). Amsterdam, The Netherlands: Elsevier.

Van Kranendonk, M. J. V., Hickman, A. H., Smithies, R. H., Nelson, D. R., & Pike, G. (2002b). Geology and Tectonic Evolution of the Archean North Pilbara Terrain,Pilbara Craton, Western Australia. *Economic Geology*, *97*(4), 695-732.

Veevers, J. J. (1984). *Phanerozoic History of Australia* (Vol. 2). Oxford, USA: Oxford University Press.

Zegers, De, W., Dann, & White. (1998). Vaalbara, Earth's oldest assembled continent? A combined structural, geochronological, and palaeomagnetic test. *Terra Nova, 10*(5), 250-259.

Zegers, T. E., Nelson, D. R., Wijbrans, J. R., & White, S. H. (2001). SHRIMP U-Pb zircon dating of Archean core complex formation and pancratonic strike-slip deformation in the East Pilbara Granite-Greenstone Terrain. *Tectonics, 20*(6), 883-908.

Chapter 3: Identification of Apex chert Hematite Pseudofossils: Strengths and Weaknesses of Raman Hyperspectral Imaging

A portion of the work presented in this chapter was published as: "Haematite Pseudomicrofossils Present in the 3.5-billion-year-old Apex chert", (2011), Marshall, C. P., Emry, J.R. and Olcott Marshall, A. O., *Nature Geoscience*, vol 4. Issue 4, p. 240-243.

ABSTRACT

The ~3.5 Ga Apex chert from Western Australia contains microstructures that have been described as among the oldest identified microbial fossils on earth. Despite their morphological resemblance to extant bacteria and presumed carbonaceous composition, the origin and biogenicity of these structures has been hotly debated. Quartz and hematite filled microveins that bear a striking resemblance to the originally described microfossils were petrographically identified in a new suite of Apex chert samples collected in 2006. Point Raman spectroscopic analyses and Raman hyperspectral imaging verified the presence of hematite and quartz in the microveins and showed that carbonaceous material is disseminated throughout the microquartz matrix instead of being associated with the microstructures as previously described. Analysis of Raman images created by utilizing intensity at a point techniques illustrated how data quality issues can lead to the misinterpretation of hematite as carbonaceous material. The potential for misinterpretation of the distribution of materials in Raman images highlighted the necessity to utilize more than one data analysis technique and reinforced the importance of careful image data quality evaluation in order to study the context and chemistry of putative microfossils.

INTRODUCTION

The Apex chert has been studied with a variety of analytical techniques primarily focused on elucidating the origin of microstructures originally described as Earth's oldest microbial fossils (Schopf and Packer, 1987). Paleontological thin sections (~300 μm thick) were used to identify microstructures that occurred within rounded lithoclasts deposited in a shallow marine or fluviomarine environment (Schopf, 1993; Schopf, 1999; Schopf and Packer, 1987). These structures were initially interpreted as the remains of ~3.5 Ga cyanobacteria based on descriptive observations of their general morphology, size, and resemblance to extant microbes (Schopf, 1993; Schopf and Packer, 1987). This interpretation was widely accepted until a large-scale mapping project led to the reinterpretation of a hydrothermal depositional environment for the Apex chert (Brasier et al., 2002; Brasier et al., 2005, Dalton, 2002). The reinterpretation of a hydrothermal environment was later accepted in favor of the fluviomarine or marine interpretation (Schopf et al., 2010). Petrographic re-examination of the original samples and examination of newly collected samples led to a re-interpretation of the microstructures as abiotic artifacts formed by hydrothermal processes (Brasier et al., 2002; Brasier et al., 2005). While microstructures were still identified within clast-like features, they were also identified within multiple paragenetic phases including several generations of chert matrix, void and fissure filling fabrics, and veins. (Brasier et al., 2002; Brasier et al., 2005). Detailed petrographic descriptions of many of the originally described microstructures and several previously undescribed microstructures showed that many of them displayed a complex, three-dimensional branching morphology inconsistent with the proposed biological origin (Brasier et al., 2002; Brasier et al., 2005). This observation was subsequently claimed to be a result of automontaging

software that caused individual microstructures occurring at different focal depths to appear as part of a continuous structure (Schopf, 2004). The competing groups of researchers utilized Raman spectroscopic techniques including point analyses and hyperspectral imaging to analyze the samples and agreed that the microstructures were carbonaceous in composition, but they debated whether the material was biogenic kerogen or abiotic amorphous graphite (Brasier et al., 2002; Schopf et al., 2002). The original debate over these structures in the early 2000's was contentious enough that it became the subject of a Nature News feature article and was discussed in a book written by a Washington Post science writer covering the scientific debate over the ALH84001 meteorite (Dalton, 2002; Sawyer, 2006).

Microbes are relatively simple in morphology and Garcia-Ruiz *et al*. (2002; 2003) produced biomorphic silica-carbonate microstructures under simulated hydrothermal conditions and showed experimentally that these microstructures could be coated with carbonaceous material resulting in structures that resemble the Apex chert microstructures suggesting a possible abiotic mechanism of formation. In contrast, De Gregorio *et al.* (2009) utilized multiple techniques including scanning transmission X-ray microscopy (STXM) to compare microtomed separates of carbonaceous material from the Apex chert to presumed biogenic carbonaceous material from the Gunflint chert. Based on similarities in morphology and structure of the carbonaceous material from these two units they interpreted the Apex chert microstructures as biogenic in origin (De Gregorio et al., 2009). In 2011, a publication including a portion of the work presented in this chapter identified hematite psedudofossils that resembled the originally described microfossils in a new suite of samples collected from the Apex chert (Marshall et al., 2011). This publication along with studies focused on the carbonaceous materials in the Apex chert and the degree and timing of hydrothermal alteration renewed scientific debate regarding

the origin of the microstructures and the likelihood that evidence for Archean life could be preserved in the Apex chert (A. O. Marshall & Marshall, 2013; Daniele L. Pinti et al., 2009; D. L. Pinti, Mineau, & Clement, 2013; J. W. Schopf & Kudryavtsev, 2011, 2012, 2013; J. W. Schopf & Kudryavtsev, 2014; Sforna et al., 2014).

The debate over the composition and origin of the Apex chert microstructures illustrates many of the difficulties involved in interpreting evidence for ancient life. Three major factors have been proposed as the most important to evaluate claims of biogenicity: context, morphology, and a chemical composition consistent with biology (Brasier and Wacey 2012, Schopf *et al.* 2010, Wacey 2009). Schopf et al., 2010). These factors are not independently indicative of a biological origin and multiple analytical techniques are necessary to address these criteria in concert. The goal of this chapter is to expand on the information presented in the original paper on hematite pseudofossils by further addressing the petrographic context and chemical composition of the pseudofossils identified in the new Apex chert samples. Raman point spectroscopy, Raman confocal depth profiling, and Raman hyperspectral imaging were used to evaluate the composition and distribution of materials in the new suite of Apex chert samples. Raman spectroscopy is a powerful technique to study minerals and mineraloids, but due to the natural heterogeneity of geological samples a variety of data quality issues may affect the ability to collect data of sufficient quality. In particular, Raman hyperspectral imaging presents unique challenges as a result of data acquisition parameters, the computer-based techniques used to create Raman images and the intrinsic chemical properties and composition of a sample (Marshall and Olcott Marshall, 2013). This chapter includes a method that utilizes multiple data collection ranges and both univariate and multivariate data analyses to evaluate hyperspectral datasets acquired from the Apex chert microstructures. This technique could be applied to other

potential microfossils to address claims of biogenicity and to provide a more robust characterization of the spatial distribution of materials in geological samples.

MATERIALS AND METHODS

Apex chert Samples

Samples from the main Apex chert dike were collected by Dr. Craig Marshall during the Geological Society of Western Australia Pilbara fieldtrip in 2006. Several hand samples were collected from 14 sampling sites located approximately every 10 m along the outcrop of the main chert dike and included samples from the original microfossil locality (Figure 1) (Schopf and Packer, 1987). Thin section blanks were cut from the hand samples using a water cooled diamond saw. Eighty-two thin sections, including single and doubly polished serial 30 µm standard petrographic thin sections and 300 µm paleontological thin sections, were made from the thin section blanks by Burnham Petrographics, Rathdrum, ID.

Microscopy and Paragenetic Description

Polarized light microscopy of rock thin sections is a technique that has been used to identify minerals and textures in thin section for over 160 years (Vernon, 2004). The standard thickness for petrographic thin sections is 30 µm because at this thickness the majority of common rock-forming minerals such as silicates and carbonates will be transparent under a microscope regardless of their appearance in hand sample (Nichols, 2009). Other minerals, including some oxides and sulfides, will still appear opaque in 30 µm petrographic thin sections.

The use of standard petrographic thin sections allows for the observation of optical characteristics in plane and cross-polarized light that are diagnostic for mineral identification including: shape, relief, cleavage, pleochroism, refractive index, interference colors, extinction angles, birefringence, and twinning (Nesse, 1991) . Although 30 µm thin sections are considered standard for mineral identification, thicker or thinner thin sections may be necessary to address certain geological questions. Thick thin sections are used to study fluid inclusions in order to observe 3-D distribution and when the features of interest are larger than 30 µm and/or have complex morphologies such as microfossils (Goldstein and Reynolds, 1994; Taylor et al., 2011). The structures in the Apex chert were originally described as microfossils from ~300 µm thin sections, therefore 300 µm thin sections were made to compare the new samples to the previously published samples. The 30 µm thin sections allowed for the use of optical techniques to identify minerals and because they were made as serial sections observations could be directly compared to those made in the 300 µm thin sections.

Paragenetic description involves documenting the sequence of events involved in the formation of sediments, minerals and cements in rocks (Bowes, 1989). Observations, such as superposition and cross-cutting relationships of the various fracture-fill features and matrix microtextures, were used to establish a relative chronology of the formation of the various mineral and mineraloid phases in the Apex chert. The paragenetic sequences were defined using both 30 µm and 300 µm thin sections for each sample utilizing two microscope systems. The first system consisted of an Olympus BX51 microscope equipped with a 10X, 20X, 50X and 100X UIS objectives and a SPOT RT3 monochromatic video camera. The second system was an Olympus BX60 microscope equipped with 10X, 20X, 40X, 50X and 100X UIS objectives and a Qicam Qimaging color Fast 1394 video camera. To calculate the average size and size range of

mineral crystal and microstructures 50 randomly sampled examples of the features of interest were measured using a 50X objective and the calibrated measurement function in SPOT software.

Raman Spectroscopy

Raman spectroscopic analyses were performed with a Renishaw Reflex Raman microprobe with an attached trinocular Leica DMLM microscope equipped with a video camera and four objectives (100/0.9 NA, 50/0.75NA, 20/0.40NA, 5/0.12NA). An argon-ion laser (Modu-Laser) emitting at 514.5 nm with a surface power of 1.0-1.5 mW was used to excite the samples, a 2400l/mm grating was utilized for analyzing the resulting scattered light at room temperature with a Peltier cooled, charge coupled device (CCD) camera (1024x256 pixels). The Raman system was calibrated by analyzing the position of the F_{1g} mode from the spectrum of silicone. After calibration an offset correction was performed to confirm that that position of the detected silicon band was at 520.50 ± 0.10 cm^{-1} if necessary. Point spectra were collected over a spectral range of 100-4000 cm^{-1}, confocal depth profiles over 100-4000 cm^{-1} or 100-4000 cm^{-1}. Hyperspectral datasets were collected utilizing Renishaw's StreamLine™ mode with an accumulation time of 0.1 second over a range of 360-1690 cm^{-1} or 100-1400 cm^{-1}. In order to directly compare the image datasets to previous studies post-acquisition baseline correction or normalization procedures were not performed.

RESULTS AND DISCUSSION

Petrography of the Apex chert Microstructures

Microstructures similar to those previously reported from the Apex chert were identified in both 300 µm (Figure 1. A-J) and 30 µm thin sections (Figure 1. K-P) of the new Apex chert samples. These features are opaque, typically reddish to dark brown in color (Figure.1, C,J, N-P) and commonly appear segmented or septated, similar to microstructures previously described from the Apex chert (Schopf, 1992; Schopf, 1993; Schopf and Kudryavtsev, 2012; Schopf and Packer, 1987). The diameter of a random sample of 50 microstructures from the 300 µm thin sections yielded a ranged from 1-20 µm in diameter with an average of 6.1 µm and a median of 5 µm. In order to determine if the average diameter of the microstructures in the new samples is equal to the previously reported average diameter measured from 1800 "cells" from 175 specimens (Schopf, 1993; Schopf and Kudryavtsev, 2011, 2012; Schopf, 1983), a one-sample t-test was performed. The null hypothesis for this test states that the two average values are equal, therefore a low p-value (typically below 0.5 at the 95% confidence level) would be necessary to reject the null hypothesis in favor of the alternate hypothesis stating that the average values are different. The calculated p value = 0.856 which is not low enough to reject the null hypothesis, therefore the average diameter of the microstructures in the new samples is statistically equal to the previously reported average diameter. A one sample t-test was used in lieu of the standard two-sample t-test generally applied to compare two sample populations because the published data includes only average values, ranges, and numbers of cells measured for the 11 taxa described from the Apex chert (Schopf, 1993; Schopf, 1983).

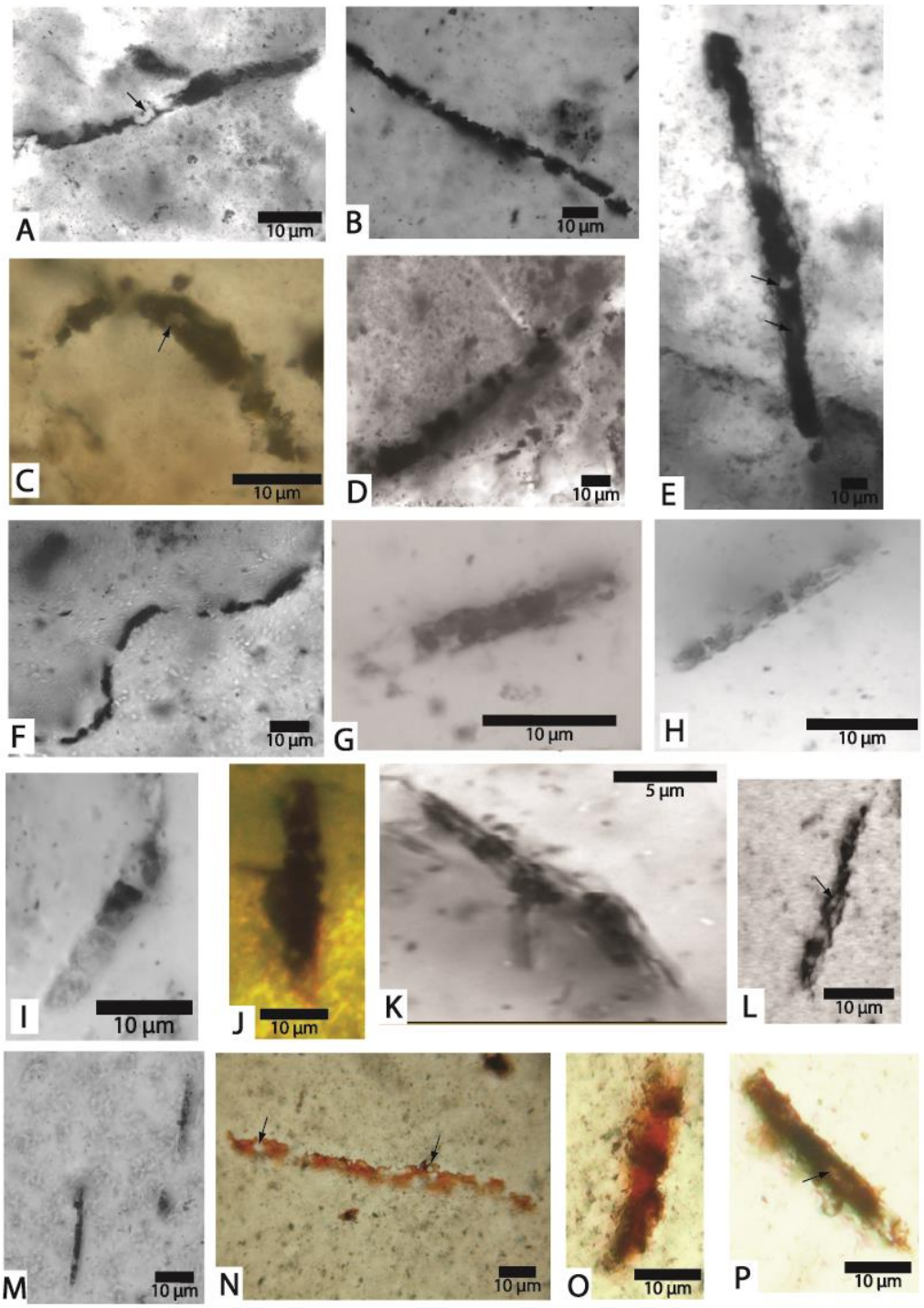

Figure 1. Representative examples of opaque microstructures found in 300 µm (A-J) and 30 µm thin sections (K-P) of the new Apex chert samples. The microstructures are composed of concentrations of a darker, more opaque phase that ranges in color from dark orange to reddish-brown or black which is separated by zones of a more transparent, lighter colored or clear phase which often gives the microstructures a septated appearance. Several of the microstructures also contain patches of the transparent material that is surrounded by the darker, more opaque phase (A, C, L, N, P indicated by arrows) which appears similar to the cell lumen described from the original microstructures (Schopf, 1992, Schopf, 1993, Schopf and Kudryavsev, 2012).

Although the largest diameter measured from the random sample of microstructures was 20 µm, larger diameter microstructures that display a septated appearance were also identified in the new samples of the Apex chert (Figure 4.2). The larger microstructures were less common than the smaller microstructures consistent with observations of a less abundant population of microstructures with a minimum diameter of 36 µm made by Brasier et al. (2005).

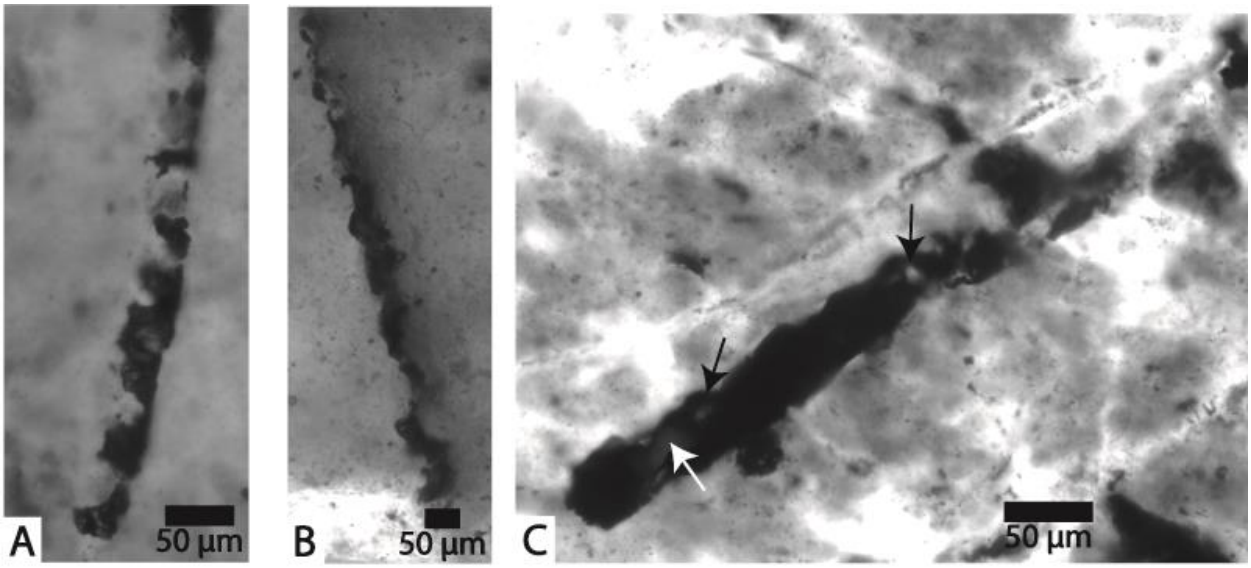

Figure 2. Representative microstructures larger than 20 µm in diameter identified in the new Apex chert samples. A = 37 µm diameter, B varies in diameter from 30-45 µm and C = 44 µm in diameter. A and B appear septated with alternating zones of opaque and clear material similar to the smaller microstructures. C appears to be more solidly composed of the opaque phase, but it does contain small inclusions of the transparent phase surrounded by the opaque material denoted by the black arrows. The white arrow marks a hole in the thin section. The observation of larger microstructures than those originally described from the Apex chert is consistent with Brasier *et al*'s (2002, 2005) reassessment of the original samples. It was also noted that the number of larger microstructures decreased as the diameter of the microstructures increased and that larger microstructures commonly appear less septated than smaller ones (Brasier et al., 2005).

The microstructures identified in the new Apex chert samples occur within several textural phases. Schopf (1993) reported "minute filamentous microstructures" within clasts in the Apex

chert. The 300 µm thin sections of the new samples contain clast-like features that are comparable to previously reported clasts (Schopf, 1993; Schopf and Kudryavtsev, 2012; Schopf and Kudryavtsev, 2014) and contain segmented microstructures that could be described as filamentous in morphology (Figure 4.3 A-H). Although the Apex chert microstructures were originally described as occuring only within lithoclasts, later work documented that up to half of the microstructures occured in other paragenetic phases including veins and filled voids (Brasier et al., 2002; Brasier et al., 2005; Brasier et al., 2011). Microstructures identified in the new Apex chert samples can also be seen in the matrix (Figure 3 A, G, H and Figure 3. F, C, K, J).

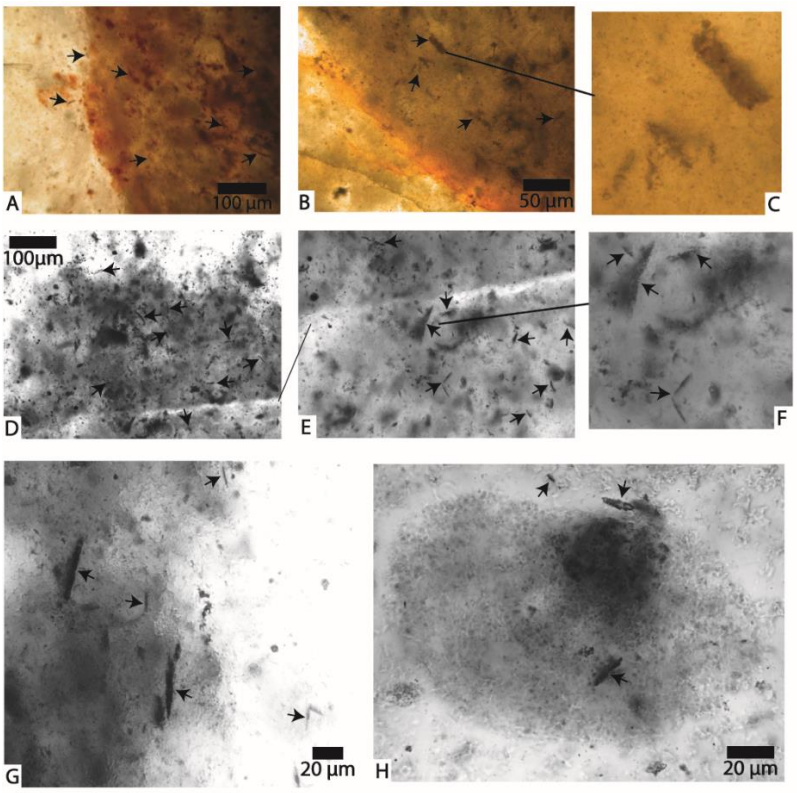

Figure 3. Clast-like structures (A, B, D, G, H) identified in 300 µm thin sections of the new Apex chert samples that are similar to previously reported clasts (Schopf and Packer, 1987, Schopf, 1992, Schopf, 1993, Schopf and Kudryavsev, 2012). The photomicrographs A, B, D, and G show the edges of four large clast-like features while a smaller feature is shown in H. Representative septated microstructures are highlighted with arrows. Enlargements (C and F) of the microstructures seen in B and E respsectively, highlight the septated appearance of these structures. Many of the microstructures occur within these clast-like features consistent with previous studies (Schopf and Packer, 1987, Schopf, 1992, Schopf, 1993, Schopf and Kudryavsev, 2012). Microstructures also occur in the matrix surrounding the clast-like features (A, D, G, and H) similar to previous reports (Brasier et al., 2002, 2005, 2011).

The Apex chert contains a variety of cross cutting fractures (Figure 4. A, G) that also contain microstructures (Figure 4. B, D, E, H, I). The identification of microstructures within clast-like features, in the chert matrix, and within veins described here is consistent with the distribution of microstructures described from the original samples (Brasier et al., 2002; Brasier et al., 2005).

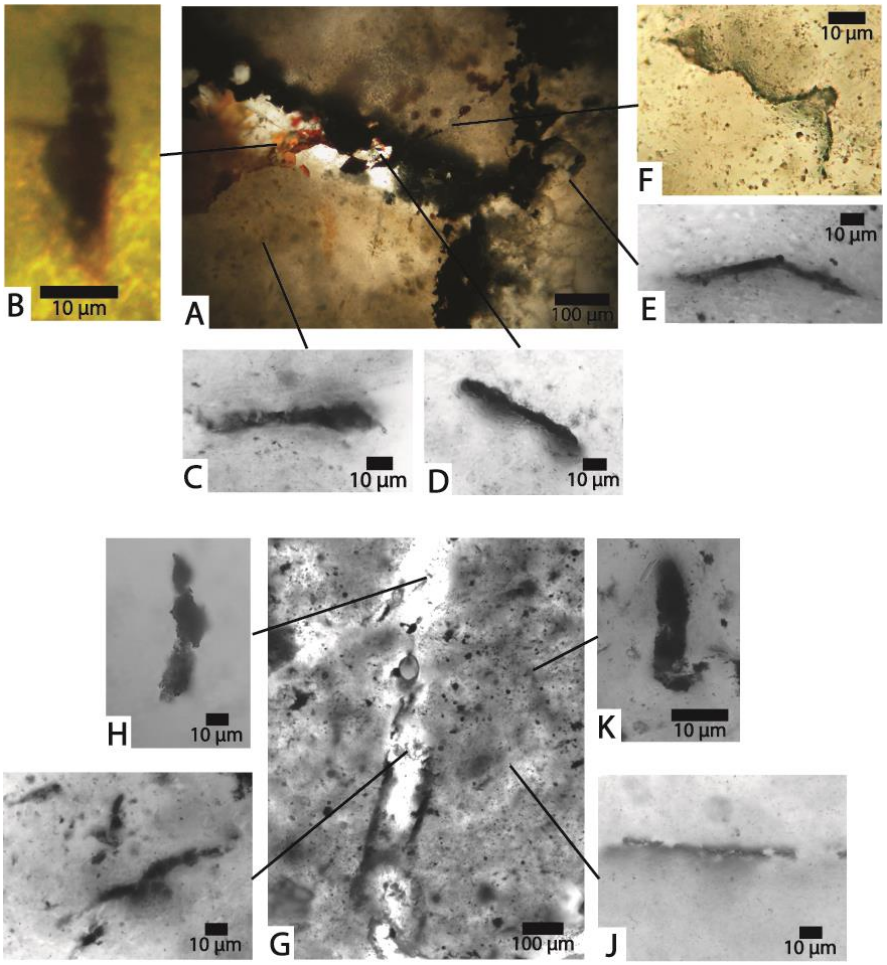

Figure 4. Distribution of microstructures within the matrix and within cross-cutting fractures in 300 µm thin sections from the new Apex chert samples. The topmost photomicrographs show intersecting fractures, microstructures that occur within these fractures (B,D,E), and microstructures that occur within the microquartz matrix (C and F). The lower photomicrographs illustrate another cross-cutting fracture, (G), examples of microstructures that occur within this fracture (H, I) and in the microquartz matrix surrounding the fracture (J, K).

Comparison of serial 300 and 30 µm thin sections made from the same blank provided additional textural information not readily apparent from observation of the 300 µm thin sections alone. Crystal boundaries are visible in the chert matrix in 30 µm thin sections which allowed for the optical identification of quartz. A random sample of 50 crystals from the matrix phase seen in the 30 µm thin sections ranged in size from 0.3-6 µm with an average of 2.2 µm. Observation of corresponding regions in serial 300 and 30 µm thin sections also demonstrated that many of the microstructures seen in 300 µm thin sections corresponded to veins in the 30 µm thin sections (Figure 5). The veins seen in the 30 µm thin sections are oriented similarly to the corresponding microstructures in the 30 µm thin sections and are comparable in size (Figure 5). Petrographic observations of the veins in the 30 µm thin sections showed that they are typically filled with a transparent, blocky, crystalline material optically identifiable as quartz and a secondary phase that typically appears red, brown, or black in color. A random sample of 50 quartz crystals measured from 50 fractures observed in the 30 µm thin sections ranged in size from 4-65 µm with an average of 17.3 µm. The ability to identify the presence of different quartz crystal sizes (microquartz matrix and meso-megaquartz vein fill) is lost in the 300 µm thin sections, where the material surrounding the microstructures appears amorphous.

The observation of an association between several microstructures in 300 µm thin sections with veins in serial 30 µm thin sections led to the hypothesis that microstructures observed in 300 µm thin sections corresponds to veins that can be more easily identified in 30 µm thin sections. Comparison of a variety of microstructures seen in 300 µm thin sections with the corresponding region in serial 30 µm thin sections showed that while a correlation between

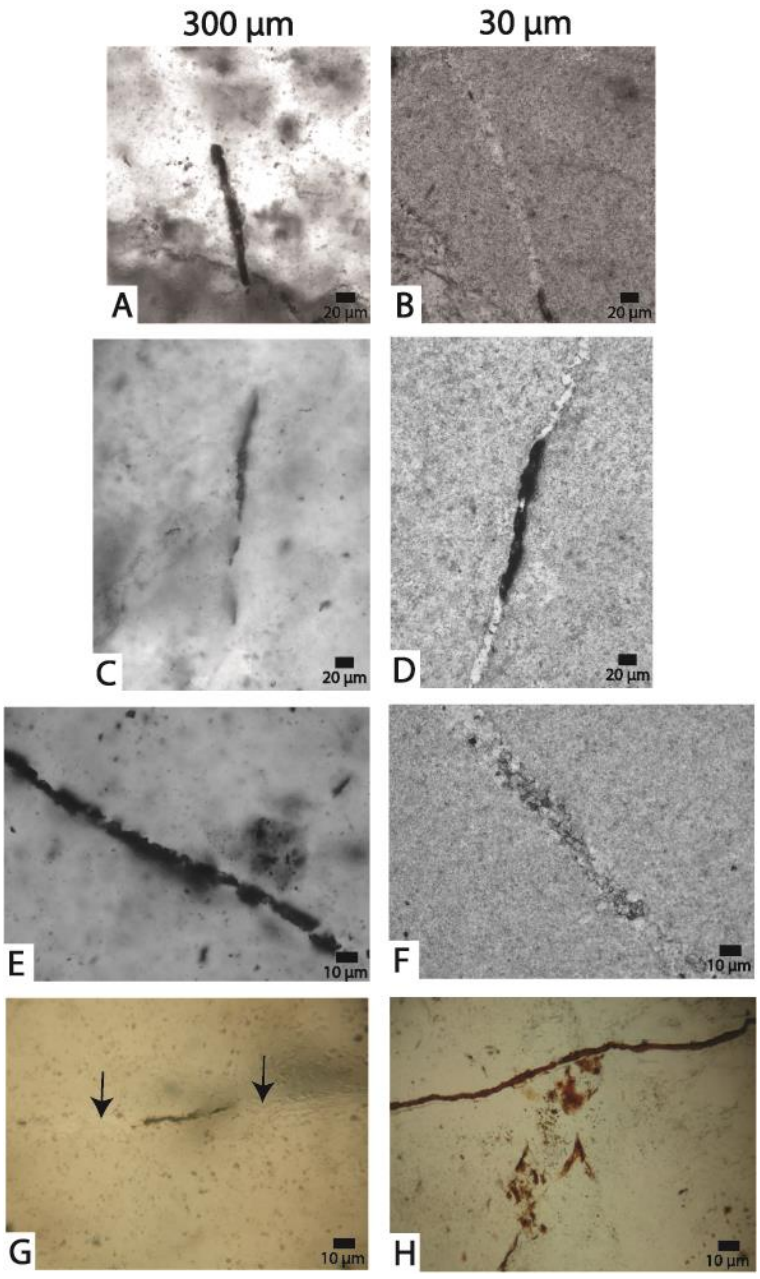

Figure 5. Microstructures observed in 300 µm thin sections and the corresponding region in serial 30 µm thin sections showing that the microstructures are veins. The veins shown in A and E provide examples of the septated or segmented appearance of many of these structures in 300 µm thin section. The veins in B and D illustrate the lateral variability of concentrations of the opaque phase and quartz seen in many of the microstructures. The vein in F shows that the opaque phase can also be concentrated in patches and along the quartz crystal boundaries in the veins which results in the segmented appearance in F. The margins of the veins are typically indistinguishable in the 300 µm thin sections (A, C, E) due to the loss of resolution, but if the microstructure occurs very near or at the surface of a 300 µm thin section the microscope can focused on the surface and careful observation can often identify a ghost of the outline of the vein margin (G, arrows). The average apparent size difference of the veins in the 300 and 30 µm thin sections is 4.2 µm.

microstructures and veins was typically observed, the association was not always as obvious as the examples shown in Figure 5. Microstructures that appear less than 10 µm in diameter in 300 µm thin sections were revealed to be associated with veins an order of magnitude larger than the microstructures. For example, the microstructure in Figure 6 A is 8 µm in diameter, but the corresponding region in the 30 µm thin sections shows a large vein (85 µm diameter) composed of equant megaquartz and a dark, opaque phase that is concentrated along the outer margins of the vein. In this instance, the microstructure seen in the 300 µm thin section appears to correspond to the edge of the large vein and the irregular, sinuous shape can be explained by the irregular distribution of the dark material along the vein margin. The microstructures shown in Figure 6 C further illustrate how relatively small features seen in 300 µm thin sections can relate to a large fractures in 30 µm thin sections. Here the 30 µm thin section shows another large fracture (132 µm diameter) filled with equant megaquartz and the dark, secondary phase which occurs as concentrations along quartz crystal boundaries and inclusions within the quartz (Figure 6 D). The two microstructures seen in the 300 µm thin section (Figure 4 C) correspond to the opaque phase concentrated along the megaquartz crystals in the vein (Figure 6 D).

Veins are highly complex and morphologically diverse structures ranging in size from the µm to km scale, two dimensional shape from linear to "S" or "Z" shaped, and three-dimensional shape including tabular bodies, lenses, and even "blobs" (Bons, 2000; Bons et al., 2012; Passchier and Trouw, 2005). The processes involved in the filling of fractures to form veins can be extremely complex and have been the subject of significant study primarily in monomineralic systems (Bons, 2001; Bons et al., 2012; Hilgers and Urai, 2002; Passchier and Trouw, 2005). The distribution of mineral phases, crystal morphology, and crystal size can vary spatially in 2-

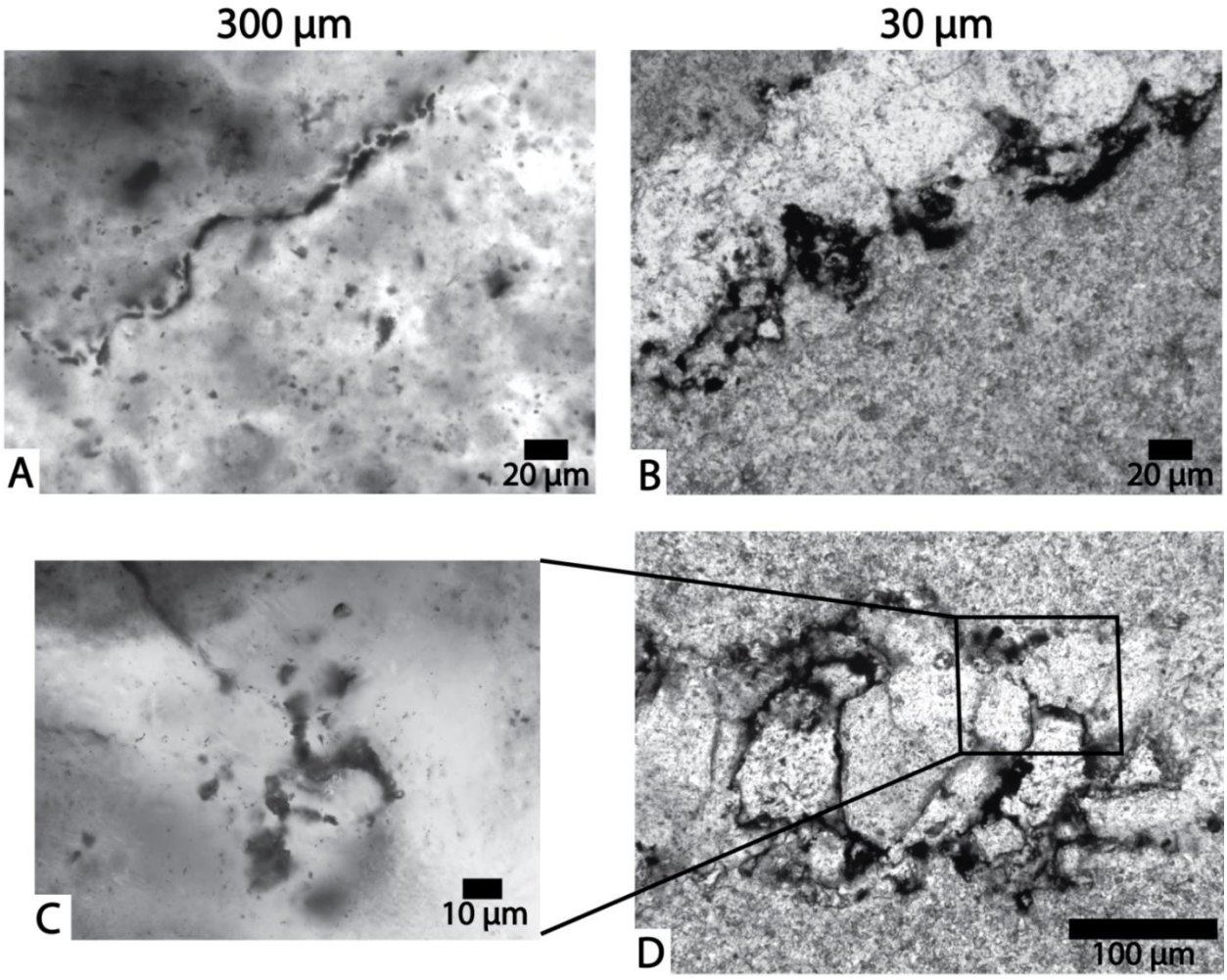

Figure 6. Microstructures identified in 300 µm thin sections that correspond to portions of large fractures in 30 µm thin sections. Photomicrograph A shows an opaque, sinuous, segmented feature surrounded by what appears to be amorphous matrix. The 30 µm thin section (B) allows for the identification of the vein margins and internal texture composed of a concentration of opaque material along the edge and equant megaquartz crystals filling the remainder of the vein. The variable distribution of the opaque phase results in the sinuous, segmented appearance of the vein in the 300 µm thin section (A). Photomicrograph C shows a curved microstructure and a small, more linear segmented microstructure (arrow) that appear to be surrounded by amorphous matrix. In the corresponding 30 µm thin section (D) the megaquartz crystal boundaries in the vein fill can be seen showing that the microstructures correspond to the opaque phase concentrated along the crystal boundaries.

and 3-dimensions due to a variety of factors such as the location within the vein, changes in fluid chemistry, timing, and the amount of space available for mineral growth (Cervantes and Wiltschko, 2010; Hossain, 2012; Urai et al., 1991). In the case of bi-or polymineralic composite veins, the accessory mineral phases are typically concentrated in discrete zones along vein

margins or centers or as inclusions along the crystal boundaries of the primary mineral phase (Becker et al., 2011; Hossain, 2012; Kuznetsov et al., 2012; Urai et al., 1991). The presence of several generations of veins in the Apex chert was documented in previous studies and it was noted that many of the microstructures appeared to occur in close proximity to veins (Brasier et al., 2005; Schopf, 1993).

Comparison of veins identified in 30 μm thin sections with corresponding regions in the 300 μm thin sections shows complex vein-fill textures composed of three-dimensional crystals or aggregates of the secondary opaque mineral visible in what appears in the 300 μm thin sections as amorphous matrix (Figure 7 and 8). The shape and distribution of the opaque mineral changes with depth in thin section and at several focal depths can create a segmented appearance (Figures 7 and 8). Additionally, the Apex chert contains veins that have complex curved or sinuous shapes that also display variable spatial distributions of quartz and the opaque material which can appear segmented at multiple focal depths (Figure 8). The spatial distribution, and therefore the outline, of where the opaque material occurs within the vein can vary dramatically at depth (Figure 8 D). Due to the complex shape of the vein, smaller segmented features can appear to branch from the main concentration of the opaque material at different focal depths (Figure 8 C, 3-6). Brasier et al. (2002; 2005) suggested that the appearance of segmentation and cellularity in the microstructures was an artifact of the irregular distribution of graphitic carbon along quartz crystal boundaries. The complex vein fills composed of quartz and the opaque phase observed in the new samples appear to exhibit a similar phenomenon. Due to the inability to resolve the quartz crystal boundaries in 300 μm thin sections, the concentrations of the opaque material in the veins can appear as elongate, segmented, three-dimensional structures encased in amorphous

matrix (Figure 7 and 8). Additionally, the previous studies used automontaging software to combine

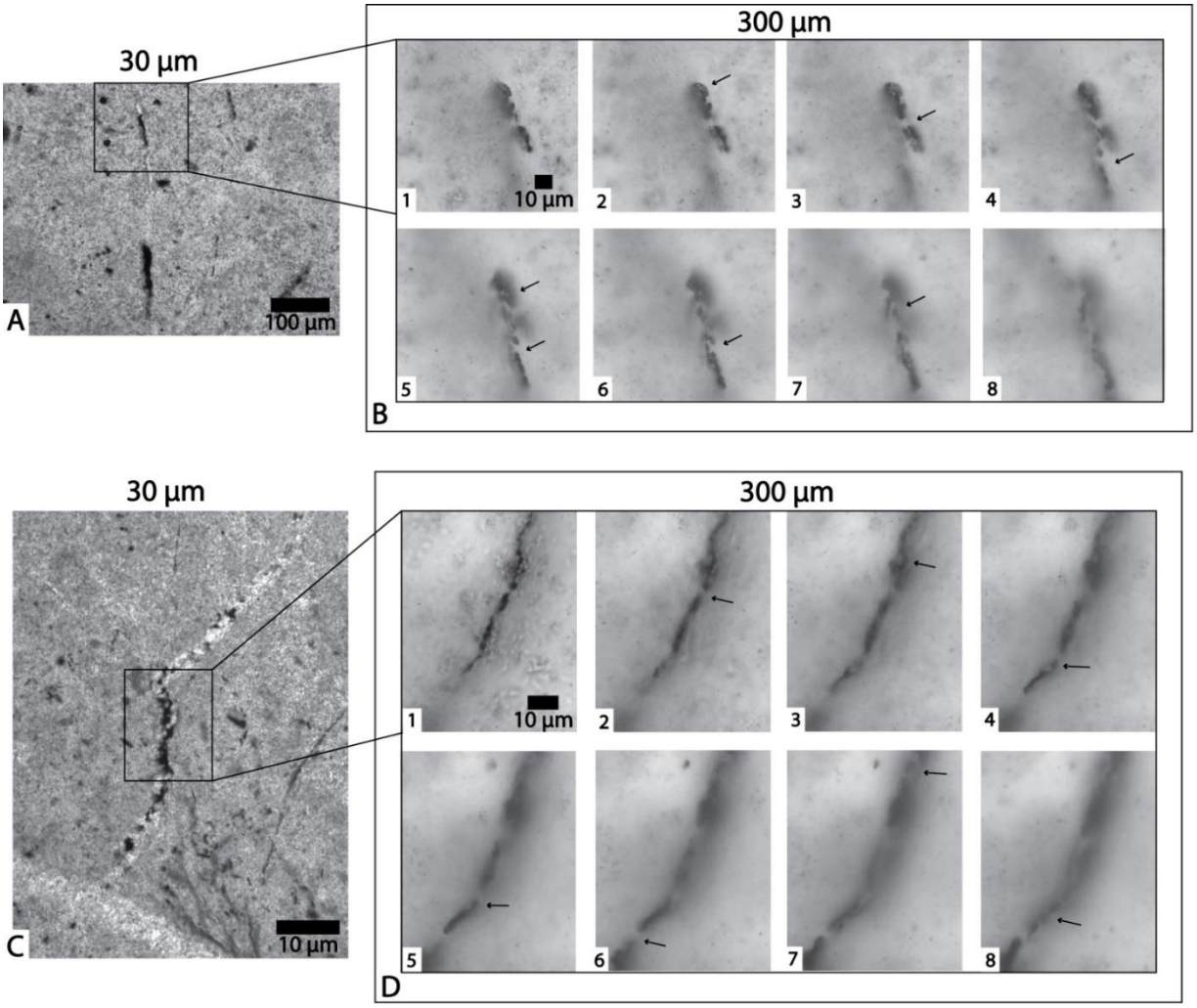

Figure 7. Comparison of veins in 30 µm thin sections with depth series photomicrographs of the veins in 300 µm thin sections. The shape and distribution of the opaque phase changes with depth and the veins display a septated or segmented appearance at and several focal depths (marked by arrows). In the depth series photomicrographs the margins of the vein are typically obscured resulting in the appearance of an isolated, tubular, opaque structure surrounded by amorphous matrix.

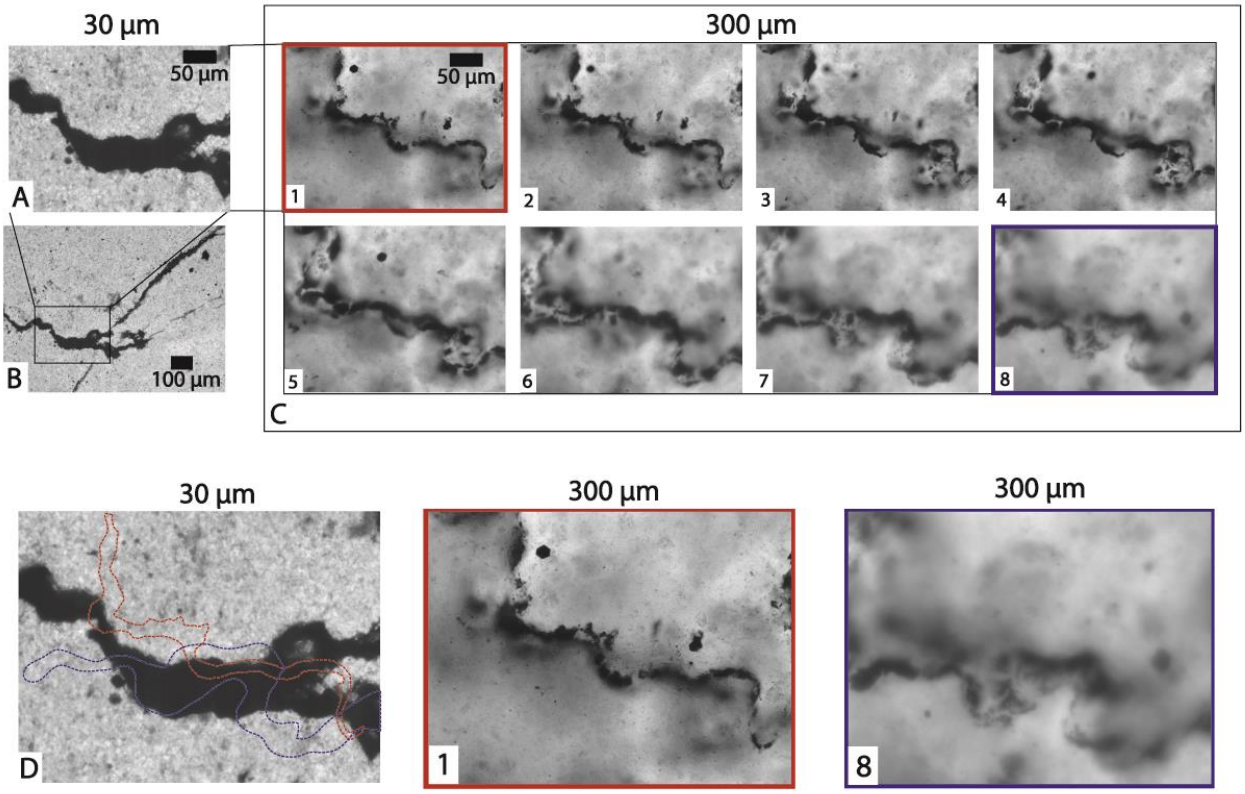

Figure 4.8. Comparison of a curved stylosuture vein in 30 µm thin sections with depth series photomicrographs of the vein in 300 µm thin section. In the 30 µm thin section, the vein appears to be filled primarily with an opaque phase and with small isolated zones of quartz. The depth profile photomicrographs show how the spatial variability of the opaque phase changes at depth within the vein. The opaque phase appears to branch due to the change in the vertical distribution within the vein (compare C 1-4, marked by arrows). At several focal depths within the photomicrographs from the 300 µm thin sections the vein display a markedly segmented appearance and because the vein margins can be difficult to distinguish, the alternating quartz and opaque phase creates the appearance of an isolated, sinuous, septated or segmented structure. Outlines of the apparent distribution of the opaque phase at the surface (red outline) and 20 µm (blue outline) illustrates how the distribution of the opaque phase can dramatically with depth within the veins (D). Colored outlines in D correspond to Figures C 1 and 8 which are magnified for comparison.

multiple focal planes at depth into composite photomicrographs of the microstructures (Brasier et al., 2002; Brasier et al., 2005; Schopf, 1993; Schopf, 1999; Schopf and Kudryavtsev, 2011, 2012;

Schopf et al., 2002; Schopf and Packer, 1987). It is possible that this technique could have enhanced the septated, cell-like appearance of the previously reported microstructures.

Observations of the larger-scale context in which microstructures identified only from 30 µm thin sections also support the interpretation that the microstructures are veins. Small features that commonly appear segmented or septated can be found in close proximity to larger veins, concentrations of veins, or stylolites (Figure 9). These features can be identified as discontinuous microveins filled with optically similar phases to the larger veins (Figure 4. 9).

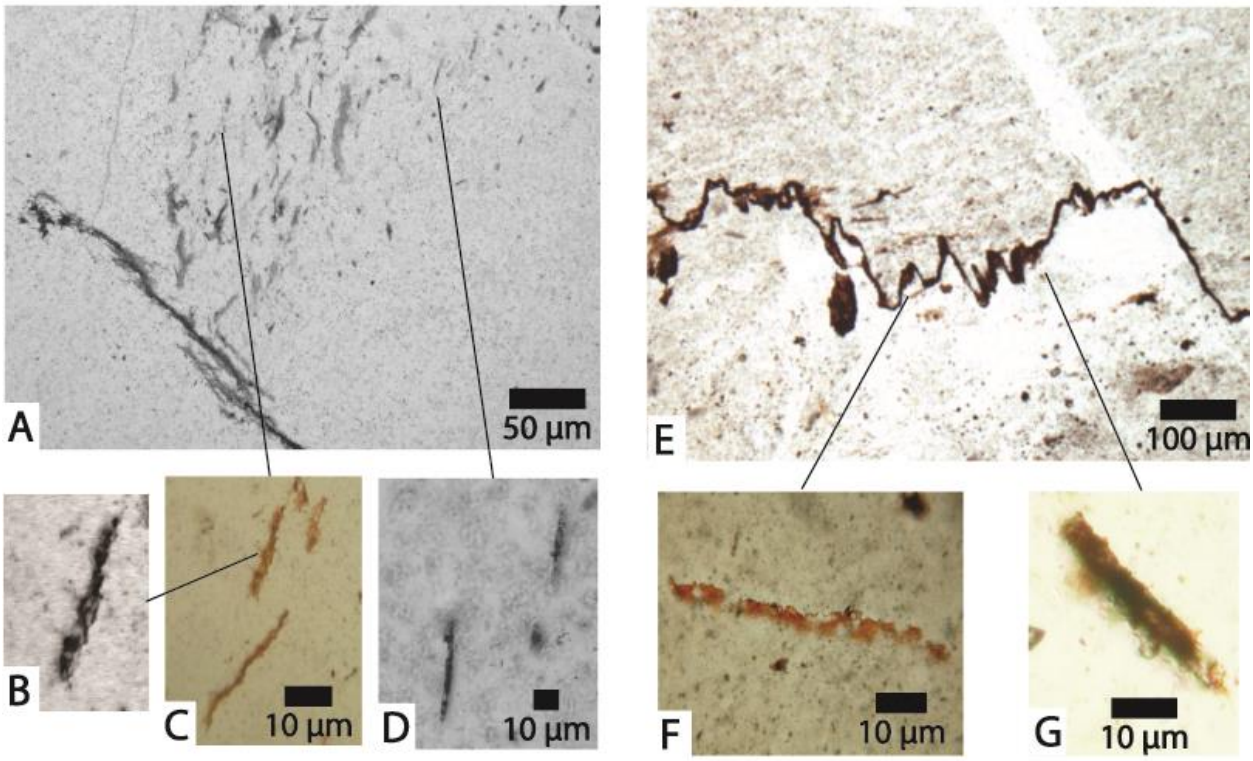

Figure 4.9. Microveins with a septated or segmented appearance identified in 30 µm thin sections. The microveins occur proximal to larger veins or stylolites and contain optically similar phases to the larger structures. The microveins can appear septated due to the distribution of crystal aggregates of the secondary phase around the microquartz crystals (B, C, F, G). Alternating crystals of microquartz and the secondary phase can also create the appearance of segmentation (D). Depending on the thickness of the microvein and the location within the thin section these structures can appear as three-dimensional tubular features (F, G).

A comparison of the photomicrograph shown in Figure 9 A with the corresponding region in the serial 300 µm thin section (Figure. 10) shows how different these structures can appear. In the 30 µm thin section the margin of the clast-like feature (Figure 4.10 A) corresponds to the concentration of veins (Figure 10 B). The microveins that can be identified in the 30 µm thin section (Figure 10 B) occur within the clast-like feature seen in the 300 µm thin section that appears to contain several septated microstructures (Figure 3 B-C and Figure 10 A).

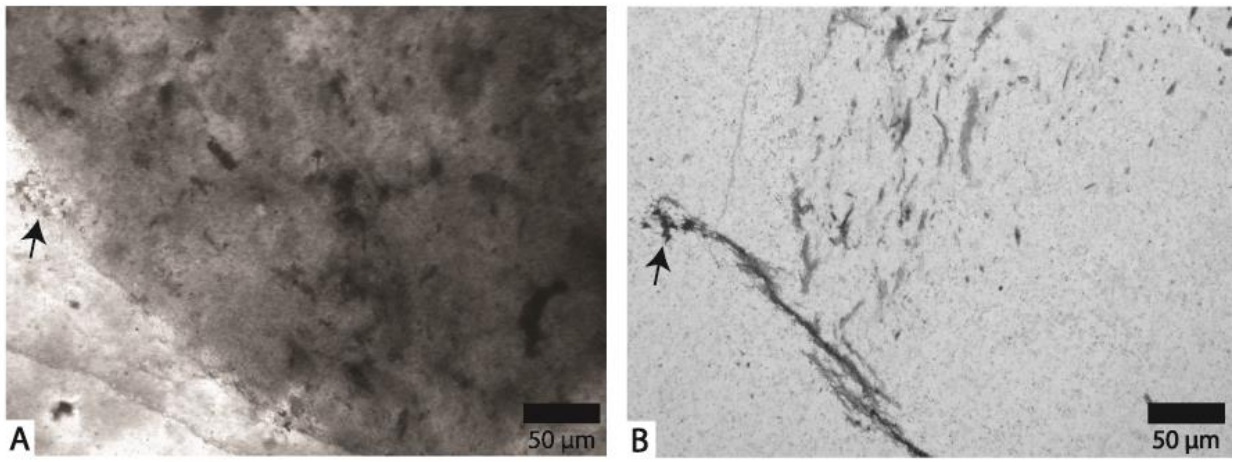

Figure 10. Comparison of a clast-like feature seen in 300 µm thin section (A) that contains segmented microstructures with the corresponding region from the serial 30 µm thin section that shows a vein array and series of microveins (B). For reference, the arrows mark the upper limit of the vein array seen in the corresponding photomicrographs.

Raman Spectroscopy

Point-Raman spectroscopy, Raman confocal depth profiling, and 3D Raman imaging were used to analyze the composition of the veins in both 300 and 30 µm thin sections. Point Raman spectra obtained from two examples of corresponding features in 300 and 30 µm thin sections are shown in Figure 11.

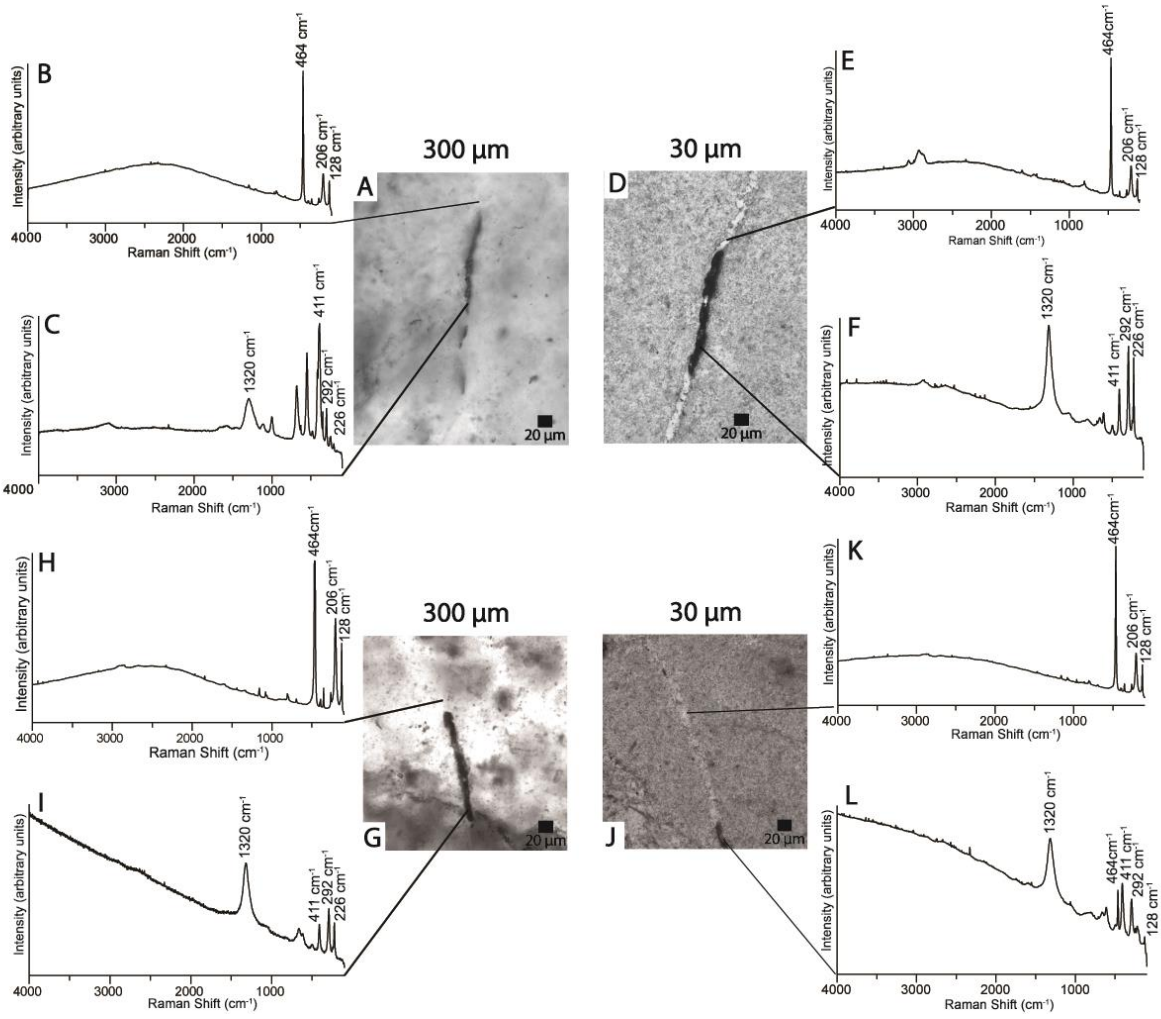

Figure 11. Representative point Raman spectra obtained from microstructure and corresponding veins in 300 and 30 µm thin sections. Raman spectra from the clear phase (B, C, H, K) can be identified as quartz based on the presence of the labeled Raman bands at 128, 206, and 464 cm^{-1} and low intensity bands at 265, 355, 394, 696 and 796 cm^{-1} present in the spectra. Raman spectra obtained from the opaque phase (C, F, I, L) can be identified as hematite by the intense Raman bands at 226, 292, 411, and 1320 cm^{-1},and lower intensity bands at 247, 299, 497, and 612 cm^{-1}. The Raman spectra from the opaque phase in L shows the presence of both minerals due to the location, laser spot size, and depth of the opaque phase in the area analyzed. Note the variation in the autofluorescence backgrounds seen in the hematite spectra and that a high autofluorescence background is seen in both the 300 and 30 thin sections.

The Raman spectra of the dark, opaque material contain diagnostic phonon modes characteristic of hematite (A_{1g} symmetry modes at 226, 497 cm^{-1} and E_g symmetry modes at 247, 292, 299, 411 and 612 cm^{-1}) (de Faria et al., 1997). The intense, broad band located at 1320 cm^{-1} is

assigned to a second order LO mode ($2E_u$ symmetry) due to the presence of hematite lattice defects (Marshall and Olcott Marshall, 2013; Shim and Duffy, 2002). The spectra acquired from the transparent material within the identifiable veins in the 30 µm thin sections (Figure 11 B, D) and at the locations indicated in the corresponding 300 µm thin section (Figure 11 A, C) contain intense bands at 128 cm^{-1} (E_{LO+TO} mode), 206, and 464 cm^{-1} (A_{1LO} modes) and less intense bands (265 and 696 cm^{-1} E_{LO+TO} modes, 394 and 796 cm^{-1} E_{TO} modes and an 355 A_1 mode) indicative of α-quartz (Gillet et al., 1990; Kingma and Hemley, 1994). Point Raman spectroscopy consistently verified the presence of hematite and quartz in veins from both 30 and 300 µm thin sections.

Point Raman spectra were also acquired from the microquartz matrix away from visible fractures and other mineral phases in both 30 and 300 µm thin sections. The spectra contain the relatively intense main quartz bands (128, 206, and 464 cm^{-1}) but also contain two broad bands in the carbon first order region centered at ~1350 and 1600 cm^{-1}, the "D" and "G" bands of disordered carbonaceous material (Figure 12). The Raman point spectra collected from the new samples show that the opaque material in the microstructures and veins is hematite instead of disordered carbonaceous material as previously reported (Brasier et al., 2002; Brasier et al., 2005; Schopf, 1993; Schopf and Kudryavtsev, 2012; Schopf and Kudryavtsev, 2014; Schopf et al., 2002). Disordered carbonaceous material is present in the Apex chert, but Raman point spectroscopy shows that it occurs within the microquartz matrix and not in the veins.

Point Raman spectroscopy is a typically a surface technique, and under the acquisition parameters used in this and previous studies (Brasier et al., 2002; Brasier et al., 2005; Schopf and Kudryavtsev, 2012; Schopf et al., 2002), a 514.5 nm laser will penetrate no more than 1 µm into siliceous samples (Yan, 2004). Confocal Raman spectroscopy utilizes a pinhole or slit to restrict

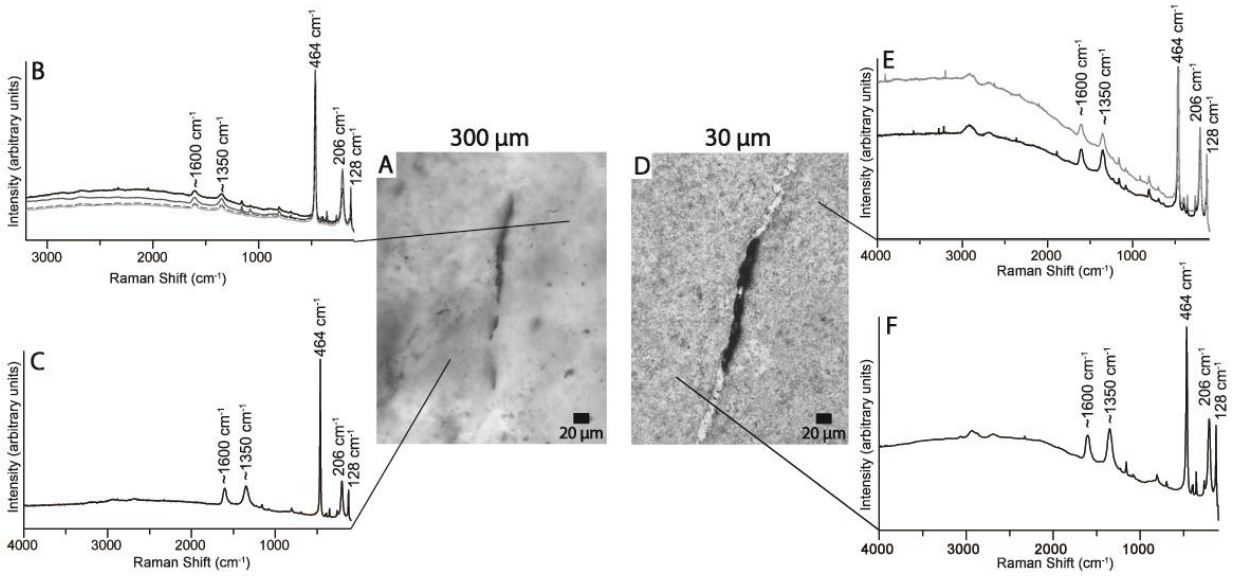

Figure 12. Representative point Raman spectra obtained from the microquartz matrix showing the characteristic Raman bands for quartz (128, 206 and 464 cm^{-1} bands are labeled, the spectra also contain low intensity bands at 265, 355, 394, 696 and 796 cm^{-1}). The spectra also contain the two broad bands located at ~1350, and ~1600 cm^{-1}, the D and G bands characteristic of disordered carbonaceous material. The multiple lines seen in A and B represent different spectra acquired from the same point with the thin section in different orientations, A1 shows spectra in 4 different orientations (grey-scale lines and dashed line) acquired by rotating the thin section 90 degrees four times, and shows spectra in two orientations (grey and black lines) after rotating the slide once 90 degrees. The spectra show no major differences in band shape, location or intensity. The spectra acquired from the 30 µm thin section show a higher background compared to the 300 µm thin section which was consistently seen in spectra acquired from the matrix on 30 µm thin sections. This difference is likely due to fluorescence from the mounting epoxy that affected Raman spectra acquired from the thinner 30 µm thin sections.

the scattered light reaching the detector to a volume centered around a specific laser focal plane within a sample (Smith and Dent, 2005). The size and shape of the volume from which the scattered light is collected depends on several factors including the numerical aperture (NA) of the microscope objective, the refractive index of the material and the wavelength of the laser (Dieing et al., 2010). Confocal depth profiling was performed in order to determine the vertical spatial distribution of the hematite, quartz and disordered carbonaceous material identified by point Raman spectroscopy in the new Apex chert samples. Data acquired from confocal Raman depth profiles is presented as false-color images showing the distribution at depth within the thin

section and as stacked plots showing representative spectra acquired at depth within the thin sections as suggested by Marshall and Olcott Marshall (2013).

Representative examples of confocal depth profiles from two regions in a vein in 30 µm thin section are shown in Figure 13. The false color image (Figure 13 B) and the stacked plot of representative spectra from the depth profile (Figure 13 C) show the presence of hematite and quartz in the region where the opaque vein fill phase occurs. The false color image (Figure 4.13 D) and representative stacked plot of spectra (Figure 13 E) from the clear region in the vein show the presence of α-quartz. Confocal depth profiles were also acquired from the same vein in the serial 300 thin section. The depth profile through the vein at the point indicated (Figure 14 A and B) verifies the presence of hematite and quartz (Figure 4.14, C and D). For comparison, a confocal depth profile was acquired from the microquartz matrix away from the fracture in the thin section (Figure 15 A and B). The false color image (Figure 15 C) and stacked plot of representative spectra (Figure 15 D) show the presence of quartz and disordered carbonaceous material from the surface of the thin section to 15 µm in depth.

Raman mapping or imaging, also called hyperspectral imaging, is becoming popular in the geosciences because it can be used to identify and determine the *in situ* spatial distribution of materials in 2-and 3-dimensions (Bernard et al., 2008; Marshall and Olcott Marshall, 2013; Nasdala et al., 2012). Raman 2-D images are a visual representation of the presence and distribution of various components in a sample based on many collected spectra over a defined x, y region of interest in a sample. Using the confocal set-up, the laser can be focused at multiple depths to collect spectra over the region of interest resulting in acquisition of a 3-D dataset (Bernard et al., 2008; Marshall and Olcott Marshall, 2013; Nasdala et al., 2012; Nasdala et al., 2004). Two-dimensional images can then be produced from the collected spectra at various

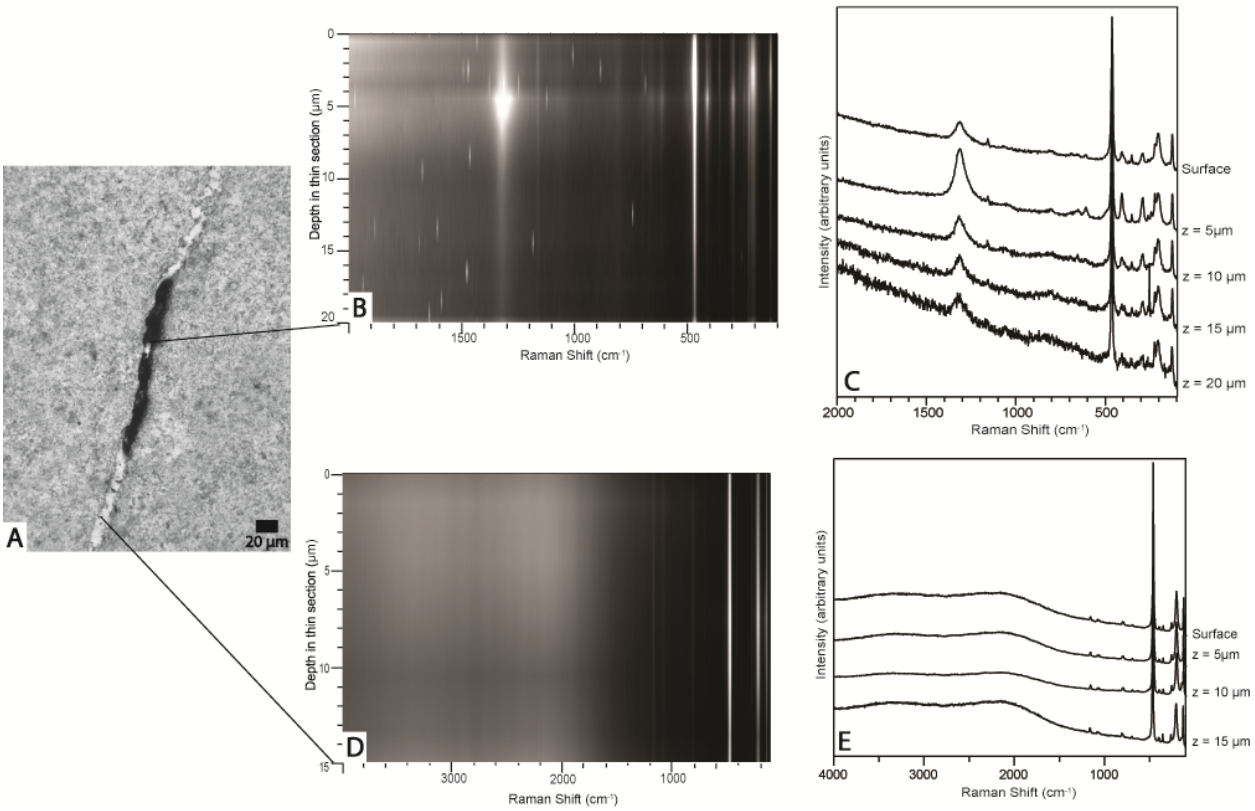

Figure 13. Confocal Raman depth profiles from a vein in 30 µm thin section. The false color image (B) from the indicated location A shows the presence of hematite (intense Raman bands at 226, 292, 411 and 1320 cm^{-1}) and quartz (intense Raman bands at 128, 206 and 464 cm^{-1}) in the opaque section of the vein from the surface to 20 µm in depth. The stacked plot shows representative spectra from the profile every 5 µm from the surface (C). The false color image (D) and the stacked plot from the surface to 15 µm from the clear phase at the indicated location (A) show the presence of quartz in the vein to 15 µm in depth (intense Raman bands at 128, 206 and 464 cm^{-1}) (E). The grey color at the high ends of the spectral range in the false color images (B and D) is due to the presence of a high fluorescence background. Note the variation in fluorescence background and the intensity of the 1320 cm^{-1} hematite band seen in the hematite spectra (B and C). The bright spot seen in B at 1320 cm^{-1} at 5 µm depth corresponds to an increased intensity of the 1320 cm^{-1} hematite band (C).

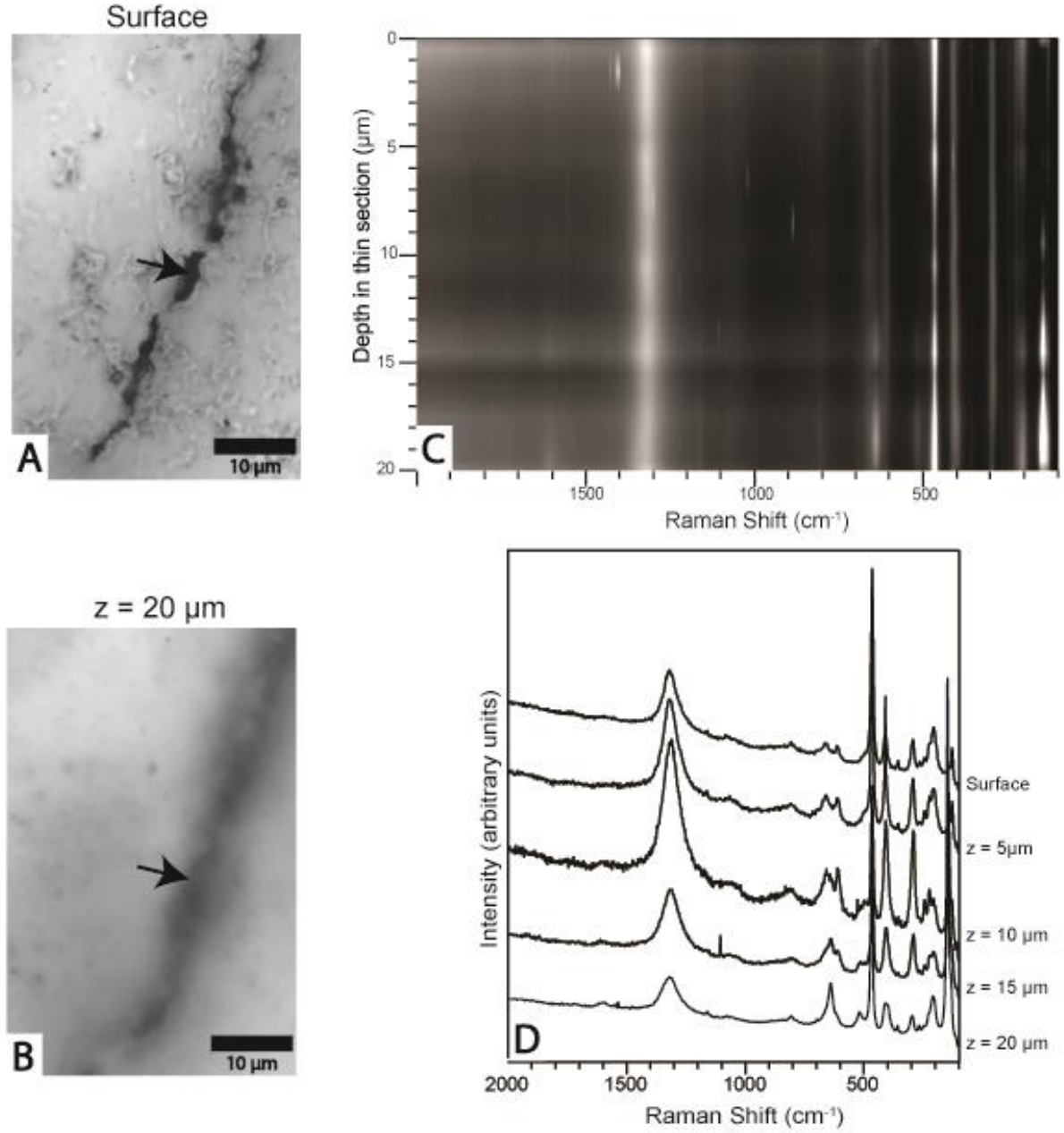

Figure 14. Confocal Raman depth profiles from the vein shown in Figure 7 C and D. The photomicrographs show the vein focused at the surface (A) and at ~20 µm (B) in the 300 µm thin section. The false color image (C) from the location indicated by the arrows (A and B) shows the presence of hematite (intense Raman bands at 226, 292, 411 and 1320 cm^{-1}) and quartz (intense Raman bands at 128, 206 and 464 cm^{-1}) in the vein from the surface to 20 µm in depth. The grey color at the high ends of the spectral range in the false color image (C) is due to the presence of a high fluorescence background. Note the variation in the fluorescence background and the intensity of the 1320 cm^{-1} hematite band at various depth within the thin section seen in the stacked plot.

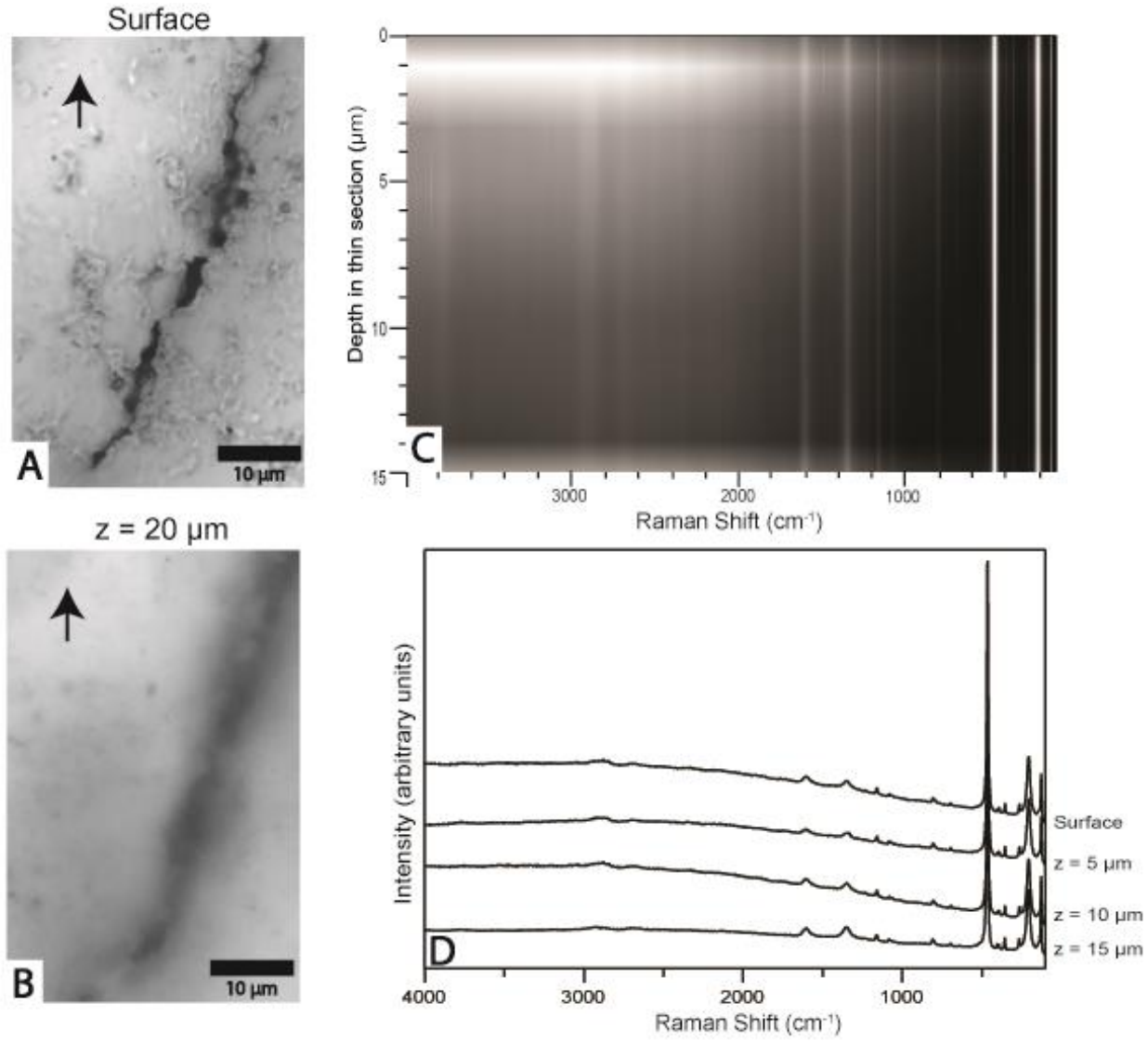

Figure 15. Confocal Raman depth profiles from the microquartz matrix from a 30 µm thin section. The false color image (C) from the indicated by the arrows (A and B) shows the presence of quartz (Raman bands at 126, 206 and 464 cm^{-1}) and disordered carbonaceous material (the D band at ~1350 cm^{-1} and the G band at ~1600 cm^{-1}) in the matrix from the surface to 18 µm in depth. The stack plot shows representative spectra from the profile every 5 µm from the surface (D). The grey color at the high ends of the spectral range in the false color images (C) is due to the presence of a high fluorescence background also seen in the stacked plot (D). Similar to the point spectra shown in Figure 12, some of the high background is due to fluorescence from the epoxy mounting media.

depths within a sample and software can be used to combine the 2-D images into composite 3-D images (Bernard et al., 2008; Marshall and Olcott Marshall, 2013; Nasdala et al., 2012; Nasdala et al., 2004). Several data analytical methods can be used to create images from hyperspectral datasets. One of the most common methods is to plot the intensity at a specific Raman shift representative of the location of a Raman band of interest against the *x*,*y* locations from which the spectra were collected (Bernard et al., 2008; Marshall and Olcott Marshall, 2013; McCreery, 2005; Nasdala et al., 2012; Nasdala et al., 2004). Other univariate methods such as sum filtering, calculating band intensity ratios, calculating the intensity sum over single or multiple Raman shift ranges where Raman bands occur, and several multivariate curve-fitting methods including direct classical least squares (DCLS), hierarchical cluster analysis (HCA) and principle components analysis (PCA) have also been applied to Raman hyperspectral images of geological samples (Bernard et al., 2008; Carter et al., 2010; Edwards and Vandenabeele, 2012; Kotková et al., 2011; Kremer et al., 2012a; Kremer et al., 2012b; Nasdala et al., 2012; Nasdala et al., 2004; O'Brien and Ziemann, 2008)

Raman imaging has been previously applied to the Apex chert and both 2-D images and 3-D images have been used to interpret a carbonaceous composition for the microstructures (Schopf, 2003; Schopf and Kudryavtsev, 2005; Schopf and Kudryavtsev, 2012; Schopf and Kudryavtsev, 2014). Hyperspectral datasets were acquired on microstructures identified from the 300 µm thin sections of the new samples in order to determine the 3-D distribution of the hematite, quartz and matrix-hosted carbonaceous material identified with point Raman spectroscopy and confocal depth profiling. The StreamLine^{TM} function used to collect the spectra is restricted to a range of ~1330 cm^{-1} and the analyst can choose the beginning and ending points or a central point over which the spectra are collected. Due to this limitation,

spectra were originally acquired between 360-1660 cm^{-1} because diagnostic Raman bands for quartz, hematite, and carbonaceous materials are all present within this region (Marshall and Olcott Marshall, 2013). In order to collect such large numbers of spectra quickly, the StreamLine^{TM} function is also restricted to a single spectral collection over short a spectral acquisition time, of typically 0.1 second, compared to point Raman spectral acquisition which can utilize multiple spectral acquisitions over longer times allowing for the optimization of signal-to noise ratios. These limitations typically result in a decreased signal-to-noise ratio compared to point Raman spectra and, therefore, lower spectral quality or resolution.

Attempts were made to acquire hyperspectral data from 22 different microstructures in the new Apex chert samples, but many of the data sets were negatively affected by autofluorescence that overwhelmed the Raman signal. Raman images were produced using two methods, plotting the intensity at specific Raman shift values and using a curve-fitting technique based on multivariate direct least classical squares regression (DCLS). The maps were made from the raw spectral data, no pre-processing was performed prior to mapping in order to directly compare the results with previous studies (Schopf, 2003; Schopf and Kudryavtsev, 2005; Schopf and Kudryavtsev, 2012; Schopf and Kudryavtsev, 2014).

Examples of representative images at depths of 0.2, 2, and 3 µm made from the intensity at the points 1320 cm^{-1} (hematite), 1350, 1600 cm^{-1} (carbonaceous material) and 465 cm^{-1} (quartz) from one microstructure in a sample from the original microfossil locality are shown in Figure 16. The intensity maps at 465cm^{-1} show that the matrix surrounding the microstructure is composed of quartz. The 465 cm^{-1} map at 0.2 µm (Figure 4.16 A) also shows isolated patches or crystals of quartz surrounded by the material that comprises the microstructures.

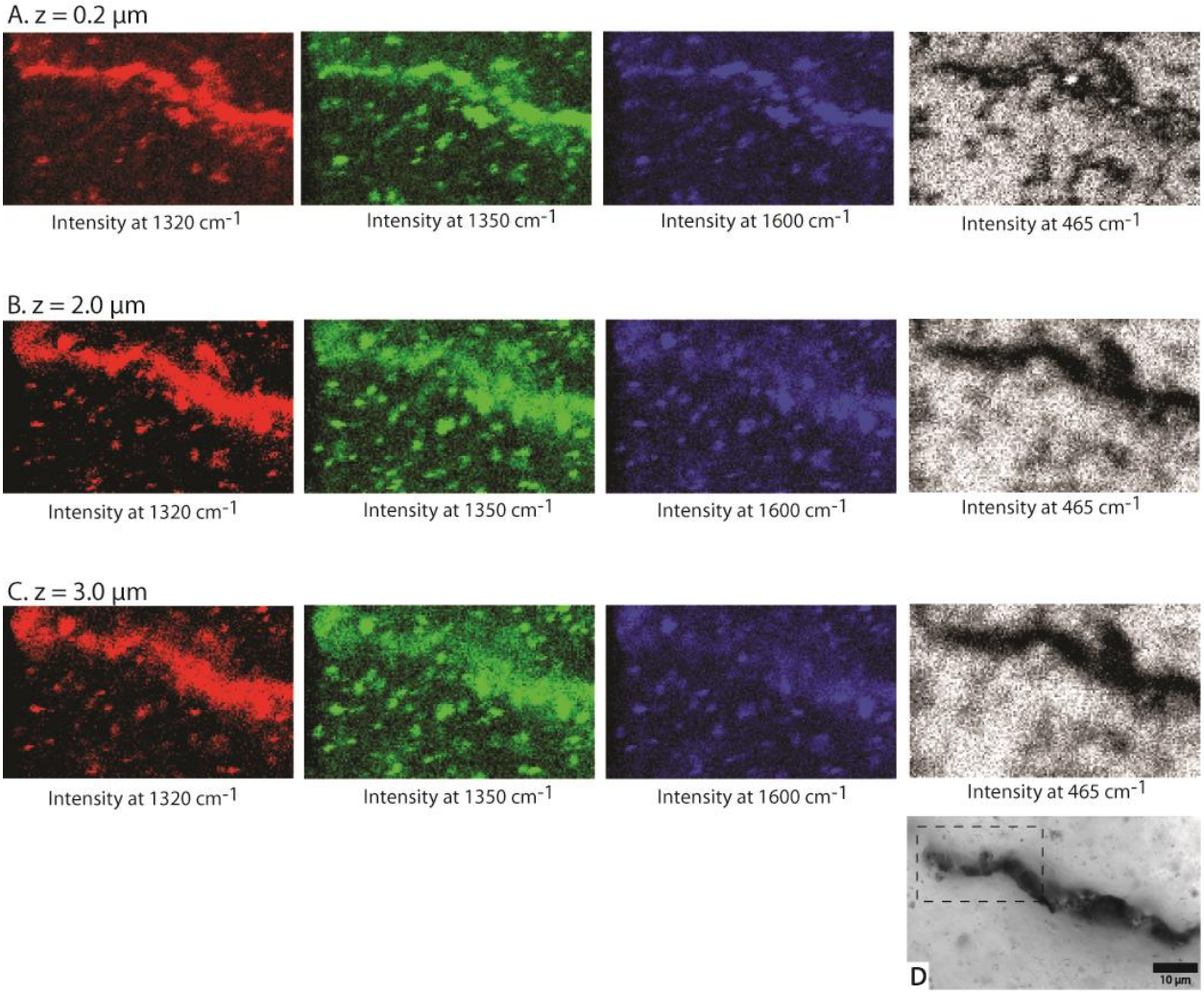

Figure 16. Representative images of the intensity at 1320 (hematite)1350, 1600 (disordered carbonaceous material) and 465 cm^{-1} (quartz) at 0.2, 2 and 3 µm depth created from a hyperspectral dataset of a microstructure identified in a 300 µm Apex chert thin section. The maps were acquired over the region shown in D from a dataset with a laser spot size (pixel size) of 0.5 µm in the *x,y* direction that consisted of 13,024 individual spectra collected every 0.2 µm from the surface to 4 µm depth in the thin section.

Close to the surface, all three maps (1320, 1350, and 1600 cm^{-1}) appear to recreate the morphology of the microstructure to some degree, but the map at 1320 cm^{-1} displays a sharper image while the maps at 1350 cm^{-1} and 1600 cm^{-1} have lower visual resolution and higher background color (Figure 16 A). Deeper within the thin section, the maps at 1320 cm^{-1} continue to recreate the morphology of the microstructure as opposed to the maps at 1350 and 1600 cm^{-1}

where the images display a high background color in which the outline of the microstructure is all but lost. Simple visual appraisal of the images support the interpretation that the microstructure is composed of hematite, but if only the images at 0.2 µm depth were considered, it could be more difficult to distinguish hematite from carbonaceous material.

The range over which the map spectra were collected included the location of a diagnostic band of hematite at 411 cm^{-1}. To further test the idea that the microstructure is composed of hematite, images of the intensity at 411 cm^{-1} were constructed and examples are shown in Figure 17. The 411 cm^{-1} images also reflect the morphology of the microstructure in a similar manner to the maps made at 1320 cm^{-1} consistent with the identification of hematite.

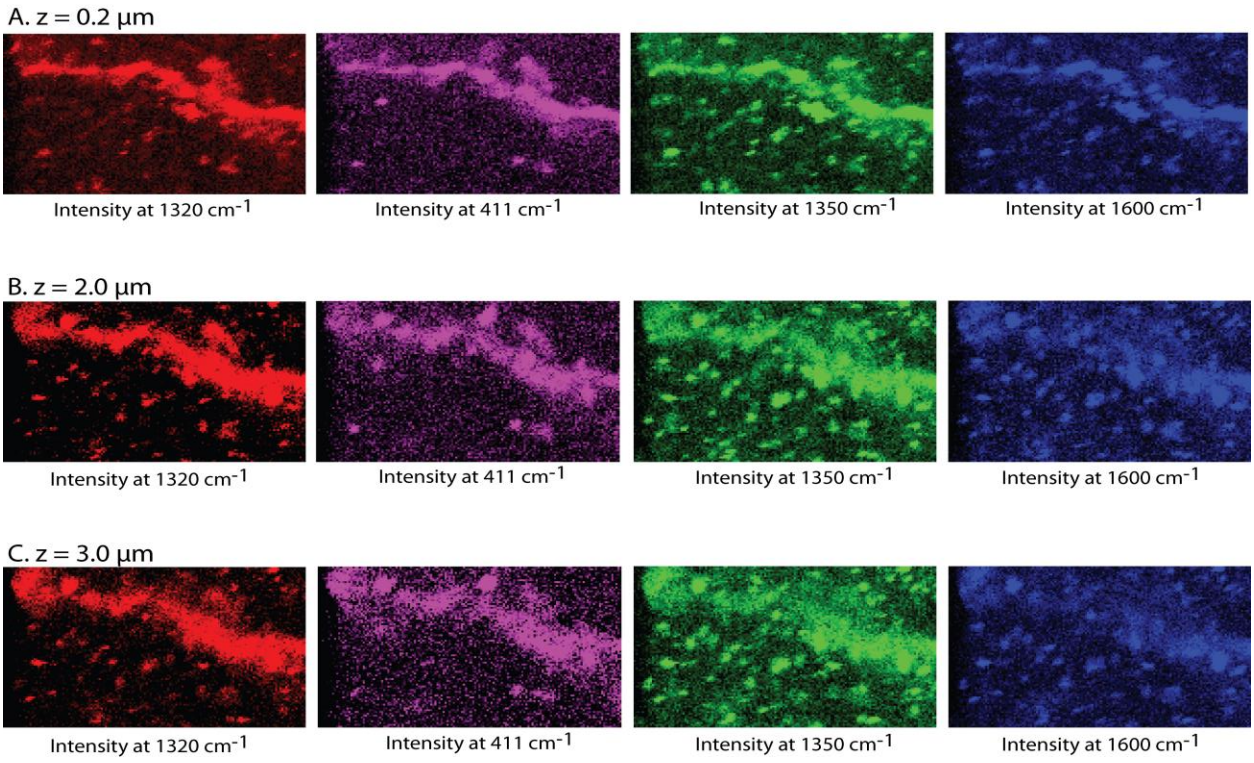

Figure 17. Representative images of the intensity at 411, 1320 (hematite) 1350, and 1600 cm^{-1} (disordered carbonaceous material) at 0.2, 2 and 3 µm depth created from the same hyperspectral dataset in Figure 16.

Multivariate curve-fitting techniques calculate the statistical likelihood that the presence, shape, and location of the Raman bands in a reference spectrum or series of reference spectra fit the sample spectra in the dataset. The DCLS algorithm is based on a linear combination of the reference spectra and calculates the contribution of each reference spectra to the sample spectra using a least squares polynomial typically resulting in a value from 0-1 that represents the contribution, or the goodness of fit, of each reference spectra to every spectra in a mapping dataset (Bernard et al., 2008; Salzer and Siesler, 2009a). The DCLS technique is commonly used on point Raman spectra and hyperspectral datasets in the pharmaceutical industry and in biomedical fields to determine the spatial distribution and concentration of materials (Bonifacio et al., 2010; Ong et al., 2012; Salzer and Siesler, 2009b; Sasic et al., 2004; Tang et al., 2013; Vajna et al., 2012; Vajna et al., 2011).

Representative reference spectra for hematite, quartz, and carbon acquired from the new samples were used to produce component images of the microstructures (Figure 18). The quartz component images show that the matrix is composed dominantly of quartz (Figure 18). The hematite component images clearly recreate the morphology of the microstructure and comparison with the quartz component images shows isolated regions of quartz within the hematite (Figure 18). The carbon component images do not recreate the morphology of the microstructure, instead they show clusters of carbonaceous material within the quartz matrix that occur outside the microstructure consistent with the results obtained from Raman point spectroscopy and confocal depth profiling (Figure 12 and 15).

These maps are based on comparison of a single reference spectra for each component, quartz, hematite, and disordered carbonaceous material, to the multitude of spectra comprising the hyperspectral dataset, therefore it is important to discuss polarization issues due to the

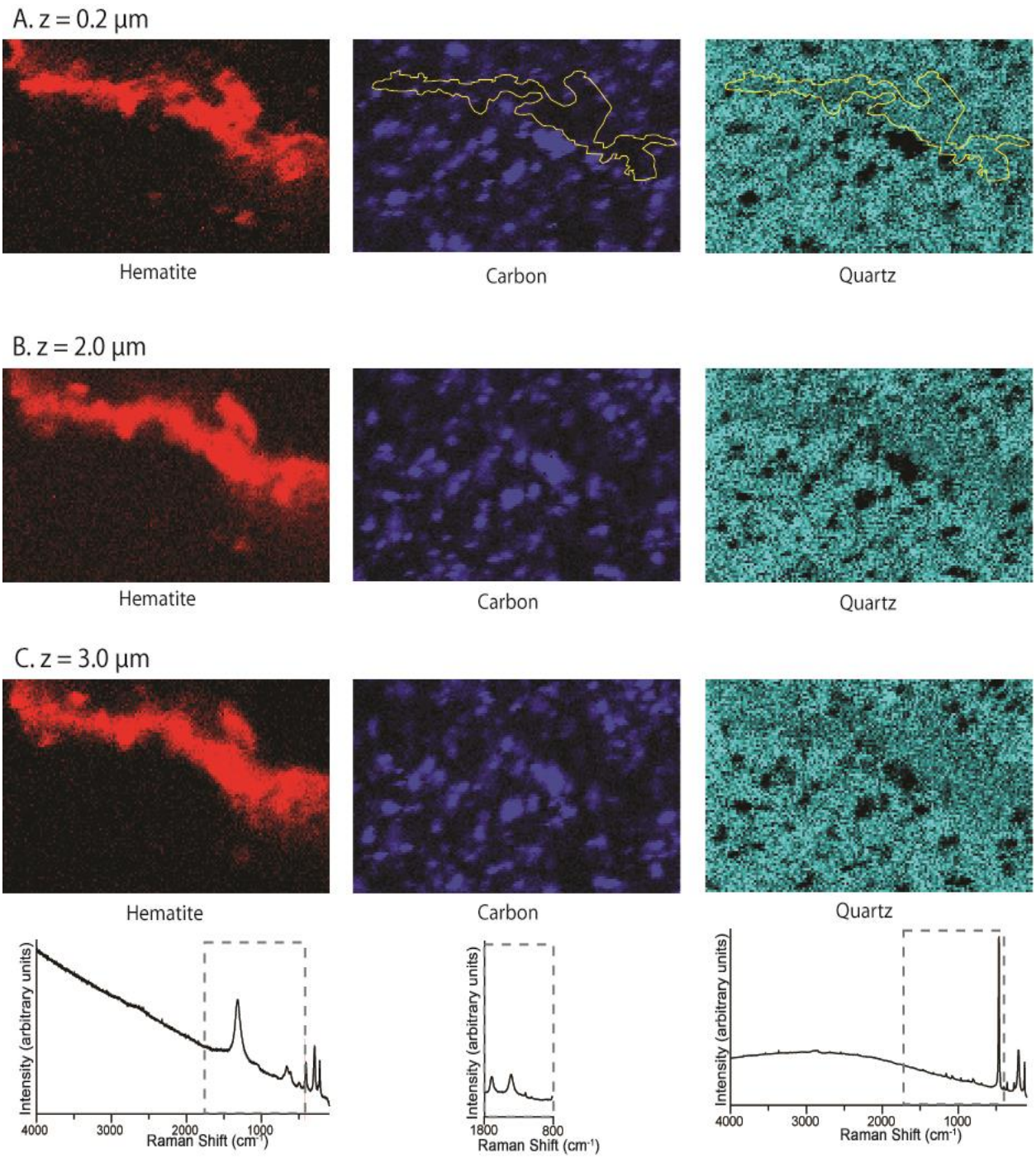

Figure 18. DCLS (direct classical least squares) component maps at 0.2, 2, and 3 µm in depth created from the hyperspectral dataset in Figures 4.16 and 4.17. The reference spectra are show below the images and the dashed boxes show the portion of the spectra used by the computer algorithm to create the images. The carbon reference spectra were acquired over the carbon first order region (800-1800 cm^{-1}) to avoid obscuring the carbon image by the presence of the matrix quartz bands that occur between 400-800 cm^{-1}. The position of the microstructure that is clearly shown in the hematite images is outlined on the carbon and quartz images at 0.2 µm depth

anisotropic nature of these materials which could affect the resulting Raman images. The presence, shape, and intensity of the bands seen in Raman spectra of anisotropic materials can be affected by the orientation of the crystals in a sample and the polarization of the incident radiation (Turrell, 1972). Research has shown that the Raman spectra obtained from highly ordered sp^2 carbonaceous materials including hexagonal graphite, highly oriented pyrolitic graphite (HOPG) and carbonaceous material present in high-grade metamorphic terrains are affected by the orientation of the crystallographic axes relative to the incident laser (Compagnini et al., 1997; Katagiri et al., 1988; Marshall and Olcott Marshall, 2013; Wang et al., 1989). Therefore, anisotropic effects could manifest themselves in Raman hyperspectral images of well-ordered carbonaceous materials which could influence any interpretations regarding the structural order of the material (Marshall and Olcott Marshall, 2013). Conversely, the effect of crystal orientation on the position, shape, and intensity of the bands in Raman spectra of more disordered sp^2 carbonaceous materials has been shown to be negligible (Aoya et al., 2010; Jehlicka and Bény, 1992; Marshall et al., 2012a; Marshall et al., 2012b; Marshall and Olcott Marshall, 2013; Wopenka and Pasteris, 1993). The presence and intensity of the Raman bands in hematite are also affected by the degree of crystalline order and by polarization effects due to anisotropy (Beattie and Gilson, 1970; Chamritski and Burns, 2005). Polarization effects on the Raman spectra of hematite and disordered carbonaceous materials bear mentioning because they do affect the presence of certain Raman bands, their relative intensities, shape, and band maxima locations which would be important to consider if interpretations were to be made regarding the structural order of these materials. In this case, the DCLS component images are presented as a complementary data analysis technique to the intensity images in order to better identify and

delineate the presence and distribution of the disordered carbonaceous material and hematite in hyperspectral datasets.

A second example of intensity images constructed from spectra collected between 400-1800 cm^{-1} from a different microstructure identified in a another thin section from a sample collected at the original microfossil locality are shown in Figure 4.19. The map of the intensity at 1320 cm^{-1} visually recreates the image of the microstructure more clearly than the maps at 1350 and 1600 cm^{-1} in a similar manner to the maps from the microstructure in Figure 16-18 supporting the identification of hematite in the microstructures.

In order to further test this hypothesis, a hyperspectral dataset was also collected from this microstructure over the range 100-1400 cm^{-1}, which does not include the 1600 cm^{-1} band for disordered carbonaceous material, but does include several other Raman bands characteristic of hematite (226, 292, 411 and 612 cm^{-1}). Collecting spectra over the range 100-1800 cm^{-1} which includes the characteristic band at 226 cm^{-1} has been recently suggested as an effective means to identify hematite in hyperspectral datasets (Marshall and Olcott Marshall, 2013). Representative maps of the intensity at 1320, 226, 292, 411 and 612 cm^{-1} at 0.2, 0.4 and 1.0 μm are also shown in Figure 4.19. The intensity images made from the locations of the hematite Raman bands all recreate the morphology of the microstructure, but the resolution of the images vary. As previously mentioned, this could be due to variations in hematite crystal sizes or anisotropy effects. Component images constructed from both datasets show that the matrix is composed dominantly of quartz, the microstructure is composed of hematite and carbonaceous material is present in clusters within the matrix outside the microstructure (Figure 20). Due to the limited range of the carbon component maps from 100-1400 cm^{-1}, the identification of carbonaceous material would be based solely on the presence and shape of the D band.

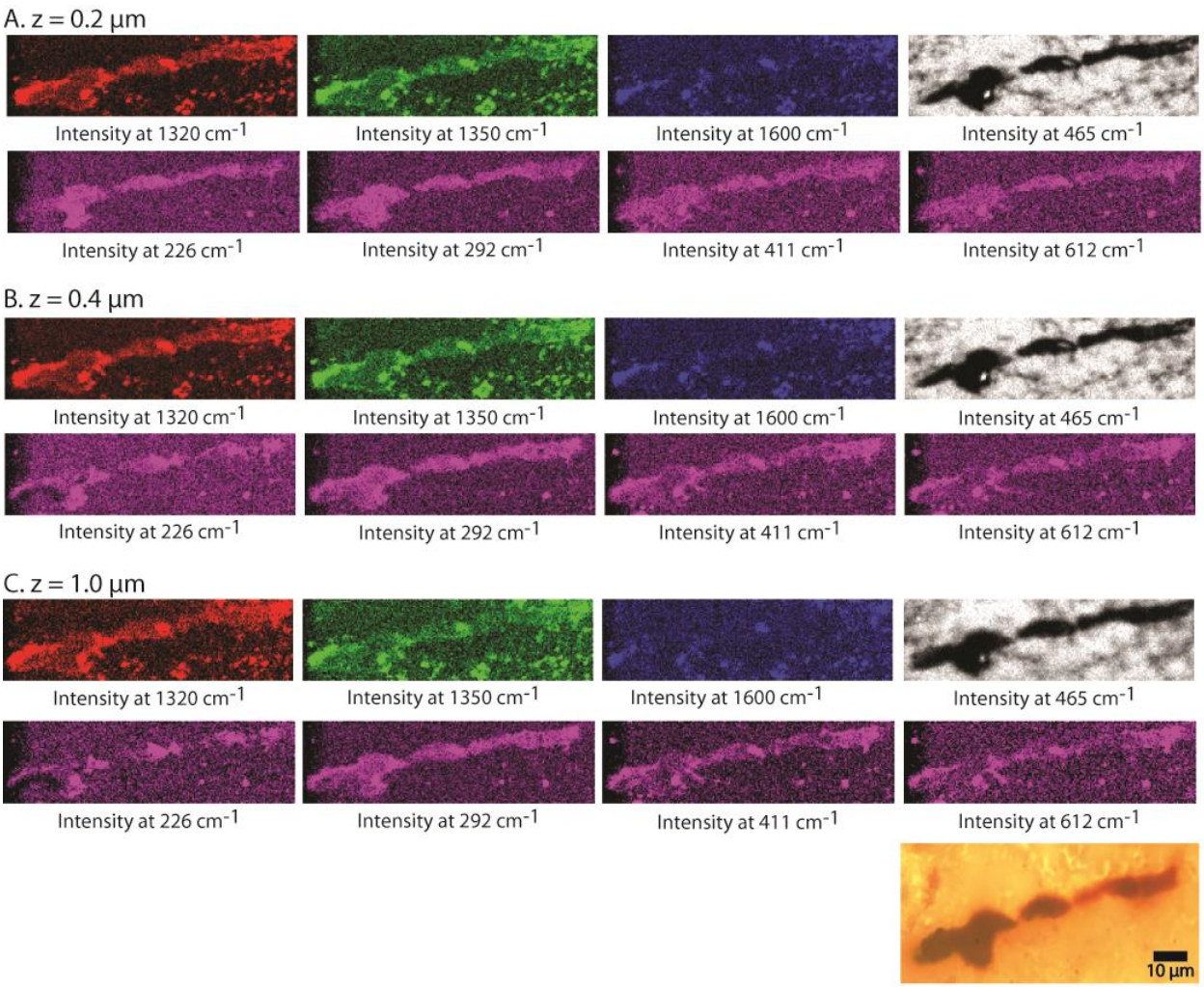

Figure 19. Representative images of the intensity of characteristic Raman bands for quartz, hematite and disordered carbonaceous material at 0.2, 0.4 and 1 µm depth from two hyperspectral datasets collected over the same microstructure. The intensity images at 1320 (hematite), 1350 and1600 (disordered carbonaceous material), and 465 cm^{-1} (quartz) were created from a dataset acquired between 400-1800 cm^{-1}. The intensity images at 226, 292, 411, and 612 cm^{-1} (hematite) were created from a dataset collected over the range 100-1400 cm^{-1}. Both datasets had the same collection parameters, a laser spot size (pixel size) of 0.5 µm in the *x,y* direction that resulted in 10,780 individual spectra. The 100-400 cm^{-1} dataset was collected every 0.2 µm to a depth of 5 µm and the 400-1800 cm^{-1} was collected every 0.2 µm to a depth of 2.2 µm.

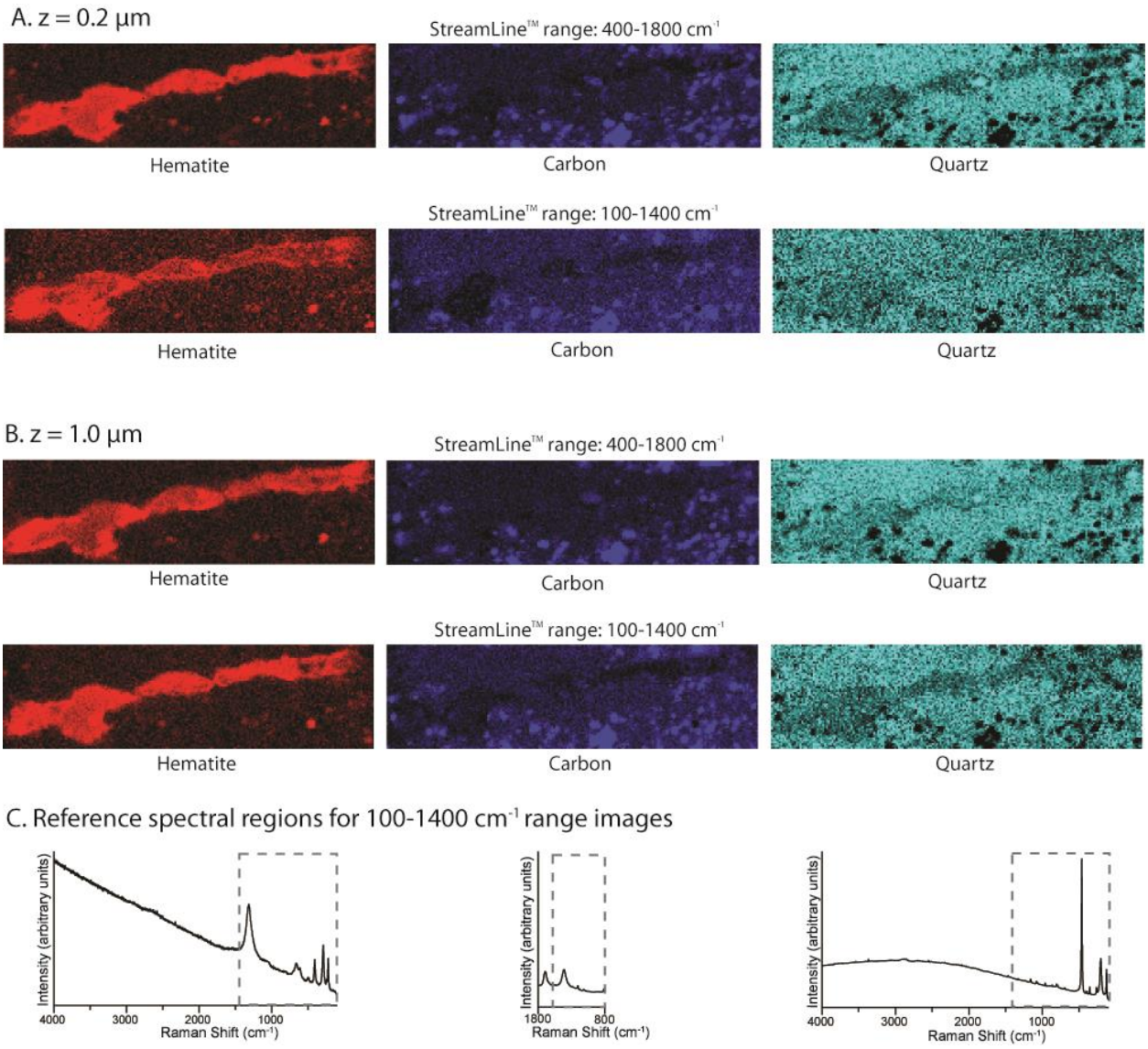

Figure 20. Representative DCLS component maps at 0.2 and 1 µm (A and B) created from the two hyperspectral datasets acquired from the microstructure shown in Figure 4.19. The same reference spectral regions seen in Figure 4.18 were used to create the images from the 400-1800 cm^{-1} dataset. The reference spectral regions used to create the images from the 100-1400 cm^{-1} dataset are shown below the maps (C). Note the correspondence between the images representing the distribution of the carbon constructed from the two datasets.

It is interesting to note that even with this limitation, the images show an almost identical distribution of carbonaceous material in the matrix and not the microstructure as seen in the images created from the 400-1800 cm^{-1} dataset.

Point Raman spectroscopy, confocal depth profiling, and Raman mapping and imaging all verified the identification of hematite as the opaque phase. This finding differs markedly from previous work that identified carbonaceous material in the microstructures using point Raman spectroscopy and Raman imaging (Brasier et al., 2002; Brasier et al., 2005; Schopf and Kudryavtsev, 2005; Schopf and Kudryavtsev, 2012; Schopf and Kudryavtsev, 2014; Schopf et al., 2002). The original samples from the Apex chert were not examined in this study, so it is possible that carbonaceous microfossils may be present in those samples. However, due to the morphological similarity and comparable petrographic distribution of the hematite microstructures in the new samples to the originally described material, and that the samples were collected with assistance from geologists with expert knowledge of the locality, it seems likely that the structures studied in the new samples are homologous to the originally described microstructures. The identification of hematite in the microstructures instead of disordered carbonaceous material could be explained in several ways. The microstructures are typically cited as reddish-brown in color which has been suggested to indicate that they are composed of moderately thermally-mature carbonaceous material (Brasier et al., 2005; Schopf et al., 2002). This is inconsistent with the previously published Raman spectra of the carbonaceous material (Brasier et al., 2005; Schopf et al., 2002) which instead show line-shapes indicative of highly-thermally mature carbonaceous material which should appear black in color (Pasteris and Wopenka, 1991). Although reddish-brown is the most commonly used description of the microstructure color in transmitted light, a range of microstructure colors from yellow, to reddish-brown, to grey and black have been described (Brasier et al., 2005). Hematite can range in color from purpleish to yellow, orange, red, grey, or black depending on particle size and shape (Hund, 1981; Torrent and Barrón, 2003; Torrent and Schwertmann, 1987). The Apex chert

samples studied have several generations of veins that contain hematite identified by Raman spectroscopy that range in color from various shades of orange to red and grey or black consistent with the colors reported for the microstructures.

Standard Point-Raman spectroscopy is a surface technique and for siliceous samples under the instrumental conditions used in this and previous studies (Brasier et al., 2002; Brasier et al., 2005; Schopf et al., 2002) a 514.5 nm laser typically penetrates less than 1 μm in depth (Yan, 2004). The 300 μm thin sections are for the most part optically transparent, but along with obscuring some of the fine-scale textural details the thickness of the sections can make it difficult to determine the depth at which objects occur. Features that appear to occur at or near the surface of the thin section can actually be located several to 10's of μm below the surface. Previously published point Raman spectra showing carbonaceous material (Brasier et al., 2002) have a similar line shape to the Raman spectra acquired from the matrix phase in the new samples, the slight difference seen in the relative intensities of the D and G bands is caused by baseline correction applied to the published spectra (Brasier et al., 2002; Marshall et al., 2010; Marshall et al., 2011). Due to the difficulty in determining the depth at which features occur and the similarity of the published spectra of the carbonaceous material to the spectra from the microquartz matrix in the new samples, it is possible that the previously published point spectra are representative of the matrix and not the microstructures (Marshall et al., 2011).

Confocal Raman hyperspectral imaging is a very useful method to address the depth of laser penetration issue encountered using standard point Raman spectroscopy, but this technique can also be subject to data interpretation issues. The 1320 cm^{-1} hematite band and the 1350 cm^{-1} carbonaceous material D band occur in close proximity to each other in the carbon first order region (Figure 21).

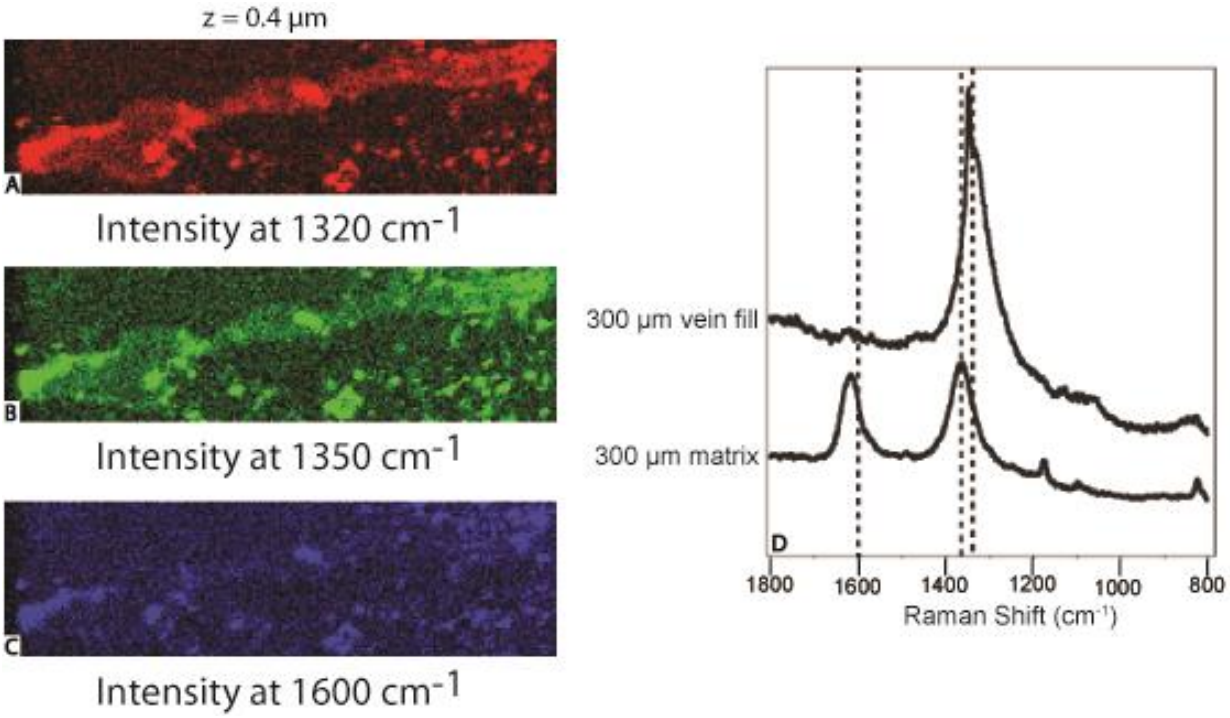

Figure 4.21. Intensity images at 1320 (hematite), 1350, and 1600 cm^{-1} (disordered carbonaceous material) at 0.2 µm depth from the microstructure shown in Figures 4.19 and 4.20 (A-C). Note that the 1320 cm^{-1} image best recreates the shape of the microstructure, but the 1350 cm^{-1} image recreates the structure more clearly than the 1600 cm^{-1} image. A stacked plot of representative point Raman spectra of hematite from a vein and carbonaceous material from the matrix in the carbon first order region (800-1800 cm^{-1}) acquired from a 300 µm thin section (D) shown to illustrate the proximity of the hematite 1320 cm^{-1} band with the disordered carbonaceous material D band at 1350 cm^{-1}.

The intensity images created from the datasets represent the relative intensity value at a specific point, not the presence or absence of a particular Raman band. It is apparent that in a sample containing hematite, maps of the D band intensity at 1350 cm^{-1} would be influenced by the presence of the hematite band at 1320 cm^{-1} and would create an image (Marshall et al., 2011; Marshall and Olcott Marshall, 2013). This phenomenon is demonstrated in the intensity images made at 0.2 µm depth from the microstructure shown in Figures 19 and 20 in which the images at 1320 cm^{-1} best recreate the morphology of the microstructure, but the intensity maps at 1350 cm^{-1} recreate the morphology of the microstructure better than the image at 1600 cm^{-1} (Figure

21). This phenomenon can also be observed in images of the microstructure shown in Figures 16-17.

A portion of the work shown in this chapter was published in 2011, and at that time the explanation for the discrepancy between the previously published 3-D Raman images said to show carbonaceous material with the current results that identify hematite in the microstructures was due to confusion of the 1320 cm^{-1} hematite band with the 1350 cm^{-1} D band (Marshall et al., 2011). The method used to produce Raman 2-D and 3-D images of previously published microfossils involved imaging the most intense band found in the many spectra comprising a mapping dataset (Schopf and Kudryavtsev, 2005). The published 3-D image of an Apex chert microstructure was constructed from the most intense band found in the mapping data collected over the carbon first order region (Schopf and Kudryavtsev, 2005; Schopf and Kudryavtsev, 2009; Schopf et al., 2007). The 1320 cm^{-1} band in the hematite spectra obtained from the new Apex chert samples can vary in intensity from relatively low to the most intense band in the Raman spectrum (Figures 4.10, 4.11, 4.13, 4.14), a phenomenon also noted by Kremer et al. (2012b) in their study of a Late Cretaceous dinosaur bone. Additionally, the use of green lasers (514.5 or 532 nm) can result in enhancement of the 1320 cm^{-1} hematite vibrational mode (Marshall and Olcott Marshall, 2013). Data acquisition over only the first order carbon region as performed in the previous studies would preclude the identification of hematite by the presence of the diagnostic bands in the mineral fingerprint region (100-800 cm^{-1}). Representative Raman spectra from the maps were not presented that would allow for the identification of a single band at 1320 cm^{-1} indicative of hematite or the D and G bands characteristic of disordered carbonaceous material. Due to these factors, it was suggested that the 1320 cm^{-1} hematite band may have been misidentified as the D band and that images actually showed the presence of

hematite instead of disordered carbonaceous material (Marshall and Olcott Marshall, 2013). Confusion of the hematite 1320 cm^{-1} band with the D band is not a trivial issue in geological samples that contain both materials and several examples of this error have been documented (Marshall and Marshall, 2011).

The original study presented 2-D Raman images of portions of Apex chert microstructures said to be created from the G band intensity (Schopf et al., 2002). A more recent study stated that the original 3-D image was created from the G band and presented two new confocal laser scanning microscopy images (CLSM) to interpret that the microstructures are indeed carbonaceous in composition (Schopf and Kudryavtsev, 2012). Raman spectra of disordered carbonaceous material will always contain a G band, therefore images created from the intensity at the G band location (~1600 cm^{-1}) should be indicative of the presence of carbonaceous material (Marshall and Marshall, 2011). But, intensity maps can be significantly affected by the presence of a high autofluorescence background in the Raman spectra which can be a "serious nuisance that limits the capabilities of Raman chemical imaging" (Sasic and Ozaki, 2010). Representative spectra from various regions in the mapping dataset at 0.2 μm from the microstructure in Figures 16-18 illustrate how a high autofluorescence background could create a false-positive identification of carbonaceous material in hyperspectral images (Figure 22). Although the spectra have lower signal to noise ratios than the point Raman spectra due to the short StreamLine™ acquisition parameters, the spectra have an acceptable resolution to identify quartz based on the presence of the 464 band, hematite based on the presence of the 1320 cm^{-1} band and in several spectra the 411 cm^{-1} band, and carbonaceous material based on the presence

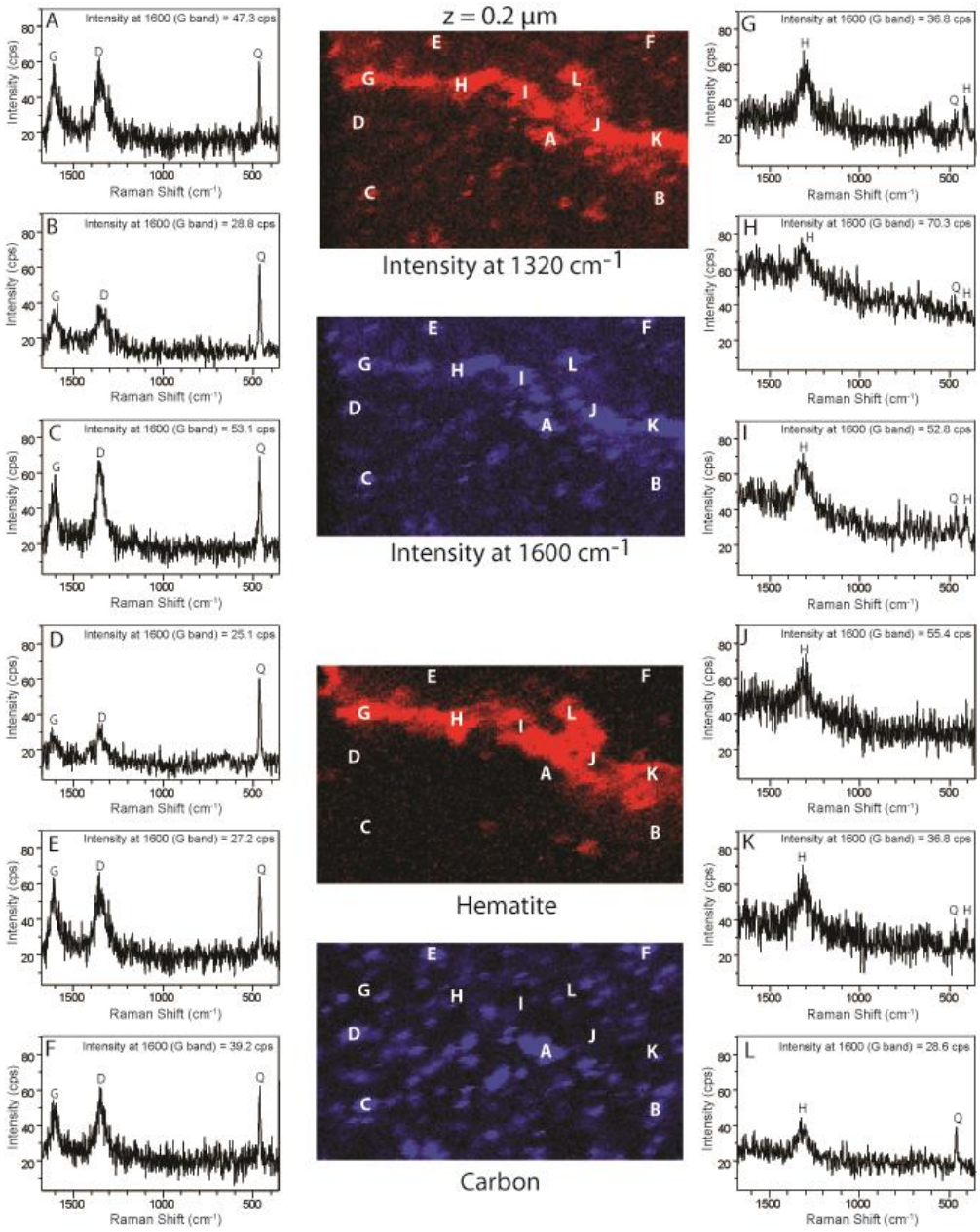

Figure 22. DCLS component images at 0.2 µm from the first microstructure from Figures 4.16-18. And representative Raman spectra from the mapping dataset. The white letters (A-L) on the images indicate the locations of the individual spectra. Hematite bands are denoted by H, quartz bands are denoted by Q and the disordered carbonaceous material bands are denoted by D and G. The representative spectra from the matrix (A-F) in regions where the carbon component map predicts the occurrence of disordered carbonaceous material show the presence of quartz (464 cm^{-1}) and disordered carbonaceous material (D band at ~1350 cm^{-1} and G band at ~1600 cm^{-1}). The representative spectra from within the microstructure (G-L) can be used to identify hematite based on the presence of the 1320 cm^{-1} band and in some cases, the presence of the 411 cm^{-1} band although the 411 cm^{-1} band can be more difficult to distinguish from the noise in the spectra. Note the high intensity values at 1600 cm^{-1} seen and labeled in the hematite spectra (A-F) which are due to the high fluorescence background. The range and average intensity value of 46.8 cps and range 28.6-70.3 cps are higher than the G band average of 34.7 cps and range of 25.1-47.3 cps seen in the disordered carbonaceous material spectra from the matrix which show a significantly lower, if not flat baseline (G-L).

of the D and G bands (Figures 4.22). The spectra showing hematite in the microstructures have significantly higher background fluorescence seen by the presence of a sloping baseline compared to the disordered carbonaceous material spectra. The average value and range of intensity values at 1600 cm^{-1} in the representative hematite spectra is higher (average = 46.8 cps; range 28.6-70.3 cps) than the actual intensity values at 1600 cm^{-1} for the G band in the representative disordered carbonaceous materials spectra (average = 34.7 cps; range 25.1-47.3 cps) (Figure 22). The high background due to the nearly ubiquitious autoflourescence seen in the hematite in the Apex chert can produce an intensity image at the location of the G band at 1600 cm^{-1} that can somewhat recreate the shape of the microstructure, even if it is not composed of disordered carbonaceous material (Figure 4.22). This phenomenon was encountered during construction of intensity images from hyperspectral datasets which resulted in images at 1320, 1350, and 1600 cm^{-1} that all equally recreated the morphology of a microstructure making it impossible to distinguish between hematite and disordered carbonaceous material from the intensity images alone (Figure 23). Comparison with DCLS component images produced from the reference spectra and interrogation of individual spectra collected during mapping became necessary to determine the actual distribution of hematite within the microstructures and carbonaceous material in the matrix (Figure 23).

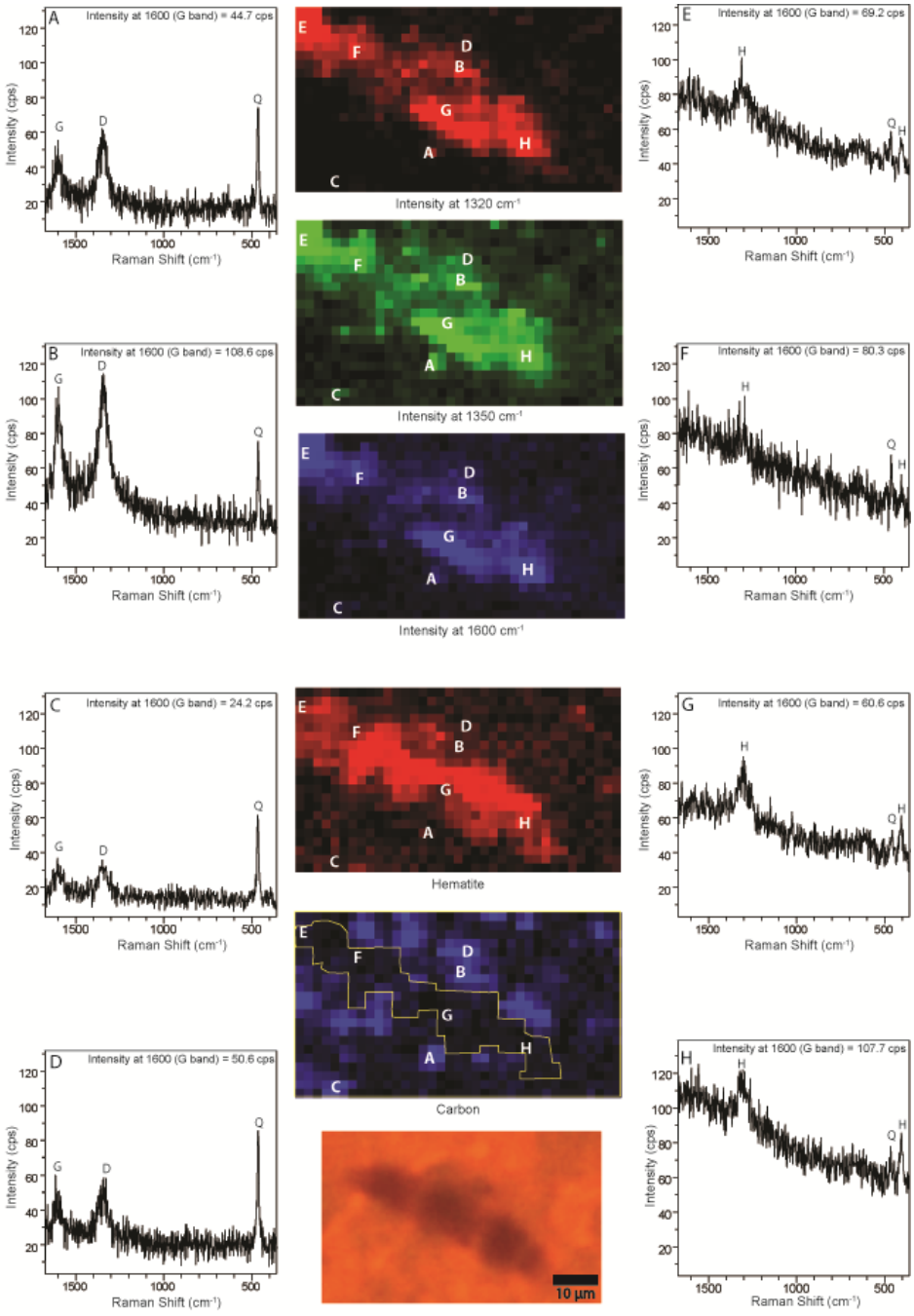

Figure 23. Intensity at a point images representing hematite and carbon and DCLS component images at 0.2 µm from a third segmented appearing microvein. And representative Raman spectra from the mapping dataset. The white letters (A-H) indicate the locations of the representative spectra. Hematite, carbon and quartz bands are denoted as in Figure 22. The representative spectra from the matrix (A-D) in regions where the carbon component map predicts the occurrence of disordered carbonaceous material show the presence of quartz and disordered carbonaceous material (D and G bands). The representative spectra from within the microstructure (E-H) can be used to identify hematite. Note the high intensity values at 1600 cm^{-1} seen and labeled in the hematite spectra (E-H) caused by high fluorescence backgrounds. The average intensity value at 1600 for the hematite spectra is 79.5 cps compared to 57.0 for the carbon spectra. It is interesting to note that the matrix quartz and carbon have nearly flat baselines especially in comparison to the substantially elevated baselines in the hematite spectra.

Confocal laser scanning fluorescence microscopy (CLSM) has been proposed as a complimentary technique to Raman imaging to study microfossils and it has been used on the Apex chert microstructures to produce images used to support the identification of carbonaceous material in the structures (Schopf and Kudryavtsev, 2009). CLSM utilizes a laser source to excite fluorescence in a sample, and due to the confocal set-up of the microscope the laser can be focused into a very small diffraction limited spot which limits out of focus regions above and below the position analyzed providing a higher resolution image than conventional optical microscopy (Pawley, 2006). CLSM alone cannot definitively show that a potential microfossil is carbonaceous in composition because a variety of minerals can also fluoresce under laser excitation (Schopf and Kudryavtsev, 2009). Both 488 nm (blue-green) and 633 nm (red) wavelengths were utilized to excite the samples, but it was not stated which wavelength was used to produce the CLSM images (Schopf and Kudryavtsev, 2009, 2012). Disordered carbonaceous materials like those found in the Apex chert can undergo fluorescence under green laser excitation as seen in the curved baselines in some of the spectra presented above, but the results shown here also illustrate that the hematite in the Apex chert can be highly fluorescent, moreso than the matrix hosted carbonaceous material. Although longer wavelength laser excitation using red or near-infrared excitation typically reduces background fluorescence in Raman spectra (Ferraro et al., 2003; Smith and Dent, 2005), Raman spectroscopic studies have shown that hematite can display high background fluorescence under excitation with a near infrared wavelength laser (785 nm) (Edwards et al., 2007; Jallad and Ben-Amotz, 2001; Sendova et al., 2005; Zoppi et al., 2006). Therefore, it is possible that the recently published CLSM image of an Apex chert microstructure may reflect the presence of fluorescent hematite instead of carbonaceous material. Because CLSM simply records the presence of fluorescence, some other

means of identifying the fluorescence material is necessary. Comparing CLSM with the results from a Raman hyperspectral datasets collected over the corresponding region in a sample could be a viable technique to test for the presence of carbonaceous material in a potential microfossil. However, because Raman images can provide false-positives for carbonaceous material depending on the technique used to create the images and problems with fluorescence, the individual spectra from a Raman hyperspectral dataset should be evaluated for the presence of diagnostic Raman bands and signal-to-noise and sloping baseline issues due to autofluorescence. This is important because in some spectra from the hyperspectral datasets the fluorescence signal can nearly overwhelm the Raman signal making the bands difficult, but not impossible to identify (e.g. Figure 4.22 H and Figure 4.24 F). Representative spectra from a dataset should be presented along with Raman images to address any potential spectral misidentification issues as suggested by Marshall and Olcott Marshall (2013).

Chemical techniques aside from Raman spectroscopy have been used to interpret that the microstructures are composed of biological carbonaceous material including transmission electron microscopy (TEM), secondary ion mass spectroscopy (SIMS), and scanning transmission X-ray microscopy (STXM). (De Gregorio et al., 2009). This study compared the structure of the Apex chert carbonaceous material to presumed biogenic carbonaceous material from the Gunflint chert , but the analyses were performed on isolated, microtomed pieces of chert, therefore the results cannot be applied to a particular microstructure in a thin section (De Gregorio et al., 2009).

Although a carbonaceous composition is often cited as a critical evidence for establishing biogenicity, microfossils can be permineralized by iron oxides (Boyd and Scott, 2001; Glasauer et al., 2013; Krepski et al., 2013; Parenteau and Cady, 2010), and it could be argued that the

identification of hematite does not necessarily preclude a biological origin. Veins or vein fill textures meet many of the morphological characteristics proposed for true microfossils: a cylindrical or ellipsoid shape, a limited range of diameters, a consistent diameter along the length of the structure and a degree of sinuosity to the microstructure (Bons, 2001; Nicholson, 1991; Nicholson and Ejiofor, 1987; Schopf et al., 2010). A hollow interior has been documented in iron permineralized filamentous microfossils and cited as an important biological characteristic (Boyd and Scott, 2001; Hinman and Walter, 2005; Nicholson and Ejiofor, 1987; Parenteau and Cady, 2010; Schopf and Kudryavtsev, 2009). The Apex chert microstructures have been described as being hollow in the center, but the results shown in this study and previously published Raman images and petrographic observations suggest that the microstructures are composed of solid material that contains isolated zones of quartz (Brasier et al., 2002; Brasier et al., 2005; Marshall et al., 2011; Schopf and Kudryavtsev, 2005; Schopf and Kudryavtsev, 2009; Schopf et al., 2007). This morphology is more consistent with mineral veins than iron permineralized microfossils (Bons, 2000; Marshall et al., 2011; Nicholson, 1991). Combined with the petrographic observations from the new samples showing that microstructures seen in 300 µm thin sections are associated with veins that can be observed in serial 30 µm thin sections, that the 30 µm thin sections contain septated-appearing microveins, and that the carbonaceous material in the Apex chert is associated with the matrix and not the veins it seems possible that microstructures described from the original samples are abiotic hematite pseudofossils associated with secondary mineralization and vein formation instead of microbial fossils.

CONCLUSIONS

The identification of the Apex chert microstructures as hematite and quartz filled fractures illustrates some of the complexities and issues encountered when searching for evidence of ancient life. Observation that a particular microstructure has a biological morphology can be subjective, which could be the reason why other researchers studying the Apex chert have not reported microfossils comparable to the published microfossils in their samples (Pinti et al., 2009; Sforna et al., 2014) or in the original samples now located at the Geological Survey of Western Australia (Dalton, 2002). Raman spectroscopy can be a powerful technique to identify materials in geological samples, but the limitations of this method and causes for potential data misinterpretations must be addressed especially when interpreting images constructed from hyperspectral datasets. This study illustrates the power of using more than one data collection range during hyperspectral mapping and multiple data analysis techniques for constructing and comparing images created from the datasets. The combination of two data collection ranges and two different data analysis techniques allowed for a more thorough interpretation of the data, a common method in other disciplines but one that is seldom used in the geological literature. An exhaustive literature search resulted in one geological study that included more than one hyperspectral data acquisition technique, but this study compared static mapping which involves the acquisition of one spectra for each pixel after which the laser aperture is closed and the stage moves the sample to the next location, to the newer technique of static mapping utilized by the StreamScan^{TM} function, where the laser illuminates a line that is continuously rastered across the surface allowing the detector to collect and average several spectra for each individual pixel (Bernard et al., 2008). The work presented in this chapter also illustrates the importance of interrogating the multitude of spectra that comprise hyperspectral

datasets and presenting representative spectra from the dataset along with Raman images in order to address variations in data quality and potential spectral misinterpretation issues as suggested by Marshall and Olcott Marshall (2013).

References

Aoya, M., Kouketsu, Y., Endo, S., Shimizu, H., Mizukami, T., Nakamura, D., Wallis, S., 2010. Extending the applicability of the Raman carbonaceous-material geothermometer using data from contact metamorphic rocks. Journal of Metamorphic Geology 28, 895-914.

Beattie, I.R., Gilson, T.R., 1970. The single-crystal Raman spectra of nearly opaque materials. Iron(III) oxide and chromium(III) oxide. Journal of the Chemical Society A: Inorganic, Physical, Theoretical, 980-986.

Becker, S., Hilgers, C., Kukla, P.A., Urai, J.L., 2011. Crack-seal microstructure evolution in bi-mineralic quartz-chlorite veins in shales and siltstones from the RWTH-1 well, Aachen, Germany. Journal of Structural Geology 33, 676-689.

Bernard, S., Beyssac, O., Benzerara, K., 2008. Raman Mapping Using Advanced Line-Scanning Systems: Geological Applications. Applied Spectroscopy 62, 1180-1188.

Bonifacio, A., Beleites, C., Vittur, F., Marsich, E., Semeraro, S., Paoletti, S., Sergo, V., 2010. Chemical imaging of articular cartilage sections with Raman mapping, employing uni- and multi-variate methods for data analysis. Analyst 135, 3193-3204.

Bons, P.D., 2000. The Formation of veins and their microstructures In: Stress, Structure and strain: a volume in honour of Win D. Means, in: Jessell, M., Urai, J.L. (Eds.), Journal of the Virtual Explorer. Electronic Edition, p. 47.

Bons, P.D., 2001. Development of crystal morphology during unitaxial growth in a progressively widening vein: I. The numerical model. Journal of Structural Geology 23, 865-872.

Bons, P.D., Elburg, M.A., Gomez-Rivas, E., 2012. A review of the formation of tectonic veins and their microstructures. Journal of Structural Geology 43, 33-62.

Boyd, T., Scott, S., 2001. Microbial and hydrothermal aspects of ferric oxyhydroxides and ferrosic hydroxides: the example of Franklin Seamount, Western Woodlark Basin, Papua New Guinea. Geochemical Transactions 2, 45.

Brasier, M.D., Green, O.R., Jephcoat, A.P., Kleppe, A.K., Van Kranendonk, M.J., Lindsay, J.F., Steele, A., Grassineau, N.V., 2002. Questioning the evidence for Earth's oldest fossils. Nature [London] 416, 76-81.

Brasier, M.D., Green, O.R., Lindsay, J.F., McLoughlin, N., Steele, A., Stoakes, C., 2005. Critical testing of Earth's oldest putative fossil assemblage from the ~3.5 Ga Apex chert, Chinaman Creek, Western Australia. Precambrian Research 140, 55-102.

Brasier, M.D., Green, O.R., Lindsay, J.F., McLoughlin, N., Stoakes, C., Brasier, A.T., Wacey, D., 2011. Geology and Putative Microfossil Assemblage of the c. 3460 Ma "Apex chert", Chinaman Creek, Western Austraila-A Field and Petrographic Guide. Geological Society of Western Australia, Perth, Austraila.

Carter, E., Pasek, M., Smith, T., Kee, T., Hines, P., Edwards, H.M., 2010. Rapid Raman mapping of a fulgurite. Analytical and Bioanalytical Chemistry 397, 2647-2658.

Cervantes, P., Wiltschko, D.V., 2010. Tip to midpoint observations on syntectonic veins, Ouachita orogen, Arkansas: Trading space for time. Journal of Structural Geology 32, 1085-1100.

Chamritski, I., Burns, G., 2005. Infrared- and Raman-Active Phonons of Magnetite, Maghemite, and Hematite: A Computer Simulation and Spectroscopic Study. The Journal of Physical Chemistry B 109, 4965-4968.

Compagnini, G., Puglist, O., Foti, G., 1997. Raman spectra of virgin and damaged graphite edge planes. Carbon 35, 1793-1797.

Dalton, R., 2002. Microfossils: Squaring up over ancient life. Nature [London] 417, 782-784.
de Faria, D.L.A., Venâncio Silva, S., de Oliveira, M.T., 1997. Raman microspectroscopy of some iron oxides and oxyhydroxides. Journal of Raman Spectroscopy 28, 873-878.

De Gregorio, B.T., Sharp, T.G., Flynn, G.J., Wirick, S., Hervig, R.L., 2009. Biogenic origin for Earth's oldest putative microfossils. Geology 37, 631-634.

Dieing, T., Hollricher, O., Toporski, J., 2010. Confocal Raman Microscopy. Springer, Berlin, Germany.
Edwards, H.G., Vandenabeele, P., 2012. Analytical Archaeometry: Selected Topics. Royal Society of Chemistry Cambridge, UK.

Edwards, H.G., Wolstenholme, R., Wilkinson, D.S., Brooke, C., Pepper, M., 2007. Raman spectroscopic analysis of the enigmatic Comper pigments. Anal Bioanal Chem 387, 2255-2262.

Ferraro, J., Nakamura, K., Brown, C., 2003. Introductory Raman Spectroscopy, 2nd ed. Elsevier, San Diego, CA.

Garcia Ruiz, J.M., 2002. Morphology: An Ambiguous Indicator of Biogenicity. Astrobiology 2, 353-369.

Garcia Ruiz, J.M., Hyde, S.T., Carnerup, A.M., Christy, A.G., Van Kranendonk, M.J., Welham, N.J., 2003. Self-Assembled Silica-Carbonate Structure sand Detection of Ancient Microfossils. Science 302, 1194-1197.

Gillet, P., Le Cléac'h, A., Madon, M., 1990. High-temperature raman spectroscopy of SiO2 and GeO2 Polymorphs: Anharmonicity and thermodynamic properties at high-temperatures. Journal of Geophysical Research: Solid Earth 95, 21635-21655.

Glasauer, S., Mattes, A., Gehring, A., 2013. Constraints on the Preservation of Ferriferous Microfossils. Geomicrobiology Journal 30, 479-489.

Hilgers, C., Urai, J.L., 2002. Microstructural observations on natural syntectonic fibrous veins: implications for the growth process. Tectonophysics 352, 257-274.

Hinman, N.W., Walter, M.R., 2005. Textural Preservation in Siliceous Hot Spring Deposits During Early Diagenesis: Examples from Yellowstone National Park and Nevada, U.S.A. Journal of Sedimentary Research 75, 200-215.

Hossain, M.D.S., 2012. Controls on vein styles and internal textures in magmatic-hydrothermal system. Himalayan Geology 33, 110-117.

Hund, F., 1981. Inorganic Pigments: Bases for Colored, Uncolored, and Transparent Products. Angewandte Chemie International Edition in English 20, 723-730.

Jallad, K.N., Ben-Amotz, D., 2001. Chemical imaging of iron oxides and oxyhydroxides using near infrared Raman imaging microscopy. Materials Science and Technology 17, 1479-1486.

Jehlicka, J., Bény, C., 1992. Application of Raman microspectrometry in the study of structural changes in Precambrian kerogens during regional metamorphism. Organic Geochemistry 18, 211-213.

Katagiri, G., Ishida, H., Ishitani, A., 1988. Raman spectra of graphite edge plane. Carbon 26, 565-571.

Kingma, K.J., Hemley, R.J., 1994. Raman spectroscopic study of microcrystalline silica. American Mineralogist 79, 269-273.

Kotková, J., O'Brien, P.J., Ziemann, M.A., 2011. Diamond and coesite discovered in Saxony-type granulite: Solution to the Variscan garnet peridotite enigma. Geology 39, 667-670.

Kremer, B., Bauer, M., Stark, R.W., Gast, N., Altermann, W., Gursky, H.-J., Heckl, W.M., Kazmierczak, J., 2012a. Laser-Raman and atomic force microscopy assessment of the chlorococcalean affinity of problematic microfossils. Journal of Raman Spectroscopy 43, 32-39.

Kremer, B., Owocki, K., Królikowska, A., Wrzosek, B., Kazmierczak, J., 2012b. Mineral microbial structures in a bone of the Late Cretaceous dinosaur Saurolophus angustirostris from

the Gobi Desert, Mongolia — a Raman spectroscopy study. Palaeogeography, Palaeoclimatology, Palaeoecology 358–360, 51-61.

Krepski, S.T., Emerson, D., Hredzak-Showalter, P.L., Luther, G.W., 3rd, Chan, C.S., 2013. Morphology of biogenic iron oxides records microbial physiology and environmental conditions: toward interpreting iron microfossils. Geobiology 11, 457-471.

Kuznetsov, S.K., Svetova, E.N., Shanina, S.N., Filippov, V.N., 2012. Minor elements in quartz from hydrothermal-metamorphic veins in the Nether Polar Ural Province. Geochem. Int. 50, 911-925.

Marshall, A.O., Emry, J.R., Marshall, C.P., 2012a. Multiple Generations of Carbon in the Apex Chert and Implications for Preservation of Microfossils. Astrobiology 12, 160-166.

Marshall, A.O., Marshall, C.P., 2013. Comment on "Biogenicity of Earth's earliest fossils: A resolution of the controversy" by J. W. Schopf and A. B. Kudryavtsev, Gondwana Research, Volume 22, Issue 3-4, Pages 761-771. Gondwana Research 23, 1654-1655.

Marshall, A.O., Wehrbein, R., Lieberman, B., Marshall, C.P., 2012b. Raman Spectroscopic Investigations of Burgess Shale-type Preservation: A New Way Forward, PALAIOS 27, 288-292.

Marshall, C.P., Edwards, H.G.M., Jehlicka, J., 2010. Understanding the Application of Raman Spectroscopy to the Detection of Traces of Life. Astrobiology 10, 229-243.

Marshall, C.P., Emry, J.R., Olcott Marshall, A., 2011. Haematite pseudomicrofossils present in the 3.5-billion-year-old Apex Chert. Nature Geosci 4, 240-243.

Marshall, C.P., Marshall, A.O., 2011. Hematite and carbonaceous materials in geological samples: A cautionary tale. Spectrochimica Acta Part A: Molecular and Biomolecular Spectroscopy 80, 133-137.

Marshall, C.P., Olcott Marshall, A., 2013. Raman hyperspectral imaging of microfossils: potential pitfalls. Astrobiology 13, 920-931.

McCreery, R.L., 2005. Raman Microscopy and Imaging, Raman Spectroscopy for Chemical Analysis. John Wiley & Sons, Inc., pp. 293-332.

Nasdala, L., Beyssac, O., William Schopf, J., Bleisteiner, B., 2012. Application of Raman-based images in the Earth sciences, in: Zoubir, A. (Ed.), Raman Imaging. Springer Berlin Heidelberg, pp. 145-187.

Nasdala, L., Smith, D.C., Kaindl, R., Ziemann, M.A., 2004. Raman spectroscopy: analytical perspectives in mineralogical research. EMU notes in mineralogy, 281-343.

Nicholson, R., 1991. Vein morphology, host rock deformation and the origin of the fabrics of echelon mineral veins. Journal of Structural Geology 13, 635-641.

Nicholson, R., Ejiofor, I.B., 1987. The three-dimensional morphology of arrays of echelon and sigmoidal, mineral-filled fractures: data from north Cornwall. Journal of the Geological Society 144, 79-83.

O'Brien, P.J., Ziemann, M.A., 2008. Preservation of coesite in exhumed eclogite: insights from Raman mapping. European Journal of Mineralogy 20, 827-834.
Ong, Y.H., Lim, M., Liu, Q., 2012. Comparison of principal component analysis and biochemical component analysis in Raman spectroscopy for the discrimination of apoptosis and necrosis in K562 leukemia cells. Opt. Express 20, 22158-22171.

Parenteau, M.N., Cady, S.L., 2010. Microbial Biosignatures in Iron-Mineralized Phototrophic Mats and Chocolate Pots Hot Springs, Yellowstone National Park, United States, PALAIOS 25, 97-111.

Passchier, C.W., Trouw, R.A.J., 2005. Microtectonics. Springer, Germany.

Pasteris, J.D., Wopenka, B., 1991. Raman-spectra of graphite as indicators of degree of metamorphism. Canadian Minerologist 29, 143-153.

Pawley, J., 2006. Handbook of Biological Confocal Microscopy, 3rd ed. Springerlink, p. 988.

Pinti, D.L., Mineau, R., Clement, V., 2009. Hydrothermal alteration and microfossil artefacts of the 3,465-million-year-old Apex chert. Nature Geosci 2, 640-643.

Pinti, D.L., Mineau, R., Clement, V., 2013. Comment on "Biogenicity of Earth's earliest fossils: a resolution of the controversy" by J. William Schopf and Anatoliy B. Kudryavtsev, Gondwana Research 22 (2012), 761-771. Gondwana Research 23, 1652-1653.

Salzer, R., Siesler, H., 2009a. Infrared and Raman Spectroscopic Imaging. Wiley, Weinheim, Germany.

Sasic, S., Clark, D.A., Mitchell, J.C., Snowden, M.J., 2004. A comparison of Raman chemical images produced by univariate and multivariate data processing-a simulation with an example from pharmaceutical practice. Analyst 129, 1001-1007.

Sasic, S., Ozaki, Y., 2010. Raman, Infrared, and Near-Infrared Chemical Imaging. Wiley, New Jersey.
Sawyer, K., 2006. The Rock from Mars: A Detective Story on Two Planets. Random House.

Schopf, J.W., 1992. The Proterozoic Biosphere: a Multidisciplinary Study. University Press, Cambridge.

Schopf, J.W., 1993. Microfossils of the Early Archean Apex Chert: New Evidence of the Antiquity of Life. Science 260, 640-646.

Schopf, J.W., 1999. Cradle of Life: Discovery of Earth's Earliest Fossils. Princeton University Press, New York.

Schopf, J.W., 2003. 3-D Raman imagery and atomic force microscopy of ancient microscopic fossils. American Geophysical Union : Washington, DC, United States, United States, p. b52c.

Schopf, J.W., 2004. Chapter 6: Evolution of life and precambrian bio-geology, in: P.G. Eriksson, W.A.D.R.N.W.U.M., Catuneanu, O. (Eds.), Developments in Precambrian Geology. Elsevier, pp. 516-539.

Schopf, J.W., Kudryavtsev, A.B., 2005. Three-dimensional Raman imagery of precambrian microscopic organisms. Geobiology 3, 1-12.

Schopf, J.W., Kudryavtsev, A.B., 2009. Confocal laser scanning microscopy and Raman imagery of ancient microscopic fossils. Precambrian Research 173, 39-49.

Schopf, J.W., Kudryavtsev, A.B., 2011. Biogenicity of Apex Chert microstructures. Nature Geosci 4, 346-347.

Schopf, J.W., Kudryavtsev, A.B., 2012. Biogenicity of Earth's earliest fossils: A resolution of the controversy. Gondwana Research 22, 761-771.

Schopf, J.W., Kudryavtsev, A.B., 2013. Reply to the comments of D.L. Pinti, R. Mineau and V. Clement, and of A.O. Marshall and C.P. Marshall on “Biogenicity of Earth's earliest fossils: A resolution of the controversy” by J. William Schopf and Anatoliy B. Kudryavtsev, Gondwana Research 22 (2012), 761-771. Gondwana Research 23, 1656-1658.

Schopf, J.W., Kudryavtsev, A.B., 2014. Biogenecity of Earth's Earliest Fossils. Springer, New York.

Schopf, J.W., Kudryavtsev, A.B., Agresti, D.G., Wdowiak, T.J., Czaja, A.D., 2002. Laser-Raman imagery of Earth's earliest fossils. Nature [London] 416, 73-76.

Schopf, J.W., Kudryavtsev, A.B., Czaja, A.D., Tripathi, A.B., 2007. Evidence of Archean life: Stromatolites and microfossils. Precambrian Research 158, 141-155.

Schopf, J.W., Kudryavtsev, A.B., Sugitani, K., Walter, M.R., 2010. Precambrian microbe-like pseudofossils: A promising solution to the problem. Precambrian Research 179, 191-205.

Schopf, J.W., Packer, B.M., 1987. Early Archean (3.3-Billion to 3.5-Billion-Year-Old) Microfossils from Warrawoona Group, Australia. Science 237, 70-73.

Schopf, J.W.a.W., MR., 1983. Archean microfossils: new evidence of ancient microbes. Princeton University Press.

Sendova, M., Zhelyaskov, V., Scalera, M., Ramsey, M., 2005. Micro-Raman spectroscopic study of pottery fragments from the Lapatsa tomb, Cyprus, ca 2500 BC. Journal of Raman Spectroscopy 36, 829-833.

Sforna, M.C., van Zuilen, M.A., Philippot, P., 2014. Structural characterization by Raman hyperspectral mapping of organic carbon in the 3.46 billion-year-old Apex chert, Western Australia. Geochimica Et Cosmochimica Acta 124, 18-33.

Shim, S.H., Duffy, T.S., 2002. Raman spectroscopy of Fe2O3 to 62 GPa. American Mineralogist 87, 318-326.

Smith, E., Dent, G., 2005. Modern Raman Spectroscopy: A Practical Approach. John Wiley and Sons, West Sussex, Engand.

Tang, M., McEwen, G.D., Wu, Y., Miller, C.D., Zhou, A., 2013. Characterization and analysis of mycobacteria and Gram-negative bacteria and co-culture mixtures by Raman microspectroscopy, FTIR, and atomic force microscopy. Analytical and bioanalytical chemistry 405, 1577-1591.

Torrent, J., Barrón, V., 2003. The Visible Diffuse Reflectance Spectrum in Relation to the Color and Crystal Properties of Hematite. Clays and Clay Minerals 51, 309-317.

Torrent, J., Schwertmann, U., 1987. Influence of Hematite on the Color of Red Beds. Journal of Sedimentary Petrology 57, 682-686.

Turrell, G., 1972. Infrared and Raman Spectra of Crystals. Academic Press, London.

Urai, J.L., Williams, P.F., van Roermund, H.L.M., 1991. Kinematics of crystal growth in syntectonic fibrous veins. Journal of Structural Geology 13, 823-836.

Vajna, B., Farkas, A., Pataki, H., Zsigmond, Z., Igricz, T., Marosi, G., 2012. Testing the performance of pure spectrum resolution from Raman hyperspectral images of differently manufactured pharmaceutical tablets. Analytica Chimica Acta 712, 45-55.

Vajna, B., Patyi, G., Nagy, Z., Bódis, A., Farkas, A., Marosi, G., 2011. Comparison of chemometric methods in the analysis of pharmaceuticals with hyperspectral Raman imaging. Journal of Raman Spectroscopy 42, 1977-1986.

Wang, A., Dhamelincourt, P., Dubessy, J., Guerard, D., Landais, P., Lelaurain, M., 1989. Characterization of graphite alteration in an uranium deposit by micro-Raman spectroscopy, X-ray diffraction, transmission electron microscopy and scanning electron microscopy. Carbon 27, 200-218.

Wopenka, B., Pasteris, J.D., 1993. Structural characterization of kerogens to granulite-facies graphite; applicability of Raman microprobe spectroscopy. American Mineralogist 78, 533-557.

Yan, J., 2004. Laser micro-Raman spectroscopy of single-point diamond macnined silicon substrates. Journal of Applied Physics 95, 2094-3002.

Zoppi, A., Lofrumento, C., Castellucci, E.M., Dejoie, C., Sciau, P., 2006. Micro-Raman study of aluminium-bearing hematite from the slip of Gaul sigillata wares. Journal of Raman Spectroscopy 37, 1131-1138.

Chapter 4: Multiple Generations of Carbon in the Apex chert and Implications for Preservation of Microfossils

Submitted as "Multiple Generations of Carbon in the Apex chert and Implications for Preservation of Microfossils, Olcott Marshall, A.O., Emry, J.R., and Marshall, C.P., Astrobiology, 2012, vol.12, number 2, p. 160-166

ABSTRACT

While the Apex chert is one of the most well-studied Archean deposits on Earth, its formation history is still not fully understood. Here, we present Raman spectroscopic data collected on the carbonaceous material (CM) present within the matrix of the Apex chert. These data, collected within a paragenetic framework, reveal two different phases of CM deposited within separate phases of quartz matrix. These multiple generations of CM illustrate the difficulty of searching for signs of life in these rocks and, by extension, in other Archean sequences.

INTRODUCTION

Billions of years of plate tectonics have erased much of the Archean rock record and left the remaining rocks metamorphically altered and deformed, with typically poor exposures that make the rocks challenging to map and correlate. The Archean-aged rocks in the Pilbara Craton

of Western Australia have been the subject of significant past research, as they have relatively good field exposure and are considered to have undergone low-grade metamorphic alteration at prehnite-pumpellyite (ca. 250-350°C) or lower greenschist facies (ca. 300-425°C) (Blatt and Tracy, 2005, Brasier et al., 2005; Schopf, 1993; Van Kranendonk, 2006). These rocks also include the Apex chert, a carbon-containing unit (Marshall et al., 2011; De Gregorio and Sharp, 2006; Braiser et al., 2005,2002) that has been proposed to contain the oldest putative microbial fossils on Earth (Schopf and Packer, 1987; Schopf, 1993). While the majority of studies have focused primarily on these structures (e.g., Marshall et al., 2011; Brasier et al., 2002; Schopf et al., 2002; Schopf and Packer, 1987), others have addressed the mode of formation and alteration of the Apex chert (e.g., Brasier et al., 2005; Van Kranendonk and Pirajno, 2004; Van Kranendonk, 2006).

This paper presents a Raman spectroscopic examination of the CM present within the Apex chert in a paragenetic context, a combined approach that allows for the determination of the relative age of formation and thermal grade of the CM recently identified within the matrix of the Apex chert (Marshall et al., 2011; De Gregorio and Sharp, 2006; Braiser et al., 2005, 2002). Furthermore, these data suggest that the formation and alteration history of CM in other Archean rocks may be more complex than previously thought, and that an understanding of the degree of alteration and petrographic position of CM found within Archean deposits is critical when prospecting for evidence of the earliest life on Earth.

GEOLOGICAL SETTING

The Pilbara Craton of Western Australia contains some of the oldest Archean rocks preserved on Earth (Figure 1). An Archean proto-continent, the Pilbara Craton formed between 3.51-2.94 Ga as a volcanic plateau that consisted of a series of granitic complexes and volcanic rocks (Brasier et al., 2005; Van Kranendonk, 2006). The Warrawoona Group, located in the East Pilbara Granite-Greenstone terrain in Western Australia, was formed between 3.15-3.42 Ga (Brasier et al., 2005; Hickman, 1983). Its rocks consist of mafic extrusive volcanics and minor amounts of chert, barite, sulfides, carbonates, volcaniclastic units, and felsic volcanic horizons that have undergone prehnite-pumpellyite to greenschist facies metamorphism under low strain conditions (Brasier et al., 2005; Van Kranendonk, 2006; Van Kranendonk et al., 2007). Found within the Warrawoona Group, the Apex Basalt Formation consists primarily of komatiitic basalt with minor amounts of tholeiitic basalt, doleritic flows and dikes, and relatively thin (<30 m) chert horizons (Brasier et al., 2005). These mafic volcanic rocks show evidence of underwater eruption, including chilled margins, hyaloclastic breccias, and pillow basalt textures (Brasier et al., 2005).

The Apex chert, which is geographically restricted to the Panorama Belt in the central part of the Pilbara Craton, is one of the thin chert horizons present in the Apex Basalt (Figure 1). It consists of a series of black chert dikes and an overlying stratiform chert unit that occurs across three structural blocks (North, South and Central) that are defined by fault systems interpreted to be synsedimentary in origin (Figure 1)

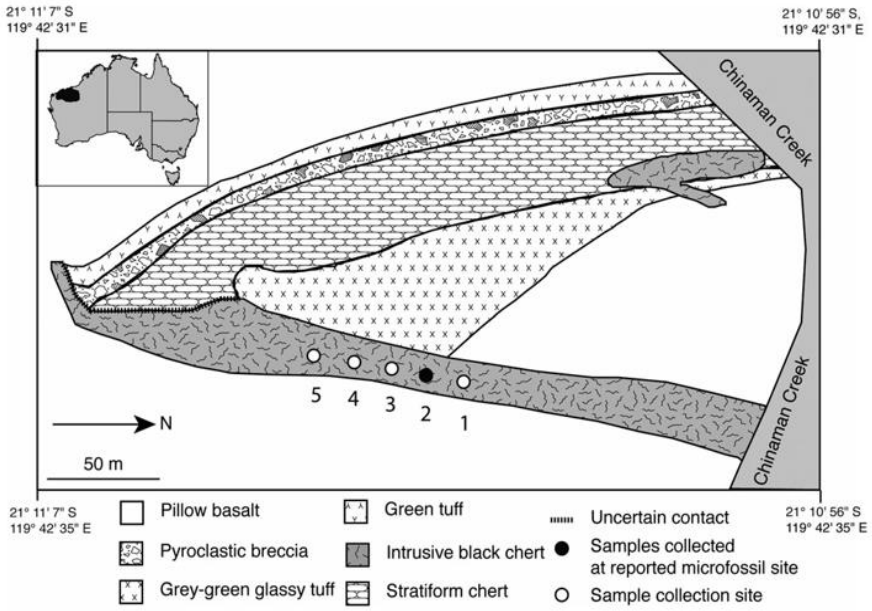

Figure 1. Geological map of the Apex Chert showing sample localities (modified from Brasier et al., 2005). Circles represent sample collection sites; filled circle indicates original microfossil locality (Schopf and Packer, 1987). Inset map shows location of Pilbara Craton in Australia.

(Brasier et al., 2005). The dikes have been interpreted as feeder dikes that channeled hydrothermal fluids upward, which resulted in the formation of the overlying stratiform chert (Brasier et al., 2005).

MATERIALS AND METHODS

Sample collection

In 2006, samples were collected from the main Apex chert dike during the Geological Society of Western Australia Pilbara fieldtrip (Figure 1). The samples were collected approximately every 10 m up the outcrop, including at the original microfossil locality.

Microscopy

Petrographic analyses of the Apex chert were conducted on standard 30 µm-thick petrological thin sections, which were made by Burnham Petrographic. Optical microscopy was performed on all thin sections with an Olympus BX51 System microscope.

Raman Microspectroscopy

Standard point Raman spectra were collected with a Renishaw inVia Reflex Raman Microprobe (Renishaw plc, Wotton-under-Edge, UK), equipped with a Peltier cooled charge-coupled device (CCD) camera (1024x256 pixels). The spectrometer is fitted with holographic notch filters and five gratings (3,600 mm/line (UV) 2,400 mm/line (vis), 1,800 mm/line (vis), 1,200 mm/line (NIR), and 830 mm/line (NIR)). The Raman light was dispersed by a diffraction grating with 2,400 mm/line, and the signal was analyzed with a Peltier cooled CCD camera at room temperature (1024x256 pixels). The attached microscope is a Leica DMLM and is equipped with four objectives (x100/ 0.9 NA, x50/0.75 NA, x20/0.40 NA, x5/0.12 NA) and a trinocular viewer that accommodates a video camera that allows direct viewing of the sample. Sample excitation was achieved with an argon ion laser (Modu-Laser, Utah, USA) emitting at 514.5 nm. Calibration of the Raman shift is achieved by recording the Raman spectrum of the silicon F_{1g} mode for one accumulation and 10 s. If necessary, an offset correction is performed to ensure that the position of the F_{1g} band is at 520.50±0.10 cm^{-1}.

The laser power impinging on the CM was between 1-5 mW to minimize laser-induced heating of the samples (Marshall et al., 2010). The Ar^{+} laser was oriented normal to the sample. Graphite and other highly ordered sp^2 carbonaceous materials have strong structural anisotropy and thus do not exhibit the same Raman spectrum when the measurement is performed parallel or perpendicular to the c-axis (e.g., Katagiri et al., 1988; Wang et al., 1989; Compagnini et al., 1997). The cherts studied here do not contain any foliation or penetrative fabric, and the disordered sp^2 carbonaceous material shows no preferred orientation. Therefore, in this case, it is possible that carbonaceous material with different orientations in a single sample were analyzed. To examine this orientation effect, multiple measurements were obtained on each sample at different orientations. Repeated measurements for a single spot at different orientations show no spectral variation. It has been shown that polishing of thin sections and slabs can induce severe structural disorder in the CM lattice network and thus strongly influence the resulting Raman spectrum (e.g., Nemanich and Solin, 1979; Pasteris, 1989; Mostefaoui et al., 2000). In addition, when investigating Archean rocks, it is important to overrule surface contamination. Therefore, to avoid the two above-mentioned problems, the Raman measurements were made on CM particles of varying size embedded below the surface.

A refractive glass 100x objective lens was used to focus the laser on a 1μm spot to collect the backscattered radiation. Collection parameters for the scans of the CM were 60 seconds at 1-5 mW with 100 accumulations over the full Raman region of 100-4000 cm^{-1}. The spectra were deconvoluted with a Gaussian/Lorentzian fit routine by using GRAMS/32 software to determine intensity of the D (I_D) and G (I_G) bands with accuracy. A mixed Gaussian/Lorentzian fit routine is used for disordered sp^2 CM (e.g., Takikawa et al., 2000; Ferrari and Robertson 2000). The parameters were fitted to the experimental envelope by a least squares iterative procedure. To

determine the goodness of fit criteria, the following aspects were considered: (1) standard errors of parameters (χ-squared), (2) local poor fits (indicative of an incorrect choice of the number of component peaks or errors in their half-widths), and (3) the degree of coincidence of the second derivative (original and fitted spectrum). A total of 10 spectra were collected, and the standard deviation was calculated on the spread of the I_D/I_G ratios.

Application of Raman Microspectroscopy to Carbonaceous Material

Raman microspectroscopy provides molecular structural information on both inorganic and organic materials. While Raman spectroscopic data are collected over the full region of 100-4000 cm^{-1}, specific smaller regions are often examined for structural information of different materials. For instance, the mineral fingerprint region (100-1800 cm^{-1}) is the portion of a Raman spectrum that contains diagnostic bands used to identify various minerals. The Raman spectrum of CM can be divided into first- and second-order regions, depending upon the degree of crystallinity of the CM. However, in the case of poor crystallinity there will be no bands in the second-order region. The carbon first-order region (800-1800 cm^{-1}) is sensitive to the degree of two-dimensional ordering present in CM, while the carbon second-order region (2200-3400 cm^{-1}) is sensitive to the three-dimensional ordering of the CM and indicates the degree of its graphitization (Lespade et al., 1982). The carbon first-order region generally contains two broad bands from CM; the first, commonly referred to as the D band, is seen at ~1350 cm^{-1} and is assigned to an A_{1g} symmetry mode that becomes Raman active with disorder. The second, referred to as the G band, is seen at ~1600 cm^{-1} and is assigned to the E_{2g2} symmetry mode. The carbon second-order region shows several bands at 2450 cm^{-1}, 2695 cm^{-1}, 2735 cm^{-1}, 2950 cm^{-1},

and 3248 cm^{-1}, bands assigned to both overtone and combination scattering. The ratio of the intensity of the D and G bands (I_D/I_G) has been shown to reflect the degree of structural order and thermal evolution in CM (e.g., Jehlicka and Bény, 1992; Jehlicka et al., 2003; Pasteris and Wopenka, 1991), and graphing the intensity of the D/G (I_D/I_G) bands of each sample against the area of the D/G (A_D/A_G) bands can reveal differences between the thermal evolution or metamorphic grades of CM (e.g., Jehlicka and Bény, 1992; Jehlicka et al., 2003; Pasteris and Wopenka, 1991; Tice et al., 2004; Wopenka and Pasteris, 1993 ; Yui et al., 1996). It should be noted that, in these studies of the thermal evolution of natural CM, either a 514.5 nm (2.41 eV) or a 532 nm (2.33 eV) laser was used. Over the 244-1064 nm range of laser excitation, the G band position and intensity are practically independent of excitation wavelength, whereas the D band shows an apparent linear variation of its position (amounting to about 180 cm^{-1} in the measured range), and its intensity (Pocsik et al., 1998) strongly depends on the excitation wavelength. This phenomenon is attributed to a resonance enhancement effect of the D band (Pocsik et al., 1998). Recently, Aoya et al. (2010) showed that there is little to no difference in I_D/I_G and A_D/A_G ratios for the same CM sample acquired from either excitation with a 514.5 nm or 532 nm laser. Therefore, it is valid to undertake a comparison of the above I_D/I_G ratios from the literature to delineate the thermal evolution of CM collected with either a 514.5 or 532 nm lasers.

Carbonaceous material contains crystallites of the order of nanometers in diameter, which are composed of graphite-like layers of aromatic clusters that are arranged turbostratically. Tuinstra and Koenig (1970a, b) clearly demonstrated a relationship between the intensity ratio of the D and G bands (commonly denoted as I_D/I_G) and the microcrystalline planar size L_a. Calibration against the in-plane crystallite size (L_a), as measured by XRD, has shown that the

ratio of Raman intensities of the D and G bands is inversely proportional to the average value of L_a. Knight and White (1989) measured the Raman spectra of numerous sp^2 CM, using an excitation wavelength of 514.5 nm (E_l = 2.41 eV), and derived an empirical expression that allows the determination of L_a from the intensity ratio of D and G bands given by: $L_a = 44[I_D/I_G]^{-1}$ (nm). Later on, Mernagh et al. (1984) showed that the I_D/I_G ratio depends strongly on the excitation laser energy (E_l) used in the Raman analysis, which thus revealed that the Knight and White (1989) empirical formula was only valid when the analysis was performed with the 514.5 nm laser line. It has been shown that this relationship holds for a wide range of sp^2-bonded carbons over the range of $2.5 < L_a < 300$ nm.

RESULTS

Raman microspectroscopy of carbonaceous material from the Apex chert

Raman microspectroscopy revealed two different phases of CM present within all samples from the Apex chert (Figure 2). Within the mineral fingerprint region (100-1800 cm^{-1}), both phases contain bands at 206, 464, and 511 cm^{-1}, all of which can be assigned to vibrational modes (A_1 symmetry) of quartz. While both phases of CM contain D (~1350 cm^{-1}) and G (~1600 cm^{-1}) bands, the line-shapes of the bands are markedly different for each phase of CM.

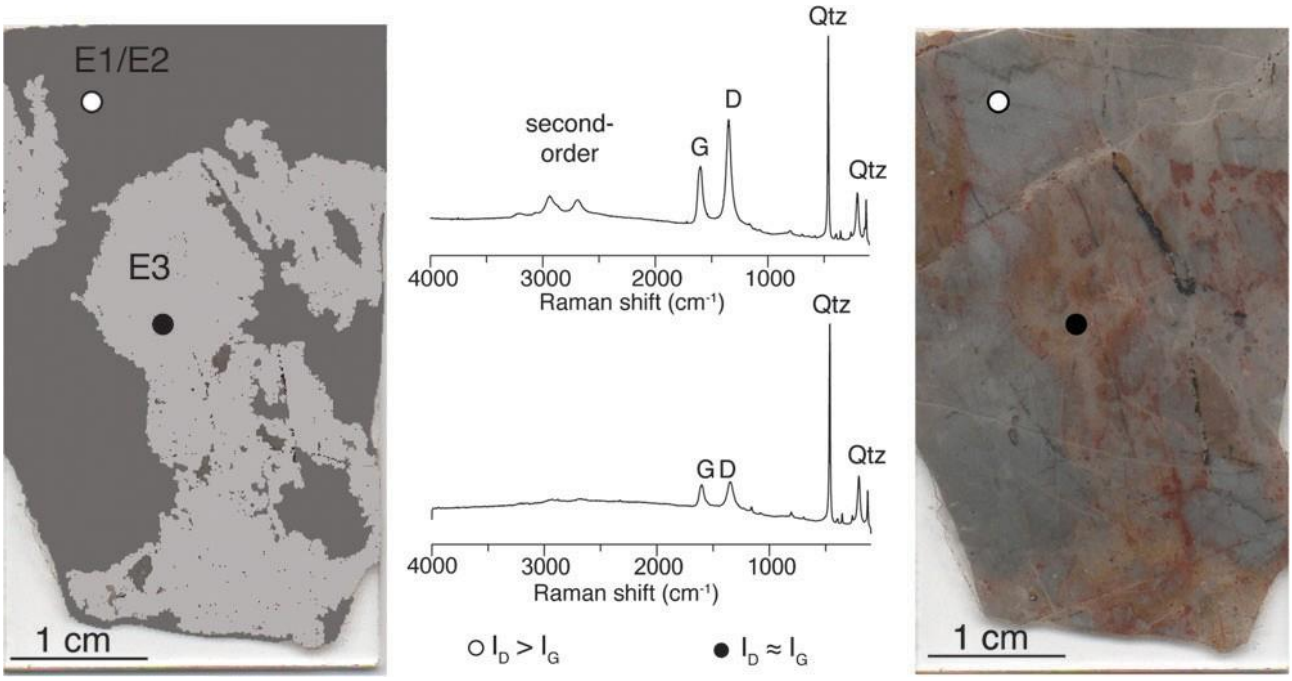

Figure 2. Raman spectra of CM within its paragenetic framework. Thin section on right, collected at the original microfossil locality, reveals the complex alteration history of the Apex Chert, most noticeably the multiple generations of matrix formation. The sketch on the left illustrates the relationship between the first two phases of the matrix formation (E1/E2) and the third phase (E3). The top Raman spectrum was collected within the E1 matrix (the white dot), while the bottom one was collected within the E3 matrix (the black dot). The carbon first-order bands are denoted "D" and "G," the carbon second-order bands are denoted "second-order," and the quartz bands are denoted "Qtz."

In one phase, the D and G bands are of similar intensity and are relatively broad. In contrast, the other phase has a D band that is more intense than the G band and most notably contains additional bands in the carbon second-order region at 2695 cm^{-1} and 2950 cm^{-1}.

The CM with D and G bands of similar intensity found within all of the Apex chert samples has an I_D/I_G ratio of 1.27±0.12, while the phase with a more intense D band has a ratio of 1.68±0.15. The microcrystalline planar size L_a also varies for each CM phase from 35 nm to 26 nm based on the Knight and White (1989) calibration. Comparison of the intensity of the D

band, I_D/I_G ratio (Figure 3), presence and absence of second-order bands, and L_a revealed that these comprise two different populations of CM.

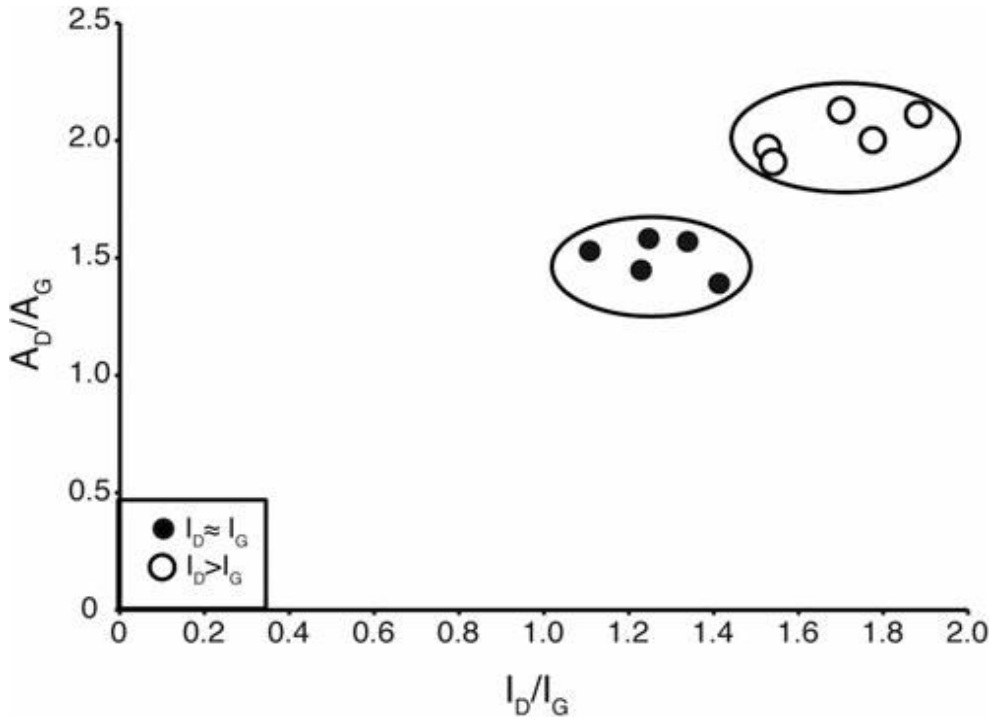

Figure 3. Graph comparing the intensity (ID/IG) and the area (AD/AG) ratios of the CM. This comparison reveals the presence of two populations of CM, one in which the D bands is roughly equal to the G band (the circles) and one in which the D band is larger than the G band (the squares).

Petrographic analysis of the Apex chert

Paragenetic analyses allowed for determination of a detailed geological history by examining mineral phases and assemblages on a microscopic scale. Furthermore, this technique can provide an understanding of the timing and thermal history of the two phases of CM identified by Raman spectroscopy. It has been interpreted that the Apex chert is a brecciated hydrothermal chert related to granitiod intrusions with multiple pulses of hydrothermal silica

during formation (Brasier et al., 2002, 2005; Van Kranendonk and Pirajno, 2004; Van Kranendonk 2006). Our petrographic analysis showed that the formation of the quartz matrix can be broken into four major phases, which may suggest four major pulses of repeated hydrothermal silica injection during vein formation.

The first phase of matrix formation (E1) was the deposition of clasts of grey microcrystalline quartz that contained small black particles of CM. Raman microspectroscopy of the CM preserved in E1 revealed the phase with a more intense D band (Figure 2), I_D/I_G ratio of 1.68±0.15 (Figure 3), a L_a of 26 nm, and the presence of well-developed second-order bands. Clasts of E1 are contained within a clear to light grey microcrystalline quartz matrix (E2) (Figure 2). E1and E2 record deposition of a clastic sediment that was then entombed in microcrystalline quartz matrix. The second major phase (E3) of matrix formation consists of light grey or grey-pink microcrystalline quartz that contains light-grey to brown clots of CM, small dark brown-black particles of CM and sub-microscopic disseminated CM (Figure 2). Raman microspectroscopy of this CM revealed that it is all composed of the phase of CM in which the D and G bands are of similar intensity (Figure 2), I_D/I_G ratio of 1.27±0.12 (Figure 3), a L_a of 35 nm, and the absence of notable second-order bands. It is apparent that the E3 phase occurred after the formation of the clasts and matrix in E1 and E2, as pieces of the E1-E2 phase are present as inclusions within the quartz matrix of the E3 phase. The relationships of the E1-E3 phases are illustrated in the sketch in Figure 2. The final phase (E4) of the matrix formation consists of clear, micro-macrocrystalline quartz that does not contain CM and occurs as irregular patches and thin veins.

DISCUSSION

Several researchers have shown that the degree of disorder in natural CM is related to the degree of thermal evolution and metamorphism, which in turn produces characteristic carbon first-order Raman spectra line-shapes (e.g., Jehlicka and Bény, 1992; Marshall et al., 2001; Jehlicka et al., 2003; Pasteris and Wopenka, 1991; Wopenka and Pasteris, 1993). Furthermore, as CM does not undergo retrograde metamorphism, it is a useful proxy for the peak metamorphic grade or thermal alteration experienced by the host rock (e.g., Jehlicka and Bény, 1992; Marshall et al., 2001; Jehlicka et al., 2003; Pasteris and Wopenka, 1991; Wopenka and Pasteris, 1993; Beyssac et al., 2002; Aoya et al., 2010). Thus, comparison of the line-shape and spectral parameters (i.e., I_D/I_G ratio etc) of the Raman spectra of CM found within the Apex chert to that of CM from deposits of known metamorphic grade and thermal evolution allows for a semi-quantitative elucidation of the thermal alteration history of the CM (but it does not allow for determination of an absolute temperature value). As the Raman spectra were collected within a paragenetic framework, it is also possible to gain an understanding of the relative timing of the deposition of the CM.

The CM found in phase E3 has a line-shape similar to carbon first-order Raman spectra from CM found in several deposits metamorphosed to lower greenschist facies, including Neoproterozoic units in the Bohemian Massif (Jehlicka et al., 2003) and Paleoproterozoic cherts from Shunga, Russia (Wopenka and Pasteris, 1993). In contrast, the CM found in phase E1 has a line-shape similar to carbon first-order Raman spectra from CM found in thermally more mature deposits. These include CM from Neoproterozoic units in the Bohemian Massif that experienced

amphibolite facies metamorphism (ca. 500-700°C) (Blatt and Tracy, 2005; Jehlicka et al., 2003), as well as upper greenschist facies (ca. 425-500°C) Archean deposits from the Swaziland sequence (Pasteris and Wopenka, 2003) and the Barberton Greenstone Belt (Tice et al., 2004; Van Zuilen et al., 2007).

These differences, as well as the fact that the CM found in the E1 phase also resolved bands in the carbon second-order region, indicate that this phase of CM has more three-dimensional ordering and thus represents a higher thermal alteration. Furthermore, Marshall et al. (2001), Marshall et al. (2007), and Lahfid et al. (2010) demonstrated that Raman spectra acquired from CM thermally altered from 230 to 300^{o}C shows that the relative intensity of the D band progressively increases. Between temperatures of 300 to 350^{o}C, the D band intensity is higher than the G band intensity (Marshall et al., 2001; Marshall et al., 2007; Lahfid et al., 2010). Additionally, there are several indicators that the CM in phase E1 must have been deposited before the less thermally mature CM in phase E3. First, the distribution of the CM within two different phases of matrix indicates that it was deposited at different times, and E3 contains a younger phase of CM than E1. Second, CM does not undergo retrograde thermal alteration or metamorphism, and instead records peak thermal stress; thus, the more thermally altered CM must have been heated before the less altered CM was deposited. Third, the fact that the CM in the E1 phase records thermal alteration to temperatures equivalent of upper greenschist or perhaps even amphibolite facies suggests several possible scenarios for the deposition and preservation of the CM. First, these observed temperatures could be due to the Apex chert experiencing a higher degree of metamorphic alteration than previously suspected. Alternatively, the CM could be allochthonous and represent a phase of transported thermally altered CM that is younger than the chert. Finally, the thermal alteration could have occurred if CM was emplaced

multiple times during pulses of hydrothermal silica precipitation of varying temperature. While the data do not allow discrimination between these scenarios, none support a biogenic origin for the CM.

Implications for the search for ancient life in Archean sequences

The presence of two phases of CM within these samples complicates the search for ancient life in the Apex chert and, by extension, in other Archean sequences. The presence of two separate generations of CM indicates that not all the carbon, if any, found within the samples is primary to deposition of the sequence, as CM was deposited after the initial formation of the rock unit. Thus, it is not possible to determine whether the CM analyzed is syngenetic. As paired Raman spectroscopic and paragenetic analyses have not been performed on other Archean sequences, it is not possible to know whether other rocks have a similar distribution of CM. However, researchers have applied Raman microspectroscopy to multiple particles of CM within single Archean samples, and these data are suggestive of the fact that other Archean sequences might also harbor multiple populations of CM. For instance, analyses of CM particles found within single samples of the 3.2-3.5 Ga Onverwacht and Fig Tree Groups of the Barberton greenstone belt in South Africa produced I_D/I_G measurements with a standard deviation of 15% (Tice et al., 2004). This value is much larger than the 9% standard deviations seen in each CM population in the Apex chert and is in fact similar to the 17% standard deviation obtained if the separate populations are considered as one (average $I_D/I_G=1.48\pm0.25$). Similarly, Raman microspectroscopy on multiple carbonaceous particles from the Pilbara Craton that are of similar age to the Apex chert but were collected ca. 50 km west of it were found to have I_D/I_G

measurements that ranged from 1.0 to 1.6 (Ueno et al., 2001), a very similar range to what was observed across the two populations of CM in the Apex Chert (1.27 to 1.68). While the only spectra pictured show the D band to be larger than the G band, similar to the CM found in the E1 matrix, an I_D/I_G measurement of 1 indicates that the D band is of equal intensity to the G band, similar to the CM found in the E3 matrix. Sugitani et al. (2010) showed that Raman spectra collected on carbonaceous microstructures from the 3.4 Ga Strelley Pool Formation had I_D/I_G ratios varying between 1.25 and 1.94.

Micrometer-scale heterogeneities in CM may be explained by a variety of mechanisms, such as micrometer-scale differences in precursor chemistry of CM, and subsequently dissimilar alteration pathways of the different precursor material, allochthonous CM, or emplacement of CM during multiple hydrothermal pulses at different temperatures. The possibility that Archean rocks contain multiple generations of CM also has ramifications for any potential carbonaceous microstructures that are found within the rocks. If CM has been deposited in different episodes of matrix formation, it is also then possible that a carbonaceous microstructure could have been deposited sometime after the initial formation of the rock. Thus, these data reveal that when searching for microfossils, it is of paramount importance to consider the paragenetic context of the carbonaceous microstructures, and not to rely on context-free kerogen isolates or paleontological thin sections (ca. 300 μm) that obscure the petrological details of the matrix fabric (Marshall et al., 2011).

CONCLUSIONS

The Raman spectroscopic analyses of the CM found within the Apex Chert revealed the presence of two generations of CM with two different thermal alteration histories. Paragenetic analyses also revealed that these two populations of CM are found within two different episodes of matrix formation. Taken together, these data indicate that there are several generations of CM contained within the Apex Chert, none of which might be syngenetic with the initial formation of the sequence. Although other Archean sequences have not yet been analyzed with this combination of techniques, Raman microspectroscopy analysis of the CM found in other Archean deposits has been suggestive of the idea that they, too, might contain multiple generations of CM. The possibility that CM is being emplaced through hydrothermal processeswithin these rocks illustrates the need for caution when searching for carbonaceous microfossils, as well as the importance of conducting this search within a paragenetic framework.

References

Aoya, M., Kouketsu, M., Endo, S., Shimizu, H., Mizukami, T., Nakamura, D., Wallis, S. (2010) Extending the applicability of the Raman carbonaceous material geothermometer using data from contact metamorphic rocks. *Journal of Metamorphic Geology* 28, 895-914.

Beyssac O., Goffé, B., Chopin C., and Rouzard, J.N. (2002) Raman spectra of carbonaceous material in metasediments: a new geothermometer. *Journal of Metamorphic Geology* 20, 859-871.

Blatt, H. and Tracy, R. (2005) Petrology: Igneous, Sedimentary, and Metamorphic, Freeman, 530 p.

Brasier, M.D., Green, O.R., Jephcoat, A.P., Kleppe, A.K., Van Kranendonk, M.J., Lindsay, J.F., Steele, A., and Grassineau, N.V. (2002) Questioning the evidence for Earth's oldest fossils. *Nature* 416, 76-81.

Brasier, M.D., Green, O.R., Lindsay, J.F., McLoughlin, N., Steele, A., and Stoakes, C. (2005) Critical testing of Earth's oldest putative fossil assemblage from the ~3.5 Ga Apex chert, Chinaman Creek, Western Australia. *Precambrian Research* 140, 55-102.

Compagnini, G., Puglist, O., Foti, G. (1997) Raman spectra of virgin and damaged graphite edge planes. *Carbon* 35, 1793-1797.

De Gregorio, B.T., Sharp, T.G. (2006) The structure and distribution of carbon in 3.5 Ga Apex chert: Implications for the biogenicity of Earth's oldest putative microfossils. American *Mineralogist* 91, 784-790.

Ferrari, A.C., Robertson, C. (2000) Interpretation of Raman spectra of disordered and amorphous carbon. *Phys. Rev. B Condens. Matter Mater. Phys.* 61, 14095-14107.

Hickman, A.H. (1983) Geology of the Pilbara Block and its environs. *Bulletin of the Geological Survey of Western Australia* 127, 1-267.

Jehlicka, J., and Bény, C. (1992) Application of Raman microspectrometry in the study of structural changes in Precambrian kerogens during regional metamorphism. *Organic Geochemistry* 18, 211-213.

Jehlicka, J., Urban, O., and Pokorný, J. (2003) Raman spectroscopy of carbon and solid bitumens in sedimentary and metamorphic rocks. *Spectrochimica Acta Part A: Molecular and Biomolecular Spectroscopy* 59, 2341-2352.

Katagiri, G., Ishida, H., Ishitani, A. (1988) Raman spectra of graphite edge plane. *Carbon* 26, 565-571.

Knight, D.S. and White, W.B. (1989) Characterization of diamond films by Raman-spectroscopy. *J. Mater. Res.* 4, 385-393.

Lahfid, A., Beyssac, O., Deville, E., Negro, F., Chopin, C., Goffe, B. (2010) Evolution of the Raman spectrum of carbonaceous material in low-grade metasediments of the Glarus Alps (Switzerland). *Terra Nova* 22, 354-360.

Lespade, P., Al-Jishi, R., and Dresselhaus, M.S. (1982) Model for Raman scattering from incompletely graphitized carbons. *Carbon* 20, 427-431.

Marshall, C.P., Mar, G.L., Nicoll, R.S. and Wilson, M.A. (2001) Organic Geochemistry of Artificially Matured Conodonts. *Organic Geochemistry* 32, 1055-1071.

Marshall, C.P., Love, G.D., Snape, C.E., Hill, A.C., Allwood, A.C., Walter, M.R., Van Kranendonk, M.J., Bowden, S.A., Sylva, S.P., and Summons, R.E. (2007) Structural characterization of kerogen in 3.4 Ga Archaean cherts from the Pilbara Craton, Western Australia. *Precambrian Research.* 155, 1-23.

Marshall, C.P., Edwards, H.G.M., and Jehlicka, J. (2010) . Understanding the application of Raman spectroscopy to the detection of traces of life. *Astrobiology* 10, 229-243.

Marshall, C.P., Emry, J.R., and Olcott Marshall, A. (2011) Haematite pseudomicrofossils present in the 3.5-billion-year-old Apex Chert. *Nature Geosci* 4, 240-243.

Mernagh, T.P., Cooney, R.P., and Johnson, R.A. (1984) Raman spectra of graphon carbon black. *Carbon* 22, 39-42.

Mostefaoui, S., Perron, C., Zinner, E., Sagon, G. (2000) Metal associated carbon in primitive chondrites: structure, isotopic composition and origin. *Geochimica et Acta* 64, 1945-1964.

Nemanich, R.J., Solin, S.A. (1979) First- and second-order Raman scattering from finite-size crystals of graphite. *Physical Review B* 20, 392-401.

Pasteris, J.D. (1989) In situ analysis in geological thin-sections by Laser Raman microprobe microspectroscopy: a cautionary note. *Applied Spectroscopy* 43, 567-570.

Pasteris, J.D., and Wopenka, B. (1991) Raman-spectra of graphite as indicators of degree of metamorphism. *Canadian Minerologist* 29, 143-153.

Pocsik, I., Hundhausen, M., Koos, M., and Ley, L. (1998) Origin of the D peak in the Raman spectrum of microcrystalline graphite. *Journal of Non-Crystalline Solids* 227–230, 1083–1086.

Schopf, J.W. (1993) Microfossils of the Early Archean Apex Chert: New Evidence of the Antiquity of Life. *Science* 260, 640-646.

Schopf, J.W., and Packer, B.M. (1987) Early Archean (3.3-Billion to 3.5-Billion-Year-Old) Microfossils from Warrawoona Group, Australia. *Science* 237, 70-73.

Schopf, J.W., Kudryavtsev, A.B., Agresti, D.G., Wdowiak, T.J., and Czaja, A.D. (2002) Laser-Raman imagery of Earth's earliest fossils. *Nature* 416, 73-76.

Sugitani, K., Lepot, K., Nagaoka, T., Mimura, K., Van Kranendonk, M., Oehler, D.Z., Walter, M.R. (2010) Biogenicity of morphologically diverse carbonaceous microstructures from the *ca.* 3400 Ma Strelley Pool Formation, in the Pilbara Craton, Western Australia. *Astrobiology* 10, 899-920.

Takikawa, H., Tao, Y., Miyano, R., Sakakibara, T., Ando, Y., Zhao, X., Hirahara, K., Iijima, S. (2001) Carbon nanotubes on electrodes in short-time heteroelectrode arc. *Mater. Sci. Eng., C* 16, 11-16.

Tice, M.M., Bostick, B.C., and Lowe, D.R. (2004) Thermal history of the 3.5-3.2 Ga Onverwacht and Fig Tree Groups, Barberton greenstone belt, South Africa, inferred by Raman microspectroscopy of CM. *Geology* 32, 37-40.

Tuinstra, F. and Koenig, J.L. (1970a) Raman spectrum of graphite. *J. Chem. Phys.* 53, 1126-1130.

Tuinstra, F. and Koenig, J.L. (1970b) Characterization of graphite fiber surfaces with Raman spectroscopy. *J. Compos. Mater.* 4, 492.

Ueno Y., Isozaki, Y., Yurimoto, H., Maruyama, S. (2001) Carbon isotopic signatures of individual Archean microfossils (?) from Western Australia. *International Geology Review* 43, 196-212.

Van Kranendonk, M.J. (2006) Volcanic degassing, hydrothermal circulation and the flourishing of early life on Earth: A review of the evidence from c. 3490-3240 Ma rocks of the Pilbara Supergroup, Pilbara Craton, Western Australia. *Earth-Science Reviews* 74, 197-240.

Van Kranendonk, M.J., Pirajno, F. (2004) Geological setting and geochemistry of metabasalts and alteration zones associated with hydrothermal chert±barite deposits in the ca. 3.45 Ga Warrawoona Group, Pilbara Craton, Australia. *Geochem. Explor. Environ. Anal.* 4, 253-278.

Van Kranendonk, M.J., Smithies, R.H., Hickman, A.H., and Champion, D.C. (2007) Review; secular tectonic evolution of Archean continental crust; interplay between horizontal and vertical processes in the formation of the Pilbara Craton, Australia. *Terra Nova* 19, 1-38.

Van Zuilen, M.A., Chaussidon M., Rollion-Bard, C., and Marty, B. (2007) Carbonaceous cherts of the Barberton Greenstone Belt, South Africa: Isotopic, chemical and structural characteristics of individual microstructures. *Geochimica et Cosmochimica Acta* 71, 655-669.

Wang, A., Dhamelincourt, P., Dubessy, J., Guerard, D., Landais, P., and Lelaurain, M. (1989) Characterization of graphite alteration in an uranium deposit by micro-Raman spectroscopy, X-ray diffraction, transmission electron-microscopy and scanning electron-microscopy. *Carbon* 27, 209–218.

Wopenka, B., and Pasteris, J.D. (1993) Structural characterization of kerogens to granulite-facies graphite; applicability of Raman microprobe spectroscopy. *American Mineralogist* 78, 533-557.

Yui, T.-F., Huang, E., and Xu, J. (1996) Raman spectrum of carbonaceous material: A possible metamorphic grade indicator for low-grade metamorphic rocks. *Journal of Metamorphic Geology* 14, 115–124.

Chapter 5: Evaluating the Effects of Autofluorescence during Raman Hyperspectral Imaging

Submitted as "Evaluating the Effects of Autofluorescence during Raman Hyperspectral Imaging" Emry, J.R., Olcott Marshall, A. O., and Marshall, CP, Geostandards and Geoanalytical Research, in press.

ABSTRACT

Raman hyperspectral imaging is becoming a popular technique to analyze geological materials. Autofluorescence can affect the quality of the spectra that comprise hyperspectral datasets. Few studies have addressed potential misinterpretation of Raman images from hyperspectral datasets affected by autofluorescence. Additionally, little work has been done to develop methods for identifying the spatial distribution of spectra affected by autofluorescence. This study illustrates how autofluorescence may lead to misinterpretation of the distribution of materials based on intensity at a point images. A method is proposed utilizing signal to axis analysis to create images which identify regions affected by autofluorescence. Post-processing baseline correction is often used to address autofluorescence, and most software programs utilize a form of Partial Least Squares regression modelling based on a subjective choice of polynomial order. This study shows that an inappropriate choice of polynomial order can introduce error

which may lead to misinterpretation of Raman images. A signal to axis analysis method is proposed to statistically compare seemingly "appropriate" baseline correction trials. Although post-processing of hyperspectral datasets and creating Raman images seems simple, data quality issues such as autofluorescence must be considered. If baseline correction is deemed necessary it should be addressed as an experiment involving statistical comparison.

INTRODUCTION

The fundamental task that geoscientists face is to identify and characterize geological materials. Historically, geoscientists have relied on optical microscopy and petrographic techniques to study geological materials. Raman spectroscopy is a generally non-destructive technique that requires little to no sample preparation and can provide a variety of chemical, structural and molecular information. These characteristics make Raman spectroscopy an extremely useful technique for geoscience applications and several authors have commented on the recent increase in its application in a variety of geoscience fields (Bernard *et al.* 2008, Marshall and Marshall 2011, Nasdala *et al.* 2012, Nasdala *et al.* 2004). Three major types of Raman spectroscopic data can be collected: point spectra, confocal depth profiles, and Raman hyperspectral imaging datasets. Point spectra can be collected from specific locations at the surface or at depth within a sample. Depth profiles {Nasdala, 2012 #508;Nasdala, 2004 #532}are an extension of point-spectral data collection where multiple spectra are collected at the same *x*,*y* location at different depths producing a vertical stack of spectra that show the vertical distribution of materials. Recent technological advances in confocal objectives, charge-coupled device detectors (CCD), laser technologies, motorized stages, and computer software

allowed for the development of Raman hyperspectral or chemical imaging (Bernard *et al.* 2008, Delhaye and Dhamelincourt 1975, Lee 2012, Rosasco *et al.* 1975).

Hyperspectral imaging involves collecting multiple spectra over an operator-defined 2-D region of a sample. The spectra may be collected in a point-mapping manner or can utilize line-scanning technologies. Point-mapping involves collecting individual spectra based on operator-defined *x,y* spatial resolution and line-focus techniques use a lens to expand the laser that is rastered across the sample allowing multiple spectra to be collected which are binned based on the an operator specified spatial resolution. Line-scanning techniques have a distinct advantage because they allow for significantly faster collection of large numbers of spectra at micron to sub-micron scale resolution (Lee 2012). Resulting datasets are 2-D arrays of spectra representative of the region of interest at a particular depth of focus. Univariate and multivariate analytical methods can then be applied to create false-color images representative of the 2-D distribution of various materials in a sample (Nasdala *et al.* 2012, Sasic and Ozaki 2010). If a confocal set-up is utilized, the laser can be focused at depth within a sample and spectra can be collected over the same *x,y* region at multiple depths to create a 3-D dataset, or Raman hypercube.

Analyzing Raman hyperspectral datasets can be extremely complex because they are composed of hundreds to thousands of individual spectra depending on the operator defined spatial resolution (Fig. 1). A variety of factors can affect the quality and resolution of each Raman spectrum in a hyperspectral dataset, however, autofluorescence is one of the most problematic which significantly affects the ability to collect meaningful hyperspectral datasets (Sasic and Ozaki 2010). Fluorescence typically manifests as a broad, sloping baseline that can overwhelm the Raman signal to varying degrees. Several techniques are available to mitigate

autofluorescence issues during point Raman spectra collection including changing laser excitation wavelength, laser power, acquisition time or the number of spectra collected at each point, photobleaching, utilizing shifted wavelength or pulse-gated techniques and surface-enhanced Raman spectroscopic methods (SERS)(Lewis and Edwards 2001). Unfortunately, altering data acquisition parameters or using photobleaching is not applicable for line-focus hyperspectral data acquisition as the software restricts the collection parameters in order to collect large numbers of spectra relatively quickly.

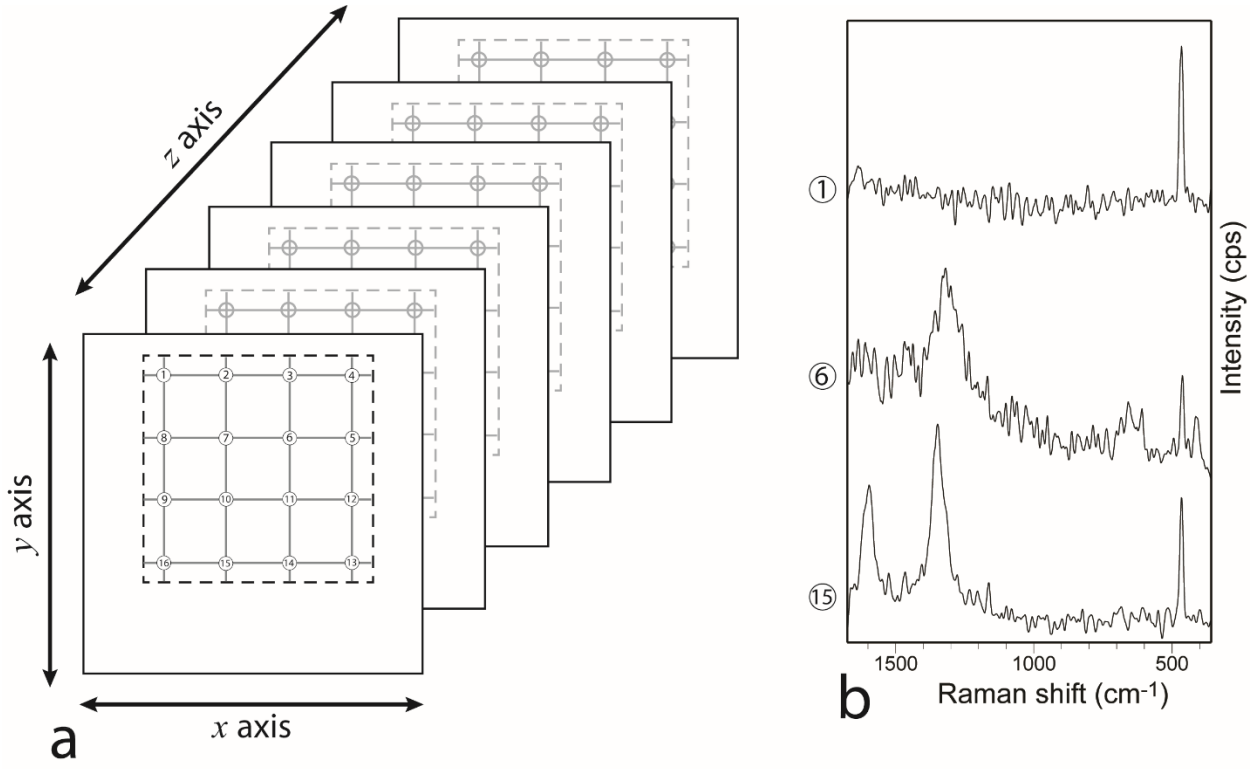

Figure 1. Schematic diagram of a Raman hyperspectral dataset. The dashed boxes represent the two-dimensional (*x*, *y* axes) region where the hyperspectral dataset was acquired at multiple focal planes at depth (*z* axis) within a sample (a). Raman hyperspectral datasets are composed of multiple spectra that are acquired based on an operator defined spatial resolution schematically represented in this figure by the numbered circles (a) which correspond to individual spectra from the dataset. Adapted from Lee, 2012.

This limitation can result in significant variations in data quality because each spectrum in a hyperspectral dataset could display a different shape and intensity of baseline deviation due to autofluorescence due to the heterogeneous nature of geological samples (Lee 2012). Several geoscience studies have documented that elevated baselines due to autofluorescence can significantly affect subsequent analyses of point Raman spectra including deconvolution and band area calculations (Burchell *et al.* 2006, Quirico *et al.* 2005, Rotundi *et al.* 2008, Schroeder *et al.* 2003, Severs *et al.* 2007, Zajacz *et al.* 2005). Due to sample heterogeneities and the high efficiency of the autofluorescence process compared to Raman scattering, it may be impossible to find a laser excitation wavelength that will completely prevent sample autofluorescence especially during hyperspectral data acquisition (Dieing *et al.* 2010). Although researchers have noted the presence of elevated baselines in geological hyperspectral datasets caused by autofluorescence (Agangi *et al.* 2014, Ciobotă *et al.* 2013, Frosch *et al.* 2007, Heim *et al.* 2012, Kremer *et al.* 2012), few studies exist which address issues that may arise due to the software-based techniques used to create and display Raman hyperspectral images or to develop methods to identify the spatial distribution of spectra affected by autofluorescence.

Post-acquisition baseline correction is commonly used to address autofluorescence in both point-Raman spectra and hyperspectral datasets (Bellot-Gurlet *et al.* 2004, Bulmer *et al.* 1975, Frosch *et al.* 2007, Jehlička *et al.* 2009, Lünsdorf *et al.* 2014, Marshall and Marshall 2011, Neff *et al.* 2006, Schroeder *et al.* 2003, Severs *et al.* 2007, Sharma *et al.* 2003, Zajacz *et al.* 2005). A plethora of manual and mathematical methods have been developed to baseline correct Raman spectra, and several studies primarily in biomedical and pharmaceutical sciences have compared the strengths and weaknesses of these methods (Afseth *et al.* 2006, Bulmer *et al.* 1975, Heraud *et al.* 2006, Jirasek *et al.* 2004, Leger and Ryder 2006, Prakash and Wei 2011, Schulze *et*

al. 2005b, Zhang *et al.* 2010a, Zhang *et al.* 2010b). Many of these methods are time consuming, iterative processes which must be applied to individual spectra (Schulze *et al.* 2005b). Accordingly, software-based automated methods are necessary to baseline correct the multitude of spectra that comprise hyperspectral datasets (Schulze *et al.* 2005b, Vandenabeele 2013).The most common approaches include: polynomial fitting, wavelet transformations, frequency domain filtering and first-and-second order derivatives (Lieber and Mahadevan-Jansen 2003, Schulze *et al.* 2005b, Zhang *et al.* 2010b). Table-top and handheld Raman spectrometer vendors including Bruker, Renishaw, FischerScientific, WiTec, PerkinElmer, Rigaku Raman Technologies, OceanOptics, and CytoSpec provide online information on their software-based baseline correction algorithm, but these resources simply generalize their proprietary methods for polynomial fitting techniques (Dilor-Jorbin Yvon-Spex 1999, Lasch 2014, Ocean Optics, Inc 2013, Pirzer and Sawatzki 2006, Rigaku 2012, Smith 2012, ThermoScientific n.d.). This makes it difficult for operators to understand how each automatic baseline correction algorithm may affect Raman image interpretation. Moreover, the majority of commercially available software programs require the operator to select one polynomial order to apply to all spectra in a hyperspectral dataset. Previous studies have shown that the polynomial order used for baseline correction can influence spectral parameters such as band location, width, and intensity which subsequently affect univariate or multivariate analyses (Liland *et al.* 2010, Lünsdorf *et al.* 2014, Quirico *et al.* 2005, Zajacz *et al.* 2005). However, few studies have addressed potential errors that may be introduced by inappropriate automated polynomial baseline correction, or methods to compare the quality of baseline corrected datasets.

In this paper we highlight how autofluorescence may lead to misidentification of materials in hyperspectral datasets. Secondly, we show how inappropriate polynomial baseline

correction can introduce error. Finally, we provide a work-flow and a statistical test for evaluating the quality of automated polynomial-based baseline correction algorithms.

EXPERIMENTAL

Apex chert background

The samples utilized in this study originate from the Apex chert, an informal unit composed of stratiform and vertical dike chert units contained within the ~3.5 Ga Apex Basalt Formation. In the field, the stratiform and dike chert units within grey-green volcaniclastics, tuffs, komatiites, and basalts that show evidence of underwater eruption including pillow textures, chilled margins, and hyaloclastic breccias (Brasier *et al.* 2005). The barite and carbon-rich chert dikes and stratiform units are interpreted as backfilled feeder conduits formed in a phreatomagmatic hydrothermal system (Van Kranendonk , 2006; Brasier *et al.* 2005). This unit is geologically significant because it contains microstructures interpreted as some of the oldest microbial fossils on Earth (Schopf and Kudryavtsev 2009, Schopf *et al.* 2002, Schopf and Packer 1987). Studies have presented Raman hyperspectral images interpreted to show these microstructures as carbonaceous in composition (Schopf and Kudryavtsev 2009, Schopf and Kudryavtsev 2012, Schopf and Kudryavtsev 2014, Schopf *et al.* 2002). In contrast, a recent study utilizing hyperspectral imaging showed that microstructures identified in new samples from this unit are instead hematite-filled veins, not carbonaceous microfossils (Marshall *et al.* 2011). The

Apex chart, therefore, provides a test-case for understanding the strengths and weaknesses of Raman hyperspectral imaging as several studies have utilized the technique to support two vastly different interpretations of the origin and composition of the microstructures.

Samples

Samples from the Apex chart dike were collected from 14 localities every 10 m along the outcrop including the original microfossil locality (Marshall *et al.* 2014, Marshall *et al.* 2011, Marshall and Olcott Marshall 2013). Thin section blanks were cut using a water-cooled diamond saw. Eighty-two thin sections including single and doubly polished serial 30 µm standard petrographic thin sections and 300 µm paleontological thin sections were made from the blanks by Burnham Petrographics, Rathdrum, ID.

Raman Spectroscopy

Raman spectroscopic analyses were performed using a Renishaw Reflex Raman microprobe with an attached trinocular Leica DMLM microscope equipped with a video camera and four objectives (100/0.9 NA, 50/0.75NA, 20/0.40NA, 5/0.12NA). An argon-ion laser (Modu-Laser) emitting at 514.5 nm was used to excite the samples, a 2400/mm grating was used and spectra were analyzed at room temperature with a Peltier cooled, charge coupled device (CCD) camera (1024x256 pixels). The Raman system was calibrated by analyzing the position of the F_{1g} silicon mode. An offset correction was performed based on the position of the detected silicon band at 520.50 ± 0.10 cm^{-1}

Raman imaging datasets were collected using the Renishaw StreamLine™ mode with an accumulation time of 0.1 sec. In StreamLine ™ mode a center value is chosen that defines the spectral range based on the instrumental parameters, in this case providing a range of ~1330 cm^{-1} from 360-1690 cm^{-1}. This range was chosen to include as many intense, diagnostic Raman bands for all the materials present as possible. Two-dimensional datasets were collected over the same *x, y* region every 0.2 μm in depth from 0.2-4.6 μm utilizing an automatic cosmic ray removal feature. Statistical calculations used to compare the quality of polynomial baseline correction trials were performed using Minitab™.

Baseline correction rationale and software settings

A Raman spectrum (x) can be thought of as the sum of three major components: the Raman signal (s), the baseline (b) and noise (n) (Cadusch *et al.* 2013).

$$x = s + b + n \quad (1)$$

The goal of baseline correction is to estimate b and subtract it from the equation leaving only the Raman signal (s) and noise (n). An ideal baseline correction will flatten an elevated baseline and place it at the zero axis which can be evaluated by looking at the corrected spectrum. Software-based polynomial baseline functions typically utilize a form of Partial Least Squares (PLS) regression to model the shape of the baseline based on a polynomial equation of the order chosen by the operator (Cadusch *et al.* 2013, Schulze *et al.* 2005a).The WiRE 3.4 baseline correction function offers several features to control the way the software calculates the polynomial.

A function called “no automatic subtraction” uses a single spectrum chosen by the operator to calculate a polynomial that is then applied to each spectrum in the dataset. The natural variation in geological samples can cause spatial variations in fluorescence, therefore the application of a single correction to every spectra is not appropriate. The Wire 3.4 software provides two techniques that will calculate a unique polynomial to model the baseline based on the intensity and shape of each individual spectrum in a dataset. The operator chooses specific points (Raman shift value) along the spectrum to be used in the polynomial calculation or defines specific regions that are either included or excluded from the calculation (“include” or “mask” regions). This technique is dependent on an operator’s experience analyzing Raman spectroscopic data as a basis for ascertaining the “best” numbers and locations for assessment. Unsurprisingly, this technique introduces a significant amount of subjectivity and uncertainty into the baseline correction. Further, this technique limits the proportion of data utilized in the calculation to the number of points chosen by the operator. The “include” or “mask” region function allows the operator to target particular regions (e.g. excluding areas where Raman bands occur in a spectrum or focusing only on regions that are most affected by fluorescence and provides more data points for the polynomial calculation. This method is still somewhat subjective as the regions of interest are still operator defined. Therefore, the rationale for including or excluding regions should be carefully considered.

Fluorescence bands comprising the background are much broader than the Raman bands. A potential drawback of polynomial baseline correction is that the use of higher order polynomials may result in a correction that fits portions of the Raman bands instead of only the broadly sloping background, therefore it has been suggested that lower-order polynomials may be a better choice (Lewis and Edwards 2001). The Raman baseline correction literature contains

a wealth of studies focused on comparing various methods and optimizing computer- based polynomial correction algorithms to model appropriate polynomial functions restricted to the shape of the baseline signal (Afseth *et al.* 2006, Baek *et al.* 2011, Cadusch *et al.* 2013, Leger and Ryder 2006, Liland *et al.* 2010, Schulze *et al.* 2005b, Zhang *et al.* 2010b). The issue of the introduction of errors through fitting higher order polynomials is well known and typically addressed using band removal or "peak-stripping" methods that remove the Raman bands before modelling the baseline (Beier and Berger 2009, Cadusch *et al.* 2013, Schulze *et al.* 2005b, Zhao *et al.* 2007). Although Raman software programs provide a variety of mathematical functions for analyzing hyperspectral datasets, a simpler and more time-efficient method to ensure that Raman bands are not included in polynomial calculations is to exclude spectral regions where Raman bands occur for minerals or mineraloids of interest. The most common materials comprising the Apex chert are quartz, hematite and carbonaceous material. Previous studies have identified other less common materials in the Apex chert (Brasier *et al*., 2005; Pinti *et a.l*, 2009, Sforna *et al.*, 2014). Image dataset analyses and inspection of multiple spectra elucidated that the regions imaged in this study were dominantely composed of quartz, hematite and carbonaceous material. Other minerals were rarely, if ever observed, in the image dataset regions. Within the collection range of 360-1690 cm^{-1} used in this study, quartz contains an intense Raman band centered at 464 cm^{-1} (A_{1g} mode) and two less intense modes at 394 cm^{-1} (E mode) and 355 cm^{-1} (A_1 mode) (Gillet *et al.* 1990, Kingma and Hemley 1994), hematite contains two bands at 411 and 612 cm^{-1} (E_g modes) (Faria *et al.* 1997) and an intense, broad band at 1320 cm^{-1} assigned to a second order LO mode ($2E_u$ symmetry) due to the presence of hematite lattice defects (Frosch *et al.* 2007, Marshall and Marshall 2011, Shim and Duffy 2002) and disordered carbonaceous material contains two bands at ~1350 and 1600 cm^{-1}(Lespade *et al.* 1982, Tuinstra and Koenig 1970).

Quartz contains two E symmetry bands at 1070 and 1160 cm^{-1} within the collection region, but these bands were rarely visible due to the signal to noise ratio. Mask regions were based on the most intense, dominant bands easily distinguishable in image dataset spectra.

Ten representative spectra from each phase (hematite, quartz and the quartz /carbonaceous material mixture in the matrix) from the dataset were visually assessed to estimate the relative widths of the bands to determine regions to be excluded from the polynomial calculations, and two scenarios were tested: Trial 1: a conservative choice of mask regions that excluded only the most intense bands visible above the S:N ratio in the dataset and, Trial 2: a liberal set of mask regions that excluded the regions covering the location of all Raman bands present in the materials of interest (Table 1).

Trial 1. Conservative Mask Regions	Trial 2. Liberal Mask Regions
400-500 cm^{-1} (hematite and quartz)	360-620 cm^{-1} quartz and hematite
590-620 cm^{-1} (hematite)	1200-1400 cm^{-1} hematite and carbonaceous material
1260-1420 cm^{-1} (hematite and carbonaceous material)	1520-1690 cm^{-1} carbonaceous material
1540-1690 cm^{-1} (carbonaceous material)	

Table 1: Spectral regions containing Raman bands for the materials of interest that were excluded from the two baseline correction trials. Linear and fifth-order polynomials were used to create baseline corrected datasets for both mask region trials.

Fourth-to-sixth order polynomials are commonly used to baseline correct Raman spectra, with fifth-order polynomials being the most popular based on empirical evidence from primarily biomedical studies (Edwards *et al.* 1995, Mahadevan-Jansen and Richards-Kortum 1996, Shim and Wilson 1997, Zhao *et al.* 2007). Google Scholar and Web of Science searches of baseline correction techniques applied to Raman spectra in the Geoscience literature showed that many

studies either did not state the method used or simply stated that a polynomial-based method was utilized (Bellot-Gurlet *et al.* 2004, Bridges *et al.* 2010, Burchell *et al.* 2006, Igisu *et al.* 2014, Jehlička *et al.* 2009, Neff *et al.* 2006, Schroeder *et al.* 2003, Sharma *et al.* 2003). Studies that provided information on the polynomial order used for baseline correction included linear, second order, fourth order, and fifth order polynomials, with linear baseline correction being the most common.(Marshall and Olcott Marshall 2013, Quirico *et al.* 2005, Rotundi *et al.* 2008, Severs *et al.* 2007, Smith and Godard 2009, Zajacz *et al.* 2005, Zinin *et al.* 2011). Because fifth-order polynomials baseline correction has been widely used on hyperspectral datasets *a priori* and linear models were the most common in geological studies, a hyperspectral dataset from the Apex chert was baseline corrected using linear and fifth-order polynomials with two different mask region scenarios (Table 1).

RESULTS AND DISCUSSION

Misidentification of materials in hyperspectral images due to autofluorescence

In hyperspectral datasets from 22 microstructures in samples from the Apex chert, high sloping baselines resulting from autofluorescence were observed in multiple spectra in every dataset. In some cases, the autofluorescence signal completely overwhelmed the Raman signal preventing acquisition of meaningful data. Although several univariate and multivariate methods are available the most common method is to plot the intensity at a point representing the location of a diagnostic Raman band (McCreery 2005). Previous studies have noted that this method can be problematic if materials contain Raman bands in similar locations, for example the hematite 1320 cm^{-1} band and the "D" band in carbonaceous material (Marshall *et al.* 2011, Marshall and Marshall 2011, Marshall and Olcott Marshall 2013). As a result it has been suggested that

intensity images representing the “G” band at 1600 cm^{-1}should be used to identify carbonaceous material. (Marshall and Marshall 2011).

Surprisingly, intensity images representing hematite (1320 cm^{-1}) and carbon (1600 cm^{-1}) from an example of segmented appearing microvein look nearly identical (Fig.2) (Location of Figure 2).

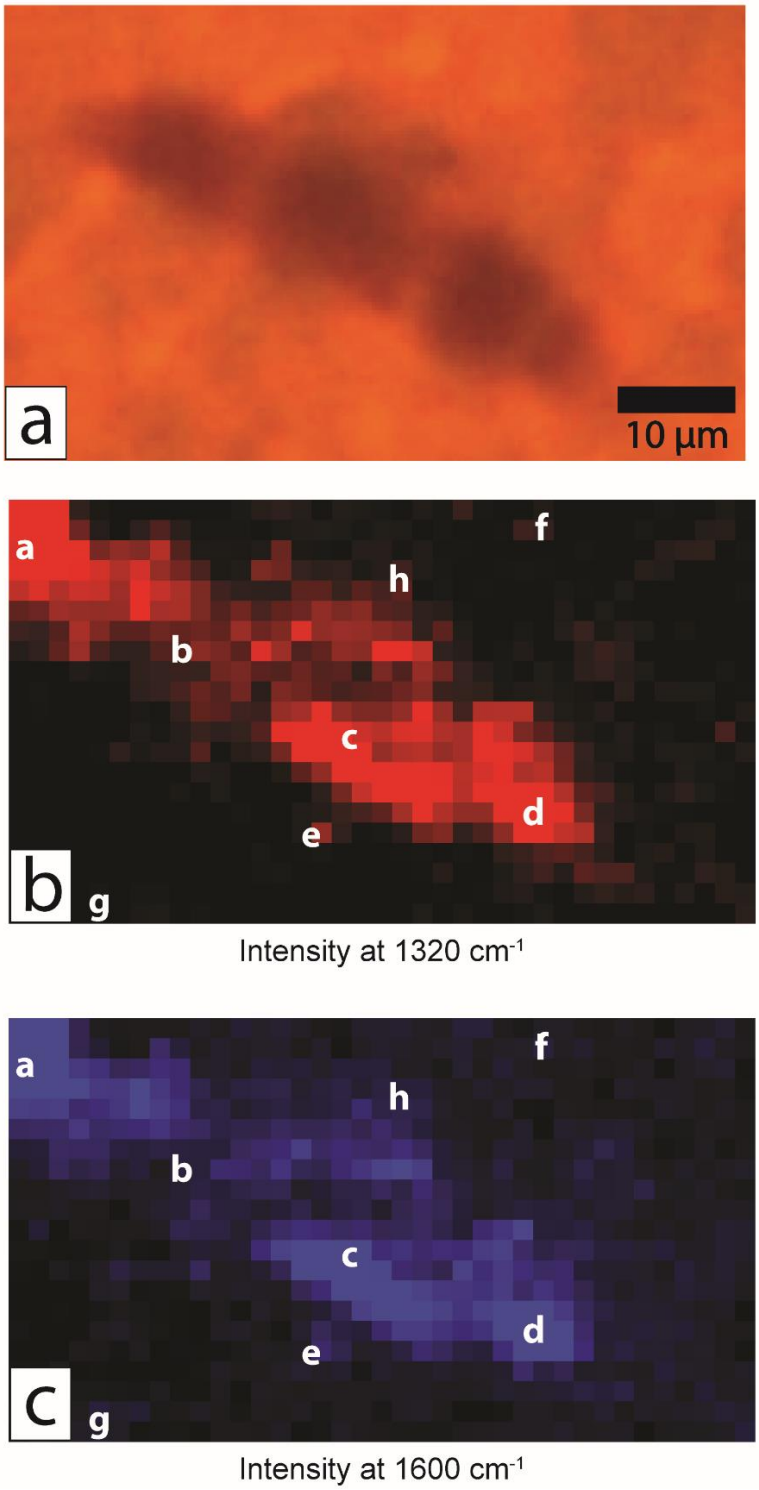

Figure 2. Photomicrograph of a segmented appearing microvein from the Apex chert (a). Intensity images representing hematite at 1320 cm^{-1} (b) and CM at 1600 cm^{-1}(c). The intensity images appear very similar making it difficult to identify the material present in the microvein. The white letters indicate the locations of the representative spectra shown in Figure 3.

Initially it appeared that the microvein was composed of carbonaceous material, and that the hematite image recreated the microstructure as a result of the co-location of the hematite 1320 cm^{-1} band and the carbonaceous material "D" band at 1350 cm^{-1}. However, inspection of multiple representative spectra from the dataset illustrated an entirely different phenomenon. Despite the signal to noise ratio, representative spectra inside the microvein indicated that the microvein was filled with hematite (Fig. 3 a-d), and the surrounding quartz matrix contained carbonaceous material. (Fig. 3 e-h).

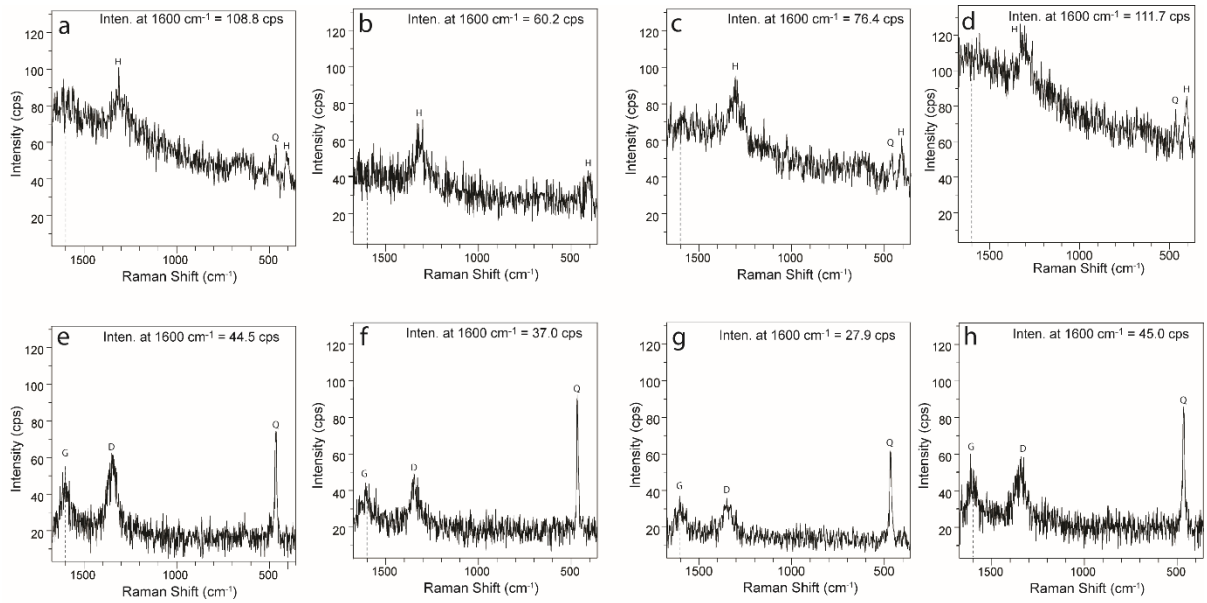

Figure 3. Representative spectra (a-d) from points within the microvein (Fig 2) show the presence of hematite identified by the 1320 cm^{-1} and 411 cm^{-1} Raman bands indicated by "H". Quartz may also be present in these spectra based on the presence of the 464 cm^{-1} Raman band indicated by "Q". Representative spectra from points within the matrix (e-h) show the presence of CM based on the occurrence of the 1350 cm^{-1} D band and 1600 cm^{-1} G band (denoted as "D" and "G") and quartz based on the presence of the 464 band ("Q"). The representative spectra are plotted at the same scale. Note the high sloping baselines present in the spectra that contain hematite (a-d) (minimum = 60.2 cps, maximum = 111.7 cps, average = 89.3 cps) compared to the quartz and CM material spectra (e-h) (minimum = 27.9 cps, maximum = 45.0 cps, average = 38.6 cps). High baselines due to autofluorescence in the hematite spectra (a-d) result in a false-positive identification of CM in the intensity image at 1600 cm^{-1}. (Fig. 2 c).

Note the relatively high intensity values at 1600 cm^{-1} in the hematite spectra (average value is 89.3 cps) compared to the values where carbonaceous material can be identified based on the

presence of the "D" and "G" bands (average value is 38.6 cps) (Fig. 3). The high sloping autofluorescence baselines resulted in relatively high intensity values in the hematite spectra producing bright areas in the carbonaceous material image at 1600 cm^{-1}, even though the "G" band is not present in the spectra. As a result, high baselines resulting from autofluorescence of the hematite resulted in a false-positive identification of carbonaceous material in the 1600 cm^{-1} intensity image. Such false-positive identifications due to autofluorescence are not restricted to carbonaceous material, it is a function of using univariate intensity at a point analysis to create images. Geological samples are composed of minerals and mineraloids which autofluorescence differently depending on composition, crystallographic structure, and the laser wavelength used to excite the sample. If a high fluorescence baseline is present in hyperspectral datasets, any material could be misidentified based strictly on visual inspection of point intensity images.

Identifying autofluorescence in hyperspectral datasets

While identifying the presence of elevated autofluorescence baselines in point spectra is relatively simple, it is impractical to visually assess every spectrum in a hyperspectral dataset. Therefore, it is necessary to develop methods utilizing software based techniques to identify regions that may be most affected by autofluorescence in hyperspectral datasets. Intensity images representing hematite (1320 cm^{-1}) and carbonaceous material (1600 cm^{-1}) from a hyperspectral dataset collected from another microvein are shown in Figure 4 (a,b). A representative spectrum from within the microvein (Fig 4. c) shows the presence of hematite while a representative spectrum from the matrix identifies quartz and carbonaceous material (Fig. 4 d) (Location of Figure 4). Although the hematite image best recreates the general shape of the microvein, there

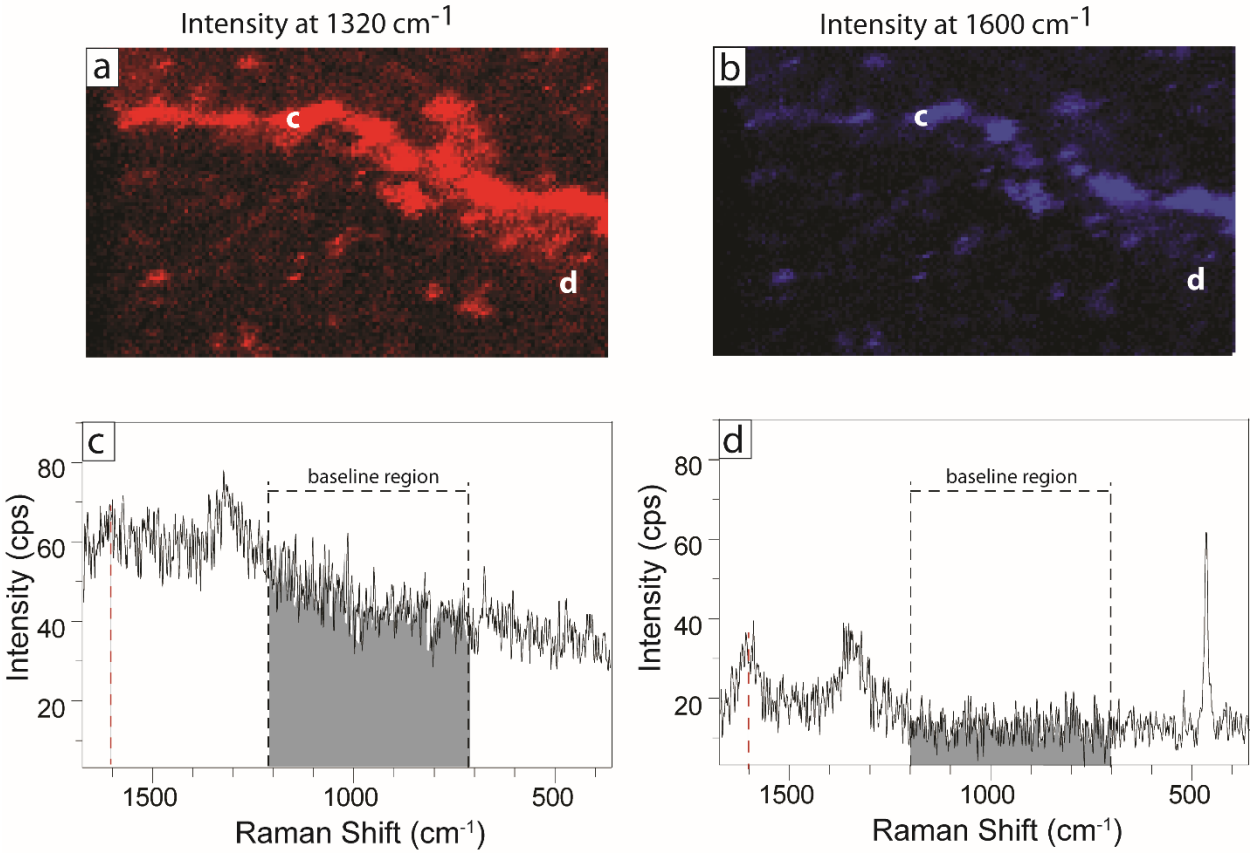

Figure 4. Intensity images representing hematite (1320 cm^{-1}) (a) and CM (1600 cm^{-1}) (b) from a second microvein. Representative hematite spectrum from a location within the microvein (c) and a quartz and CM spectrum from a location within the matrix (d). The locations of the spectra are shown by the white letters in the images. Note the sloping elevated baseline in the hematite spectrum (c). The grey regions in the spectra (c,d) represent the area under the spectra for a representative baseline region from 700-1200 cm^{-1} which was calculated for each spectrum in this HS dataset using a signal to axis function. The resulting signal to axis image (e) shows that the areas most affected by elevated baselines due to autofluorescence are associated with the hematite filled microvein. All images were made by setting the Look-up table (LUT) to display the central 90% of the data.

are ambiguous areas where both images display "positive" responses. Based on the intensity images alone, distinguishing between the presence of hematite or carbonaceous material at these locations would be difficult. High autofluorescence baselines in the hematite spectra result in bright regions in the carbonaceous material image in the same manner as in the previous microvein (Fig. 2 and 3)

Univariate “signal to axis” analysis over a representative baseline signal region can provide an image that identifies areas where the spectra are relatively more affected by an increased autofluorescence baseline The signal to axis function calculates the area under each spectrum for an operator-defined region, therefore spectra with sloping baselines will have relatively higher values than spectra with flat baselines (Fig. 4, c,d).

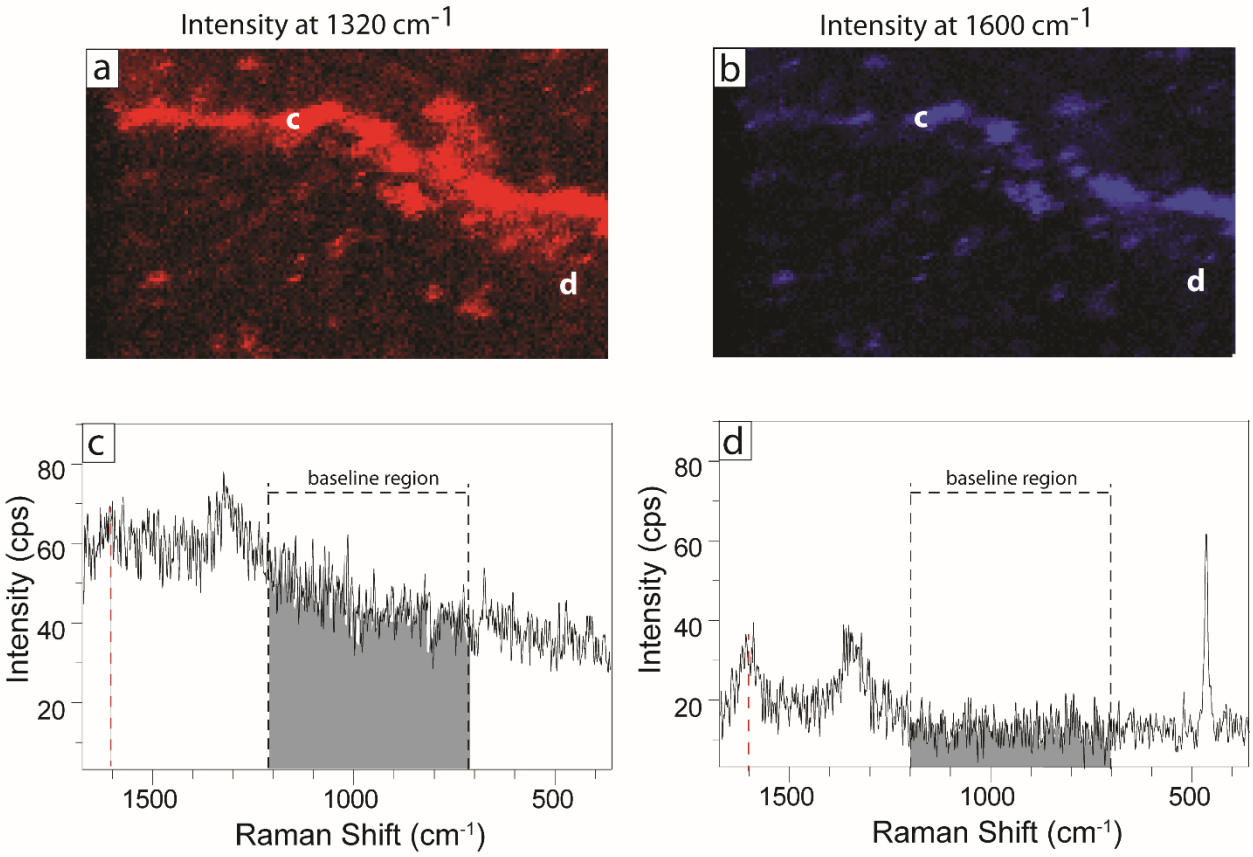

Figure 4. Intensity images representing hematite (1320 cm^{-1}) (a) and CM (1600 cm^{-1}) (b) from a second microvein. Representative hematite spectrum from a location within the microvein (c) and a quartz and CM spectrum from a location within the matrix (d). The locations of the spectra are shown by the white letters in the images. Note the sloping elevated baseline in the hematite spectrum (c). The grey regions in the spectra (c,d) represent the area under the spectra for a representative baseline region from 700-1200 cm^{-1} which was calculated for each spectrum in this HS dataset using a signal to axis function. The resulting signal to axis image (e) shows that the areas most affected by elevated baselines due to autofluorescence are associated with the hematite filled microvein. All images were made by setting the Look-up table (LUT) to display the central 90% of the data.

The signal to axis image in Figure 5 was created from a representative baseline region ranging from 700-1200 cm^{-1}. Interestingly, the resulting image also recreates the shape of the hematite-filled microvein (Marshall *et al.* 2011). Apparently, the hematite in the microveins autoflouoresces significantly more than the matrix quartz and carbonaceous material under the acquisition parameters used in this study.

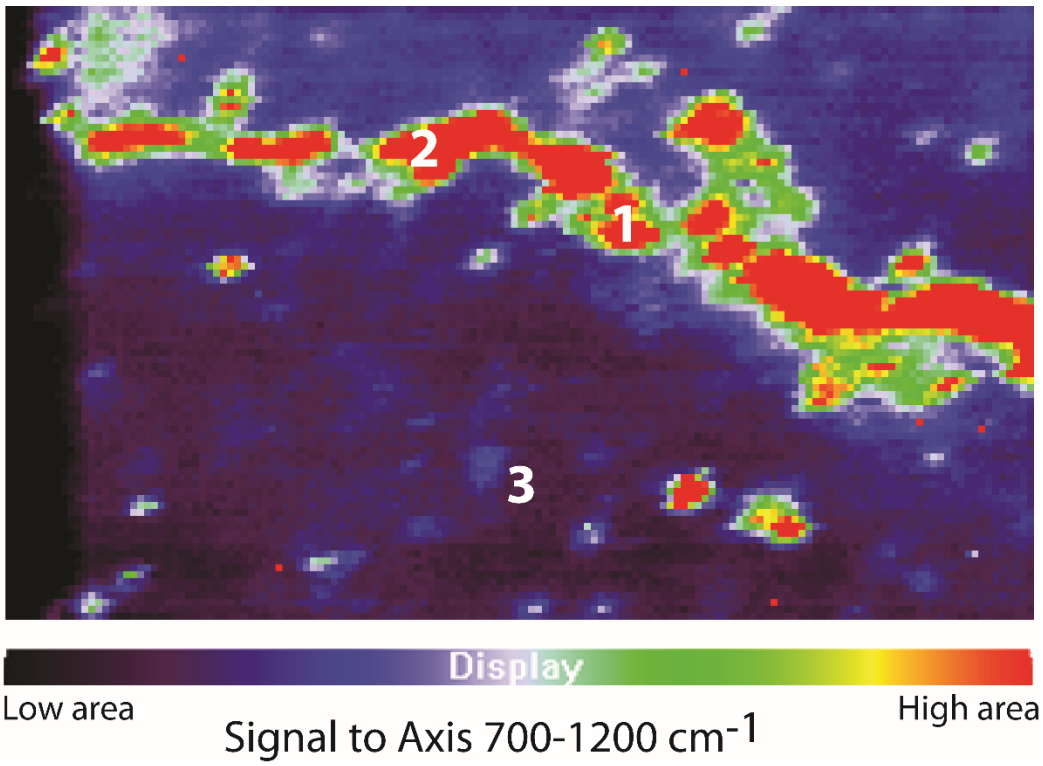

Figure 5. Signal to axis image over a representative baseline region from 700-1200 cm^{-1} calculated from the Apex chert microvein shown in Figure 4. The white letters indicate the locations of the representative spectra shown in Figure 7. Note that the relatively higher area values shown in red recreate the shape of the microvein.

Geoscientists typically have a general idea of the dominant composition of a sample. This knowledge permits the determination of an appropriate baseline region for signal to axis calculations on hyperspectral datasets. If the composition is unknown, petrographic techniques and/or point-Raman spectroscopy could be performed to identify the primary minerals and mineraloids present in the sample. Definition of an appropriate baseline-only region may be

impossible where heterogeneity in geological samples is particularly high (e.g. a sample with multiple minerals displaying more complex Raman spectra with overlapping bands,). In this case, a signal to axis image over the entire spectral region may serve as a proxy to identify autofluorescence. This method should be approached with caution, however, as differences in relative intensity and the incidence of multiple Raman bands will increase the total area to some extent as well (Figure S1). Because of this global response, multiple spectra from regions with high area values should be visually assessed to differentiate relative intensity issues or multiple or overlapping Raman bands from elevated autofluorescence baselines. When autofluorescence issues are identified, post-processing baseline correction will be necessary if intensity at a point analyses are used to create Raman images in order to avoid potential misidentification of materials.

Comparisons of polynomial baseline correction techniques

Visual comparison of intensity images created from the original data and linear and fifth-order corrected datasets from Trial 1 shows that the linear correction (Fig. 6, c,d) resulted in higher contrast images that spatially distinguish the presence of hematite (intensity at 1320 cm^{-1}) and carbonaceous material (intensity at 1600 cm^{-1}) compared to those created from the fifth-order polynomial correction (Fig. 6 e,f).

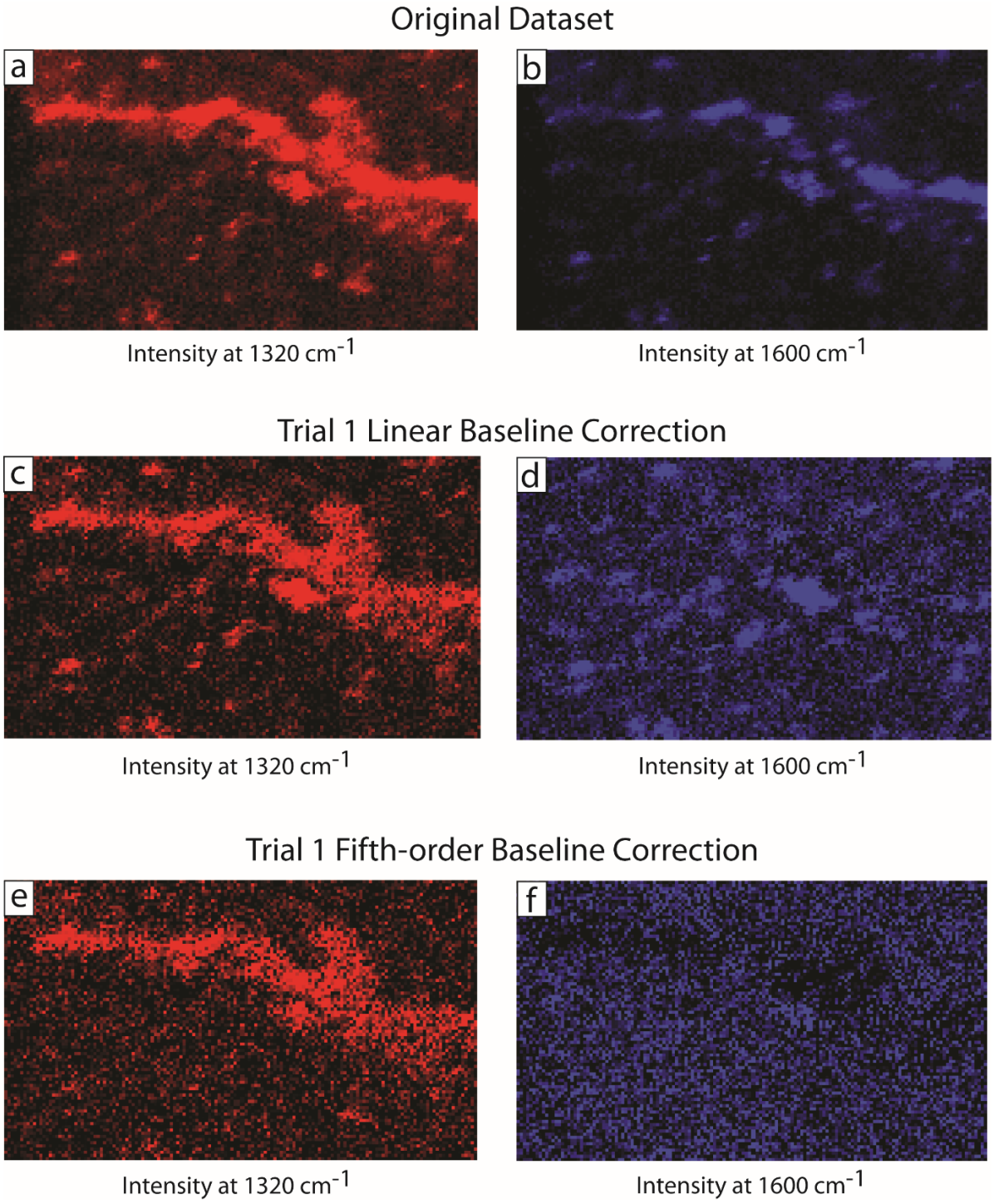

Figure 6. Intensity images representing hematite (1320 cm^{-1}) and CM (1600 cm^{-1}) for the original dataset (a,b) the linear baseline corrected dataset (c,d) and the fifth-order corrected dataset from baseline correction Trial 1. The linear correction resulted in images that spatially distinguish the presence of hematite in the microvein and CM concentrated in clusters within the matrix (c,d). The images from the fifth-order baseline correction are significantly lower in resolution making it more difficult to identify the distribution of the materials in the sample, especially the distribution of CM material based on image f. All images were made by setting the LUT to display the central 90% of the data.

Representative spectra from the linear and fifth-order corrected datasets illustrate the effects that the two different corrections had on the dataset (Fig. 7).

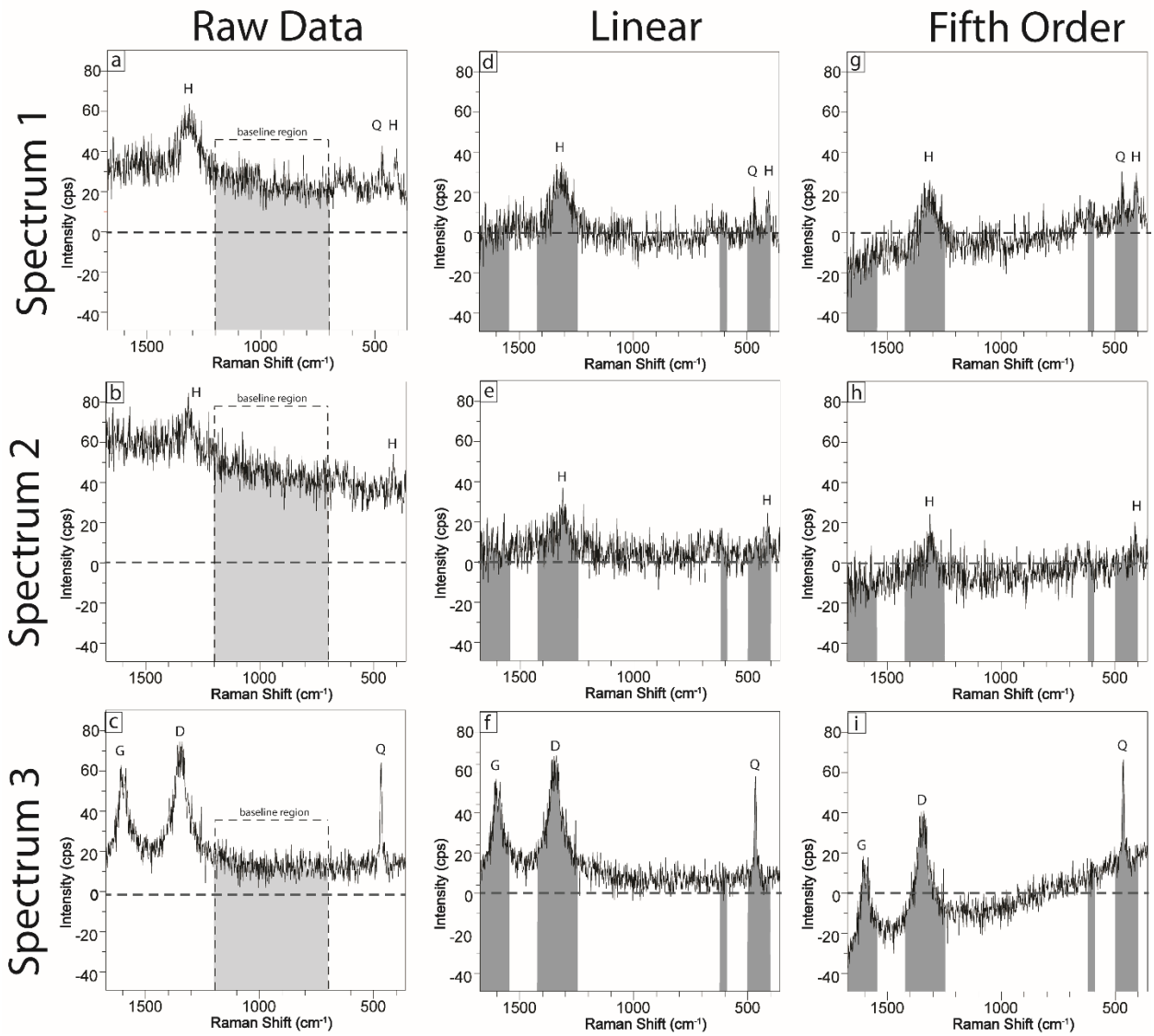

Figure 7. Representative spectra from the original dataset (a-c), the linear baseline corrected dataset (d-f) and the fifth-order corrected dataset (g-i) from baseline correction Trial 1. The representative baseline region is marked on the original spectra (a-c) and the mask regions are colored grey in the baseline corrected spectra (d-i). The locations of the spectra are shown by the numbers on the signal to axis image in Figure 6. The linear correction effectively flattened the baseline in two spectra (d,e) that had elevated baselines (a,b) and did introduce error into a spectrum that had an initially flat baseline (compare f and g). The fifth-order polynomial overcorrected the data resulting in negatively sloping baselines in all three spectra (g-i).

Representative raw data spectra from two locations display sloping baselines due to autofluorescence (Fig. 7 a,b). The linear correction effectively flattens the baseline of both spectra (Fig. 7 d,e). The fifth-order polynomial overcorrected the spectra resulting in a negatively sloping baseline causing a majority of the baseline region values and some of the values in the hematite 1320 cm^{-1} region to be negative (Fig.7, g,h). The raw data spectrum in Figure 7 (c) has a slightly elevated, but flat baseline and the linear correction moves the baseline closer to zero without introducing subsequent error (Fig. 7 f). Conversely, the fifth-order correction resulted in a negative slope that caused part of the baseline region, of the points in the "D" band region, and the majority of the points in the "G" band region to be negative (Fig. 7 i). In this case, the fifth-order polynomial correction introduced error into some spectra that decreased the intensity values resulting in lower resolution images that making identification of material distribution difficult.

The Trial 2 liberal mask regions used to baseline correct with linear and fifth-order polynomials created intensity images that appear surprisingly similar (Fig. 8). Inspection of representative spectra (Fig. 9 d-f) elucidates that the fifth-order polynomial again introduced error into some spectra. The spectrum at location 1 was baseline corrected relatively well by both the linear and fifth-order polynomial (Fig. 9 a, d). Conversely, the spectrum from location 2 shows that the fifth order polynomial overcorrected the spectrum in the low Raman shift region resulting in negative values and slightly elevated values in the high Raman shift region (Fig. 9 e). In location 3, however, the-fifth order correction introduced error into the spectrum elevating the intensity values in the low Raman shift region (Fig. 9 f). The low Raman shift mask region for this trial was from 400-500 cm^{-1} and the intensity values from 360-400 cm^{-1} were included in the polynomial calculation. Under the original Trial 1 parameters, all of the high Raman shift values

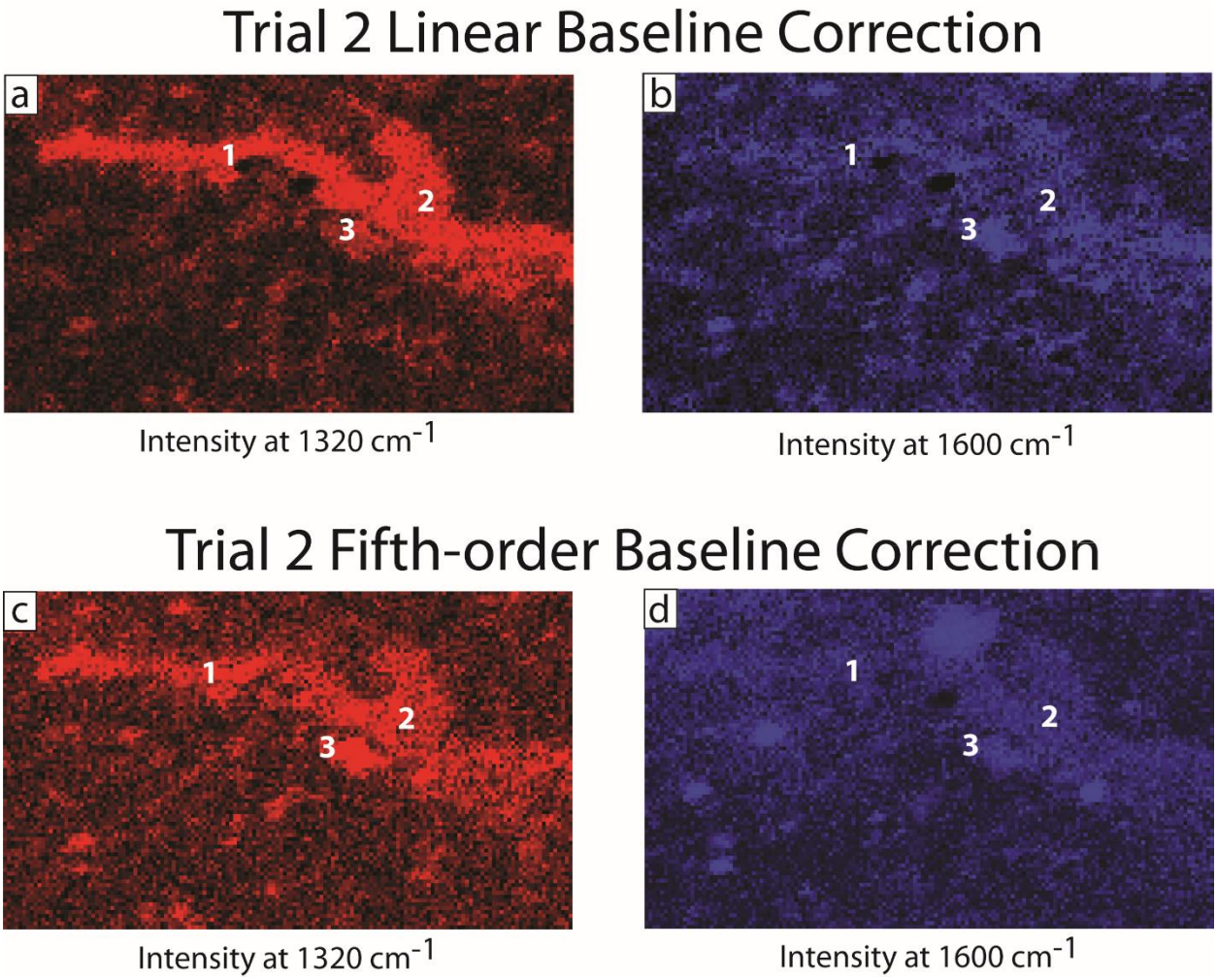

Figure 8. Intensity images representing hematite (1320 cm^{-1}) and carbonaceous material (1600 cm^{-1}) from the Trial 1 linear and fifth-order polynomial corrections. Note that the intensity images appear very similar in resolution. All images were made by setting the LUT to display the central 90% of the data values.

were masked, therefore excluded from the calculation (Table 1). A modified Trial 1 correction was performed by setting the mask region to include 40 cm^{-1} values similar to the low Raman shift mask settings in order to test the hypothesis that the fifth order polynomial overcorrection in the high Raman shift region may be due to a lack of data points. The modified Trial 1 correction commonly performed better in the low Raman shift region but still overcorrected and in some cases lowered values in the high Raman shift region (Figure S2).Although regions containing

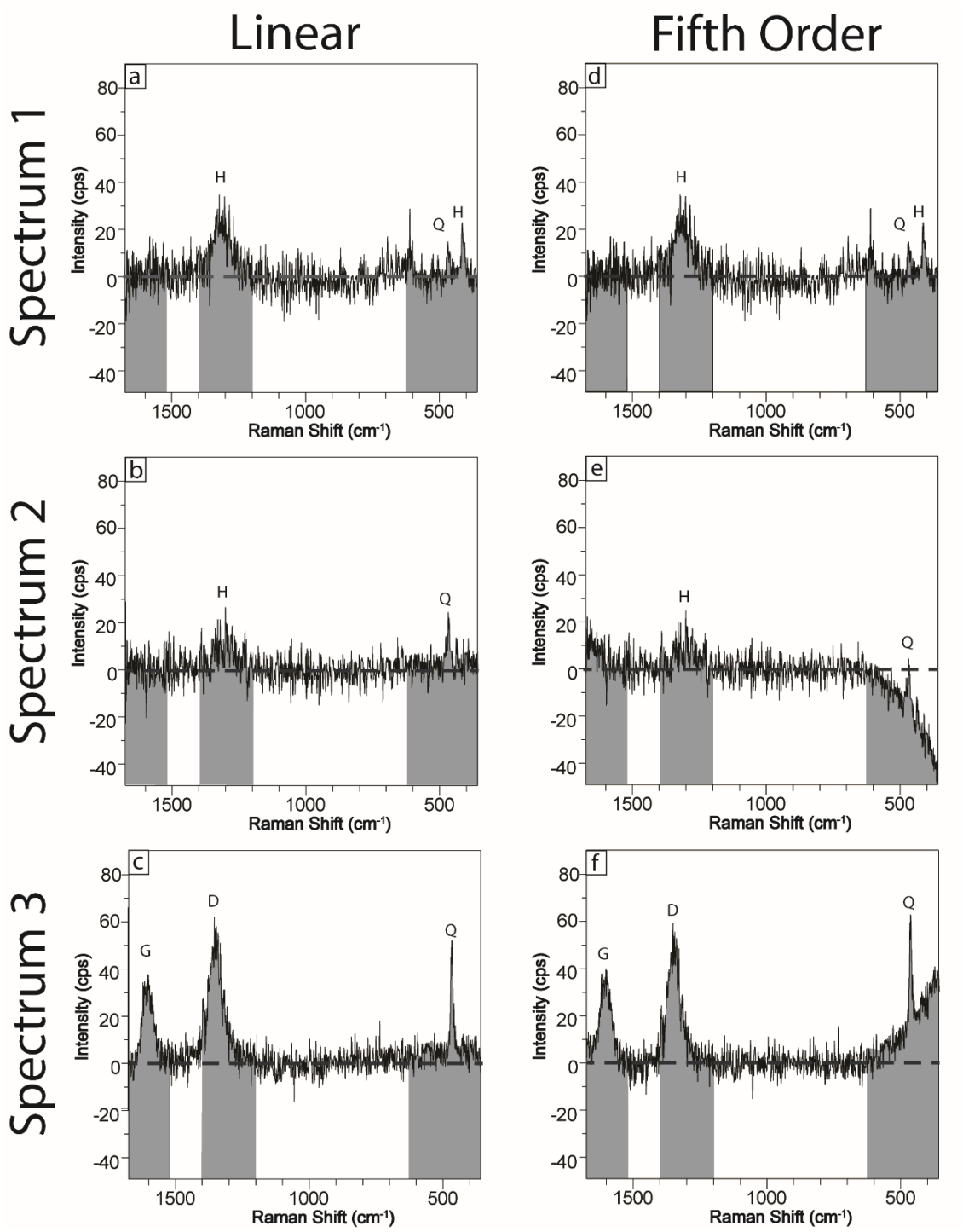

Figure 9. Representative spectra from the linear baseline corrected dataset (a-c) and the fifth-order corrected dataset (d-f) from baseline correction Trial 2. The locations of the spectra are shown by the numbers on the intensity images shown in Figure 8. The linear correction effectively corrected all three spectra without introducing subsequent error (a-c). The fifth-order polynomial correction effectively corrected spectrum 1 (d) but introduced error in spectrum 2 (e) resulting in a negative slope in the low Raman shift region and slight positive slope in the high Raman shift region. The fifth-order correction also introduced error into spectrum 3 resulting in a positive slope in the low Raman shift region (f).

Raman bands were excluded from the polynomial calculations, Figures 5, 7-9 and S2 illustrate that using higher order polynomials to baseline correct hyperspectral datasets can still introduce error into a hyperspectral dataset.

The WiRE 3.4 baseline correction function utilizes a (PLS) based regression calculation to produce a polynomial function that best models the shape of the baseline. Regression analyses are commonly used to model the relationship between *x* and *y* variables in order to produce a function for predicting a response (*y*) based on a predictor variable (*x*) (Sokal and Rohlf 1995). In this case regression analyses are not used to create an equation that best predicts an intensity value based on a specific Raman shift value, but to create a mathematical function that describes the overall shape of the Raman shift values and their corresponding intensities. PLS regression techniques were primarily developed to address issues of collinearity or non-independence between response and predictor variables (Dijkstra 2010). For example, in a Raman spectrum the intensity values and, therefore, the presence of Raman bands is a linear function of the Raman shift values based on the physics of Raman scattering and the molecular composition and structure of the material. (Vickers *et al.* 2001). Spectroscopic data are by definition collinear (Workman and Springsteen 1998). Therefore, a variety of PLS based regression modelling techniques have been used on many different types of spectroscopic data for various applications particularly chemometric analyses (Mark and Workman 2007, Salzer and Siesler 2009).

During predictive regression analysis the addition of terms that increase the polynomial order are based on measurable real-world variables. When regression analyses are used to model the shape of a Raman spectrum baseline, powers of the Raman shift values are used in in the

equation to define inflection points to model a curved line (Vickers *et al.* 2001). An implicit assumption in PLS regression used to model a baseline polynomial is that all the variability in the *y*-values (intensity) is due to a single factor, an elevated autofluorescence baseline. This is why the regions that contained Raman bands were excluded from the baseline correction calculations, but it is important to remember that the variability in the intensity values within the baseline region is a combination of the baseline signal and noise (Eq. 1). Noise in Raman spectra manifests as intensity values that oscillate around average background and Raman band intensity values. There are a variety of types of noise that can be present in Raman spectra: photon shot noise, sample-generated noise due to sample heterogeneity or effects like as black body radiation or luminescence, instrument-generated noise such as detector thermal or fixed pattern noise or calibration drift, computational noise due to computerized signal processing, and even externally-generated noise (Pelletier 2003). All of these factors can affect the signal to noise ratio (S:N) for each individual spectrum in a hyperspectral dataset. Standard regression analyses calculate the coefficients that describe linear or polynomial functions based primarily on minimizing the variance between the x and y values to determine the best fit model (Sokal and Rohlf 1995). PLS regression calculates the coefficients of a linear or polynomial function in a similar manner, but it also minimizes the residual values which is the difference between the model and the original values. Because PLS regression is sensitive to the number of data points and small variations in the data values higher order polynomial functions may also over fit the data. Over fitting is a well-know and problematic issue in correlation and regression analyses and involves using a model that is more complex or flexible than necessary (Hawkins 2004). In this case, higher order polynomials used in PLS regression baseline modelling may attempt to account for the higher frequency noise along with the general signal of the baseline. They can

also be more sensitive to rounding errors than lower-order polynomials during computerized regression calculations (James 2000). Error can also be introduced by the use of higher order polynomials in PLS regression because the number of points used to calculate the equation is higher than the order of the polynomial, the so-called Runge Phenomenon (Boyd and Xu 2009, Dahlquist and Bjorck 2003).

Software programs utilize different mathematical derivations of polynomial based-regression modelling in their automatic baseline correction algorithms and many researchers may be unfamiliar with the statistical underpinnings and potential errors that can arise from these algorithms. Further, because these algorithms are often based on proprietary information, it may be difficult to find information on the specific statistical algorithms used in order to fully understand the strengths and weaknesses of each specific technique. Finally, the "best" polynomial order for modelling the shape of the autofluorescence baseline present in each spectrum in a hyperspectral dataset may vary due to the spatial distribution of different materials. Software limitations requiring operators to choose a single polynomial order for an entire hyperspectral dataset result in a situation where subjectivity is unavoidable. Therefore, automated baseline correction of hyperspectral datasets should not be thought of as a simple, one-shot preprocessing step prior to univariate or multivariate analyses to create Raman images. Instead, it will likely be necessary to test several polynomial orders on a single hyperspectral dataset and inspect many representative spectra to identify potential errors that may be introduced by baseline correction in order to choose an appropriate polynomial correction.

What is a researcher to do if two different baseline corrections appear to be adequate? Many studies have used a variety of statistical methods to compare the effects various baseline correction methods have on Raman spectra. These studies, however, are often based on synthetic spectra and/or direct comparisons between individual baseline corrected spectra (Afseth *et al.* 2006, Liland *et al.* 2010, Schulze *et al.* 2005b, Vickers *et al.* 2001) and are impractical for evaluating the multitude of spectra in a hyperspectral dataset. Techniques utilizing the same software based analyses used in creating hyperspectral images need to be developed to evaluate the quality of baseline corrections on hyperspectral datasets. Two main factors should be considered when evaluating the quality of a baseline correction performed on a hyperspectral dataset. First, the correction should flatten the baseline in spectra that contained a sloping baseline while avoiding the introduction of error into spectra which originally had flat baselines. Secondly, an ideal baseline correction would place the baseline of every spectrum in a hyperspectral dataset at zero, but a perfect baseline correction for every spectrum is unlikely due to sample heterogeneity and factors including surface topography and instrument drift during collection. Thus, an "acceptable" baseline correction will place the baseline for each spectrum in a hyperspectral dataset at a vertical location (cps intensity value) as consistently as possible.

Both linear baseline correction trials tested in this study seem to have resulted in an "acceptable" baseline correction, resulting in visually similar intensity images created at 1320 cm^{-1} and 1600 cm^{-1} (Fig. 5 c,d and Fig. 8 a,b). Both trials effectively flattened the baseline in spectra with initially sloping baselines (Fig. 7d,e and Fig. 9 a,b) without introducing error into a spectrum with a flat baseline (Fig. 7 f and Fig. 9 c). Therefore, both baseline correction trials fulfill the first criterion stated above. But visual inspection of the intensity images alone does not provide information on the effects of the baseline corrections on every spectrum in the dataset.

While visual evaluation of every spectrum in a hyperspectral dataset is impossible, signal to axis analysis may be used to calculate datasets that can be statistically tested to compare two seemingly "acceptable" baseline corrections. The rationale for this technique is illustrated by two hypothetical "acceptable" baseline correction trials in Figure 10.

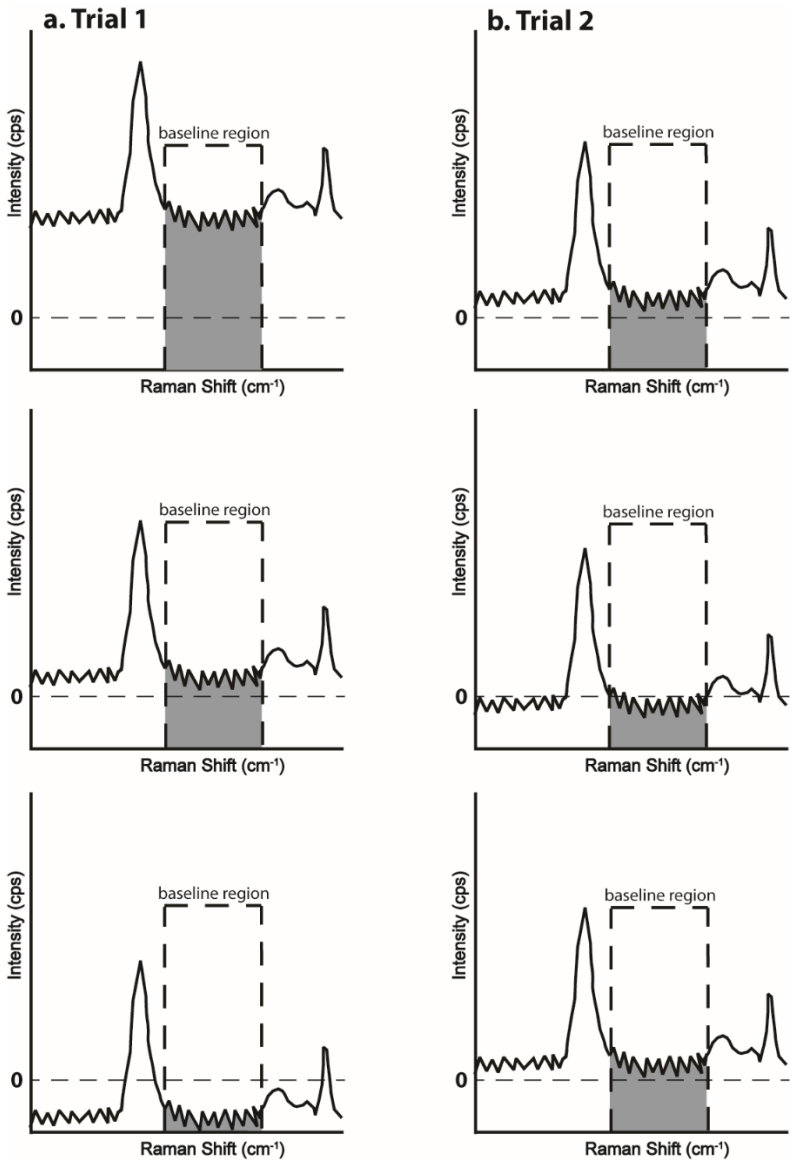

Figure 10. Three representative spectra from two hypothetical baseline correction trials. Both correction trials are "acceptable" because the spectra have flat baselines, but they differ in the relative vertical placement (y-axis intensity). The grey regions represent the area under the spectra for a representative baseline region that can be used in signal to axis calculations to compare the quality of the correction trials. Note that the signal to axis areas are more consistent among the Trial 2 spectra compared to those among the Trial 1 spectra. Datasets that results from signal to axis analyses can be subsequently statistically compared to determine the "best" baseline correction.

Both hypothetical baseline correction trials resulted in flat baselines in the Raman spectra fulfilling the first criterion, but the spectra in Trial 1 (Fig. 10, a) have baselines that are more variable in vertical placement compared to those in Trial 2 (Fig. 10, b). The grey areas represent baseline regions over which signal to axis calculations could be performed to create datasets which can be statistically compared to determine the "best" baseline correction.

In order to minimize the inclusion of possible correction errors that may have occurred in the spectral regions containing Raman bands, the representative baseline region from 700-1200 cm^{-1} was used to calculate the area under the each spectrum. This is illustrated schematically in Figure 10 for the two linear baseline correction trials based on different mask regions. The data were then exported as numerical files that consisting of the *x,y* locations and the calculated signal to axis area for each spectrum from the two baseline correction trials. An F-test was used to determine that the variation in the area values between the two datasets were significantly different ($p<0.000$). Trial 1 which utilized the more conservative mask regions also had a substantially lower standard deviation, i.e. variation in the areas calculated under the baseline region (Trial 1 $\sigma = 338.4$, Trial 2 $\sigma = 1619.4$). Ultimately, the goal is to minimize the differences in the relative vertical placement of the baseline in all the spectra in a dataset as shown in hypothetical Trial 2 (Figure 10 b). Following this line of thinking, Trial 1 provided the "best" baseline correction for the hyperspectral dataset. Two sample F-tests compare the variance of datasets regardless of the magnitude of the values, therefore this method can be applied to complex datasets where a representative baseline region cannot be defined by using signal to axis analysis over the full spectral region. Full spectral region area calculations provided the same result as the baseline region calculation (the two datasets were different, $p<0.000$, and Trial 1 had a substantially lower standard deviation: Trial 1 $\sigma = 848.7$, Trial 2 $\sigma = 8868.9$). It is worth noting

that the “best” baseline correction may not result in placement of the baseline at the zero axis for every spectrum in a hyperspectral dataset, but software-based normalization techniques may be utilized to correct for this discrepancy as necessary.

Comparison of the error introduced by the fifth-order polynomial corrections shed light on a potential cause for the difference in the quality of the linear corrections based on the use of different mask regions. The fifth-order correction from Trial 1 introduced error that resulted in sloping baselines over the whole spectral region (Fig 7.), whereas in Trial 2 the fifth-order correction introduced error primarily in the lower Raman shift region (Fig. 9). The more liberal mask regions used in Trial 2 excluded more points from the polynomial calculation in the lower Raman shift region, likely the causing the observed differences in the quality of the baseline corrections. The results from this study strongly indicate the need for careful selection of mask regions. Furthermore, in order to maximize the data utilized by the computer program to calculate the polynomial, it might be best to exclude smaller regions where only the most intense Raman bands occur. Where necessary, normalization techniques appropriate to the analyses being conducted may be used to address the differences in the vertical locations of the baseline of the corrected spectra.

CONCLUSIONS

Raman hyperspectral imaging can be a powerful technique identifying and characterizing the spatial distribution of materials in geological samples, it is critical, however that researchers utilizing this technique understand, the variety of factors that can affect data quality. Elevated baselines as a result of autofluorescence can lead to misidentification of materials in hyperspectral images created from intensity at a point and other univariate calculations. When

generating Raman images using these types of analyses it is important to know if the spectra in a Raman hyperspectral dataset were affected by autofluorescence during data acquisition. Signal to axis images which can aid in identification and visualization of spectra affected by autofluorescence should be used to determine whether or not baseline correction is necessary.

Unfortunately, the vast majority of software programs implement a single, operator-designated polynomial order to baseline correct every spectrum in a hyperspectral dataset resulting in a certain amount of subjectivity. Due to the inherent heterogeneity of geological samples and differences in software capabilities and implemented mathematical algorithms, polynomial-based baseline correction should not simply be performed once on a hyperspectral dataset based on an *a priori* choice of polynomial order. Baseline correction of Raman hyperspectral datasets needs to be approached as an experiment involving several trials that are qualitatively evaluated by critically inspecting of multiple spectra from the dataset to determine if potential errors may have been introduced. Caution should be exercised when using higher-order polynomials to baseline correct geological hyperspectral datasets due to inherent errors that can be introduced based on the way PLS regression functions during computerized baseline correction. Visual inspection of every spectrum in large hyperspectral datasets is nearly impossible making evaluation of baseline correction quality difficult. However, datasets created from signal to axis calculations can be used to statistically evaluate the goodness of fit of different baseline correction trials that qualitatively appear appropriate.

References

Afseth N.K., Segtnan V.H. and Wold J.P. (2006) Raman Spectra of Biological Samples: A Study of Preprocessing Methods **Applied Spectroscopy, 60,** 1358-1367.

Agangi A., Kamenetsky V.S., Hofmann A., Przybyłowicz W. and Vladykin N.V. (2014)
Crystallisation of magmatic topaz and implications for Nb–Ta–W mineralisation in F-rich silicic melts — The Ary-Bulak ongonite massif **Lithos, 202–203,** 317-330.

Baek S.-J., Park A., Shen A. and Hu J. (2011)
A background elimination method based on linear programming for Raman spectra **Journal of Raman Spectroscopy, 42,** 1987-1993.

Beier B.D. and Berger A.J. (2009)
Method for automated background subtraction from Raman spectra containing known contaminants **Analyst, 134,** 1198-1202.

Bellot-Gurlet L., Bourdonnec F.-X.L., Poupeau G. and Dubernet S. (2004)
Raman micro-spectroscopy of western Mediterranean obsidian glass: one step towards provenance studies? **Journal of Raman Spectroscopy, 35,** 671-677.

Bernard S., Beyssac O. and Benzerara K. (2008)
Raman Mapping Using Advanced Line-Scanning Systems: Geological Applications **Applied Spectroscopy, 62,** 1180-1188.

Boyd J.P. and Xu F. (2009)
Divergence (Runge Phenomenon) for least-squares polynomial approximation on an equispaced grid and Mock–Chebyshev subset interpolation **Applied Mathematics and Computation, 210,** 158-168.

Brasier M.D., Green O.R., Lindsay J.F., McLoughlin N., Steele A. and Stoakes C. (2005)
Critical testing of Earth's oldest putative fossil assemblage from the ~3.5 Ga Apex chert, Chinaman
Creek, Western Australia **Precambrian Research, 140,** 55-102.

Bridges J.C., Burchell M.J., Changela H.C., Foster N.J., Creighton J.A., Carpenter J.D., Gurman S.J., Franchi I.A. and Busemann H. (2010)
Iron oxides in comet 81P/Wild 2 **Meteoritics & Planetary Science, 45,** 55-72.

Bulmer J.T., Irish D.E., Grossman F.W., Herriot G., Tseng M. and Weerheim A.J. (1975)
Baseline Modeling with a Computerized Raman System **Applied Spectroscopy, 29,** 506-511.

Burchell M.J., Mann J., Creighton J.A., Kearsley A.T., Graham G. and Franchi I.A. (2006)
Identification of minerals and meteoritic materials via Raman techniques after capture in hypervelocity impacts on aerogel **Meteoritics & Planetary Science, 41,** 217-232.

Cadusch P.J., Hlaing M.M., Wade S.A., McArthur S.L. and Stoddart P.R. (2013)
Improved methods for fluorescence background subtraction from Raman spectra **Journal of Raman Spectroscopy, 44,** 1587-1595.

Ciobotă V., Lu S., Tarcea N., Rösch P., Küsel K. and Popp J. (2013)
Quantification of the inorganic phase of the pelagic aggregates from an iron contaminated lake by means of Raman spectroscopy **Vibrational Spectroscopy, 68,** 212-219.

Dahlquist G. and Bjorck A. (2003)
Numerical Methods. **Dover (Mineola, NY)**.

Delhaye M. and Dhamelincourt P. (1975)
Raman microprobe and microscope with laser excitation **Journal of Raman Spectroscopy, 3,** 33-43.

Dieing T., Hollricher O. and Toporski J. (2010)
Confocal Raman Microscopy. **Springer (Berlin, Germany),** 289 pp.

Dijkstra T.K. (2010)
Methods. **In: Vinzi V.E., Chin W.W., Henseler J. and Wang H. (eds), Handbook of Partial Least Squares : Concepts, Methods and Applications. Springer (Heidelberg, Germany),** 23-46.

Dilor-Jorbin Yvon-Spex, HORIBA. (1999)
LabSpec Software User Guide. http://www.horiba.com/us/en/scientific/products/raman-spectroscopy/downloadslast accessed 18 November 2014)

Edwards H.G.M., Williams A.C. and Barry B.W. (1995)
Potential applications of FT-Raman spectroscopy for dermatological diagnostics **Journal of Molecular Structure, 347,** 379-387.

Faria D.L.A.d., Silva S.V. and Oliveira M.T.d. (1997)
Raman microspectroscopy of some iron oxides and oxyhydroxides **Journal of Raman Spectroscopy, 28,** 873-878.

Frosch T., Tarcea N., Schmitt M., Thiele H., Langenhorst F. and Popp J. (2007)
UV Raman ImagingA Promising Tool for Astrobiology: Comparative Raman Studies with Different Excitation Wavelengths on SNC Martian Meteorites **Analytical Chemistry, 79,** 1101-1108.

Gillet P., Le Cléac'h A. and Madon M. (1990)
High-temperature raman spectroscopy of SiO2 and GeO2 Polymorphs: Anharmonicity and thermodynamic properties at high-temperatures **Journal of Geophysical Research: Solid Earth, 95,** 21635-21655.

Hawkins D.M. (2004)
The problem of overfitting **Journal of Chemical Information and Computer Sciences, 44,** 1-12.

Heim C., Lausmaa J., SjÖVall P., Toporski J., Dieing T., Simon K., Hansen B.T., Kronz A., Arp G., Reitner J. and Thiel V. (2012)
Ancient microbial activity recorded in fracture fillings from granitic rocks (Äspö Hard Rock Laboratory, Sweden) **Geobiology, 10,** 280-297.

Heraud P., Wood B.R., Beardall J. and McNaughton D. (2006)
Effects of pre-processing of Raman spectra on in vivo classification of nutrient status of microalgal cells **Journal of Chemometrics, 20,** 193-197.

Igisu M., Komiya T., Kawashima M., Nakashima S., Ueno Y., Han J., Shu D., Li Y., Guo J., Maruyama S. and Takai K. (2014)
FTIR microspectroscopy of Ediacaran phosphatized microfossils from the Doushantuo Formation, Weng'an, South China **Gondwana Research, 25,** 1120-1138.

James K. (2000)
PC Interfacing and Data Acquisition: Techniques for Measurement, Instrumentation and Control. **Newnes (Oxford, UK)**.

Jehlička J., Vítek P., Edwards H.G.M., Hargreaves M.D. and Čapoun T. (2009)
Fast detection of sulphate minerals (gypsum, anglesite, baryte) by a portable Raman spectrometer **Journal of Raman Spectroscopy, 40,** 1082-1086.

Jirasek A., Schulze G., Yu M.M., Blades M.W. and Turner R.F. (2004)
Accuracy and precision of manual baseline determination **Appl Spectrosc, 58,** 1488-99.

Kingma K.J. and Hemley R.J. (1994)
Raman spectroscopic study of microcrystalline silica **American Mineralogist, 79,** 269-273.

Kremer B., Owocki K., Królikowska A., Wrzosek B. and Kazmierczak J. (2012)
Mineral microbial structures in a bone of the Late Cretaceous dinosaur Saurolophus angustirostris from the Gobi Desert, Mongolia — a Raman spectroscopy study **Palaeogeography, Palaeoclimatology, Palaeoecology, 358–360,** 51-61.

Lasch P. (2014)
Manual (CytoSpec v. 2.0). http://www.cytospec.com/index.php. (last accessed 18 November 2014)

Lee E. (2012)
Imaging Modes. **In: Zoubir A. (ed), Raman Imaging. Springer Berlin Heidelberg,** 1-37.

Leger M.N. and Ryder A.G. (2006)
Comparison of Derivative Preprocessing and Automated Polynomial Baseline Correction Method for Classification and Quantification of Narcotics in Solid Mixtures **Applied Spectroscopy, 60,** 182-193.

Lespade P., Al-Jishi R. and Dresselhaus M.S. (1982)

Model for Raman scattering from incompletely graphitized carbons **Carbon, 20,** 427-431.

Lewis I.R. and Edwards H.G. (2001)
Handbook of Raman Spectroscopy: From the Research Labratory to the Process Line. **Marcel Dekker Inc. (Switzerland),** 1055 pp.

Lieber C.A. and Mahadevan-Jansen A. (2003)
Automated method for subtraction of fluorescence from biological Raman spectra **Appl Spectrosc, 57,** 1363-7.

Liland K.H., Almoy T. and Mevik B.H. (2010)
Optimal Choice of Baseline Correction for Multivariate Calibration of Spectra **Applied Spectroscopy, 64,** 1007-1016.

Lünsdorf N.K., Dunkl I., Schmidt B.C., Rantitsch G. and von Eynatten H. (2014)
Towards a Higher Comparability of Geothermometric Data obtained by Raman Spectroscopy of Carbonaceous Material. Part I: Evaluation of Biasing Factors **Geostandards and Geoanalytical Research, 38,** 73-94.

Mahadevan-Jansen A. and Richards-Kortum R.R. (1996)
Raman spectroscopy for the detection of cancers and precancers **Journal of Biomedical Optics, 1,** 31-70.

Mark H. and Workman J.J. (2007)
Chemometrics in Spectroscopy. **Elsevier Inc. (London, UK)**.

Marshall A.O., Jehlicka J., Rouzaud J.N. and Marshall C.P. (2014)
Multiple generations of carbonaceous material deposited in Apex chert by basin-scale pervasive hydrothermal fluid flow **Gondwana Research, 25,** 284-289.

Marshall C.P., Emry J.R. and Olcott Marshall A. (2011)
Haematite pseudomicrofossils present in the 3.5-billion-year-old Apex Chert **Nature Geosci, advance online publication**.

Marshall C.P. and Marshall A.O. (2011)
Hematite and carbonaceous materials in geological samples: A cautionary tale **Spectrochimica Acta Part A: Molecular and Biomolecular Spectroscopy, 80,** 133-137.

Marshall C.P. and Olcott Marshall A. (2013)
Raman hyperspectral imaging of microfossils: potential pitfalls **Astrobiology, 13,** 920-31.

McCreery R.L. (2005)
Raman Microscopy and Imaging. **Raman Spectroscopy for Chemical Analysis. John Wiley & Sons, Inc.,** 293-332.

Nasdala L., Beyssac O., William Schopf J. and Bleisteiner B. (2012)

Application of Raman-based images in the Earth sciences. **In: Zoubir A. (ed), Raman Imaging. Springer Berlin Heidelberg,** 145-187.

Nasdala L., Smith D.C., Kaindl R. and Ziemann M.A. (2004)
Raman spectroscopy: analytical perspectives in mineralogical research **EMU notes in mineralogy,** 281-343.

Neff D., Bellot-Gurlet L., Dillmann P., Reguer S. and Legrand L. (2006)
Raman imaging of ancient rust scales on archaeological iron artefacts for long-term atmospheric corrosion mechanisms study **Journal of Raman Spectroscopy, 37,** 1228-1237.

Ocean Optics, Inc. (2013)
Ocean View Spectrometer Operating Software: Installation and Operation Manual. http://www.oceanoptics.com/oceanview/OceanViewI&O-1.pdf (last accessed 18 November 2014)

Pelletier M.J. (2003)
Quantitative Analysis Using Raman Spectrometry **Applied Spectroscopy, 57,** 20A-42A.

Pinti D.L., Mineau R. and Clement V. (2009)
Hydrothermal alteration and microfossil artefacts of the 3,465-million-year-old Apex chert **Nature Geosci, 2,** 640-643.

Pirzer M. and Sawatzki J. (2006)
Method and device for correcting a spectrum. Bruker Optik Gmbh Ettlingen (DE), assignee. **Patent US 11/358,697.** Print.

Prakash B.D. and Wei Y.C. (2011)
A fully automated iterative moving averaging (AIMA) technique for baseline correction **Analyst, 136,** 3130-3135.

Quirico E., Rouzaud J.-N., Bonal L. and Montagnac G. (2005)
Maturation grade of coals as revealed by Raman spectroscopy: Progress and problems **Spectrochimica Acta Part A: Molecular and Biomolecular Spectroscopy, 61,** 2368-2377.

Rigaku (2012)
Xantus™ and FirstGuard™ Handheld Raman Analyzers. http://www.bas.cz/spektrometr-raman-rigaku/rigaku-raman-firstguard-xantus.pdf (last accessed 18 November 2014)

Rosasco G.J., Etz E.S. and Cassatt W.A. (1975)
The Analysis of Discrete Fine Particles by Raman Spectroscopy **Applied Spectroscopy, 29,** 396-404.

Rotundi A., Baratta G.A., Borg J., Brucato J.R., Busemann H., Colangeli L., D'Hendecourt L., Djouadi Z., Ferrini G., Franchi I.A., Fries M., Grossemy F., Keller L.P., Mennella V.,

Nakamura K., Nittler L.R., Palumbo M.E., Sandford S.A., Steele A. and Wopenka B. (2008)
Combined micro-Raman, micro-infrared, and field emission scanning electron microscope analyses of comet 81P/Wild 2 particles collected by Stardust **Meteoritics & Planetary Science, 43,** 367-397.

Salzer R. and Siesler H. (2009)
Infrared and Raman Spectroscopic Imaging. **Wiley (Weinheim, Germany)**.

Sasic S. and Ozaki Y. (2010)
Raman, Infrared, and Near-Infrared Chemical Imaging. **Wiley (New Jersey)**.

Schopf J.W. and Kudryavtsev A.B. (2009)
Confocal laser scanning microscopy and Raman imagery of ancient microscopic fossils **Precambrian Research, 173,** 39-49.

Schopf J.W. and Kudryavtsev A.B. (2012)
Biogenicity of Earth's earliest fossils: A resolution of the controversy **Gondwana Research, 22,** 761-771.

Schopf J.W. and Kudryavtsev A.B. (2014)
Biogenecity of Earth's Earliest Fossils. **Springer (New York),** 333-349 pp.

Schopf J.W., Kudryavtsev A.B., Agresti D.G., Wdowiak T.J. and Czaja A.D. (2002)
Laser-Raman imagery of Earth's earliest fossils **Nature, 416,** 73-76.

Schopf J.W. and Packer B.M. (1987)
Early Archean (3.3-Billion to 3.5-Billion-Year-Old) Microfossils from Warrawoona Group, Australia **Science, 237,** 70-73.

Schroeder P.A., Melear N.D. and Pruett R.J. (2003)
Quantitative analysis of anatase in Georgia kaolins using Raman spectroscopy **Applied Clay Science, 23,** 299-308.

Schulze G., Jirasek A., Yu M.M., Lim A., Turner R.F. and Blades M.W. (2005a)
Investigation of selected baseline removal techniques as candidates for automated implementation **Appl Spectrosc, 59,** 545-74.

Schulze G., Jirasek A., Yu M.M.L., Lim A., Turner R.F.B. and Blades M.W. (2005b)
Investigation of Selected Baseline Removal Techniques as Candidates for Automated Implementation **Applied Spectroscopy, 59,** 545-574.

Sforna M.C., van Zuilen M.A. and Philippot P. (2014)

Structural characterization by Raman hyperspectral mapping of organic carbon in the 3.46 billion-year-old Apex chert, Western Australia **Geochimica Et Cosmochimica Acta, 124,** 18-33.

Severs M.J., Azbej T., Thomas J.B., Mandeville C.W. and Bodnar R.J. (2007)
Experimental determination of H2O loss from melt inclusions during laboratory heating: Evidence from Raman spectroscopy **Chemical Geology, 237,** 358-371.

Sharma S.K., Lucey P.G., Ghosh M., Hubble H.W. and Horton K.A. (2003)
Stand-off Raman spectroscopic detection of minerals on planetary surfaces **Spectrochim Acta A Mol Biomol Spectrosc, 59,** 2391-407.

Shim M.G. and Wilson B.C. (1997)
Development of an In Vivo Raman Spectroscopic System for Diagnostic Applications **Journal of Raman Spectroscopy, 28,** 131-142.

Shim S.H. and Duffy T.S. (2002)
Raman spectroscopy of Fe2O3 to 62 GPa **American Mineralogist, 87,** 318-326.

Smith B. (2012)
Estimation of background radiation in spectral data by polynomial fitting. RenishawPlc, assignee. Patent EP20110250504

Smith D.C. and Godard G. (2009)
UV and VIS Raman spectra of natural lonsdaleites: Towards a recognised standard **Spectrochimica Acta Part A: Molecular and Biomolecular Spectroscopy, 73,** 428-435.

Sokal R.R. and Rohlf F.J. (1995)
Biometry. **W.H. Freeman and Company (New York)**.

ThermoScientific. (n.d)
Thermo Scientific GRAMS Suite – A Solution for Visualizing, Processing, and Managing Spectroscopic Data
http://www.thermoscientific.com/content/dam/tfs/ATG/CMD/CMD%20Documents/DS-GRAMS-UG410.pdf (last accessed 18 November 2014)

Tuinstra F. and Koenig J.L. (1970)
Raman Spectrum of Graphite **The Journal of Chemical Physics, 53,** 1126-1130.

Van Kranendonk M.J. (2006)
Volcanic degassing, hydrothermal circulation and the flourishing of early life on Earth: A review of the evidence from c. 3490-3240 Ma rocks of the Pilbara Supergroup, Pilbara Craton, Western Australia **Earth-Science Reviews, 74,** 197-240.

Vandenabeele P. (2013)
Practical Raman Spectroscopy. **John Wiley & Sons (Chichester, UK),** 192 pp.

Vickers T.J., Wambles J.R. and Mann C.K. (2001)
Curve Fitting and Linearity: Data Processing in Raman Spectroscopy **Applied Spectroscopy,**

55, 389-393.

Workman J.J. and Springsteen A. (1998)
Applied Spectroscopy: A Compact Reference for Practitioners. **Academic Press (Chestnut Hill, MA)**.

Zajacz Z., Halter W., Malfait W., Bachmann O., Bodnar R., Hirschmann M., Mandeville C., Morizet Y., Müntener O., Ulmer P. and Webster J. (2005)
A composition-independent quantitative determination of the water content in silicate glasses and silicate melt inclusions by confocal Raman spectroscopy **Contributions to Mineralogy and Petrology, 150,** 631-642.

Zhang Z.-M., Chen S., Liang Y.-Z., Liu Z.-X., Zhang Q.-M., Ding L.-X., Ye F. and Zhou H. (2010a)
An intelligent background-correction algorithm for highly fluorescent samples in Raman spectroscopy **Journal of Raman Spectroscopy, 41,** 659-669.

Zhang Z.M., Chen S. and Liang Y.Z. (2010b)
Baseline correction using adaptive iteratively reweighted penalized least squares **Analyst, 135,** 1138-46.

Zhao J., Lui H., McLean D.I. and Zeng H. (2007)
Automated autofluorescence background subtraction algorithm for biomedical Raman spectroscopy **Appl Spectrosc, 61,** 1225-32.

Zinin P., Tatsumi-Petrochilos L., Bonal L., Acosta T., Hammer J., Gilder S. and Fuller M. (2011)
Raman spectroscopy of titanomagnetites: Calibration of the intensity of Raman peaks as a sensitive indicator for their Ti content **American Mineralogist, 96,** 1537-1546.

SUPPLEMENTARY MATERIAL

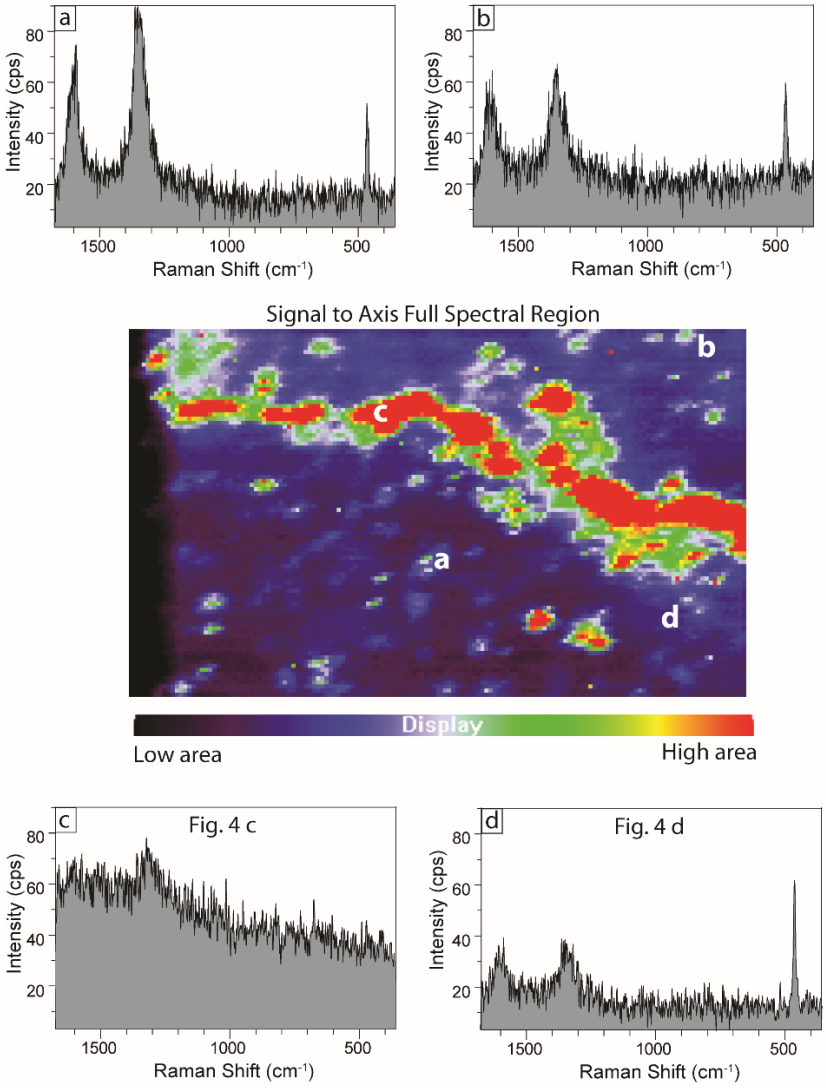

Figure S1. Signal to axis image over the full spectral region (360-1690 cm-[1]) (a) closely resembles the distribution of high area values in Figure 6. Regions of moderately high area values in the full region image in the quartz matrix shaded green can be seen (a,b) as compared to Figure 6. Note that these spectra have flat baselines unaffected by autofluorescence. Spectra c and d from Figure 4 are shown for reference. Comparison of spectra (a) and (b) with spectrum (c) illustrates the presence of very intense D and G bands in carbonaceous material as the primary cause in relative increase in area values shown in the image. Increased heterogeneity in geological and related datasets increases the likelihood of relative differences in intensity, more complex spectra with multiple Raman bands, or the occurrence of overlapping bands representing more complex mixtures. This complexity may reduce the ability to define an appropriate representative baseline region. All of these factors may increase signal to axis area values over the full spectral region along with potential autofluorescence issues. Signal to axis imaging over the full collection region can identify regions with relatively higher area values facilitating identification of autofluorescence. While not as definitive as utilizing a representative baseline region, this technique can identify regions displaying relatively high area values. Because inspection of each individual spectrum in a hyperspectral dataset is nearly impossible, signal to axis imaging over the full spectral region can identify regions of interest where spectra may be more affected by autofluorescence to investigate more comprehensively. Determining the cause(s) of higher area values will require visual inspection of multiple spectra in the areas of interest.

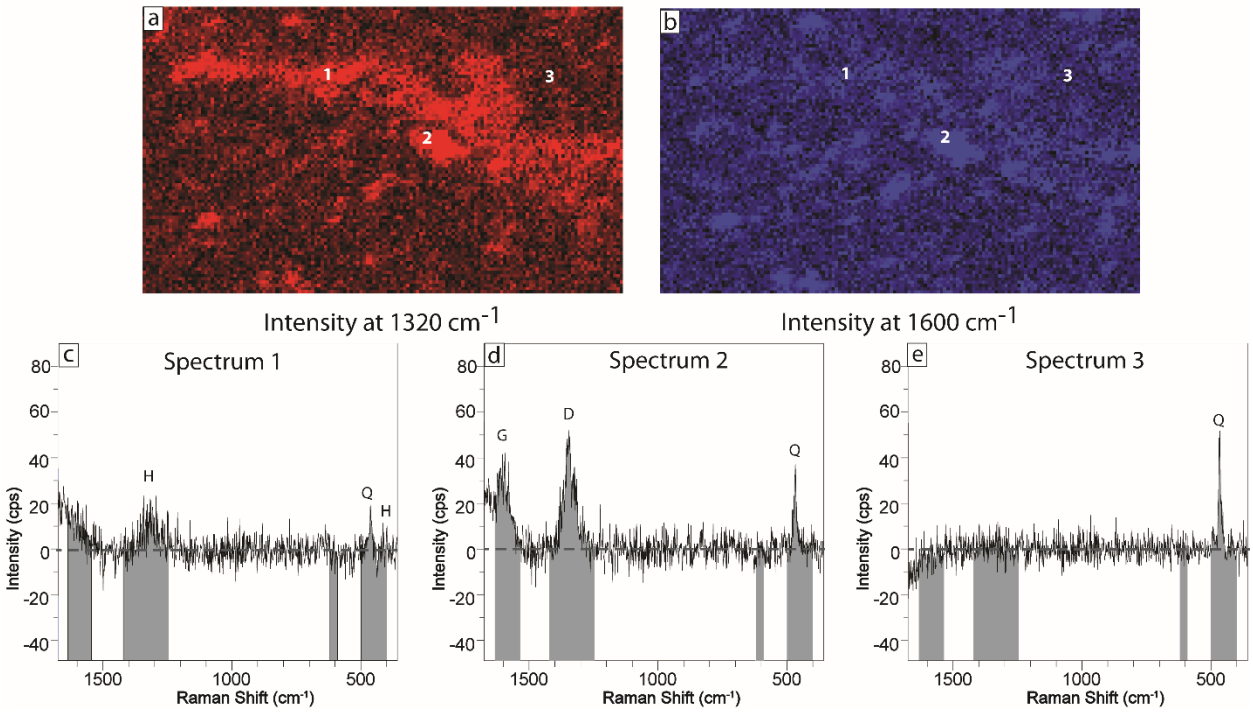

Figure S2. Intensity images representing hematite (1320 cm^{-1}) (a) and carbonaceous material (b) (1600 cm^{-1}) from a modified Trial 1 fifth-order polynomial correction. The original Trial 1 mask regions contained 40 cm^{-1} values in the low Raman shift region, however in the high region all values were masked. This trial was performed to determine if the fifth-order correction overcorrected spectra as a result of too few data points in the high Raman shift region. Qualitatively, these images appear to illustrate the distribution of hematite and carbonaceous material better than the original Trial 1 images (Fig. 5). Visual inspection of representative spectra indicate that the modified Trial 1 mask regions still overcorrect spectra in a similar manner to the original trial. Spectra 1 and 2 (c,d) display elevated baselines in the high Raman shift region, and spectrum 3 (e) a decrease in the intensity values. Therefore, we conclude that the overcorrection resulting from the fifth-order polynomial was not due to a lack of data points, but more likely due to S:N ratio, PLS regression mathematics or issues associated with the Runge phenomenon.

Appendix A: Avoiding Software Based Data Beautification and Misinterpretation in Raman Imaging

ABSTRACT

Raman hyperspectral imaging is becoming an increasingly utilized technique in geoscience and geomaterials research. Software programs available from the most commonly utilized commercial Raman instruments (Renishaw, WITec and Jobin-Yvon Horiba) provide comparable analytical and image manipulation capabilities. Software based manipulation can be useful to improve image visual quality, but may lead to misinterpretations in Raman images if used inappropriately. To date, there has been little discussion regarding software-based Raman image creation or manipulation. To illustrate issues associated with the creation and manipulation of Raman images, examples of different analytical and image display techniques are shown and a method that can be used to evaluate the appropriateness of software based image manipulation is presented. A series of best practices are proposed to help educate geoscientists regarding software-based Raman image creation and manipulation, and to illustrate the importance of reporting methods used to create Raman images. Careful consideration of these issues will help to promote scientific transparency and increase our ability to objectively compare Raman image based interpretations of geological data from different samples and studies.

INTRODUCTION

Raman hyperspectral imaging is an increasingly popular technique used to identify and characterize the spatial distribution of materials in geological samples (Bernard *et al.* 2008, Marshall and Olcott Marshall 2013, Nasdala *et al.* 2012). A Web of Science search reveals an exponential increase in the number of peer-reviewed geoscience-related Raman imaging publications over the last 22 years (Fig. 1). This increase is primarily due to the improved availability of commercial Raman systems and development of advanced imaging techniques that allow for the acquisition of high resolution datasets consisting of thousands to tens of thousands of spectra in relatively short periods of time (Lee 2012).

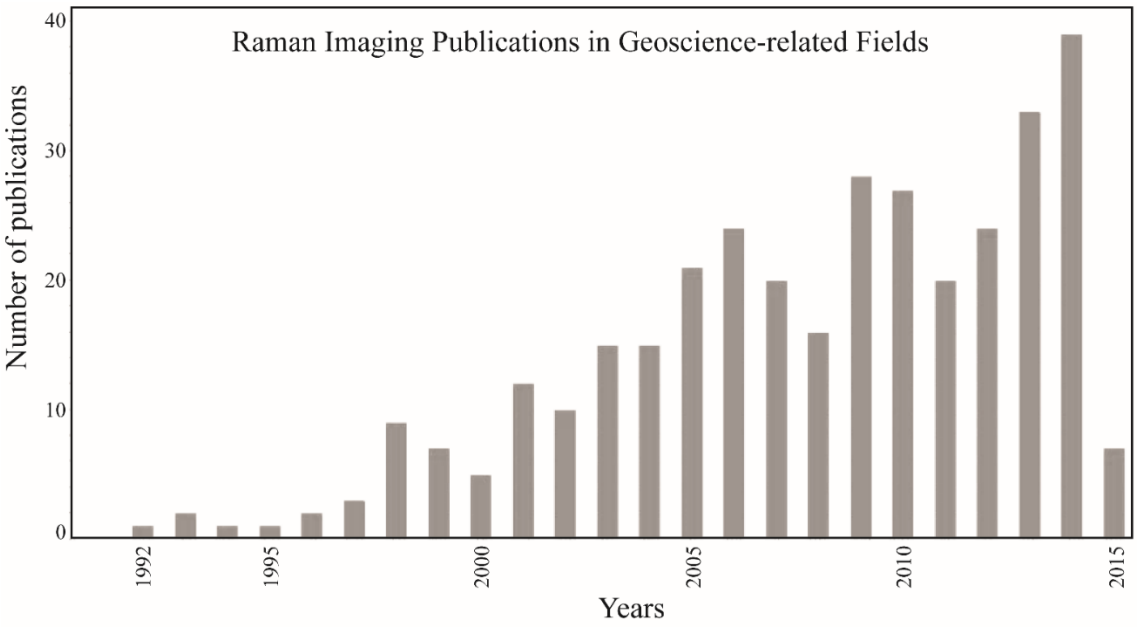

Figure 1. Number of peer-reviewed publications in the geoscience-related fields incorporating Raman hyperspectral imaging, 1992-present from Thompson Reuter's Web of Science database. The search terms utilized were: archeology, anthropology, art, crystallography, geology, geochemistry, geophysics, geoscience interdisciplinary, mineralogy, mining mineral processing and paleontology.

Hyperspectral datasets are analyzed using univariate or multivariate computer-based algorithms to create false-color images that are subsequently used to interpret the spatial distribution of materials in samples. False-color images are created by plotting the range of values that result from these analyses using a linear interpolated color scale. Compared to point Raman spectral acquisition, hyperspectral imaging of geological materials present a broader array of challenges due to the natural heterogeneity of geological samples, data collection limitations, software-based data analysis, and the variety of potential analytical methods that can be used to create Raman images. Finally, geoscientists are typically not experts in Raman spectroscopy or statistically-based computer analysis algorithms and may be unaware of the impact that these multiple factors may have on the creation and display of Raman images.

An internet search of geoscience departments with Raman spectrometers shows that the most common commercial systems are provided by Renishaw, WITec, and Jobin-Yvon-Horiba (Fig. S1). Web of Science and Google Scholar searches of the systems utilized for Raman imaging geoscience and geomaterials studies published in the past 10 years support this observation (Fig. S2). The software programs developed by these vendors provide a variety of univariate and multivariate analytical techniques and methods to manipulate the appearance of the resulting Raman images. Raman vendors provide some information regarding software capabilities in publically available documents, sales brochures, and videos, but the information is typically generalized due to proprietary issues. In order to better understand the methods that these commercial software programs provide for manipulating image quality, I contacted company representatives requesting further information based on four questions (Table 1).

VENDOR QUESTIONS	RENISHAW	HORIBA	WITec
Does the software display a graph that shows the user the shape of the data distribution?	X	X	X
Does the software provide a method that allows the user to modify the contrast or brightness of the displayed color by modifying the range of the data displayed or changing the minimum or maximum value assigned to an end member color bar?	X	X	X
Does the software provide a method to overlay several Raman images to create a composite image, or a display of the distribution of two or more materials in a single Raman image?	X	X	X
If so, are composite images created by software settings that exclude or set to transparent portions of one dataset in order to visualize different colors representative of the distribution of multiple components in a single image?	X		X
If composite images are created by excluding or setting portions of the data displayed in an image to transparent, can the user choose the range of data included or excluded for each dataset displayed in the resulting composite image?	X		X

Table 1. Questions posed to company representatives to provide information regarding software based Raman image manipulation capabilities.

According to these interviews, the software programs provide comparable methods that allow users to change the color contrast seen in Raman images by altering the range or amount of data values that are assigned to a color scale. This seems like a simple method for improving image quality. However, it is important to realize that these techniques allow users to subjectively alter the amount and range of data values from univariate or multivariate analyses displayed in an image and are, thusly, a form digital image manipulation. In other fields that heavily rely on data presented as images, both scientists and journal editors are becoming increasingly concerned with the ethical and scientific transparency issues associated with digital image manipulation (Benos and Vollmer 2010, Cromey 2010, Hayden 2000, Kremenak and Siegel 2008, Martin and Blatt 2013, Rossner and Yamada 2004a). Two important issues are commonly discussed; first, the intrinsic expectation of scientific honesty and transparency in presenting scientific image data for publication. Secondly, that scientists are aware of and understand the consequences of processing techniques that may affect image quality, accuracy,

reproducibility and subsequent interpretation of digital images. These concerns are profound enough that researchers have proposed "best practice" guidelines for the manipulation of scientific images and both journals and publishing companies have begun to establish policies regarding appropriate image manipulation techniques (Cromey 2010, Nature 2010, Nature, 2009, Cromey, 2013).

For those who are not experts in Raman spectroscopy, it may be tempting to think of a Raman image as simply a display of the distribution of materials, but it is important to remember that Raman images are derivative data, a software-based representation of the results of univariate or multivariate analyses. Researchers have discussed the importance of treating scientific images as data and noted that caution is needed in performing what seem like "artistic" modifications to make images more simple or convincing because image manipulation may result in bias or misinterpretation (Cromey 2013, Rossner and Yamada 2004b).

Researchers have discussed instrumental, analytical technique, and sample based issues that may lead to misinterpretations (e.g. Clark and Šašić 2006, Emry *et al.* 2015, Lünsdorf *et al.* 2014, Marshall and Marshall 2011, Marshall and Olcott Marshall 2013, Nasdala *et al.* 2012, Nasdala *et al.* 2004, Sasic and Ozaki 2010) but there has been little discussion regarding software based digital image manipulation techniques for Raman image datasets in the geosciences. Clarke and Šašić (2006) noted difficulty in creating composite images from Principle Component Analyses (PCA) to display multiple components in a pharmaceutical tablet due to the method the software utilized to overlay multiple Raman images. It has also been noted that the color scale range should be carefully chosen because it can significantly affect the appearance of Raman images (Dieing *et al.* 2010), but little work has been done to compare and evaluate how different software programs allow users to create and digitally manipulate Raman

images and understand potential issues that may arise. Standards have been suggested for Raman spectrometer capabilities and the presentation of Raman spectra in publications (e.g. ASTM 2010, ASTM 2014, Grasselli 1991, McCreery 2006) but there has been little discussion regarding the appropriate use of software-based digital manipulation or standards or best practices for Raman image display. Open discussion of the use of available image manipulation techniques is important to educate geoscientists about potential errors and promote the ability to meaningfully compare Raman images from different systems, datasets, and studies.

Additionally, software innovations have greatly expanded the variety and ease of use of univariate and multivariate analytical techniques. These methods have different strengths and weaknesses and are prone to different types of interpretation error (see Dieing *et al.* 2010, Lewis and Edwards 2001 for a review of various available techniques and their potential errors). Although researchers in other fields have compared the applicability of various analytical techniques on individual datasets (e.g. Almeida *et al.* 2015, Andrew and Hancewicz 1998, Boiret *et al.* 2015, Gendrin *et al.* 2008, Ghasemzadeh-Barvarz *et al.* 2013, Krafft *et al.* 2012, Sacré *et al.* 2014, Sasic *et al.* 2004, Slobodan 2007, Vajna *et al.* 2012, Vajna *et al.* 2011), geoscientists typically present Raman images derived from a single analytical method. The purpose of this paper is to raise awareness of the strengths and weaknesses of both the analytical and image manipulation techniques that are commonly available to geoscientists. Additionally, it presents methods that can be utilized to evaluate the appropriateness of software-based image display. Only by promoting open discussion of the strengths and weaknesses of these techniques can inquiry be maintained when comparing and interpreting Raman images from different systems, samples and studies.

MATERIALS AND METHODS

The hyperspectral datasets presented in this paper were acquired from a thin section of the ~3.5 Ga Apex chert from Western Australia. Raman hyperspectral data were collected utilizing a Renishaw Reflex Raman microprobe with an attached trinocular Leica DMLM microscope. An argon-ion laser (Modu-Laser) emitting at 514.5 nm was used to excite the sample. Renishaw's StreamLine^{TM} mode with an accumulation time of 0.1 sec over a range of 360-1690 cm^{-1} was utilized to collect the hyperspectral dataset. Renishaw's WiRE 3.4 software Partial Least Squares based baseline correction algorithm was used to baseline correct the dataset using a linear polynomial function. For more detailed information on the data collection and baseline correction parameters see (Emry *et al.* 2015).

RESULTS AND DISCUSSION

Raman images created from intensity at a point analyses representing the two best resolved hematite Raman bands (411 and 1320 cm^{-1}) displayed with two different manipulation techniques are shown in Figure 2 (B,C,F,G). Screen captures of Renishaw's WiRE 3.4 software look up tables (LUT) show the proportion and range of data assigned to the color scale for each image (Fig. 2, A,D,E,H). Images B and C display the full range of data and images F and G display the central 90% of the data values excluding the upper and lower 5% of the data distribution. Note the differences in visual contrast, or relative brightness of the colors displayed in the images. In order to understand why the images differ in contrast, we need to consider how software programs translate an image dataset composed of a grid of numerical values into a false color image. Computer programs interpolate a color space or map, which is a series of numerical

values representing a range of visual color, to the range of data values calculated from univariate or multivariate analyses. Linear interpolation is the most common method utilized, but software engineers have developed other non-linear interpolation techniques (Burger and Burge 2013, Lee 2005).

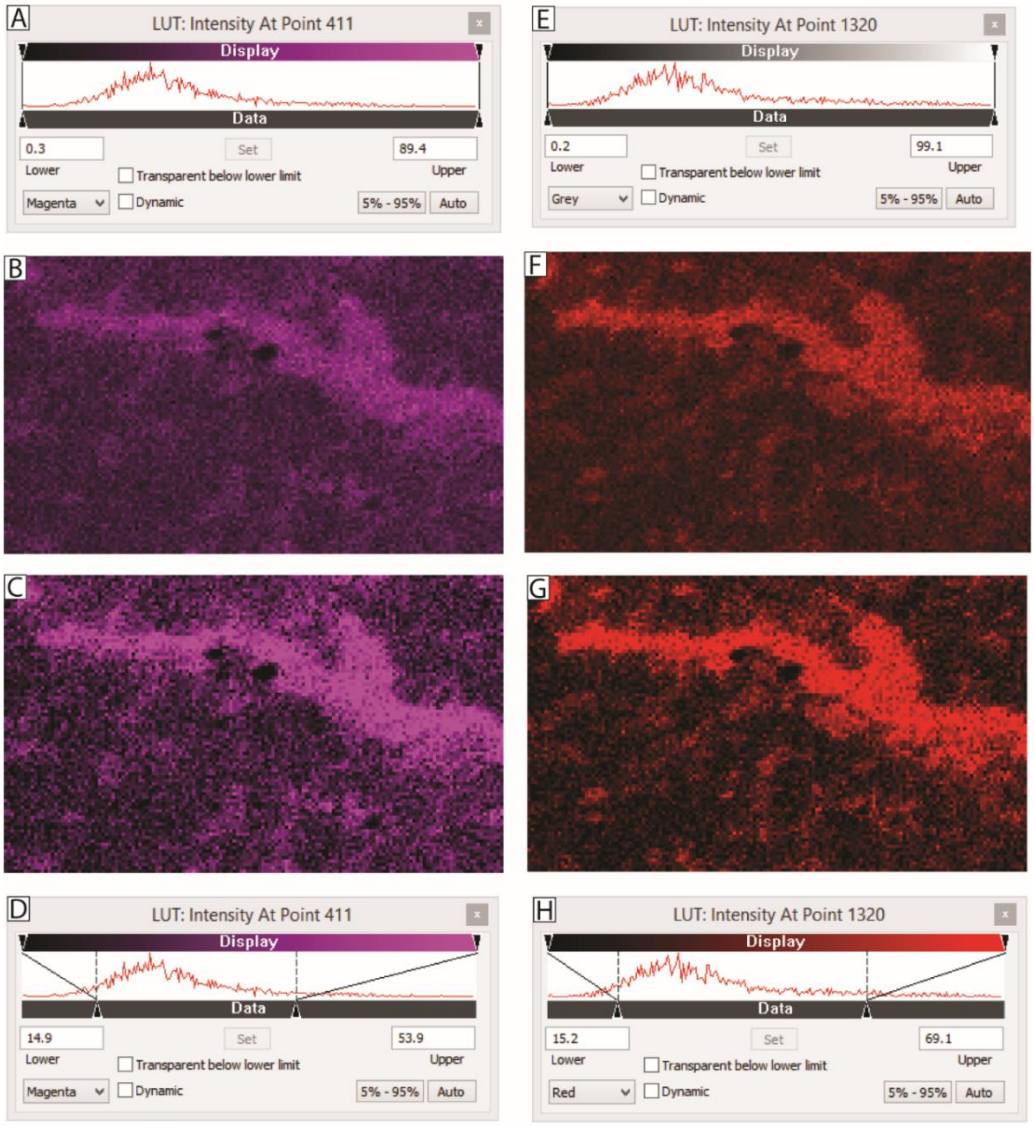

Figure 2. Raman intensity at a point images representing hematite (411 and 1320 cm^{-1}) generated from the same hyperspectral dataset from a sample of the Apex chert. Images B and F display the entire range of data assigned to the color interpolation procedure. Images C and G were created by utilizing a standard setting that assigns the central 90% of the data distribution (excluding the upper and lower 5% of data values in the tails of the data distribution. Screencaptures of the LUT's show the range of data assigned to the color map interpolation used to create the images. The blue dashed lines in D and F illustrate the location of the 5-95% cut off data values.

Color maps are typically limited to a range of values from 0-255 that are interpolated onto a range of data values that are displayed as colored pixels in an image. It is important to remember that the data visualized in Raman images is a two-step derivative from the spectral data collected during Raman imaging and both the univariate or multivariate technique utilized and the color interpolation process can affect the color contrast displayed in the resulting Raman image. Image contrast enhancement is a common technique utilized in Remote sensing because spectral data often have values outside the range of human vision (i.e. infrared or UV) and can be performed with a variety of methods including linear stretch, histogram equalization, density slicing, and edge enhancement (Campbell 2007).

The image contrast manipulation technique provided by the Renishaw, WITec, and Jobin-Yvon-Horiba Raman software programs is analogous to saturating linear contrast enhancement. This technique is performed by expanding a range of spectral data values for a feature of interest and applying these values to the color map interpolation and the rest of the spectral values are then assigned to the two end member colors in the color space (Richards 2013). Similar to remote sensing image manipulation, the shape of the data distribution will affect the proportion of data values assigned to a particular numeric color value that creates visual image contrast (Richards 2013). For example, the data intensity values shown in the LUT's (Fig. 2, A,D,E,H) at first glance appear relatively normally distributed, but there is a relatively small number of higher intensity values forming a right-skewed tail. The 5% of data values in the right tail of the data distribution represent 30% of the total numerical range of the intensity values (upper 5% values range from 99.1-69.1 cps and the total data range is from 0.2-99.1 cps). The skewed nature of the data distribution results in a small number of high intensity

values (5%) being assigned to a relatively large proportion of the "brightest" color map values resulting in a reduction of the visual contrast of the Raman images (Fig. 2, B and F). Utilizing software available image alteration techniques can be useful to improve the visual quality of Raman images, but it is important to remember that this is a form of digital data manipulation. Datasets created from univariate or multivariate analyses are composed of a single derivative numerical value for each spectrum calculated from the original spectral dataset (Dieing *et al.* 2010). These numerical values therefore "imply" the presence or absence of a material and these values are subsequently reassigned a numerical value that represents a color based on the range and shape of the data distribution that is displayed as a colored pixel in a Raman image. The high values in the right side of the data distribution are numbers that we assume will imply the presence of a material in a Raman image, in this example intensity measurements in cps at two Raman shift positions representing the presence of two Raman bands in the Raman spectrum of hematite. Therefore, the question we need to ask is; does this type of data manipulation affect the ability to accurately interpret the spatial distribution of hematite? We assume that univariate intensity at 411 and 1320 cm^{-1} analyses will appropriately identify hematite and the resulting Raman images will visually illustrate its spatial occurrence. As a result, we can hypothesize that these higher values should occur within the microvein if this feature contains hematite. This hypothesis can be tested by creating a Raman image that displays the spatial distribution of the colored pixels representing the excluded high intensity values, observing spatial distribution of these pixels and subsequently verifying the presence of hematite by visually assessing multiple representative spectra. An example from the intensity in cps at 1320 cm^{-1} dataset is shown in Figure 3. In this example, the hypothesis is supported by the observation that these values occur within the microvein and the representative spectra contain Raman bands indicative of hematite

(Fig. 3.). Excluding these values from the color map interpolation improves the visual quality of the images without negatively affecting the ability to accurately visualize the spatial distribution of hematite.

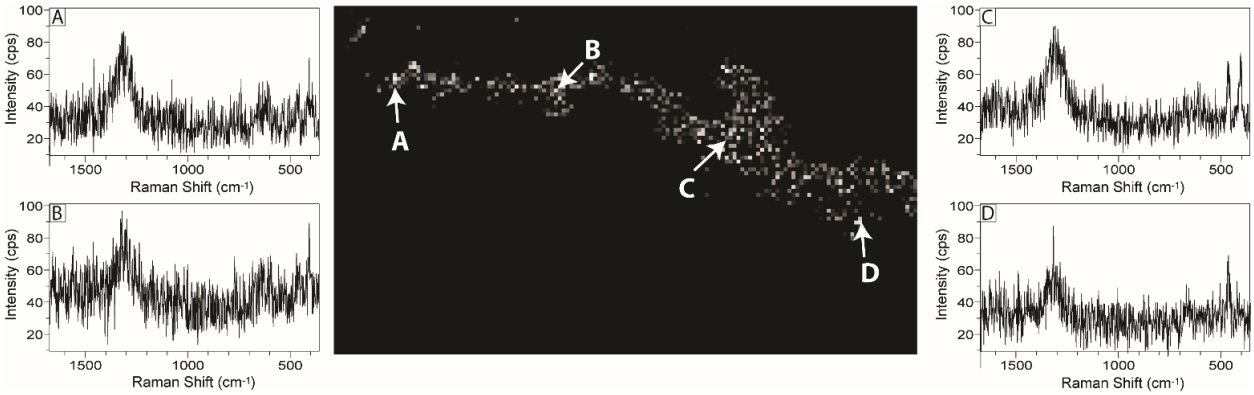

Figure 3. Raman image showing the distribution of the high 5% of data values excluded from the color interpolation process to create the image shown in Figure 2G. Note that the pixels are located within the microvein and representative spectra from the original dataset verify the presence of hematite (A-D). The image was created utilizing the standard 5-95% setting.

Additionally, image quality may also be improved by excluding low data values in the left side of the data distribution from the color map interpolation process. This data manipulation seems relatively straightforward, univariate methods such as intensity at a point and sum of area under a Raman band create datasets in which high numerical values should imply the presence of a material and low values are due to noise in the spectra. Excluding a range of lower values due to noise from the color map interpolation process seems like a relatively simple and appropriate method to increase the visual quality of a Raman image, but this type of data manipulation is more complex and potentially problematic. A variety of factors influence the relative intensity, shape, and position of Raman bands including: Raman scattering cross-section and efficiency, crystallinity, crystal orientation, and particle size (Lee 2012, Lewis and Edwards 2001). The quality of the spectra in a hyperspectral dataset may also be influenced by a sample based issues

such as autofluorescence or various instrumental and external issues that affect the signal to noise (S:N) ratio (Pelletier 2003). These factors are important to consider as they can result in significant variation in the intensity, position, and shape of diagnostic Raman bands and the overall quality of the spectra in a hyperspectral dataset. Computer-based algorithms are necessary to analyze the large number of spectra comprising image datasets to create Raman images, but it's important to remember that the result of these analyses is not the same as inspection of all the collected spectra to visually identify or utilize group theory to identify a particular material. Determining an appropriate minimum value that both improves the visual quality and accurately represents the absence of a particular material that can be excluded from a color assignment is a difficult prospect due to variations in intensity, data quality, the analytical technique used, the inherent heterogeneity of geological samples, and the impracticality of visually inspecting every spectrum.

The hematite images in Figure 2 C and D were created by also excluding the lower 5% of the data values in the left side of the data distributions. Therefore, we should ask the same question as before; does excluding these values from the color interpolation affect the ability to accurately visualize the distribution of hematite in this sample? We hypothesize that a certain range of low values are due to noise and we can test this hypothesis by creating a Raman image of these values and interrogating representative spectra. Figure 4 shows that these values are distributed throughout the background of the image and typically outside the microvein region. Representative spectra show the presence of quartz and the absence of hematite, therefore excluding these values does not negatively affect the ability to identify the distribution of hematite in the resulting Raman image. Due to the impracticality of visually evaluating every spectrum in a hyperspectral dataset, it is difficult to empirically determine an appropriate lower

cut off value that represents the absence of a material, and it may be tempting to exclude more values in the lower end of the data distribution

Figure 4. Raman image showing the distribution of the low 5% of data values excluded from the color interpolation process to create the image shown in Figure 2G. Note that the pixels are located throughout the matrix portion of the image and representative spectra (A-D) from the original dataset verify the absence of hematite, and the presence of quartz (the intense Raman band at 464cm^{-1}). The image was created utilizing the standard 5-95% setting.

to create a more "aesthetically pleasing" image with better contrast. In this case, verifying that the excluded pixels did not misrepresent the spatial distribution of hematite showed that this manipulation was reasonable. But this type of manipulation can be problematic because it may create bit depth saturation artifacts, due to "truncation at brightest and darkest ends of the spectrum" caused by "overly zealous adjustments…to suppress background or make the image more striking" (Cromey, 2013). Two examples are shown in Raman images representing the distribution of carbonaceous material created from two common univariate methods and displayed with 3 different ranges of data assigned to the color interpolation (Fig. 5). Images A

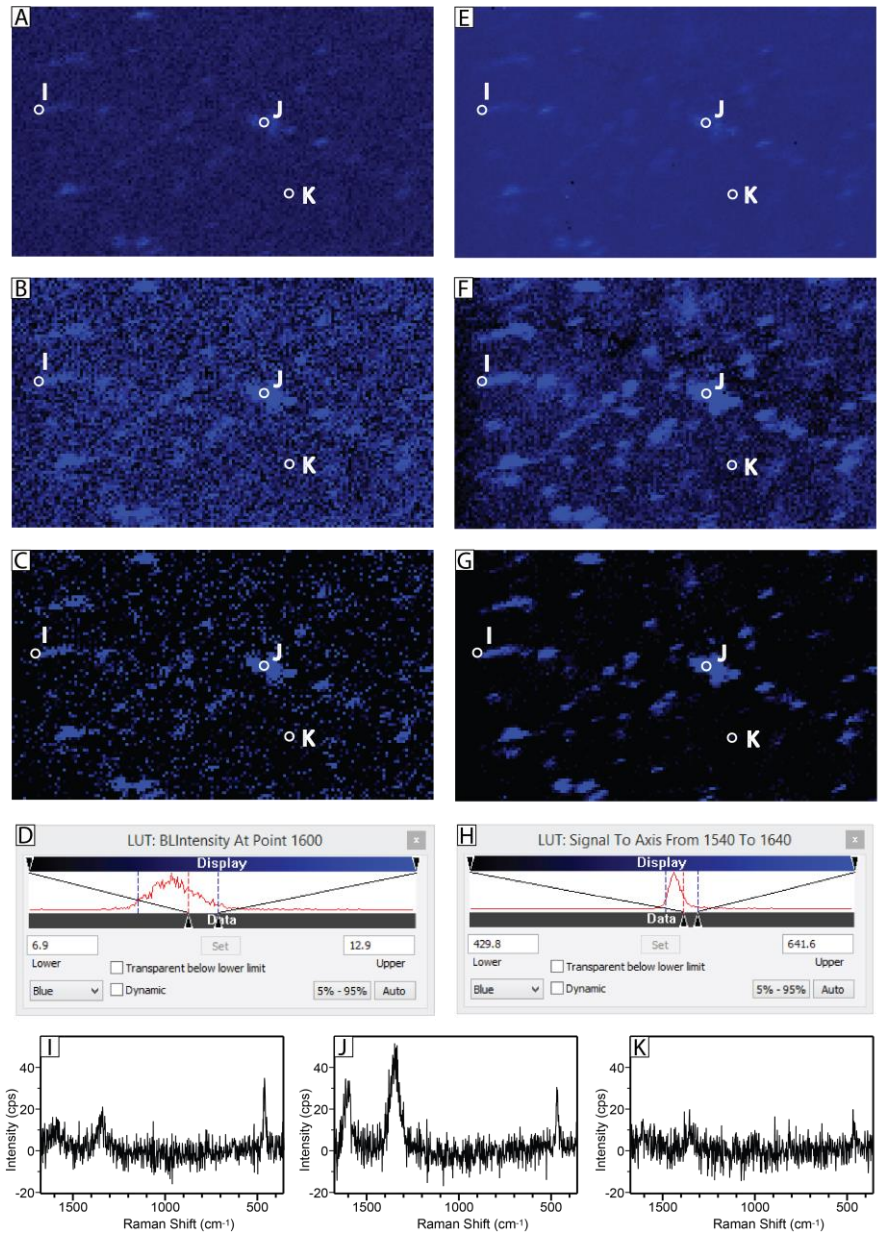

Figure 5. Raman images created from intensity at 1600 cm^{-1} analysis (A-C) and area under the G band region (1540-1640 cm^{-1}) representing the distribution of carbonaceous material displayed using three different image manipulation techniques. Images A and E were created by assigning the full range of data to the color map, B and F by assigning the central 90% of the data distribution and C and G by arbitrarily moving the left triangle sliders to exclude more data in the low value region of the data distributions from the color interpolation process. The blue dashed lines on the LUT screencaptures show the location of the upper and lower 5% data distribution cut off values and the dashed red lines show the position of the arbitrarily chosen low cut-off value (D and H).Representative spectra from three pixels that verify the presence of carbonaceous material as seen by the presence of the D and G bands are shown in I-K. Images A and E have very low visual color contrast due to the skewed shape of the data distributions. Images B and F have better contrast compared to A and E. Images C and G have substantially "better" color contrast, but this arbitrary manipulation resulted in false negative identification of carbonaceous material in pixels I and K in the intensity image (C) and in pixel I in the area image (G).

and E display the full range of data, images B and F were made by assigning the central 90% of the data distributions to the color map, and images C and G were created by setting the upper range of data to exclude the highest 5% of intensity or area values and arbitrarily manipulating the lower range of data values assigned to the color map interpolation process (Figure 5). The images based on the central 90% of the data have substantially better visual contrast than the full range images, but still have relatively low color contrast between pixels. Although the "enhanced" images (Fig. 5 C and G) have better color contrast, it is important to consider how an arbitrary definition of the range of numerically low data values (in these examples, intensity in cps or sum of intensity values under a defined area in cps) may have affected the accuracy of the spatial distribution of carbonaceous material depicted in the Raman images. For example, the spectrum at pixel J contains a relatively intense "G" band (Fig 5. J) which results in a positive carbon signal displayed by a colored pixel in all the images created from both analyses (Fig.5 A-C and E-G). The spectra at locations I and K have substantially less intense G bands, but carbonaceous material can be identified in the Raman images from both analyses when the images display the central 90% of the data (Fig. 5 B,F). Conversely, the manipulation applied to create images C and G (Fig. 5) excluded a larger range of the low intensity and area values calculated from the dataset from a color assignment resulting in false-negative depictions of carbonaceous material in pixel I in both images. Additionally, the relatively low intensity value calculated from spectrum K was also excluded from a color assignment resulting in a false-negative identification in the intensity image (Fig 5C), but the relatively low area value was not excluded in the area image (Fig. 5G) providing an accurate identification of carbonaceous material for spectrum K in that pixel. The images created from displaying the central 90% of the data and arbitrarily defining the range of data applied to the color map from both types of

univariate analyses depict carbonaceous material distributed throughout the quartz matrix of the sample, but vary in accuracy at the individual spectrum (pixel) scale. In this case, arbitrary manipulation of the amount and range of data in the low end of the data distributions assigned to the color interpolation process reduced the ability to accurately visualize the distribution of carbonaceous material in the resulting Raman images.

Researchers have noted that the appearance of Raman images can be influenced by software display settings and that careful consideration is necessary to determine appropriate settings (Clark and Šašić 2006, Dieing *et al.* 2010)**.** It may not be obvious to non-specialists that utilizing software-based image display manipulation techniques mathematically alters the underlying numerical results from univariate or multivariate analyses of Raman hyperspectral datasets. The power of Raman imaging is the ability to better understand and spatially depict the distribution of materials or variations in structure or chemistry in heterogeneous geological samples and it is "good to remember that serendipity has a wonderful role in science and that a published image may mean something entirely different to a reader from outside of our specific field of expertise" (Cromey, 2013). If the goal of presenting Raman images is to illustrate the general relative distribution of materials in a hyperspectral dataset, restricting the range of data assigned to a color map and displayed in a Raman image may be an appropriate form of data manipulation as long as the accuracy is unaffected and verified by visually assessing multiple representative spectra. But, caution is needed and verification is necessary when arbitrarily defining the range of data applied to a color interpolation if the goal of presenting Raman images is to illustrate the spectral (or pixel) scale distribution or to highlight subtle differences in spectral parameters, for example intensity, band area, or band shifts. If assigning the full range of data to a color map results in low contrast images, appropriate ranges of data to apply to the

color interpolation can be determined by testing several settings, creating Raman images showing the spatial distribution of the excluded data values, and verifying the presence or absence of materials by interrogating multiple representative spectra. Providing the results of verification analyses by presenting images and representative spectra in the methods or in supplementary material can aid in strengthening interpretations increasing the ability to compare and discuss results from different Raman systems, studies, and samples to better understand geological questions and the strengths and weaknesses of Raman hyperspectral imaging.

Additionally, it can be useful to utilize multiple analytical techniques and compare the resulting Raman images to obtain a more robust interpretation of complex geological hyperspectral datasets. For example, univariate intensity at a point analyses for the two best resolved hematite Raman bands shown in Figure 2 consistently show that hematite is present in the microvein. The univariate intensity at a point (1600 cm^{-1}) and area under the G band analyses and resulting Raman images both show that carbonaceous material occurs distributed throughout the quartz matrix in this sample (Fig. 5). Univariate analyses are based on a single, simple mathematical calculation, but multivariate analyses utilize and compare more information from all the spectra in a dataset. (Dieing et al. 2010). There are two categories of multivariate techniques that have been adapted by software developers to analyze Raman hyperspectral datasets: supervised analyses which depend on the input of reference information or spectra, and unsupervised techniques which use various statistical algorithms to identify components based on the shape of the spectra in a dataset (Lewis and Edwards 2001). Unsupervised techniques like Principle Component Analyses (PCA) calculate loadings spectra from a statistical model based on a linear combination of multiple spectral features. The resulting loadings spectra may or may not correspond to actual Raman spectra representing the chemical constituents in a sample due to

the statistical algorithm used, the presence of mixed spectra, the S:N ratio and data quality issues like autofluorescence (Dieing *et al.* 2010). Unsupervised multivariate techniques can be a useful first step in analyzing hyperspectral datasets especially if there is no *a priori* knowledge of sample composition, but caution is needed if techniques like PCA are solely used to create Raman images because the loadings spectra may not accurately reconstruct the characteristic spectra of all the materials in a dataset (Salzer and Siesler 2009).

Supervised techniques can provide a statistical likelihood of the contribution of a particular material to each spectrum in a dataset, but may be limited by prior knowledge of the composition of a sample (Zhang *et al.* 2005). Supervised multivariate techniques provide similar datasets to univariate analyses in which higher values represent a statistically higher correlation or relative contribution of a reference spectrum to the spectra in a dataset, and lower values represent the opposite situation. Previous work has shown that quartz, hematite, and carbonaceous material are the most common materials present in these samples (Emry *et al.* 2015, Marshall *et al.* 2011). Multivariate Direct Classical Least Squares analyses utilizing reference spectra acquired from the sample are shown in Figure 6. Least squares based methods calculate a value (typically between 0-1) that represents the relative contribution of each reference spectrum to all the spectra in the hyperspectral dataset, therefore the same issues arise when defining an appropriate minimum value that accurately represents the absence or statistically small contribution of a material in a Raman image at the pixel scale. This issue becomes more complex considering the heterogeneous nature of geological samples and the likelihood of spectra that represent mixtures of components. Mixed spectra can result from two general situations; first the presence of actual mixtures of materials present at the spectral acquisition point. For example, in the datasets shown here carbonaceous material is present in the

quartz matrix and the individual spectra therefore contain Raman bands diagnostic of both materials (e.g. the 464cm^{-1} quartz band and the D and G carbon bands). Secondly, confocal Raman acquisition methods excite a particular volume at depth within a sample depending on a variety of factors including: laser excitation wavelength, objective magnification, aperture type and size, the type of detector, and the structural details and refractive index of the sample (De Grauw *et al.* 1997, Everall 2000, Salzer and Siesler 2009).

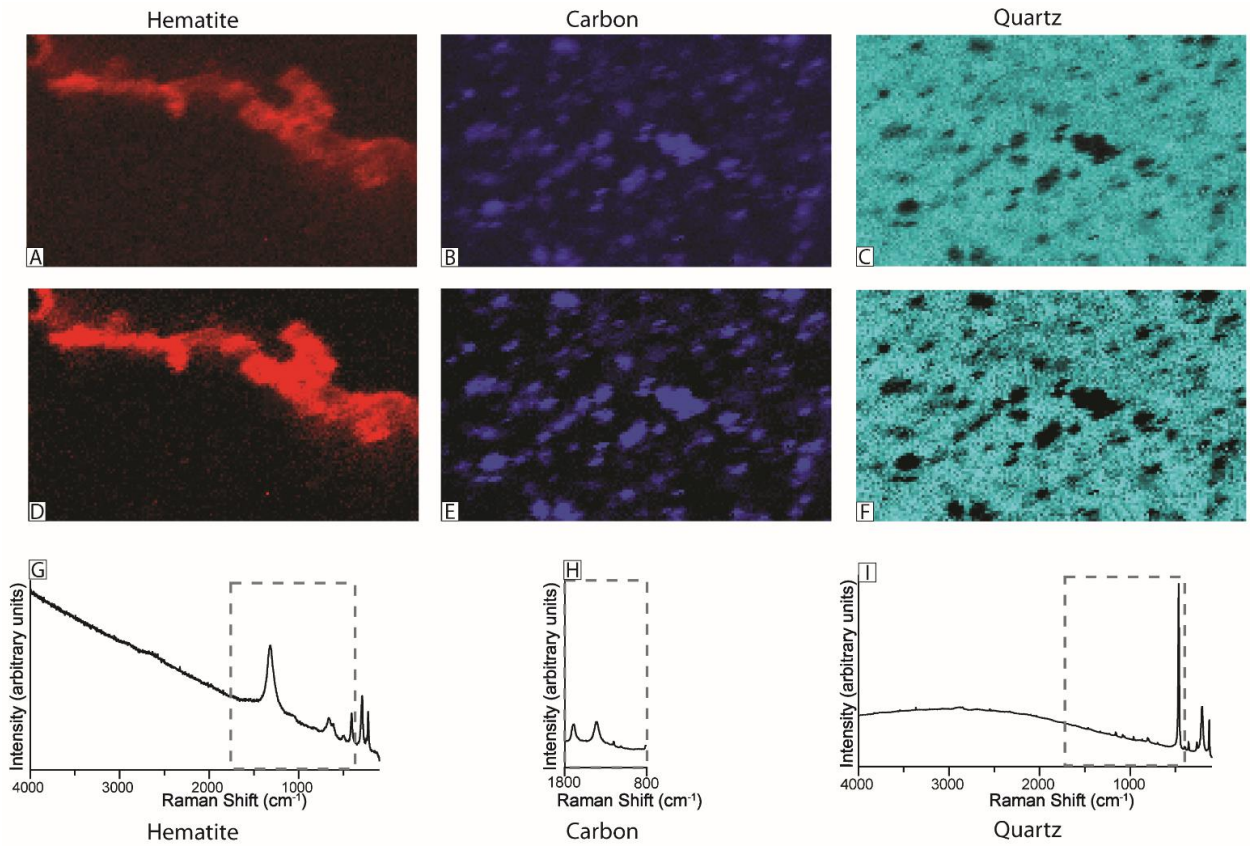

Figure 6. Images created utilizing DCLS analysis representing hematite (A,D), carbonaceous material (B,E) and quartz (C,F) and the reference spectra used in the calculation (G-I). The dashed boxes in the reference spectra show the portion of the spectra utilized by the DCLS algorithm. Images A-B were created by assigning the full range of data to the color interpolation process. Images D-F were created by assigning the central 90% of the data distribution to the color space providing improved visual contrast. Images created from DCLS analysis clearly show the presence of hematite in the microvein (A,D) and carbonaceous material (B,E) disseminated throughout the quartz matrix (C,F) in this sample.

These factors coupled with the depth, size, and orientation of a feature of interest may result in spectra that show the contribution of materials distributed around the feature as well as the feature itself. Therefore, arbitrary definition of the lowest classification value that accurately represents the absence of a material based on classified multivariate analysis may result in the same misidentification issues that can occur with univariate analyses. As a result, appropriate display parameters for multivariate images should also be experimentally evaluated and verified in the same manner as univariate analyses. In this case, the application of the color interpolation to the central 90% of the data distributions provided appropriate images that illustrate the spatial distribution of hematite and carbonaceous material (Fig. 6). Comparison of the images created from the various univariate analyses and DCLS multivariate analyses provide a consistent and robust interpretation of the distribution of materials present in the Raman hyperspectral dataset.

Software programs also provide methods to create composite Raman images that can display the spatial distribution and relationships between multiple materials. Horiba's software creates composite images using two different methods. The operator can choose between two settings, the software will either mix the colors in each pixel or display the brightest colored pixel at each point. Renishaw and WITec's software programs allow users to create and manipulate composite images by blending images and/or setting a user defined range of low value colored pixels to transparent. Identifying an appropriate minimum value that will not lead to misidentification of the spatial distribution of materials may be even more difficult when creating composite Raman images due to the ease of subjectively altering the range and amount of data that will appear in the image, the numerical range and shape of the different data distributions from different analyses, the number of images combined, and the variable software methods available to overlay or blend images. Caution should therefore be exercised when

creating composite Raman images and researchers should repeatedly ground truth the implied spatial distribution of materials created by different software display settings by evaluating Raman images created from the excluded values and visual inspection of these spectra from the original hyperspectral dataset.

CONCLUSIONS AND RECOMMENDATIONS

Software-based image manipulation techniques can be useful methods to enhance the visual quality of Raman images, but these techniques may lead to misrepresentation of the heterogeneities and complexities inherent in geological samples. Careful application of available software image manipulation techniques, verification, and explicit reporting of the techniques utilized can help foster objective comparison of interpretations based on Raman images from different Raman systems, samples, and studies and promote cross-disciplinary scientific discussion and progress. It is helpful to remember that "just because something can be done via imaging processing doesn't mean that it should be done" (Cromey, 2013). The selection of software-based settings used to generate images and any post-processing image manipulation should be afforded the same careful consideration as any other sample analysis or data processing method and tested, evaluated, and clearly reported. In order to avoid some of the potential pit-falls associated with Raman image processing of hyperspectral datasets, we suggest that researchers consider the following steps:

1) Avoid the temptation to create "good" Raman images that accentuate a preferred interpretation, instead consider the display of Raman images as an experiment. Test different software based image manipulation techniques, and evaluate the precision and accuracy of the

image in the context of the research goal. Reporting the results of verification analyses in the methods or supplementary material can strengthen interpretations made from Raman hyperspectral datasets.

2) If assigning the full range of data from univariate or multivariate analyses results in low contrast images, consider utilizing a standardized image manipulation technique. An example of this would be assigning the central 90% of the data distribution to the software generated color map. If the software does not have the capability to automatically perform this function, statistical analyses can be used to determine the cut-off values that can be manually entered. Raman software programs allow users to export image data as text files which can be imported into statistical analysis software programs that can be used to analyze the shape of the data distribution and calculate the upper and lower five percentile numerical values that can be assigned as cut-off values. While this technique may create images that are less "aesthetically pleasing" than arbitrary manipulation, utilizing a standardized method can foster the comparison of images created from datasets from different Raman systems, analytical techniques, data distribution shapes, and samples.

3) Explicitly report any software based image manipulation techniques utilized to create or modify Raman images and the rationale behind the use of the technique in the research methodology. Reporting the results of verification analyses of the appropriateness of the image manipulation techniques utilized can strengthen interpretations based on Raman images. For example, images showing the spatial distribution of data values excluded from the color map interpolation procedure and representative spectra from the original dataset. Due to space limitations, software manipulation technique verification analyses may not be easily included in

the main body of published studies, but the increasing availability of including online supplementary information can be a useful way to present this type of data.

4) Consider utilizing several software-provided univariate and multivariate techniques to create multiple Raman images for components from a single hyperspectral dataset. Comparing multiple images can provide for more robust and consistent interpretation of the distribution of materials in Raman hyperspectral datasets.

Acknowledgements

The authors would like to thank Michael Oweimrin, Dr. Wei Liu, Dr. Charles Ye, and Dr. Dina Bower for input and resources regarding Raman software capabilities. This work was funded by NSF grant EAR-1053241 and the Australian Research Council.

References

Almeida M.R., Correa D.N., Zacca J.J., Logrado L.P.L. and Poppi R.J. (2015) Detection of explosives on the surface of banknotes by Raman hyperspectral imaging and independent component analysis **Analytica Chimica Acta, 860,** 15-22.

Andrew J.J. and Hancewicz T.M. (1998) Rapid Analysis of Raman Image Data Using Two-Way Multivariate Curve Resolution **Applied Spectroscopy, 52,** 797-807.

ASTM (2010) Standard Terminology Relating to Molecular Spectroscopy. **(West Conshohocken, PA)**.

ASTM (2014) Standard Guide for Testing the Resolution of a Raman Spectrometer. **(West Conshohocken, PA)**.

Benos D. and Vollmer S. (2010) Generalizing on Best Practices in Image Processing: A Model for Promoting Research Integrity **Science and Engineering Ethics, 16,** 669-673.

Bernard S., Beyssac O. and Benzerara K. (2008) Raman Mapping Using Advanced Line-Scanning Systems: Geological Applications **Applied Spectroscopy, 62,** 1180-1188.

Boiret M., de Juan A., Gorretta N., Ginot Y.-M. and Roger J.-M. (2015) Distribution of a low dose compound within pharmaceutical tablet by using multivariate curve resolution on Raman hyperspectral images **Journal of Pharmaceutical and Biomedical Analysis, 103,** 35-43.

Burger W. and Burge M.J. (2013) Principles of Digital Image Processing: Advanced Methods. **Springer-Verlag (London),** 368 pp.

Campbell J.B. (2007) Introduction to Remote Sensing. **The Guilford Press (New York),** 626 pp.

Clark D. and Šašić S. (2006) Chemical images: Technical approaches and issues **Cytometry Part A, 69A,** 815-824.

Cromey D. (2010) Avoiding Twisted Pixels: Ethical Guidelines for the Appropriate Use and Manipulation of Scientific Digital Images **Science and Engineering Ethics, 16,** 639-667.

Cromey D.W. (2013) Digital Images Are Data: And Should Be Treated as Such **Methods in molecular biology (Clifton, N.J.), 931,** 1-27.

De Grauw C.J., Sijtsema N.M., Otto C. and Greve J. (1997) Axial resolution of confocal Raman microscopes: Gaussian beam theory and practice **Journal of Microscopy-Oxford, 188,** 273-279.

Dieing T., Hollricher O. and Toporski J. (2010) Confocal Raman Microscopy. **Springer (Berlin, Germany),** 289 pp.

Emry J.R., Marshall A.O. and Marshall C.P. (2015) Evaluating the Effects of Autofluorescence during Raman Hyperspectral Imaging **Geostandards and Geoanalytical Research,** DOI: 0.1111/j.1751-908X.2015.00354.x

Everall N.J. (2000) Confocal Raman microscopy: Why the depth resolution and spatial accuracy can be much worse than you think **Applied Spectroscopy, 54,** 1515-1520.

Gendrin C., Roggo Y. and Collet C. (2008) Pharmaceutical applications of vibrational chemical imaging and chemometrics: A review **Journal of Pharmaceutical and Biomedical Analysis, 48,** 533-553.

Ghasemzadeh-Barvarz M., Ramezani-Kakroodi A., Rodrigue D. and Duchesne C. (2013) Multivariate Image Regression for Quality Control of Natural Fiber Composites **Industrial & Engineering Chemistry Research, 52,** 12426-12436.

Grasselli J.G. (1991) JCAMP-DX, A STANDARD FORMAT FOR EXCHANGE OF INFRARED-SPECTRA IN COMPUTER READABLE FORM **Pure and Applied Chemistry, 63,** 1781-1792.

Hayden J.E. (2000) Digital manipulation in scientific images: some ethical considerations **J Biocommun, 27,** 11-9.

Krafft C., Cervellati C., Paetz C., Schneider B. and Popp J. (2012) Distribution of Amygdalin in Apricot (Prunus armeniaca) Seeds Studied by Raman Microscopic Imaging **Applied Spectroscopy, 66,** 644-649.

Kremenak N. and Siegel S.C. (2008) Images: To Alter or Not to Alter? The Ethics of Image Modification **Journal of Prosthodontics, 17,** 79-80.

Lee E. (2012) Imaging Modes. **In: Zoubir A. (ed), Raman Imaging. Springer Berlin Heidelberg,** 1-37.

Lee H.-C. (2005) Introduction to Color Imaging Science. **Cambridge University Press (Cambridge, UK),** 695 pp.

Lewis I.R. and Edwards H.G. (2001) Handbook of Raman Spectroscopy: From the Research Labratory to the Process Line. **Marcel Dekker Inc. (Switzerland),** 1055 pp.

Lünsdorf N.K., Dunkl I., Schmidt B.C., Rantitsch G. and von Eynatten H. (2014) Towards a Higher Comparability of Geothermometric Data obtained by Raman Spectroscopy of Carbonaceous Material. Part I: Evaluation of Biasing Factors **Geostandards and Geoanalytical Research, 38,** 73-94.

Marshall C.P., Emry J.R. and Olcott Marshall A. (2011) Haematite pseudomicrofossils present in the 3.5-billion-year-old Apex Chert **Nature Geosci, 4,** 240-243.

Marshall C.P. and Marshall A.O. (2011) Hematite and carbonaceous materials in geological samples: A cautionary tale **Spectrochimica Acta Part A: Molecular and Biomolecular Spectroscopy, 80,** 133-137.

Marshall C.P. and Olcott Marshall A. (2013) Raman hyperspectral imaging of microfossils: potential pitfalls **Astrobiology, 13,** 920-31.

Martin C. and Blatt M. (2013) Manipulation and Misconduct in the Handling of Image Data **The Plant Cell, 25,** 3147-3148.

McCreery R.L. (2006) Photometric Standards for Raman Spectroscopy. **Handbook of Vibrational Spectroscopy. John Wiley & Sons, Ltd**.

Nasdala L., Beyssac O., William Schopf J. and Bleisteiner B. (2012) Application of Raman-based images in the Earth sciences. **In: Zoubir A. (ed), Raman Imaging. Springer Berlin Heidelberg,** 145-187.

Nasdala L., Smith D.C., Kaindl R. and Ziemann M.A. (2004) Raman spectroscopy: analytical perspectives in mineralogical research **EMU notes in mineralogy,** 281-343.

Nature (2009) Image integrety and standards.
http://www.nature.com/authors/policies/image.html

Nature (2010) To err is human **Nature: Structural and Molecular Biology, 17,** 917-917.

Pelletier M.J. (2003) Quantitative Analysis Using Raman Spectrometry **Applied Spectroscopy, 57,** 20A-42A.

Richards J.A. (2013) Remote sensing Digital Image Analysis: An Introduction. **Springer-Verlag (Berlin),** 494 pp.

Rossner M. and Yamada K.M. (2004a) What's in a picture? The temptation of image manipulation **The Journal of Cell Biology, 166,** 11-15.

Sacré P.Y., De Bleye C., Chavez P.F., Netchacovitch L., Hubert P. and Ziemons E. (2014) Data processing of vibrational chemical imaging for pharmaceutical applications **Journal of Pharmaceutical and Biomedical Analysis, 101,** 123-140.

Salzer R. and Siesler H. (2009) Infrared and Raman Spectroscopic Imaging. **Wiley (Weinheim, Germany)**.

Sasic S., Clark D.A., Mitchell J.C. and Snowden M.J. (2004) A comparison of Raman chemical images produced by univariate and multivariate data processing-a simulation with an example from pharmaceutical practice **Analyst, 129,** 1001-1007.

Sasic S. and Ozaki Y. (2010) Raman, Infrared, and Near-Infrared Chemical Imaging. **Wiley (New Jersey)**.

Slobodan (2007) An In-Depth Analysis of Raman and Near-Infrared Chemical Images of Common Pharmaceutical Tablets **Applied Spectroscopy, 61,** 239-250.

Vajna B., Bodzay B., Toldy A., Farkas I., Igricz T. and Marosi G. (2012) Analysis of car shredder polymer waste with Raman mapping and chemometrics **Express Polymer Letters, 6,** 107-119.

Vajna B., Patyi G., Nagy Z., Bódis A., Farkas A. and Marosi G. (2011) Comparison of chemometric methods in the analysis of pharmaceuticals with hyperspectral Raman imaging **Journal of Raman Spectroscopy, 42,** 1977-1986.

Zhang L., Henson M.J. and Sekulic S.S. (2005) Multivariate data analysis for Raman imaging of a model pharmaceutical tablet **Analytica Chimica Acta, 545,** 262-278.

SUPPLEMENTARY MATERIAL

ORGANIZATION	LOCATION	RAMAN SYSTEM
University of Manitoba	Winnepeg, Manitoba, Canada	Bruker
Macquarie University	Sydney, Austraila	Jobin-Yvon Horiba
University of Bradford	Bradford, United Kingdom	Jobin-Yvon Horiba
Yale University	New Haven, CT, USA	Jobin-Yvon Horiba
University of Leicester	Leicester, United Kingdom	Jobin-Yvon Horiba
Arizona State	Tempe, AZ, USA	Jobin-Yvon Horiba
Duke University	Durham, NC, USA	Jobin-Yvon Horiba
Helmholtz-Zentrum Potsdam	Potsdam, Germany	Jobin-Yvon Horiba
Universite de Geneve	Geneva, Switzerland	Jobin-Yvon Horiba
University of Cincinatti	Cincinatti, OH, USA	Jobin-Yvon Horiba
Boston College	Boston, MA, USA	Jobin-Yvon Horiba
Laurentian University Sudbury (DES)	Ontario, Canada	Jobin-Yvon Horiba
Institut de Ciències de la Terra Jaume Almera	Barcelona, Spain	Jobin-Yvon Horiba
Museum für Naturkunde, Leibniz Institute at the Humboldt University Berlin	Berlin, Germany	Jobin-Yvon Horiba
University of Wisconsin Materials Science Center	Madison, WI, USA	Jobin-Yvon Horiba
Virginia Polytech	Blacksburg, VA, USA	Jobin-Yvon Horiba
University of Kansas	Lawrence, Kansas, USA	Renishaw
University of Cambridge	Cambridge, United Kingdom	Renishaw
University of Arizona	Tucson, AZ, USA	Renishaw
Stonybrook University	New York, NY, USA	Renishaw
Auburn University	Auburn, AL, USA	Renishaw
Washington University, St. Louis, MO	St. Louis, MO, USA	Renishaw
Rice University	Houston, TX, USA	Renishaw
St. Francis Xavier University	Antiqonish, Nova Scotia, Canada	Renishaw
National Center for Earth Science Studies, Ministry of Earth Sciences, Government of India	Thiruvananthapuram, Kerala, India	Renishaw
University of Auckland	Auckland, New Zealand	Renishaw
Montana Tech of the University of Montana	Butte, MT, USA	Renishaw
Hebrew University of Jerusalem	Jerusalem, Israel	Renishaw

University of Western Ontario	London, Ontario, Canada	Renishaw
Université de Lorraine	Lorraine, France	Renishaw
University of Waterloo	Waterloo, Ontario, Canada	Renishaw
Cornell University, Center for Materials Research	Ithaca, NY, USA	Renishaw
University of Glasgow	Glasgow, UK	Renishaw
Université Pierre et Marie Curie, Institut de Minéralogie, de Physique des Matériaux et de Cosmochimie (IMPMC)	Paris, France	Renishaw
China University of Geosciences	Wuhan, China	Renishaw
Charles University in Prague,	Prague, Czech Republic	Renishaw
State Key Laboratory of Geological Processes and Mineral Resources in China University of Geosciences.	Beijing, China	Renishaw
Institut für Mineralogie und Kristallographie, University of Vienna	Vienna, Austria	Renishaw and Jobin-Yvon Horiba
Western Kentucky University	Bowling Green, KY, USA	ThermoScientific
Stanford University	Stanford, CA, USA	WITec
University of Hawaii at Manoa	Honolulu, HI, USA	WITec
Centre de biophysique moleculaire	Orleans, France	WITec
Colorado School of Mines	Golden, CO, USA	WITec
Max Planck Institute for Astronomy	Jena, Germany	WITec

Figure S1. Survey of commercial Raman systems in geoscience academic departments and geological research organizations based on publically available online English language information. This survey was primarily based on attendees at the 2014 GeoRaman Conference and restricted to geoscience related departments and organizations excluding outside departments that may have Raman instruments accessible to geoscientists. Although this list is non-comprehensive, it illustrates that the most commonly available commercial systems are provided by Renishaw, WITec and Jobin Yvon Horiba. The author would appreciate any correspondence with updated or further information regarding the availability of commercial Raman systems in these entries and other geoscience departments and governmental or non-governmental organizations.

REFERENCE	RAMAN SYSTEM
Krishna *et al.*, 2015	Bruker
Caggiani *et al.*, 2014	Bruker
Kremer, Owocki, *et al.*, 2012	Jobin-Yvon_Horiba
Schopf and Kudryavtsev, 2009	Jobin-Yvon_Horiba
O'Brien and Ziemann, 2008	Jobin-Yvon_Horiba
Schopf *et al.*, 2005	Jobin-Yvon_Horiba
Schopf and Kudryavtsev, 2005	Jobin-Yvon_Horiba
Nguyen *et al.*, 2015	Jobin-Yvon_Horiba
Lamadrid *et al.*, 2014	Jobin-Yvon_Horiba
Baita *et al.*, 2014	Jobin-Yvon_Horiba
Gutierrez *et al.*, 2014	Jobin-Yvon_Horiba
Gayathri *et al.*, 2014	Jobin-Yvon_Horiba
Kazemi-Zanjani *et al.*, 2014	Jobin-Yvon_Horiba
dos Santos *et al.*2014	Jobin-Yvon_Horiba
Sharma *et al.*, 2013	Kaiser
Acosta-Maeda *et al.*, 2013	Kaiser
Marshall and Olcott Marshall, 2013	Renishaw
Corvisier *et al.*, 2010; Kremer, Bauer, *et al.*, 2012	Renishaw
Carter *et al.*, 2010	Renishaw
Bernard *et al.*, 2008	Renishaw
Souche *et al.*, 2012	Renishaw
Wang *et al* 2014	Renishaw
Sforna *et al.*, 2014	Renishaw
Veneranda *et al.*, 2014	Renishaw
Collins *et al.*, 2014	Renishaw
Lambert *et al.*, 2014	Renishaw
Konorov *et al.*, 2014	Renishaw
Mizukami *et al.*, 2008	ThermoScientific
Słaby *et al.*, 2014	WITec
de Castro *et al.*, 2014	WITec
Mikhno *et al.*, 2013	WITec
Foucher and Westall, 2012	WITec
Steele *et al.*, 2007	WITec
Steele *et al.*, 2012	WITec
Manjunath and Nair, 2015	WITec
Böttger *et al.*, 2014	WITec
Hambrock *et al.*, 2014	WITec
Singh *et al.*, 2014	WITec
Beierlein *et al.*, 2015	WITec

Figure S2. Web of Science survey of 40 examples of the commercial Raman systems utilized in published geoscience and geomaterials studies over the past 10 years based on the search terms "Raman imaging" in the geoscience related categories of: archeology, anthropology, art, crystallography, geology, geochemistry, geophysics, geoscience interdisciplinary, mineralogy, mining mineral processing and paleontology. Full cited references are included below:

Acosta-Maeda T.E., Scott E.R.D., Sharma S.K. and Misra A.K. (2013)
The pressures and temperatures of meteorite impact: Evidence from micro-Raman mapping of mineral phases in the strongly shocked Taiban ordinary chondrite **American Mineralogist, 98,** 859-869.

Baita C., Lottici P.P., Salvioli-Mariani E., Vandenabeele P., Librenti M., Antonelli F. and Bersani D. (2014) An integrated Raman and petrographic characterization of Italian mediaeval artifacts in pietra ollare (soapstone) **Journal of Raman Spectroscopy, 45,** 114-122.

Beierlein L., Nehrke G. and Brey T. (2015) Confocal Raman microscopy in sclerochronology: A powerful tool to visualize environmental information in recent and fossil biogenic archives **Geochemistry, Geophysics, Geosystems, 16,** 325-335.

Bernard S., Beyssac O. and Benzerara K. (2008) Raman Mapping Using Advanced Line-Scanning Systems: Geological Applications **Applied Spectroscopy, 62,** 1180-1188.

Böttger U., Meessen J., Martinez-Frias J., Hübers H.-W., Rull F., Sánchez F.J., de la Torre R. and de Vera J.-P. (2014) Raman spectroscopic analysis of the calcium oxalate producing extremotolerant lichen Circinaria gyrosa **International Journal of Astrobiology, 13,** 19-27.

Caggiani M.C., Acquafredda P., Colomban P. and Mangone A. (2014) The source of blue colour of archaeological glass and glazes: the Raman spectroscopy/SEM-EDS answers **Journal of Raman Spectroscopy, 45,** 1251-1259.

Carter E., Pasek M., Smith T., Kee T., Hines P. and Edwards H.M. (2010) Rapid Raman mapping of a fulgurite **Analytical and Bioanalytical Chemistry, 397,** 2647-2658.

Collins L., Tselev A., Jesse S., Okatan M.B., Proksch R., Mathews J.P., Mitchell G.D., Rodriguez B.J., Kalinin S.V. and Ivanov I.N. (2014) Breaking the limits of structural and mechanical imaging of the heterogeneous structure of coal macerals **Nanotechnology, 25,** 435402.

Corvisier J., Brunet F., Fabbri A., Bernard S., Findling N., Rimmelé G., Barlet-Gouédard V., Beyssac O. and Goffé B. (2010) Raman mapping and numerical simulation of calcium carbonates distribution in experimentally carbonated Portland-cement cores **European Journal of Mineralogy, 22,** 63-74.

de Castro I.A., Avansi W. and Ribeiro C. (2014) WO3/TiO2 heterostructures tailored by the oriented attachment mechanism: insights from their photocatalytic properties **CrystEngComm, 16,** 1514-1524.

dos Santos T.J.S., Amaral W.d.S., Ancelmi M.F., Pitarello M.Z., Fuck R.A. and Dantas E.L. U–Pb age of the coesite-bearing eclogite from NW Borborema Province, NE Brazil: Implications for western Gondwana assembly **Gondwana Research**.

Foucher F. and Westall F. (2012) Raman Imaging of Metastable Opal in Carbonaceous Microfossils of the 700–800 Ma Old Draken Formation **Astrobiology, 13,** 57-67.

Gayathri S., Jayabal P., Kottaisamy M. and Ramakrishnan V. (2014) Synthesis of few layer graphene by direct exfoliation of graphite and a Raman spectroscopic study **AIP Advances, 4,** 027116.

Gutierrez G., Normand F., Aweke F., Muller D., Speisser C. and Antoni F. (2014) Mechanism of Thin Layers Graphite Formation by 13C Implantation and Annealing **Applied Sciences, 4,** 180-194.

Hambrock C., Vincze-Minya K., Hild S. and Hassel A.W. (2014) Raman imaging for surface characterisation of annealed electrical steel surfaces **physica status solidi (a), 211,** 1429-1438.

Kakoulli I., Prikhodko S.V., King A. and Fischer C. (2014) Earliest evidence for asbestos composites linked to Byzantine wall paintings production **Journal of Archaeological Science, 44,** 148-153.

Kazemi-Zanjani N., Gobbo P., Zhu Z., Workentin M.S. and Lagugné-Labarthet F. (2014) High-resolution Raman imaging of bundles of single-walled carbon nanotubes by tip-enhanced Raman spectroscopy **Canadian Journal of Chemistry, 93,** 51-59.

Konorov S.O., Schulze H.G., Blades M.W. and Turner R.F.B. (2014) Silicon–Gold–Silica Lamellar Structures for Sample Substrates That Provide an Internal Standard for Raman Microspectroscopy **Analytical Chemistry, 86,** 9399-9404.

Kremer B., Bauer M., Stark R.W., Gast N., Altermann W., Gursky H.-J., Heckl W.M. and Kazmierczak J. (2012a) Laser-Raman and atomic force microscopy assessment of the chlorococcalean affinity of problematic microfossils **Journal of Raman Spectroscopy, 43,** 32-39.

Kremer B., Owocki K., Królikowska A., Wrzosek B. and Kazmierczak J. (2012b) Mineral microbial structures in a bone of the Late Cretaceous dinosaur Saurolophus angustirostris from the Gobi Desert, Mongolia — a Raman spectroscopy study **Palaeogeography, Palaeoclimatology, Palaeoecology, 358–360,** 51-61.

Krishna R., Jones A.N., Edge R. and Marsden B.J. (2015) Residual stress measurements in polycrystalline graphite with micro-Raman spectroscopy **Radiation Physics and Chemistry, 111,** 14-23.

Lamadrid H.M., Lamb W.M., Santosh M. and Bodnar R.J. (2014) Raman spectroscopic characterization of H2O in CO2-rich fluid inclusions in granulite facies metamorphic rocks **Gondwana Research, 26,** 301-310.

Lambert D., Muehlethaler C., Gueissaz L. and Massonnet G. (2014) Raman analysis of multilayer automotive paints in forensic science: measurement variability and depth profile **Journal of Raman Spectroscopy, 45,** 1285-1292.

Manjunath G.L. and Nair R.R. (2015) Implications of the 3D micro scale coal characteristics along with Raman stress mapping of the scratch tracks **International Journal of Coal Geology, 141–142,** 13-22.

Marshall C.P. and Olcott Marshall A. (2013) Raman hyperspectral imaging of microfossils: potential pitfalls **Astrobiology, 13,** 920-31.

Mikhno A.O., Schmidt U. and Korsakov A.V. (2013) Origin of K-cymrite and kokchetavite in the polyphase mineral inclusions from Kokchetav UHP calc-silicate rocks: evidence from confocal Raman imaging **European Journal of Mineralogy, 25,** 807-816.

Mizukami T., Wallis S., Enami M. and Kagi H. (2008) Forearc diamond from Japan **Geology, 36,** 219-222.

Nguyen V.T., Nam D., Gansukh M., Park S.-N., Sung S.-J., Kim D.-H., Kang J.-K., Sai C.D., Tran T.H. and Cheong H. (2015) Influence of sulfate residue on Cu2ZnSnS4 thin films prepared by direct solution method **Solar Energy Materials and Solar Cells, 136,** 113-119.

O'Brien P.J. and Ziemann M.A. (2008) Preservation of coesite in exhumed eclogite: insights from Raman mapping **European Journal of Mineralogy, 20,** 827-834.

Schopf J.W. and Kudryavtsev A.B. (2005) Three-dimensional Raman imagery of precambrian microscopic organisms **Geobiology, 3,** 1-12.

Schopf J.W. and Kudryavtsev A.B. (2009) Confocal laser scanning microscopy and Raman imagery of ancient microscopic fossils **Precambrian Research, 173,** 39-49.

Schopf J.W., Kudryavtsev A.B., Agresti D.G., Czaja A.D. and Wdowiak T.J. (2005) Raman Imagery: A New Approach to Assess the Geochemical Maturity and Biogenicity of Permineralized Precambrian Fossils **Astrobiology, 5,** 333-371.

Sforna M.C., van Zuilen M.A. and Philippot P. (2014) Structural characterization by Raman hyperspectral mapping of organic carbon in the 3.46 billion-year-old Apex chert, Western Australia **Geochimica Et Cosmochimica Acta, 124,** 18-33.

Sharma S.K., Porter J.N., Misra A.K., Helsley C.E. and Bates D.E. (2013) Scanning time-resolved standoff Raman instrument for large-area mineral detection on planetary surfaces **European Journal of Mineralogy, 25,** 715-720.

Singh V.K., Elomaa O., Johansson L.-S., Hannula S.-P. and Koskinen J. (2014) Lubricating properties of silica/graphene oxide composite powders **Carbon, 79,** 227-235.

Słaby E., Domonik A., Śmigielski M., Majzner K., Motuza G., Götze J., Simon K., Moszumańska I., Kruszewski Ł. and Rydelek P. (2014) Protomylonite evolution potentially revealed by the 3D depiction and fractal analysis of chemical data from a feldspar **Contributions to Mineralogy and Petrology, 167,** 1-23.

Souche A., Beyssac O. and Andersen T.B. (2012) Thermal structure of supra-detachment basins: a case study of the Devonian basins of western Norway **Journal of the Geological Society, 169,** 427-434.

Steele A., Fries M.D., Amundsen H.E.F., Mysen B.O., Fogel M.L., Schweizer M. and Boctor N.Z. (2007) Comprehensive imaging and Raman spectroscopy of carbonate globules from Martian meteorite ALH 84001 and a terrestrial analogue from Svalbard **Meteoritics & Planetary Science, 42,** 1549-1566.

Steele A., McCubbin F.M., Fries M.D., Golden D.C., Ming D.W. and Benning L.G. (2012) Graphite in the martian meteorite Allan Hills 84001 **American Mineralogist, 97,** 1256-1259.

Veneranda M., Irazola M., Pitarch A., Olivares M., Iturregui A., Castro K. and Madariaga J.M. (2014) In-situ and laboratory Raman analysis in the field of cultural heritage: the case of a mural painting **Journal of Raman Spectroscopy, 45,** 228-237.

Wang A., Korotev R.L., Jolliff B.L. and Ling Z. (in press) Raman imaging of extraterrestrial Materials **Planetary and Space Science**. http://dx.doi.org/10.1016/j.pss.2014.10.005

Appendix B: Preliminary Evidence of Thermal Alteration of the ~3.45 Ga Apex chert from Fluid Inclusion Microthermometry

INTRODUCTION

Studying early Earth history presents a significant challenge because plate tectonic processes have recycled most of the early Earth's crust and left the remaining rocks metamorphically altered. Dewit (1998) estimated that early Archean (3-4 Ga) and late Archean (2.5-3 Ga) rocks combined comprise only 7.5% of the present-day exposed continental area. Approximately 35 large Archean-age cratonic fragments have been identified and dated, but the majority of them are poorly exposed making them difficult to map and correlate (Bleeker, 2003). The Pilbara craton in Western Australia is perhaps the most extensively studied of the four cratonic fragments that have relatively good field exposure. It is also commonly believed to be the least tectonically deformed or metamorphically altered and is therefore a major target for studies of the Archean environment (de Wit, 1998; Wacey, 2009). Rocks from the Pilbara craton have been used to study a wide range of topics including the timing of oxygenation of the atmosphere, ocean chemistry, and Archean plate tectonics; but the majority of studies have focused on elucidating evidence for the early life (Allwood *et al.*, 2007; Kato *et al.*, 2009; Orberger *et al.*, 2006; Pinti *et al*., 2009; Scott *et al*., 2011; Van Kranendonk, 2006a).

The Apex chert is among the most well publicized of the Archean geological units from the Pilbara craton that have been studied for evidence for the oldest life on Earth. Several types of data including mineralogy, textures, carbon isotopes, and the presence and structural characteristics of the carbonaceous material in the Apex chert have been used to interpret how the rocks formed and provide evidence of early life. (De Gregorio *et al*., 2009; Schopf, 1993; Schopf *et al*., 2005; Schopf *et al.*, 2002). However, the fact that these lines of evidence can be

affected by later metamorphic alteration of the rocks is rarely considered. For example, metamorphism can affect carbon isotope values (Hayes *et al.*, 1983; Hoefs and Frey, 1976; McKirdy and Powell, 1974) and later fluid alteration can introduce exogenous carbonaceous material (Papineau *et al.*, 2011; Olcott Marshall *et al*, 2014). Studies of Archean rocks rarely address the potential effects of secondary alteration which can lead to the misinterpretation of data regarding the original formation of the rocks and evidence for ancient life. This lack of information on metamorphic alteration of Archean rocks has led to many debates on the interpretation of evidence cited for Archean environments and ancient life (Dauphas *et al*., 2007; Fedo and Whitehouse, 2002; Gruau *et al*., 1992; Naraoka *et al*., 1996; Rasmussen *et al*., 2008). Therefore, any study of Archean rocks should address evidence for both the original formation of the rocks and for the degree of later alteration or metamorphism.

The Apex chert is generally believed to have undergone relatively low-grade metamorphism to prehnite-pumpellyite (~250-350 °C) or lower greenschist facies (~300-425 °C) based on mineral assemblages from surrounding units (Blatt *et al*., 2005; Brasier *et al*., 2005; Schopf, 1993; Van Kranendonk, 2006b). The metamorphic of alteration of the Apex chert has not been determined directly because it is composed dominantly of quartz and does not contain mineral assemblages diagnostic of metamorphic grade. Background information on the Apex chert discussed in Chapter 2 illustrates that the unit may have a much more complex formational and alteration history than previously thought.

Fluid inclusion microthermometry has been used to study the pressure and temperature (P/T) conditions involved in metamorphic alteration of other quartz-rich Archean rocks, especially ore deposits (Channer and Spooner, 1994; Klemd, 1999; Poutiainen and Partamies, 2003). Although fluid inclusion studies of metamorphic rocks can be complex, laboratory and

field studies have shown the potential to obtain data addressing the original P/T conditions of formation, P/T conditions associated with prograde or retrograde metamorphism and even peak metamorphic conditions (Barker, 1995; Touret, 2001; Vityk and Bodnar, 1995a; Vityk and Bodnar, 1998). Fluid inclusion microthermometry research was originally planned as a part of this dissertation in order to better understand the formation and alteration of the Apex chert. This appendix documents preliminary fluid inclusion microthermometry work done in during this dissertation. Further work was not performed for two reasons, first the focus of my research transitioned towards better understanding important Raman spectroscopic based methodical issues. Secondly, although a suite of fluid inclusion thin sections were made by Burnham Petrographic for use in this research, they were constructed with epoxy that could not be dissolved. Therefore, these samples were not able to be used because the rock chips could not be removed from the glass slide for use in a fluid inclusion heating and cooling stage as per standard practice.

MATERIALS AND METHODS

Apex chert Samples

The main Apex chert dike at the Chinaman Creek locality was sampled during the Geological Society of Western Australia Pilbara fieldtrip in 2006. Fourteen samples were collected approximately 10 m apart up the outcrop starting 10 m below the original microfossil locality and ending at the contact with the overlying stratiform chert. Suites of standard 30 µm thin sections and 300 µm paleontological sections were made for petrographic description. Approximately 100 µm thick fluid inclusion thin sections were prepared for fluid inclusion microthermometry according to the methods outlined in (Goldstein and Reynolds, 1994).

Analytical Methods

Microscopy and paragenetic description were done using an Olympus BX60 microscope equipped with 40X and 100X UIS objectives and a Qicam Qimaging color Fast 1394 video camera. Fluid inclusion microthermometry was performed under the microscope with a Linkam THMS 600 heating and freezing stage attached to a PC running LinkSys software. Heating runs to measure homogenization temperatures were performed on pieces of thin-sections that had been cut and removed from the glass slide using a self-sealing 100X objective attached to the Linkham stage. Fluid inclusion assemblages, the most finely discriminated suites of petrographically associated fluid inclusions that formed during a specific event (such as a single healed fracture or a mineral growth zone) were described according to the method outlined in Goldstein and Reynolds (1994). Fluid inclusions were classified according to the 4-fold classification (primary, secondary, pseudosecondary and indeterminable) as described by (Goldstein and Reynolds, 1994). For this study, two cross-cutting fluid inclusion assemblages were chosen and a total of 7 fluid inclusions were analyzed. Homogenization temperatures were obtained using a cycling technique that allowed for careful determination of homogenization values (Goldstein and Reynolds, 1994). For the fluid inclusions that homogenized below 300° C, each individual fluid inclusion homogenization temperature was measured three times and an average value was obtained. Several fluid inclusions did not homogenize below a temperature of 300° C. In these cases, the heating run was stopped at this point to avoid heating damage, therefore this temperature only represents a minimum threshold value for these fluid inclusions. Phase changes during cooling runs were difficult to observe, and eutectic temperatures could not be determined. The final phase change identified when the bubble reappeared in the fluid

inclusions was recorded as a final melting temperature, but it is unclear if this value represents a true melting temperature or a metastable phase. Therefore, these data were not included and will not be discussed in this study.

RESULTS

Generalized Paragenesis

Paragenesis of the Apex chert is highly complex due to the predominance of brecciated fabrics and variety of textures evident in the rocks. A sequence of events was described for each individual sample to attempt to establish repeating patterns of reoccurring paragenetic phases. The majority of the Apex chert consists of microcrystalline quartz matrix (≤10 μm) that displays a wide variety of textures. There appears to be more consistency in the cross-cutting veins that occur in the matrix. There are at least 2 generations of quartz veins and a generation of quartz and hematite-rich veins that cross-cut the matrix in several samples. In some areas the earliest set of cross-cutting veins contain relic fibrous quartz textures ("chalcedony") interspersed with recrystallized, equant meso-to macroquartz that has triple-junction crystal boundaries. This paragenetic phase was the focus of the fluid inclusion analysis presented below.

Fluid Inclusion Petrography

Fluid inclusions are extremely abundant and occur in multiple cross-cutting assemblages within and across crystal boundaries. Both fluid inclusion assemblages were from a single crystal in one of these veins and both assemblages contained larger (~2-5 μm) two-phase gas/liquid fluid inclusions and smaller (≤ 2 μm) single-phase all-liquid fluid inclusions. The two-phase

inclusions had somewhat consistent liquid to vapor (L:V) ratios. Homogenization temperature data (T_h) from the two-phase inclusions in two cross-cutting fluid inclusion assemblages (FIA A and FIA B) from a recrystallized relic-fibrous textured quartz veins are shown in Table 1. Both fluid inclusion assemblages analyzed occur in three-dimensional, curvilinear arrays that cross-cut crystal growth zone boundaries, but terminate before the crystal edges. Figure 1 illustrates the relationship of the fluid inclusion assemblages that were analyzed. The two fluid inclusions measured from FIA A have a wide range in T_h values, although two samples are not enough to define a statistically significant trend. The fluid inclusion T_h from FIA B are bimodal in distribution with one suite ranging from 158-169° C and a second suite that had not homogenized at 300° C when the analyses were stopped.

Flinc	T_h °C
1	157.5
4	180.5
2	166.4
3	158
5	162.5
6	169
7	>300
8	>300

Table 1. Homogenization temperature data for the 2 fluid inclusion assemblages analyzed in this study. FIA A is in red and FIA B is in blue and correspond to the location of the fluid assemblages in Fig. 1.

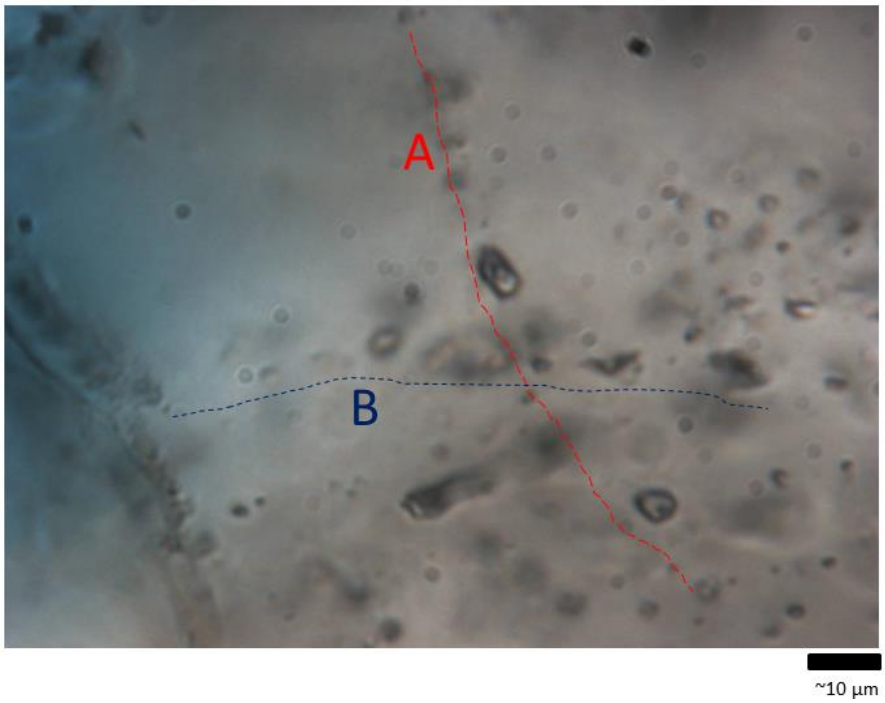

Figure 1. Photomicrograph showing the locations of FIA A and B. Colors correspond to data presented in Table 1.

DISCUSSION

FIA A and B are likely pseudosecondary in origin due to their shape and distribution within the macroquartz crystal. In general, the T_h values are highly variable, but within the 6 fluid inclusions analyzed in FIA B there are two data clusters: a lower temperature cluster (range, 158-169 ° C, average of 165.7° C) and a cluster that had not homogenized at 300° C. Large ranges in the low-temperature suite could be due to several factors including heterogeneous entrapment, necking down after a phase change, or thermal re-equilibration (Goldstein and Reynolds, 1994). Petrographic pairing of liquid-rich and gas-rich inclusions was not observed, therefore necking down after a phase change is a less likely explanation for the data variability, but more work is required to completely rule this possibility out. In FIA B there was evidence for some variation in the L:V ratio, but the observed variation was not as high as typically seen

resulting from heterogeneous entrapment. Further work defining and studying multiple FIA's in these rocks is needed to fully address the possibility of heterogeneous entrapment.

Thermal re-equilibration of the fluid inclusions is a significant possibility as these rocks have undergone metamorphic alteration. Highly variable T_h are common in metamorphic systems as a variety of factors including size, shape, and composition affect if and how a particular fluid inclusion will re-equilibrate (Bodnar, 2003).

Currently, the composition of the fluid inclusions in this study remains unknown, but the T_h can provide a rough estimate of one aspect of the thermal history. It is unclear if the lower temperature suite of fluid inclusions records the original temperatures of formation or a later relatively low grade metamorphic event, but the higher temperature suite suggests that the Apex chert may have experienced a phase of higher alteration temperatures. Homogenization temperatures of >300° C from two of the fluid inclusions is consistent with higher grade (greenschist to possibly amphibolite facies) metamorphism suggested by Raman spectroscopy analysis of thermally mature carbonaceous material in the Apex chert (Olcott Marshall *et al.*, 2012). But, more work will be necessary to further characterize the thermal alteration history of this unit.

FIA identification in a paragenetic framework, careful identification of L:V ratios in FIA's and evidence for necking-down or reequilibration of fluid inclusions must be documented. If phase changes continue to be difficult to observe in other samples, Raman spectroscopy could be utilized to determine the composition of the fluid inclusions in order to apply the appropriate phase diagrams and evaluate the validity of T_h data.

Studies of both synthetic and natural metamorphic fluid inclusions have shown that microthermometric data commonly have characteristic distributions and can be used to interpret

evidence for isobaric versus isothermal metamorphic pathways, multiple generations of metamorphic alteration and estimates of maximum metamorphic P/T conditions given careful identification of FIA's and large samples sizes (Touret, 2001; Vityk and Bodnar, 1995b; Vityk and Bodnar, 1998).

The presence of single-phase all-liquid and 2-phase liquid/vapor fluid inclusions within the FIA's could be a result of nucleation metastability in the smaller fluid inclusions (Goldstein and Reynolds, 1994). Conversely, research has shown that shock-metamorphism can affect fluid inclusions and commonly reequilibrates two-phase liquid/vapor inclusions to all–liquid single phase inclusions (Madden *et al.*, 2004; Madden *et al*., 2006). Evidence for a meteorite impact in the Antarctic Chert member of the Apex Basalt suggests that impact-related reequilibration of fluid inclusions in the Apex chert could be a factor, but more work will need to be done to distinguish between this mechanism and nucleation metastability.

Fluid inclusions have the potential to provide data critical to unraveling the complex deformational and metamorphic histories of Archean rocks. When applied appropriately this technique can be a powerful tool to evaluate the likelihood that Archean rocks could preserve evidence of Archean environments or ancient life and evaluate the metamorphic processes that have affected Archean rocks.

CONCLUSIONS

Although the Apex chert has been studied for over 20 years, questions remain regarding its environment of formation and subsequent metamorphic alteration history. The Pilbara region has undergone multiple episodes of regional, contact and impact related metamorphism and

recent studies have suggested that the metamorphic history of the Apex chert is more complex than previously thought. More work needs to be done to understand the thermal history of these rocks because metamorphism can affect the lines of evidence used to study Archean environments and evidence for early life. Preliminary fluid inclusion microthermometry data support previous interpretations that the Apex chert has been affected by multiple alteration events and that that these rocks may have seen higher grade metamorphism (>300° C) than what is typically ascribed to this unit. Future work will focus on fluid inclusion microthermometry within a parageneticframework that will allow for a greater understanding of the style, relative timing, and degree of metamorphic conditions that have affected the Apex chert.

References

Allwood, A.C., Walter, M.R., Burch, I.W., Kamber, B.S., 2007. 3.43 billion-year-old stromatolite reef from the Pilbara Craton of Western Australia: Ecosystem-scale insights to early life on Earth. Precambrian Research 158, 198-227.

Barker, A.J., 1995. Post-entrapment modification of fluid inclusions due to overpressure: evidence from natural samples. Journal of Metamorphic Geology 13, 737-750.

Blatt, H., Tracey, R., Owens, B., 2005. Petrology: Igneous, Sedimentary and Metamorphic, 3rd ed. . W. H. Freeman and Company, New York

Bleeker, W., 2003. The late Archean record: a puzzle in ca. 35 pieces. Lithos 71, 99-134.

Blewett, R.S., 2002. Archaean tectonic processes: a case for horizontal shortening in the North Pilbara Granite-Greenstone Terrane, Western Australia. Precambrian Research 113, 87-120.

Bodnar, R.J., 2003. Reequilibration of fluid inclusions. Short Course Series - Mineralogical Association of Canada 32, 213-231.

Brasier, M.D., Green, O.R., Lindsay, J.F., McLoughlin, N., Steele, A., Stoakes, C., 2005. Critical testing of Earth's oldest putative fossil assemblage from the ~3.5 Ga Apex chert, Chinaman Creek, Western Australia. Precambrian Research 140, 55-102.

Channer, D.M.D., Spooner, E.T.C., 1994. Combined gas and ion chromatographic and analysis of fluid inclusions; applications to Archean granite pegmatite and pegmatite and gold-quartz vein fluids. Geochimica et Cosmochimica Acta 58, 1101-1118.

Dauphas, N., van Zuilen, M., Busigny, V., Lepland, A., Wadhwa, M., Janney, P.E., 2007. Iron isotope, major and trace element characterization of early Archean supracrustal rocks from SW Greenland: Protolith identification and metamorphic overprint. Geochimica et Cosmochimica Acta 71, 4745-4770.

De Gregorio, B.T., Sharp, T.G., Flynn, G.J., Wirick, S., Hervig, R.L., 2009. Biogenic origin for Earth's oldest putative microfossils. Geology 37, 631-634.

de Wit, M.J., 1998. On Archean granites, greenstones, cratons and tectonics: does the evidence demand a verdict? Precambrian Research 91, 181-226.

Fedo, C.M., Whitehouse, M.J., 2002. Metasomatic Origin of Quartz-Pyroxene Rock, Akilia, Greenland, and Implications for Earth's Earliest Life. Science 296, 1448-1452.

Goldstein, R.H., Reynolds, T.J., 1994. Systematics of Fluid Inclusions in Diagenetic Minerals. SEPM, Tulsa, Oklahoma.

Gruau, G., Tourpin, S., Fourcade, S., Blais, S., 1992. Loss of isotopic (Nd, O) and chemical (REE) memory during metamorphism of komatiites: new evidence from eastern Finland. Contributions to Mineralogy and Petrology 112, 66-82.

Hayes, J.M., Kaplan, I.R., Wedeking, K.W., 1983. Precambrian organic geochemistry; preservation of the record. Princeton Univ. Press, Princeton, NJ.

Hoefs, J., Frey, M., 1976. The isotopic composition of carbonaceous matter in a metamorphic profile from the Swiss Alps. Geochimica et Cosmochimica Acta 40, 945-951.

Kato, Y., Suzuki, K., Nakamura, K., Hickman, A.H., Nedachi, M., Kusakabe, M., Bevacqua, D.C., Ohmoto, H., 2009. Hematite formation by oxygenated groundwater more than 2.76 billion years ago. Earth and Planetary Science Letters 278, 40-49.

Klemd, R., 1999. A comparison of fluids causing post-depositional hydrothermal alteration in Archaean basement granitoids and the Witwatersrand Basin. Mineralogy and Petrology 66, 111-122.

McKirdy, D.M., Powell, T.G., 1974. Metamorphic Alteration of Carbon Isotopic Composition in Ancient Sedimentary Organic Matter: New Evidence from Australia and South Africa. Geology 2, 591-595.

Naraoka, H., Ohtake, M., Maruyama, S., Ohmoto, H., 1996. Non-biogenic graphite in 3.8-Ga metamorphic rocks from the Isua district, Greenland. Chemical Geology 133, 251-260.

Olcott Marshall, A., Jehlicka, J., Rouzaud, J. N., & Marshall, C. P. (2014). Multiple generations of carbonaceous material deposited in Apex chert by basin-scale pervasive hydrothermal fluid flow. *Gondwana Research, 25*(1), 284-289.

Olcott Marshall, A., Emry, J.R., Marshall, C.P., 2012. Multiple Generations of Carbon in the Apex Chert and Implications for Preservation of Microfossils. Astrobiology 12, 160-166.

Orberger, B., Rouchon, V., Westall, F., de Vries, S.T., Pinti, D.L., Wagner, C., Wirth, R., Hashizume, K., 2006. Microfacies and origin of some Archean cherts (Pilbara, Australia). Geological Society of America Special Papers 405, 133-156.

Papineau, D., De Gregorio, B.T., Cody, G.D., O/'Neil, J., Steele, A., Stroud, R.M., Fogel, M.L., 2011. Young poorly crystalline graphite in the >3.8-Gyr-old Nuvvuagittuq banded iron formation. Nature Geosci 4, 376-379.

Pinti, D.L., Mineau, R., Clement, V., 2009. Hydrothermal alteration and microfossil artefacts of the 3,465-million-year-old Apex chert. Nature Geosci 2, 640-643.

Poutiainen, M., Partamies, S., 2003. Fluid Inclusion Characteristics of Auriferous Quartz Veins in Archean and Paleoproterozoic Greenstone Belts of Eastern and Southern Finland. Economic Geology 98, 1355-1369.

Rasmussen, B., Fletcher, I. R., Brocks, J. J., & Kilburn, M. R. (2008). Reassessing the first appearance of eukaryotes and cyanobacteria. *Nature, 455*, 1101-1104.

Schopf, J.W., 1993. Microfossils of the Early Archean Apex Chert: New Evidence of the Antiquity of Life. Science 260, 640-646.

Schopf, J.W., Kudryavtsev, A.B., Agresti, D.G., Czaja, A.D., Wdowiak, T.J., 2005. Raman Imagery: A New Approach to Assess the Geochemical Maturity and Biogenicity of Permineralized Precambrian Fossils. Astrobiology 5, 333-371.

Schopf, J.W., Kudryavtsev, A.B., Agresti, D.G., Wdowiak, T.J., Czaja, A.D., 2002. Laser-Raman imagery of Earth's earliest fossils. Nature [London] 416, 73-76.

Schopf, J.W., Kudryavtsev, A.B., Czaja, A.D., Tripathi, A.B., 2007. Evidence of Archean life: Stromatolites and microfossils. Precambrian Research 158, 141-155.

Scott, C.T., Bekker, A., Reinhard, C.T., Schnetger, B., Krapez, B., Rumble, D., III, Lyons, T.W., 2011. Late Archean euxinic conditions before the rise of atmospheric oxygen. Geology 39, 119-122.

Touret, J.L.R., 2001. Fluids in metamorphic rocks. Lithos 55, 1-25.

Van Kranendonk, M.J., 2006a. Volcanic degassing, hydrothermal circulation and the flourishing of early life on Earth: A review of the evidence from c. 3490-3240 Ma rocks of the Pilbara Supergroup, Pilbara Craton, Western Australia. Earth-Science Reviews 74, 197-240.

Van Kranendonk, M.J., 2006b. Volcanic degassing, hydrothermal circulation and the flourishing of early life on Earth: A review of the evidence from c. 3490-3240 Ma rocks of the Pilbara Supergroup, Pilbara Craton, Western Australia. Earth-Science Reviews 74, 197-240.

Vityk, M.O., Bodnar, R.J., 1995a. Do fluid inclusions in high-grade metamorphic terraines preserve peak metamorphic density during retrograde decompression? American Mineralogist 80, 641-644.

Vityk, M.O., Bodnar, R.J., 1995b. Textural evolution of synthetic fluid inclusions in quartz during reequilibration, with applications to tectonic reconstruction. Contributions to Mineralogy and Petrology 121, 309-323.

Vityk, M.O., Bodnar, R.J., 1998. Statistical microthermometry of synthetic fluid inclusions in quartz during decompression reequilibration. Contributions to Mineralogy and Petrology 132, 149-162.

Wacey, D., 2009. Early Life on Earth: A Practical Guide. Springer.